11-22-2023

Tidal Bed Stress Asymmetry and Sediment Transport in Estuaries

Austin Scott Hudson
Portland State University

Recommended Citation

Tidal Bed Stress Asymmetry and Sediment Transport in Estuaries

by

Austin Scott Hudson

A dissertation submitted in partial fulfillment of the
requirements for the degree of

Doctor of Philosophy
in
Civil and Environmental Engineering

Dissertation Committee:
David Jay, Chair
Stefan Talke
Scott Wells
Dacian Daescu

Portland State University
2023

Abstract

Rivers and estuaries provide numerous ecological, economic, and cultural resources. The value of these resources is greatly influenced by sediment transport processes, which can be affected by human activities and climate variability. A key driver of sediment transport in tidal rivers and estuaries is tidal asymmetry of velocity and bed stress, which can manifest from both non-linear tidal interactions and linear interactions among astronomical tidal constituents.

In this study, an analytical framework is developed to examine and describe the dynamics of bed stress asymmetry in semidiurnal, diurnal, and mixed-tide estuaries (Chapter 1). While tidal velocity asymmetry has been previously analyzed, this study is the first of its kind to directly evaluate spatial and temporal variability of bed stress asymmetry in rivers and estuaries. Because erosion and subsequent sediment transport is fundamentally a function of bed stress, this study improves understanding of how tidal asymmetry influences residual (subtidal) sediment transport.

The analytical framework is summarized by three non-dimensional numbers that scale and classify the dynamics of bed stress asymmetry and sediment transport in rivers and estuaries. The framework provides thresholds for ebb- and flood-dominant sediment transport, and illustrates that flood dominant sediment transport can prevail in ebb dominant velocity fields (and vice versa). Particles with low thresholds for transport can also exhibit different and even opposing transport to those with higher thresholds. Furthermore, sediment transport can be driven by diurnal tidal constituents in systems that are traditionally classified as semidiurnal, and vice versa. This can confound efforts

to understand sediment transport patterns, but is clarified by the non-dimensional numbers developed herein. Because bed stress asymmetry is controlled by the relative velocity amplitudes and phases of tidal constituents, which vary over fortnightly, semiannual, interannual, and decadal cycles, residual sediment transport patterns in estuaries are constantly changing. As a result, morphological stability of estuaries and alluvial rivers is ephemeral and likely attained only in an approximate sense.

Application of the framework to observations in real systems suggests that bed stress asymmetry can contribute to particle trapping, channel shoaling, and may even act as a filter or seasonal barrier for sediment moving through an estuary (Chapter 2). A particular case of bed stress asymmetry was also examined in fuller detail for ebb-dominant, convergent estuaries with large river discharge (Chapter 3). In such systems, opposing along-channel gradients in tidal and fluvial velocity establish a global bed stress minimum, which can also contribute to particle trapping/sorting and seasonal storage of sediments. Analytical expressions for along channel profiles of bed stress and the location of the bed stress minimum were developed to study how changes in river discharge and channel geometry might influence particle trapping and were found to agree well with AdH 2D numerical model simulations. Channel development and flow regulation can alter tidal bed stress asymmetry and thereby shift sediment transport thresholds, with implications for channel shoaling; sediment supply to estuary turbidity maxima, wetlands, and the coastal margin; and the concentration and distribution of sediment-borne contaminants. Many estuaries experience tidal asymmetry, so the framework developed herein can be applied to a wide range of systems.

This work is dedicated to Becky.

Doing something great is all about teamwork.

And she is the best teammate I have ever had.

Acknowledgements

I would like to acknowledge and thank my family and friends who have supported and inspired me and, in most cases, have made great sacrifices of their own to make this journey possible; my friends and coworkers at the United States Army Corps of Engineers who profoundly shaped my perspective of the world and of my profession; and my dissertation committee for their personal and professional guidance, and for providing me with the knowledge and skills that have enhanced my sense of purpose and fulfillment in life.

And finally, I would like to acknowledge and give my humble gratitude to the dedication and sacrifice of all the other crazy and aspiring scientists in the world. Without their contributions, my work would not be possible, and more importantly, we would still be living in the dark. I would like to especially acknowledge those who judiciously apply their craft in a fast-paced, fast-changing world, without whom, we may live in the dark once again.

Table of Contents

List of Tables

List of Figures

Preface

When mountains rise out of the earth like monuments of stone

For ages does she persevere to oust them from their throne

She charges forth and strikes their brow, then rallies back to sea

By ocean spray, rain and ice, all things return to me

And in the middle of the din, man tries to find a way

Doing what they must or can to make it through the day

Till the land, build a house, reach beyond the sky

Crown thy head above earth, so goes the battle cry

But like a net clutched in fist, she gathers what was won

To bring the bounty of the land to where the rivers run

And in the stream entombed in clay their history she sows

To be reborn on wing or fin so all that was is one

For ages will she persevere, so the cycle goes

And all is one within her sphere, so the cycle goes

Austin Scott Hudson

Mosier, OR

25-Aug-2023

Introduction

Rivers and estuaries are woven into the fabric of our history and future as a species. They symbolize life, energy, and change—and for good reason. Estuaries are some of the most biologically productive places on earth (Bianchi 2007), and most of the world population live near rivers and estuaries (Bianchi and Allison 2009). Some of the earliest civilizations on earth are synonymous with the rivers along which they were founded—the Tigris and Euphrates in Mesopotamia, the Nile in Egypt, and the Yellow River in China, to name a few. And the importance of rivers to humans and life as we know it has not decreased in modern times. For example, salmon and the Columbia River are a part of the cultural and spiritual identity of many tribes in the Pacific Northwest, and they are central subjects for many of the land use policies throughout the region today (CRITFC 2023). The Colorado River alone supplies water to over 25 million people, and the Delaware River supplies water to over 15 million people (EPA 2016a). More than 40,000 kilometers of inland and intracoastal waterways are operated and maintained in the United States (USACE 2023), upon which about $1.8 trillion of international imports and exports traveled in 2021 (USDOT 2023). Hydropower projects accounted for about 7% of electricity generation—and over 99% of electrical energy storage—in the United States in 2019 (USDOE 2021). And in 2020, the United States commercial seafood industry landed about 8.4 billion pounds of fish, supported 1.1 million jobs, and generated $154.7 billion in sales (NMFS 2020), much of which was supported by ports, infrastructure and/or fisheries in estuaries and rivers.

In the middle of all this activity, however, many of the nation's rivers and estuaries are losing ecological function, are increasingly polluted, and verging on becoming hazardous liabilities. For example, over half of the 220 million acres of wetlands that existed in the conterminous United States prior to European settlement have been drained and converted to other uses—over 60 acres per hour between the 1780's and the 1980's (Dahl 1990). Today, more than 175,000 river miles of in-stream fish habitat, and 280,000 river miles of riparian habitat, are considered to be in poor condition, according to the United States Environmental Protection Agency (EPA 2020). And in a recent nationwide survey, 40% (over 24,000 river miles) of river miles sampled contained fish with PCB (polychlorinated biphenyl) concentrations above EPA's human health fish tissue benchmark for cancerous effects (18 ppb; EPA 2020). Projected future increases in human population and climate variability will only deepen our reliance—and impact—on estuaries and rivers further yet (Elliot et al. 2019), and so our very survival requires knowledgeable and conservative stewardship of the natural processes that make a river.

Rivers are dynamic in every sense, changing and evolving over timescales ranging from seconds to millennia. As the transition zone between rivers and the ocean, estuaries can be even more dynamic because they are affected by both coastal (e.g., tides) and fluvial forcing. Changes in rivers and estuaries occur naturally, for example, fluctuations in precipitation drive seasonal variability in river discharge, and the relative positioning of celestial bodies drive daily, monthly, annual, and decadal fluctuations in water level. However, anthropogenic changes in rivers and estuaries can match and even eclipse those delivered by nature (Meybeck 2003; Williams et al. 2014). For example,

present-day withdrawals from the Colorado River are so great that over 90% of the river discharge no longer reaches the sea (Schmidt et al. 2022). Natural and anthropogenic changes can affect water supply (Richter et al. 2013) and water quality (Cloern 2001) in rivers and estuaries, but also the supply and quality of sediment (Walling and Fang 2011; USEPA 1987), which in turn influences virtually every aspect of estuarine and riverine environments. For example, spring rains and/or snowmelt runoff in temperate regions can, within a few days or weeks, provide most of the sediment delivered to an estuary during the year (Naik and Jay 2011; Moftakhari et al. 2015; Mckee et al. 2013; Sommerfield and Wong 2011; Woodruff et al. 2001). This sediment can either accumulate on wetlands to sustain their morphology (Friedrichs and Perry 2001; Boyd et al. 2016; Morris et al. 2022); deposit on the riverbed, which in some cases blocks navigation (Meade et al. 1969; Hickson 1930) and can even lead to channel avulsions (Chatanantavet et al. 2012; Nittrouer et al. 2012); or move out to sea and supply material for beaches (Gelfenbaum and Kaminsky 2010). Flow regulation by dams can reduce spring runoff events considerably and the associated sediment supply further yet, which can limit the amount of sediment available to downstream locations (Naik and Jay 2011; Moftakhari et al. 2015). Sometimes, human activities introduce contaminants into rivers that bind to sediments, which are then redistributed throughout a water body and can pose a risk to human health and wildlife (Haushild et al. 1973; Hubbel and Glenn 1973; Sheldon and Hites 1978; Bopp et al. 1981; Hornberger et al. 1999; Davis et al. 2007). Human activities can also alter sediment transport processes in a river and estuary, which can lead to erosion/deposition hot spots on the bed (Hickson 1961; Meade 1969), beach

3

accretion/erosion (Kaminsky et al. 2010), hyperturbid and/or hypoxic conditions (Chernetsky et al. 2010; Talke et al. 2009), and a restructuring of the food web (Crossland et al.2005; Sherwood et al. 1990; Woodland et al. 2022).

Federal and local governments are spending billions of dollars to remediate the negative or adverse impacts of humans on rivers and estuaries (e.g., EPA 2014, 2016b, 2017), and to restore and conserve riverine and estuarine habitats (e.g., BPA 2023). However, restoration and remediation efforts are only as effective as the science that guides them, and knowledge gaps can minimize benefit, increase cost, and may even nullify management activities (i.e., increase risk). The purpose of this study is to better understand river-estuary sediment transport processes in order to provide guidance for management activities in rivers and estuaries and their supporting watersheds. The analysis focuses on sediment transport in rivers and estuaries that are influenced by the motion of the tides, because the physics of sediment transport in these systems is complex and not fully understood, as will be discussed below. The paper is organized into three chapters:

1. Tidal Bed Stress Asymmetry and Sediment Transport in Estuaries, Part I: Theory

2. Tidal Bed Stress Asymmetry and Sediment Transport in Estuaries, Part II: Application to observations and system classification

3. The Bed Stress Minimum in Tidal Rivers

where each chapter represents a standalone paper that has been submitted to (or published in) a peer-reviewed journal. Chapter 1 presents a generalized analytical framework for studying bed stress asymmetry and sediment transport in estuaries, and Chapter 2 applies

this framework to observations in real systems. Chapter 3 represents a particular case of the first two chapters, by focusing on spatial patterns of ebb-tide bed stress, which help describe sediment transport patterns in rivers with strong river discharge. Following these chapters, the main results and potential pathways for future research are summarized in the Conclusion.

A common theme among the chapters is a focus on the fluid mechanics term, "bed stress". Bed stress defines the amount of shear force per unit area imparted by the water on the riverbed and is an important consideration for informed sediment management practices because of its strong influence on the fate and transport of sediment (Dyer 1986). As water flows through a river, a sediment particle resting on the riverbed will be exposed to drag and lift forces proportional to the bed stress, and when these mobilizing forces outweigh stabilizing forces (e.g., gravity), the particle will move. Once particles are in motion, the rate of transport (number of particles moving in a certain direction per unit time) is also proportional to the bed stress. Note that bed stress is non-linearly related to water velocity, and so modest changes in water velocity can lead to large changes in bed stress and sediment transport. Because water velocity is spatially variable in rivers and estuaries, spatial gradients in bed stress develop, which can create sediment convergent zones, contribute to particle trapping and alter morphology (Friedrichs 1995; Lanzoni and Seminara 2002; Pittaluga et al 2015; Schuttelaars and De Swart 1997). Thus, the bed stress controls two important aspects of sediment transport that are relevant to management decisions in estuaries: 1) when will sediment move? And 2) how much sediment will move, and to where? Because the physical characteristics of estuaries

varies system-to-system, the answers to these questions are not always simple or straightforward. By studying spatial and temporal variability of the bed stress, this dissertation helps to add clarity to these two questions in the following ways:

- Defining non-dimensional numbers to classify the dynamics of bed stress in estuaries and tidal rivers.
- Developing an analytical framework that can be used to interpret in-situ observations of velocity, water levels, and discharge to infer sediment transport patterns.
- Applying the framework to observations in real systems to identify and characterize physical mechanisms that can contribute to particle transport, sorting, and trapping in estuaries.

The physics of many estuaries in the world have been altered by humans in one of two ways (or both): 1) changes in river discharge due to dams, irrigation, and/or diversion, and 2): changes in channel morphology by dredging, flow/water level control structures, and/or land reclamation. Climate variability can also fall into one of these two categories (e.g., changes to river basin hydrology and alteration of mean sea level that alter water depths or the spatial distribution of tidal flats). Hence, this study approaches the questions of sediment transport through the lens of how changes in river discharge and channel geometry influence sediment transport mechanisms in estuaries. The results and analytical framework, therefore, are intended to guide management activities and capital investments that are influenced by (or agents of) changes in river discharge and channel geometry. Because the framework is generalized, it is applicable to a wide range of systems, and can help clarify (and perhaps correct) notions of sediment transport in many estuaries, as will be shown below.

References

Bianchi, T. S. (2007). *Biogeochemistry of estuaries*. Oxford University Press.

Bianchi, T. S., & Allison, M. A. (2009). Large-river delta-front estuaries as natural
    "recorders" of global environmental change. *Proceedings of the National
    Academy of Sciences*, *106*(20), 8085-8092.

Bopp, R. F., Simpson, H. J., Olsen, C. R., & Kostyk, N. (1981). Polychlorinated
    biphenyls in sediments of the tidal Hudson River, New York. *Environmental
    Science & Technology*, *15*(2), 210-216.

Boyd, B. M., & Sommerfield, C. K. (2016). Marsh accretion and sediment accumulation
    in a managed tidal wetland complex of Delaware Bay. *Ecological
    Engineering*, *92*, 37-46.

BPA. (2023). https://www.cbfish.org/Report.mvc/BudgetsAndExpenditures. *Accessed 02-
    Sep-2023*.

Chatanantavet, P., Lamb, M. P., & Nittrouer, J. A. (2012). Backwater controls of avulsion
    location on deltas. *Geophysical Research Letters*, *39*(1).

Chernetsky, A. S., Schuttelaars, H. M., & Talke, S. A. (2010). The effect of tidal
    asymmetry and temporal settling lag on sediment trapping in tidal
    estuaries. *Ocean Dynamics*, *60*(5), 1219-1241.

Cloern, J. E. (2001). Our evolving conceptual model of the coastal eutrophication
    problem. *Marine ecology progress series*, *210*, 223-253.

CRITFC. (2023). https://critfc.org/salmon-culture/we-are-all-salmon-people/. *Accessed 27-Aug-2023.*

Crossland, C. J., Baird, D., Ducrotoy, J. P., Lindeboom, H., Buddemeier, R. W., Dennison, W. C., ... & Swaney, D. P. (2005). The coastal zone—a domain of global interactions. In *Coastal fluxes in the Anthropocene: the land-ocean interactions in the coastal zone project of the International Geosphere-Biosphere Programme* (pp. 1-37). Berlin, Heidelberg: Springer Berlin Heidelberg.

Dahl, T. E. (1990). *Wetlands losses in the United States, 1780's to 1980's*. US Department of the Interior, Fish and Wildlife Service.

Davis, J. A., Hetzel, F., Oram, J. J., & McKee, L. J. (2007). Polychlorinated biphenyls (PCBs) in San Francisco Bay. *Environmental Research*, *105*(1), 67-86.

Dyer, K. (1986). Coastal and estuarine sediment dynamics. *John Wiley and Sons, Chichester, Sussex (UK), 1986, 358.*

Elliott, M., Day, J. W., Ramachandran, R., & Wolanski, E. (2019). A synthesis: what is the future for coasts, estuaries, deltas and other transitional habitats in 2050 and beyond?. In *Coasts and estuaries* (pp. 1-28). Elsevier.

EPA. (2014). "RECORD OF DECISION, Lower Duwamish Waterway Superfund Site".

EPA. (2016a). National Rivers and Streams Assessment 2008-2009: A Collaborative Survey (EPA/841/R-16/007). Washington, D.C. http://www.epa.gov/national-aquatic-resource-surveys/nrsa.

EPA. (2016b). "RECORD OF DECISION, Lower 8.3 Miles of the Lower Passaic River Part of the Diamond Alkali Superfund Site Essex and Hudson Counties, New Jersey".

EPA. (2017). "RECORD OF DECISION, Portland Harbor Superfund Site Portland, Oregon".

EPA. (2020). National Rivers and Streams Assessment 2013–2014: A Collaborative Survey. EPA 841-R-19-001. Washington, DC. https://www.epa.gov/national-aquatic-resource-surveys/nrsa.

Friedrichs, C. T. (1995). Stability shear stress and equilibrium cross-sectional geometry of sheltered tidal channels. *Journal of Coastal Research*, 1062-1074.

Friedrichs, C. T., & Perry, J. E. (2001). Tidal salt marsh morphodynamics: a synthesis. *Journal of Coastal Research*, 7-37.

Gelfenbaum, G., & Kaminsky, G. M. (2010). Large-scale coastal change in the Columbia River littoral cell: An overview. *Marine Geology*, *273*(1-4), 1-10.

Haushild, W. L., Dempster Jr, G. R., & Stevens Jr, H. H. (1973). *Distribution of radionuclides in the Columbia River streambed from the nuclear reactors, Hanford Reservation to Longview, Washington* (No. TID-26531). Geological Survey, Portland, Oreg.(USA). Water Resources Div.

Hickson, R. E. (1930). Shoaling on the lower Columbia River. *The Military Engineer*, *22*(123), 217-219.

Hickson, R. E. (1961). Columbia River ship channel improvement and maintenance. *Journal of the Waterways and Harbors Division*, *87*(3), 71-94.

Hornberger, M. I., Luoma, S. N., van Geen, A., Fuller, C., & Anima, R. (1999). Historical trends of metals in the sediments of San Francisco Bay, California. *Marine Chemistry*, *64*(1-2), 39-55.

Hubbell, D. W., & Glenn, J. L. (1973). *Distribution of radionuclides in bottom sediments of the Columbia River estuary*. US Government Printing Office.

Kaminsky, G. M., Ruggiero, P., Buijsman, M. C., McCandless, D., & Gelfenbaum, G. (2010). Historical evolution of the Columbia River littoral cell. *Marine Geology*, *273*(1-4), 96-126.

Lanzoni, S., & Seminara, G. (2002). Long-term evolution and morphodynamic equilibrium of tidal channels. *Journal of Geophysical Research: Oceans*, *107*(C1), 1-1.

McKee, L. J., Lewicki, M., Schoellhamer, D. H., & Ganju, N. K. (2013). Comparison of sediment supply to San Francisco Bay from watersheds draining the Bay Area and the Central Valley of California. *Marine Geology*, *345*, 47-62.

Meade, R. H. (1969). Landward transport of bottom sediments in estuaries of the Atlantic coastal plain. *Journal of Sedimentary Research*, *39*(1), 222-234.

Meybeck, M. (2003). Global analysis of river systems: from Earth system controls to

    Anthropocene syndromes. *Philosophical Transactions of the Royal Society of*

    London. Series B: Biological Sciences, *358*(1440), 1935-1955.

Moftakhari, H. R., Jay, D. A., Talke, S. A., & Schoellhamer, D. H. (2015). Estimation of

    historic flows and sediment loads to San Francisco Bay, 1849–2011. *Journal of*

    hydrology, *529*, 1247-1261.

Morris, J. T., Drexler, J. Z., Vaughn, L. J., & Robinson, A. H. (2022). An assessment of

    future tidal marsh resilience in the San Francisco Estuary through modeling and

    quantifiable metrics of sustainability. *Frontiers in Environmental Science*, *10*,

    1039143.

Naik, P. K., & Jay, D. A. (2011). Distinguishing human and climate influences on the

    Columbia River: Changes in mean flow and sediment transport. *Journal of*

    hydrology, *404*(3-4), 259-277.

Nittrouer, J. A., Shaw, J., Lamb, M. P., & Mohrig, D. (2012). Spatial and temporal trends

    for water-flow velocity and bed-material sediment transport in the lower

    Mississippi River. *Bulletin*, *124*(3-4), 400-414.

NMFS. (2023). Fisheries Economics of the United States, 2020. U.S. Dept. of

    Commerce, NOAA Tech. Memo. NMFS-F/SPO-236, 231 p.

Pittaluga, M.B., Tambroni, N., Canestrelli, A., Slingerland, R., Lanzoni, S., & Seminara,

    G. (2015). Where river and tide meet: The morphodynamic equilibrium of alluvial

    estuaries. *Journal of Geophysical Research: Earth Surface*, *120*(1), 75-94.

Richter, B. D., Abell, D., Bacha, E., Brauman, K., Calos, S., Cohn, A., ... & Siegfried, E. (2013). Tapped out: how can cities secure their water future?. *Water Policy*, *15*(3), 335-363.

Schmidt, J. C., Bruckerhoff, L., Salehabadi, H., & Wang, J. (2022). The Colorado River. *Large Rivers: Geomorphology and Management, Second Edition*, 253-319.

Schuttelaars, H. M., & De Swart, H. E. (1997). An idealized long-term morphodynamic model of a tidal embayment.

Sheldon, L. S., & Hites, R. A. (1978). Organic compounds in the Delaware River. *Environmental Science & Technology*, *12*(10), 1188-1194.

Sherwood, C. R., Jay, D. A., Harvey, R. B., Hamilton, P., & Simenstad, C. A. (1990). Historical changes in the Columbia River estuary. *Progress in Oceanography*, *25*(1-4), 299-352.

Sommerfield, C. K., & Wong, K. C. (2011). Mechanisms of sediment flux and turbidity maintenance in the Delaware Estuary. *Journal of Geophysical Research: Oceans*, *116*(C1).

Talke, S. A., de Swart, H. E., & De Jonge, V. N. (2009). An idealized model and systematic process study of oxygen depletion in highly turbid estuaries. *Estuaries and coasts*, *32*, 602-620.

USACE. (2023). https://www.usace.army.mil/Missions/Civil-Works/Navigation/. *accessed 26-Aug-2023*.

USDOE. (2021). U.S. Hydropower Market Report, January 2021.

USDOT. (2023). 2023 Port Performance Freight Statistics Program: Annual Report to

Congress. https://doi.org/10.21949/1528357

USEPA. (1987). An overview of sediment quality in the United States.

Walling, D. E., & Fang, D. (2003). Recent trends in the suspended sediment loads of the

world's rivers. *Global and planetary change*, *39*(1-2), 111-126.

Williams, M., Zalasiewicz, J., Davies, N., Mazzini, I., Goiran, J. P., & Kane, S. (2014).

Humans as the third evolutionary stage of biosphere engineering of

rivers. *Anthropocene*, *7*, 57-63.

Woodland, R. J., Harris, L., Reilly, E., Fireman, A., Schott, E., & Heyes, A. (2022). Food

web restructuring across an urban estuarine gradient. *Ambio*, *51*(4), 888-900.

Woodruff, J. D., Geyer, W. R., Sommerfield, C. K., & Driscoll, N. W. (2001). Seasonal

variation of sediment deposition in the Hudson River estuary. *Marine

Geology*, *179*(1-2), 105-119.

Chapter 1: Tidal Bed Stress Asymmetry and Sediment Transport in Estuaries, Part I: Theory

This chapter has been submitted to the Journal of Geophysical Research: Earth Surface.

See author contribution statement below.

Contributing Authors:

Austin Scott Hudson

David A. Jay

Stefan A. Talke

1.1 Abstract

Tidal asymmetry in estuaries is a key driver of residual sediment transport. Accordingly, this contribution provides an improved, more-general formulation of how river flow-tide interactions influence tidal asymmetry and flood/ebb dominance of sediment transport in estuaries. We here extend previous analytical relationships for bed stress and tidal asymmetry to include the effects of tidal amplitude, tidal phase, and residual velocity into a single, one-dimensional framework to evaluate residual sediment transport patterns in estuaries. The framework includes asymmetry caused by the phase relationships between tidal constituents at diurnal, semidiurnal, terdiurnal, and quarterdiurnal frequencies, and is summarized by three non-dimensional numbers that scale and classify the dynamics of bed stress asymmetry in semidiurnal, diurnal, and mixed-tide estuaries. Comparison of these numbers to different sediment transport metrics shows that even modest residual velocities ($\sim \frac{1}{9}$ of the tidal current amplitude in semidiurnal systems) can reverse the asymmetry in bed stress and sediment transport that is induced by tidally asymmetric currents. Moreover, because sediment transport is a time integrated process, we show that flood dominant sediment transport can prevail in ebb dominant velocity fields (and vice versa). Particles with low thresholds for erosion/transport can also exhibit different and even opposing transport than those with higher thresholds. Many estuaries experience tidal asymmetry, and residual velocities sufficiently large to alter or reverse asymmetry, so the framework described herein applies to a wide range of systems.

15

1.2   Introduction

This study analyzes residual frequency (subtidal, or tidally filtered) bed stress patterns to better understand how tides and residual currents influence the tidal asymmetry of bed stress and sediment transport in estuaries. Clarifying how tidal asymmetry affects sediment transport can inform sediment management because tidal asymmetry influences many aspects of estuaries such as long-term morphological changes (Guo et al. 2014), the magnitude and location of estuary turbidity maxima (ETM; Jay and Musiak, 1994; Burchard and Baumert 1998; Jay et al., 2007; Chernetsky et al. 2010), the distribution of sediment-borne contaminants (Chant et al. 2011), and accretion rates in wetlands due to sea level rise and/or subsidence (Friedrichs and Perry 2001; Deverel et al., 2014). Understanding how tides and river discharge influence tidal asymmetry is critical because the tidal properties, river discharge, and channel geometry in many estuaries have been, and are being, altered by human activities and/or climate change, which can alter the magnitude and direction of sediment transport. For example, tidal flats play an important role in maintaining ebb-dominant transport in estuaries (Speer and Aubrey 1985), and the loss of tidal flat area due to mean sea level rise can induce flood dominant sediment transport (Guo et al. 2018). Because river discharge has such a strong influence on tidal amplitudes and phases (Godin 1985, 1991; Jay and Flinchem 1997), dams and flow regulation can also alter tidal asymmetry (Yu et al. 2020). Similarly, channel modifications and harbor development that increase water depths or reduce friction can enhance tidal asymmetry, modifying the distribution and

16

location of sediment deposition (Cox et al. 2021; Vellinga et al. 2014) and in some cases leading to hyperturbid conditions (Chernetsky et al. 2010).

The direction and magnitude of residual sediment transport can be influenced by many tidally-asymmetric processes such as settling and scour lag (Chernetsky et al. 2010; Friedrichs et al. 1998; Postma 1961), tidal asymmetry in velocity magnitudes and durations (Allen et al. 1980; Hoitink et al. 2003; Guo et al. 2018; Speer and Aubrey 1985), correlations of velocity shear and vertical mixing (Jay and Musiak 1994; Jay et al., 2007; 2015; Burchard and Baumert 1998; Dijkstra et al., 2017), stratification effects on mixing (Geyer 1993), and tidal covariance of velocity and sediment concentration (Burchard et al. 2018). In a macrotidal estuary, tidal asymmetry of velocity is a dominant mechanism for sediment transport and particle trapping, especially in the freshwater zone upstream of salinity intrusion (Allen et al. 1980). Because tidal velocity asymmetry is spatially variable, due to amplification and damping of tidal velocities along the channel and changes in the phasing of tidal constituents, sediment convergence zones can develop, leading to deposition on the bed and/or local turbidity maxima (Allen et al. 1980; Chernetsky et al., 2010). Tidal asymmetry in velocity can result from non-linear interactions through friction and channel geometry as tides propagate into shallow water, but can also manifest linearly between astronomical tidal constituents. Thus, nonlinear, barotropic tidal asymmetry in a semidiurnal estuary (where M_2 is the principal tidal constituent), will lead to greater velocities during flood tide (flood dominant) when the M_2 and M_4 velocity constituents (u_{M2} and u_{M4}) reinforce one another during flood (Figure 1.1a), and greater during ebb tide velocities (ebb dominant) when u_{M2} and u_{M4} reinforce

17

one another during ebb (Speer and Aubrey 1985). Similarly, linear barotropic tidal

asymmetry can occur in mixed-tidal systems driven by the K_1, O_1 and M_2 constituents,

with asymmetry alternating between flood and ebb dominant velocities over the sidereal

month (Hoitink et al. 2003; Figure 1.1c).
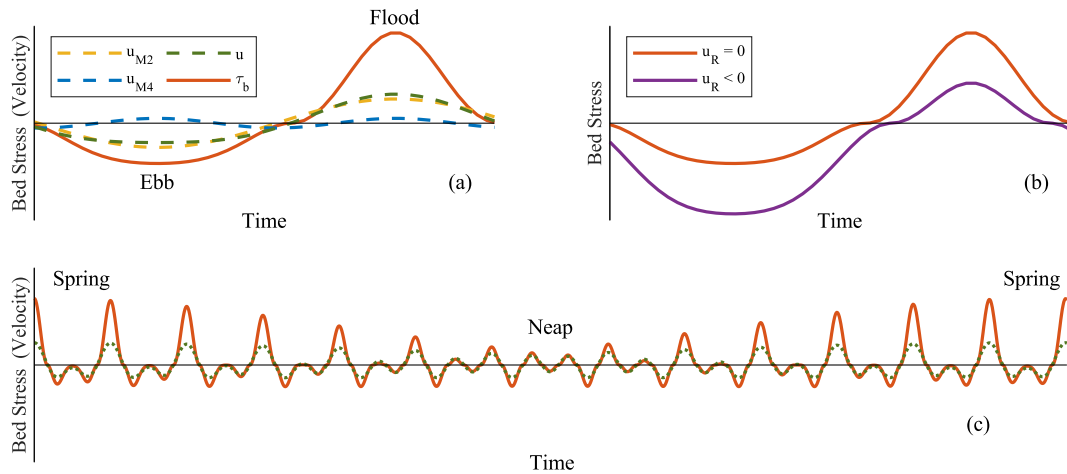
Figure 1.1. (a) An example of how bed stress (sold line) and velocity (dashed lines) can vary over one M2 tidal cycle for a flood dominant semidiurnal system without residual currents ($u = u_{M2} + u_{M4}$); as shown, the M4 reduces total velocity and stress during ebb, and amplifies during flood (b) Flood dominant bed stress (red line) can become ebb dominant (yellow line) if residual velocity is negative. (c) Bed stress and velocity can alternate between flood and ebb dominant over the diurnal (K1 +O1) declinational cycle for mixed tidal systems ($u = u_{M2} + u_{K1} + u_{O1}$), even without overtides or residual current.

However, velocity asymmetry does not, by itself, adequately define residual

sediment transport patterns because sediment transport scales with the bed stress, or the

velocity raised to some power greater than one (Dyer 1986). Thus, asymmetries observed

in the velocity field are amplified in the bed stress (see Figure 1.1) and by extension the

sediment transport. Furthermore, sediment transport results from transport process

integrated over time, rather than the maximum and minimum values over a tidal cycle,

and sediments may not move at all if the bed stress is insufficient to erode them. One

metric that is often used to estimate sediment transport is the excess bed stress ($|\tau_b|-\tau_c$), which is based on the idea that whenever the bed stress τ_b exceeds the critical bed stress for a given particle τ_c, sediment will move (see Dyer 1986; Sanford & Maa, 2001). Integrating the excess bed stress over the tidal cycle captures the approximate time history of particle movement (neglecting lag and water column effects) and can be used as a proxy for residual sediment transport (Dronkers 2016; Hoitink et al. 2003).

The value of τ_c depends on particle size and density, even for non-cohesive sediments (Dyer 1986), so different sediment size classes may, in principle, move differently, possibly even in different directions, in the same velocity field. For example, a given particle may experience net flood transport in flood-dominant locations because the bed stress does not exceed τ_c during ebb. At the same time, a particle with a lower τ_c may experience net ebb transport because the area between τ_b and τ_c (i.e., the excess bed stress) is greater during ebb than flood (Figure 1.2). Thus, tidal asymmetry in bed stress and transport thresholds work together to control residual transport patterns for a given grainsize and can act to sort particles in the estuarine environment (Chernetsky et al. 2010; Dronkers 1986), though, in practice, hiding, consolidation, biotic, and flocculation effects can also influence the spatial distribution of sediment (Manning et al. 2010).
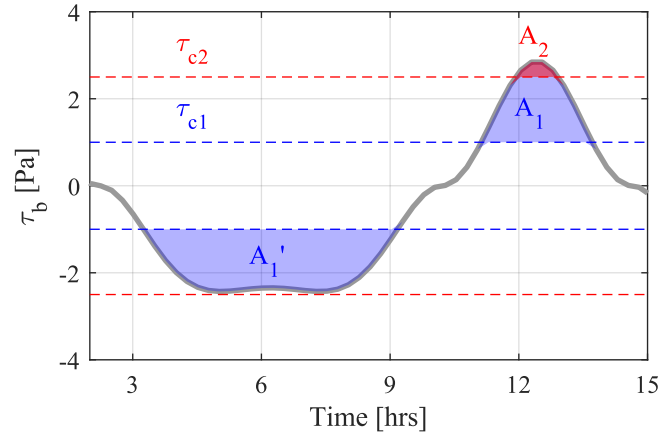
Figure 1.2. Time series of bed stress τ_b (solid line) during one tidal cycle for flood dominant velocity field driven by M_2, M_4 and residual currents. Dashed lines show critical bed stress τ_c for two different grainsizes. The area between τ_b and τ_c defines the net transport during the tidal cycle. Because $A_1' > A_1$, more erodible particles experience net ebb transport, while particles with a higher τ_c may show flood-dominant transport. In this figure the M_2 and M_4 amplitudes are 1 ms^{-1} and 0.3 ms^{-1}, respectively, and the phases are set to zero. The residual current is -0.25 ms^{-1}.

The origins and consequences of tidal asymmetry in sediment transport have been

well analyzed, but most studies have focused on semidiurnal estuaries with river

discharge and residual (subtidal, or tidally filtered) velocities that are weak compared to

tidal velocities. However, the residual flow can alter and even switch ebb/flood

dominance of the bed stress, and hence sediment transport, when the residual velocity is

large enough (Figure 1.1b). Hoitink et al. (2003) extended the discussion of tidal

asymmetry into diurnal regimes, and Nidzieko (2010) demonstrated that asymmetry in

mixed tide systems can be diminished or reversed by compound overtides (MK_3 in that

study), but neither study includes the influence of residual velocity. Guo et al. (2016)

examined residual sediment transport and long-term morphological changes induced by

semidiurnal and diurnal tidal velocity asymmetry in the Yangtze Estuary (monthly

averaged river discharge ranging from 10,000 to 60,000 m^{3}s^{-1}), and found that river

discharge and river-tide interactions can significantly modify residual sediment transport driven by tidal asymmetry (see also Gong et al. 2017, and Guo et al. 2019). Tidal velocity asymmetry in semidiurnal systems has also been shown to enhance (or weaken) particle trapping driven by density driven residual currents and thereby modulate the magnitude and location of ETM (Burchard and Baumert 1998; Burchard et al. 2018; Chernetsky et al. 2010). However, the specifics of how residual currents influence tidal asymmetry in sediment transport remain unclear. For example, when the velocity is tidally asymmetric, what is the residual velocity threshold that induces a transition from ebb to flood dominant sediment transport?

This study builds on previous work to show how tidal properties and residual velocity influence bed stress asymmetry and sediment transport in semidiurnal, diurnal, and mixed estuarine systems. The purpose of the study is to provide a relatively simple and widely applicable framework for scientists and resource managers who are concerned with residual sediment transport patterns in estuaries. Though we leave it for further study, the bed stress patterns examined herein also influence turbulent mixing, stratification, salinity intrusion, and settling lag effects. In particular we will address the following research questions:

- How do tidal and residual currents influence tidal asymmetries in bed stress and sediment transport?

- How does the critical bed stress influence residual sediment transport?

- How do the properties of residual bed stress and transport compare between semidiurnal, diurnal, and mixed-tide estuaries?

This is the first part of a two-part contribution. Part II applies the theory developed here to two river-estuary systems, Delaware Estuary and North San Francisco Bay; these illustrate how a variety of types of bed stress asymmetry arise in estuaries that are nominally semidiurnal or mixed, in terms of the vertical tide.

1.3   Analytical Framework

We develop here a one-dimensional (1D) framework that describes sediment transport in terms of the near-bed velocity. The framework uses the bed stress approximation of Doodson (1924) and Godin (1991), and extends previous metrics of asymmetry to include the influence of residual velocity and multiple tidal constituents that are observed in estuaries. Bed stress defines the amount of shear force per unit area imparted by the water on the riverbed, typically over an averaging period that is long compared to turbulent coherent structures but small compared to tidal variability (10-20 minutes; see e.g., Stacey et al., 1999; Talke et al. 2013). Informed sediment management practices must consider spatiotemporal patterns in bed stress because of its strong influence on the fate and transport of sediment (Dyer 1986). Following standard practice, we define bed stress in terms of the near-bed fluid velocity u, fluid density ρ, and a drag coefficient representing the roughness of the bed C_d (Proudman 1952):

$$\tau_b = \rho C_d u |u| \tag{1},$$

where the absolute value represents the reversal in stress direction that occurs when tidal velocities change sign. Assuming bed velocity is driven by tidal constituents and residual (subtidal) currents, the product $u|u|$ creates a broad spectrum of frequencies. For our

purposes, the drag coefficient is assumed constant in space and time, and we assume that tidal velocities are smoothly varying (i.e., have been averaged over 10-20 minutes). We neglect the variability in bed stress that can be driven by variability in bed-form shapes and distributions, and by turbulent coherent motions (Fong et al, 2009; Talke et al., 2013; Branch et al., 2021). Similarly, we assume that the residual and tidal velocities are evaluated at the same vertical location within the water column and are representative of the influence of residual and tidal motions on bed stress. Our 1D framework also neglects rotational effects, and lateral sediment transport associated with channel curvature and lateral variations in density and/or depth. These "secondary circulation" effects have their own distinctive frequency signatures in an estuary, but are beyond our present scope.

In the analytical expressions below, we assume the velocity is composed of the diurnal constituents K_1 and O_1; the semidiurnal constituents M_2, S_2 and N_2; the terdiurnal constituents M_{O3} and M_{K3}; the quarter diurnal constituents M_4 M_{S4}, and M_{N4}; and a residual (subtidal) component u_R, which represents low frequency motions (e.g., river discharge, stokes drift, gravitational circulation) and can be either positive or negative. By convention, we assume that positive velocity is directed landward (flood). To clarify exposition, this analysis omits many tidal constituents that appear in velocity records collected in estuaries. For example, M_6 is sometimes important in D_2-dominant systems with low river inflow (see e.g., Godin, 1991; Talke et al., 2018). Nevertheless, our analysis includes the dominant constituents in systems in which river flow is prominent. Also, a number of constituents are neglected because they primarily act to modulate those considered; for example, P_1 modulates K_1, and K_2 modulates S_2 over a six-month cycle,

because each pair is separated in frequency by 2 cy/yr. Insight into the effects of these modulations can be obtained through varying the K_1 or S_2 amplitude and phase. Additionally, more (or entirely different) constituents can be readily included in the velocity field without changing the non-dimensional numbers that scale tidal bed stress asymmetry (below).

Finally, the analytical framework used here considers only the first three of the six frequencies commonly used to describe tides by Doodson (1921) and subsequent works (e.g., Godin, 1972) in terms of "Doodson numbers"; these frequencies are 1 cy/day, 1 cy/sidereal month, and 1 cy/yr. Neglect of the last three Doodson numbers, involving periods of 8.85, 18.6 and 20,940 years, is justified because: a) tidal properties in the river systems of primary interest here are modulated by river flow, both on short and seasonal time scales; b) the effects of longer-term tidal variability can be assessed by piecewise experimentation with different constituent values; and (c) our tidal analysis approach used in Part II assesses tidal species on short 6-8 day time scales, rather than constituents, effectively subsuming long-period tidal variations into the variability due to other processes; see below. The Doodson number representations of the constituents used herein are provided in Table 1.1.

Table 1.1. Doodson number representations of constituents used in Equations 2-4.

Tidal Constituent	Frequency [hr^{-1}]	Doodson Numbers.
O1	0.0387306589	[1,-1,0,0,0,0]
K1	0.04178074180	[1,1,0,0,0,0]
N2	0.0789992532	[2,-1,0,1,0,0]
M2	0.0805114007	[2,0,0,0,0,0]
S2	0.0833333333	[2,2,-2,0,0,0]
MO3	0.1192420005	[3,-1,0,0,0,0]
MK3	0.1222921425	[3,1,0,0,0,0]
MN4	0.15951065449	[4,-1,0,1,0,0]
M4	0.1610228169	[4,0,0,0,0,0]
MS4	0.1638447414	[4,2,-2,0,0,0]

Hoitink et al. (2003) evaluated tidal asymmetry related to the K_1-O_1-M_2 triad by representing the diurnal (D_1) tidal species by combining K_1 and O_1 oscillations as a single wave (u_1) with time variable amplitude and phase. Here, this approach is extended to other tidal species. The semidiurnal (D_2) species is described by M_2, S_2, and N_2 oscillations combined as a semidiurnal wave (u_2). In the D_3 and D_4 species, the MK_3 and MO_3 oscillations are represented by a combined terdiurnal wave (u_3); and the M_4, MS_4, MN_4 oscillations are represented by a combined quarterdiurnal wave (u_4). The general expression for combining n constituents into a single wave for species k is:

$$u_k = \sum_{i=1}^{n} U_i \cos(\omega_i t - \phi_i) = U_k \cos(\omega_k t - \phi_k) \hspace{2cm} (2a),$$

where U_i, ω_i and ϕ_i are the tidal current amplitude, angular frequency, and phase of the

i^{th} constituent. While u is understood to indicate current velocity here, a similar analysis

can be done for tidal fluctuations in water level, ζ (e.g., Hoitink et al. 2006). The

velocity amplitude (U_k) and phase (ϕ_k) of the combined wave are:

$$U_k^2 = \sum_{i,j}^n U_i U_j \cos(\theta_i - \theta_j) \tag{2b},$$

$$\tan(\phi_k) = \frac{\sum_i^n U_i \sin(\theta_i)}{\sum_i^n U_i \cos(\theta_i)} \tag{2c},$$

where $\theta_i = \omega_i t - \phi_i$, and the summation in Equation 2b occurs over constituents i and j.

Equations 2a-c embody a "two-timescale" assumption. Tidal currents, described

by $U_k \cos(\omega_k t - \phi_k)$, vary during the tidal day (the "short" timescale) over which the U_k

and θ_k are constant. The velocity amplitude U_k and phase θ_k vary on a "long" timescale

(fortnightly to tidal monthly), as does the residual velocity, u_R. Not surprisingly, this

framework does not fully describe estuarine and tidal river variability. Thus, the river

inflow power spectrum may have variability on daily to weekly time scales, especially in

systems managed for hydropower generation ("power peaking"); however, this variability

is typically relatively small in natural rivers compared to monthly flow variability (Jay

and Naik, 2011). Similarly, two-layer density driven circulation varies from day to day

due to variable vertical mixing and density stratification, a fact that has not prevented the

widespread use of similar two-timescale theories (e.g., Jay and Musiak, 1996). Overall,

our approach improves clarity of exposition, at a (generally) small cost in realism.

Substitution of u_{K1} and u_{O1} into Equation 2a gives the diurnal wave as follows:

$$u_1 = u_{K1} + u_{O1} = U_1 \cos(\omega_1 t - \phi_1) \tag{3a},$$

where: U_1 and ϕ_1 are given by:

$$U_1 = [U_{K1}^2 + U_{O1}^2 + 2U_{K1}U_{O1}\cos(2\omega_2 t + \phi_{O1} - \phi_{K1})]^{1/2} \tag{3b},$$

$$\phi_1 = tan^{-1}\left(\frac{U_{K1}\sin(\phi_{K1}-\omega_2 t)+U_{O1}\sin(\phi_{O1}+\omega_2 t)}{U_{K1}\cos(\phi_{K1}-\omega_2 t)+U_{O1}\cos(\phi_{O1}+\omega_2 t)}\right) \tag{3c},$$

and ω_1, ω_2 are the first two basic angular frequencies introduced by Doodson (1921) and correspond to the first two Doodson numbers.

Likewise, substitution of u_{M2}, u_{S2} and u_{N2} into Equation 2a gives the semidiurnal (D$_2$) wave:

$$u_2 = u_{M2} + u_{S2} + u_{N2} = U_2 \cos(2\omega_1 t - \phi_2) \tag{4a},$$

$$\begin{aligned}U_2 = [U_{M2}^2 + U_{S2}^2 + U_{N2}^2 + 2U_{M2}U_{S2}\cos(2(\omega_2 - \omega_3)t + \phi_{M2} - \phi_{S2}) \\ + 2U_{M2}U_{N2}\cos(\omega_2 t + \phi_{N2} - \phi_{M2}) \\ + 2U_{S2}U_{N2}\cos((3\omega_2 - 2\omega_3)t + \phi_{N2} - \phi_{S2})]^{1/2}\end{aligned} \tag{4b},$$

$$\phi_2 = tan^{-1}\left(\frac{U_{M2}\sin(\phi_{M2})-U_{S2}\sin(2(\omega_2-\omega_3)t-\phi_{S2})+U_{N2}\sin(\omega_2 t+\phi_{N2})}{U_{M2}\cos(\phi_{M2})+U_{S2}\cos(2(\omega_2-\omega_3)t-\phi_{S2})+U_{N2}\cos(\omega_2 t+\phi_{N2})}\right) \tag{4c}.$$

where ω_3 is the third basic angular frequency introduced by Doodson (1921). Equations (3b,c) and (4b,c) differ in form (even if N$_2$ is neglected), because S$_2$ is separated in frequency from M$_2$ by 2 cy/mo, while K$_1$ and O$_1$ (and M$_2$ and N$_2$) differ by only 1 cy/mo (Table 1.1). Also, our representation of N$_2$ is imprecise by $\frac{1\ cy}{8.85\ yr}$, because the fourth Doodson number is neglected.

The terdiurnal wave shares a similar form with the diurnal wave (substituting u_{MK3} and u_{MO3} for u_{K1} and u_{O1}, respectively), and the quarterdiurnal wave follows the semidiurnal wave (see Equations S4 and S5 in Appendix 1.8.1). Altogether, the velocity can be represented as a combination of diurnal, semidiurnal, terdiurnal, quarterdiurnal and residual motions:

$$u = U_1 \cos(\omega_1 t - \phi_1) + U_2 \cos(2\omega_1 t - \phi_2) \\ + U_3 \cos(3\omega_1 t - \phi_3) + U_4 \cos(4\omega_1 t - \phi_4) + u_R \tag{5}.$$

To illustrate how tidal-fluvial interactions influence bed stress asymmetry, we next develop an approximation of $u|u|$ through an expansion of the contributing terms. While there are a number of approaches, we employ a two-term approximation following Doodson (1924) and Godin (1991), which limits the number of terms resulting from the approximation:

$$u'|u'| \approx au' + bu'^3 \tag{6},$$

where u' is the dimensionless velocity:

$$u \stackrel{\text{def}}{=} Uu' \tag{7},$$

and U is the dimensional velocity scale equal to the maximum value of the current such that $-1 \leq u' \leq 1$. The coefficients a and b were determined in a least-squares sense to be 0.3 and 0.7, respectively (Godin 1991). Godin (1991) evaluated six different approximations to $u|u|$, including a three-term approximation ($u'|u'| \approx au' + bu'^3 + cu'^5$), and found that while Equation 6 is not the most numerically accurate approach, "it provides an adequate overall representation of the physical effects of friction even though

it cannot reproduce them in all their details." Equation 6 has been used in numerous applications, including investigations of tidal propagation (Godin 1999), subtidal water levels (Buschman et al. 2009), and storm surge (Familkhalili et al. 2020). This approach results in far fewer terms than the Dronkers (1964) expansion, with its flow-dependent coefficients, but is also arguably somewhat less accurate. Given the relatively large number of tidal constituents considered here, simplicity (and the resulting conceptual clarity) is the primary consideration.

Substituting Equation 5 into Equation 6, and then expanding the cubic term, results in 40 terms corresponding to residual (subtidal) and tidal frequencies (See Appendix 1.8.3). Seven terms contribute to the residual frequency bed stress τ_R:

$$
\begin{aligned}
\tau_R = \rho C_d \Bigg\{ & \underbrace{aUu_R}_{(1)} + \frac{b}{U}\frac{3}{4}\Bigg[\underbrace{\frac{4}{3}u_R^3}_{(2)} + \underbrace{2(U_1^2 + U_2^2 + U_3^2 + U_4^2)u_R}_{(3)} \\
& + \underbrace{U_2^2 U_4 cos(2\phi_2 - \phi_4)}_{(4)} + \underbrace{U_1^2 U_2 cos(2\phi_1 - \phi_2)}_{(5)} \\
& + \underbrace{2U_1 U_2 U_3 cos(\phi_1 + \phi_2 - \phi_3)}_{(6)} + \underbrace{2U_1 U_3 U_4 cos(\phi_1 + \phi_3 - \phi_4)}_{(7)} \Bigg] \Bigg\}
\end{aligned}
\tag{8a,}
$$

which shows that the residual bed stress is driven by a linear residual velocity term (1); non-linear velocity term (2); tidal and residual interactions (term 3); the semidiurnal asymmetry (term 4); and diurnal asymmetries (terms 5-7). While u_2 contributes to the last three terms in Equation 8a, we label these asymmetries diurnal because they are not possible without the diurnal constituents, and because "M_2" in strongly diurnal systems is partially an overtide of K_1 and O_1. Note that terms 4 and 5 in Equation 8a correspond to the tidal asymmetry of bed load transport relationship introduced by Hoitink et al. (2003),

but Equation 8a retains tidal-monthly variability that is important for sediment transport, especially in mixed tides systems that experience large diurnal inequalities during spring tide. Nidzieko (2010) develops similar expressions when introducing skewness of a tidal signal as a metric to define asymmetry in mixed-tide estuaries, but neither study includes the influence of residual velocity (such as caused by baroclinic circulation or river flow). Note that by residual bed stress, we are referring to the subtidal terms given in Equation 8a, which, as will be shown below, are representative of tidally-averaged bed stress, tidal asymmetry of bed stress magnitudes during ebb and flood tide, and net (tidal cycle average) sediment transport patterns.

Equation 8a may appear challenging to interpret but in a semidiurnal system without overtides ($u = u_2 + u_R$), the right hand side reduces to about $-\rho C_d \{U_R^2 + U_2^2\}$ when $U_R \geq U_2$, and about $-\rho C_d \left\{\frac{9}{8} U_R U_T\right\}$ when $U_R < U_2$ (see Godin 1991 and Hudson et al. 2022). Equation 8a can also be simplified by treating the last two terms on the right-hand side as modulations to the fifth term:

$$\tau_R = \rho C_d \left\{ \underbrace{aUu_R}_{(1)} + \frac{b}{U}\frac{3}{4}\left[\underbrace{\frac{4}{3}u_R^3}_{(2)} + \underbrace{2((1+\varepsilon_1^2)U_1^2 + (1+\varepsilon_2^2)U_2^2)u_R}_{(3)} \right.\right.$$
$$\left.\left. + \underbrace{\varepsilon_2 U_2^3 \cos(2\phi_2 - \phi_4)}_{(4)} + \underbrace{U_1^2 U_2(1 + 2\varepsilon_1\delta_3 + 2\varepsilon_1\varepsilon_2\delta_4)\cos(2\phi_1 - \phi_2)}_{(5)} \right]\right\}$$

(8b),

Where $\varepsilon_1 = \frac{U_3}{U_1}$ and $\varepsilon_2 = \frac{U_4}{U_2}$ scale the tidal velocity amplitudes of terms 6 and 7 relative to term 5 (see list of parameters in Table 1.4 of Appendix 1.8.2). Thus, while the amplitude of term 5 appears to first-order in Equation 8b, term 6 and 7 appear to $\mathcal{O}(\varepsilon)$ and $\mathcal{O}(\varepsilon^2)$,

respectively. Moreover, the semidiurnal asymmetry appears at $\mathcal{O}(\varepsilon)$, because U_4 is small, further emphasizing the importance of the diurnal (linear) asymmetry. The tidal asymmetry phase parameters $\delta_3 = \frac{cos(\phi_1+\phi_2-\phi_3)}{cos(2\phi_1-\phi_2)}$ and $\delta_4 = \frac{cos(\phi_1+\phi_3-\phi_4)}{cos(2\phi_1-\phi_2)}$, which can be positive or negative, scale the strength of the tidal asymmetry phase relationship (e.g., strongly flood/ebb dominant vs symmetrical), and suggests that terms 6 and 7 may become important to residual bed stress patterns during certain windows of the tidal month when $cos(2\phi_1 - \phi_2) \cong 0$ (i.e., when the diurnal inequality is small in mixed systems, see Section 3.3), even if ε_1 and ε_2 are small (see Section 3.2). Thus, while it may be generally sound practice to ignore term (7) or other terms involving two overtides, these terms may sometimes be important.

The amplitude and phases of tidal species, U_k and ϕ_k, vary over the tidal month due to the interaction between the constituents in a given frequency band, which will modify the tidal asymmetry in bed stress (Figure 1.3a,c). We leave the term "tidal month" ambiguous because different combinations of constituents interact over periods of about 27.3 to 29.5 days. For example, because M$_2$ and S$_2$ differ in frequency by about 2cy/mo (Table 1.1), they interact over the spring-neap cycle (14.77d) in relation to the phases of the moon, with a cycle lasting half a synodic month (length 29.531d; Gerkema, 2019). On the other hand, M$_2$ and N$_2$ differ by about 1 cy/mo and interact, therefore, over the anomalistic month of 27.555d (the apogee-perigee cycle), while K1 and O1 (differing by 1 cy/mo) interact over the declination cycle of the moon, one sidereal month (27.321d). Tidal monthly variability in tidal mixing can also alter residual currents driven by

baroclinic circulation (Jay 1991; Jay and Musiak 1996), and thus lead to further modulation of τ_R, as will be shown in Part II.
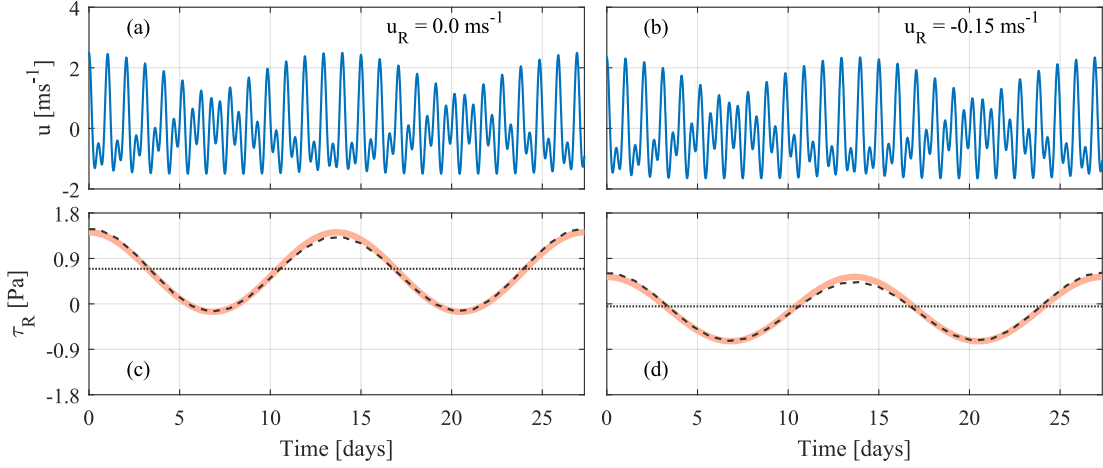
Figure 1.3. Timeseries of velocity described by Equation 5 (blue lines) and residual bed stress estimated by Equation 8a (red lines) for residual velocity $u_R = 0$ m s^{-1} (left) and $u_R = -0.15$ m s^{-1} (right). Tidal average of $\rho C_d (au' + bu'^3)$ is shown by dashed lines and tidal-monthly average by dotted lines. In this figure, $U_{M2} = U_{K1} = 1$ m s^{-1}, $U_{O1} = 0.5$ m s^{-1}, and all constituent phases are set to zero.

Tidal asymmetry can also be induced by other tidal constituents not included in Equation 8a, for example non-linearly by M_2-M_4-M_6 or linearly by P_1-K_1-S_2. However, their influence on tidal asymmetry is typically smaller than those included in Equation 8a (see Song et al. 2011) and are omitted herein to clarify the analysis. The purpose of this paper is to present a framework for studying how the residual velocity field influences sediment transport driven by tidal bed stress asymmetry. Accordingly, further investigation of other tidal interactions could be carried out by including more, or entirely different, constituents in Equation 8a. Nevertheless, we next explore additional tidal species and demonstrate that the species considered in Equation 5 represent the primary influence on tidal bed stress asymmetry. The most prominent species missing from

32

Equation 5 are u_5 and u_6, which represent overtides of the astronomical constituents (e.g.,

MK$_5$ and M$_6$) and are typically much smaller in magnitude than the lower frequency

species. Including u_5 and u_6 in the cubic term of Equation 6 would introduce seven

additional tidal interactions to the residual bed stress (Table 1.2). Note that the functional

form of the additional terms is similar to those in Equation 8 (e.g., $6u_2u_4u_6$ mirrors

terms 6 and 7 in Equation 8a), so the additional terms can be treated as modulations to the

semidiurnal and diurnal asymmetry (analogous to the formulation of Equation 8b).

However, because the additional terms scale with the product of two or more overtide

amplitudes, the modulations are $\mathcal{O}(\varepsilon^2)$ or $\mathcal{O}(\varepsilon^3)$ and can be ignored under most

circumstances. Terms involving overtides above M$_6$ are even smaller and have not been

demonstrated to be important, even though they have been measured in sediment

concentration time series (e.g., Van de Kreeke et al., 1997).

Table 1.2. Additional tidal interactions generated by including u_5 and u_6 in the cubic term of Equation 6.

$$3u_R u_5^2 = \frac{3}{2} u_R U_5^2$$

$$3u_R u_6^2 = \frac{3}{2} u_R U_6^2$$

$$3u_3^2 u_6 = \frac{3}{4} U_3^2 U_6 \cos{(2\phi_3 - \phi_6)}$$

$$6u_1 u_4 u_5 = \frac{6}{4} U_1 U_4 U_5 \cos{(\phi_1 + \phi_4 - \phi_5)}$$

$$6u_1 u_5 u_6 = \frac{6}{4} U_1 U_5 U_6 \cos{(\phi_1 + \phi_5 - \phi_6)}$$

$$6u_2 u_3 u_5 = \frac{6}{4} U_2 U_3 U_5 \cos{(\phi_2 + \phi_3 - \phi_5)}$$

$$6u_2 u_4 u_6 = \frac{6}{4} U_2 U_4 U_6 \cos{(\phi_2 + \phi_4 - \phi_6)}$$

1.4   Bed Stress Asymmetry and Species Factor

In Equation 8a, there are two groups of terms: 1) The three terms that contain u_R and u_R^3 (terms (1) to (3)) and will always have the same sign as the residual velocity u_R; and 2) four terms that change sign according to the phase relations between tidal constituents (terms (4) to (7)). Equation 8b condenses the second group of four terms in Equation 8a to two and emphasizes the importance of constituent ratios. A comparison of these two groups determines when the bed stress will be ebb dominant ($\tau_R < 0$) or flood dominant ($\tau_R > 0$). As will be shown below, relatively small residual velocities that oppose tidally induced asymmetry are capable of switching the ebb/flood dominance in bed stress, even if the velocity field remains relatively unchanged (Figure 1.3). According to Equation 8b the residual bed stress is negative (ebb dominant) when:

34

$$\left(\frac{4}{7}U^2 + 2\left((1 + \varepsilon_1^2)U_1^2 + (1 + \varepsilon_2^2)U_2^2 + \frac{2}{3}u_R^2\right)\right)u_R <$$

(9).

$$-\varepsilon_2 U_2^3 cos(2\phi_2 - \phi_4) - U_1^2 U_2(1 + 2\varepsilon_1\delta_3 + 2\varepsilon_1\varepsilon_2\delta_4)cos(2\phi_1 - \phi_2)$$

For example, in a semidiurnal estuary ($u \cong u_2 + u_4 + u_R$), the tidal currents are flood dominant when u_2 and u_4 reinforce one another on flood ($cos(2\phi_2 - \phi_4) > 0$), and the right-hand side of the equation is negative. In this case, the bed stress can become ebb dominant if the residual velocity u_R is negative and the left-hand side of Equation 9 becomes less than the right-hand side. The tidal currents are ebb dominant when $cos(2\phi_2 - \phi_4) < 0$, which makes the right-hand side of Equation 9 positive. In this case, the bed stress is ebb dominant so long as the left-hand side of Equation 9 remains smaller than the right-hand side, even when u_R is positive.

Bed stress asymmetry can be classified as predominantly semidiurnal (D_2-dominant), diurnal (D_1-dominant), or mixed (D_1-D_2) according to the relative magnitudes of the two terms on the right-hand side of Equation 9b. Thus, we define a non-dimensional number Π (the "Species Factor"), which scales the magnitude of the diurnal to the semidiurnal bed-stress asymmetry in terms of tidal species velocities and relative phases:

$$\Pi \overset{\text{def}}{=} \left|\frac{U_1^2(1 + 2\varepsilon_1\varepsilon_3 + 2\varepsilon_1\varepsilon_2\varepsilon_4)cos(2\phi_1 - \phi_2)}{\varepsilon_2 U_2^2 cos(2\phi_2 - \phi_4)}\right|$$

(10a).

We classify the asymmetry to be semidiurnal when $\Pi \ll 1$, mixed when $\Pi \approx 1$, and diurnal when $\Pi \gg 1$. Equation 10a highlights the importance of tidal phases in setting bed stress asymmetry, because, for example, even though $\varepsilon_2 U_2^2$ may be much larger than

35

U_1^2, the asymmetry may still be largely diurnal if $cos(2\phi_2 - \phi_4) \approx 0$. Typically, $2\varepsilon_1\varepsilon_3 + 2\varepsilon_1\varepsilon_2\varepsilon_4 < 1$, and so for classification purposes, Equation (10a) can be simplified to

$$\Pi \cong \left| \frac{U_1^2 cos(2\phi_1-\phi_2)}{\varepsilon_2 U_2^2 cos(2\phi_2-\phi_4)} \right| = \frac{F_u^2}{\varepsilon_2} \left| \frac{cos(2\phi_1-\phi_2)}{cos(2\phi_2-\phi_4)} \right| \tag{10b},$$

Where $\varepsilon_2 = \frac{U_4}{U_2}$ (as previously defined) and $F_u = \frac{U_1}{U_2}$ is the "Tidal Velocity Form Factor", which scales the diurnal and semidiurnal velocity amplitudes following Pugh (1987) who defined a "Tidal Form Factor" F in terms of the vertical amplitudes (ζ_i) of the diurnal and semidiurnal tidal constituents: $F = \frac{\zeta_{K1}+\zeta_{O1}}{\zeta_{M2}+\zeta_{S2}}$, by which tides may be roughly classified as follows:

$F = 0 \ to \ 0.25$ semidiurnal

$F = 0.25 \ to \ 1.50$ mixed-semidiurnal

$F = 1.50 \ to \ 3.00$ mixed-diurnal

$F > 3.00$ diurnal

Thus, tidal bed stress asymmetry in estuaries that are traditionally classified as semidiurnal (F<0.25), can be predominantly diurnal ($\Pi \gg 1$) if $cos(2\phi_2 - \phi_4) \cong 0$. In the following sections, the dynamics of bed stress asymmetry are explored in further detail for semidiurnal (D_2-dominant), diurnal (D_1-dominant), and mixed (D_1-D_2) tide estuaries.

1.4.1 Bed Stress Asymmetry in Semidiurnal-Dominant Systems

Consider first D_2-dominant systems ($\Pi \ll 1$), where term 5 in Equation 8b is small relative to term 4. From Equation 9, the bed stress is ebb dominant ($\tau_R < 0$) when:

$$\left(\frac{4}{7}U^2 + 2\left((1 + \varepsilon_1^2)U_1^2 + (1 + \varepsilon_2^2)U_2^2 + \frac{2}{3}u_R^2\right)\right)u_R < -\varepsilon_2 U_2^3 cos(2\phi_2 - \phi_4) \quad (11).$$

Note that the diurnal species appear on the left-hand side of Equation 11 and so can influence bed stress asymmetry in semidiurnal systems. Rearranging Equation 11 provides a relationship which describes the transition of bed stress from flood to ebb-dominance:

$$\varepsilon_{R2} < -\Lambda_2 cos(2\phi_2 - \phi_4) \quad (12),$$

where $\varepsilon_{R2} = \frac{u_R}{U_2}$ (the "Residual Asymmetry Parameter" for semidiurnal tides) scales the strength of the residual velocity relative to the semidiurnal velocity amplitude, $\Lambda_2 = $

$$\frac{\varepsilon_2 U_2^2}{\left(\frac{4}{7}U^2 + 2\left((1+\varepsilon_1^2)U_1^2 + (1+\varepsilon_2^2)U_2^2 + \frac{2}{3}u_R^2\right)\right)}$$ (the "Semidiurnal Asymmetry Parameter", Λ_2) scales

the semidiurnal nonlinear asymmetry amplitude, and the phase difference $cos(2\phi_2 - \phi_4)$ scales the semidiurnal asymmetry phase relationship. See Table 1.4 in Appendix 1.8.2 for a list of parameters used in the analytical framework.

Equation 12 states that whenever ε_{R2} is less than $-\Lambda_2 cos(2\phi_2 - \phi_4)$, the bed stress is ebb dominant; otherwise, the bed stress is flood dominant (Figure 1.4a). In the absence of residual velocity ($u_R = 0$), the requirement for ebb-dominant asymmetry reduces to $cos(2\phi_2 - \phi_4) < 0$, which is the classical condition cited in the literature for

a semidiurnal estuary (Dronkers 1964; Speer and Aubrey 1985). We note that ε_{R2} and Λ_2 vary over the tidal month, because U_k and ϕ_k are species values and vary with the phase of the moon and other factors.
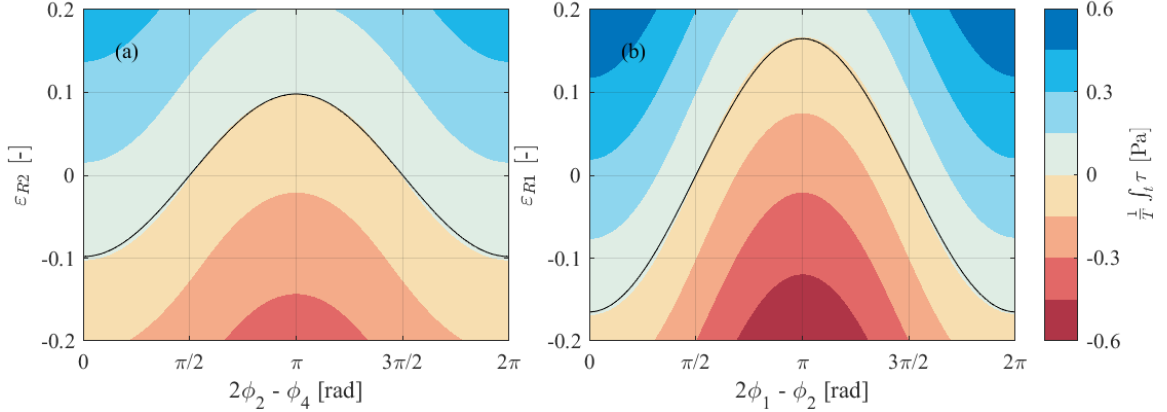
Figure 1.4. Example colormap of bed stress (Equation 1) averaged over several tidal cycles plotted vs $\varepsilon_{R2} = \frac{u_R}{U_2}$ and phase difference $2\phi_2 - \phi_4$ (a); and vs $\varepsilon_{R1} = \frac{u_R}{U_1}$ and phase difference $2\phi_1 - \phi_2$ (b). Solid line denotes $-\Lambda_2 cos(2\phi_2 - \phi_4)$ (see Equation 12) (a); and $-\Lambda_1 cos(2\phi_1 - \phi_2)$ (see Equation 14) (b). Averaged bed stress is positive (flood dominant) above this line and negative (ebb dominant) below this line. In this figure, $U_2 = 0.6$ ms^{-1}, $U_4 = 0.2$ ms^{-1}, and $u_R = [-0.15,0.15]$ ms^{-1} (a); and $U_2 = U_1 = 0.6$ ms^{-1}, and $u_R = [-0.15,0.15]$ ms^{-1} (b).

Because the semidiurnal asymmetry parameter $\Lambda_2 < 1$ and $cos(2\phi_2 - \phi_4) \leq 1$, Equation 12 shows that the residual bed stress switches sign for values of $|\varepsilon_{R2}| < 1$, or when $|u_R| < U_2$. For example, when $u = u_2 + u_4 + u_R$ and $cos(2\phi_2 - \phi_4) = 1$, the tidal currents are flood dominant, and the residual velocity must be less than $-\Lambda_2 U_2$ for the bed stress to be ebb dominant (i.e., $|u_R| > \Lambda_2 U_2$). Assuming that $U_4 \cong \frac{1}{3}U_2$, and that the bed stress switches sign for $|u_R| \ll U_k$ implies that the bed stress is ebb dominant when $u_R < -\frac{1}{9}U_2$ (Figure 1.4a; i.e., $|u_R| > \frac{1}{9}U_2$). The diurnal species can reduce the threshold for ebb dominant bed stress further, even if $\Pi \ll 1$, because U_1 appears in the

denominator of Λ_2. For example, if $U_1 \cong \frac{1}{3}U_2$, but for $cos(2\phi_1 - \phi_1) = 0$, the bed stress would be ebb dominant approximately when $u_R < -\frac{1}{12}U_2$ (e.g., potentially for smaller river flow magnitudes).

1.4.2 Bed Stress Asymmetry in Diurnal-Dominant Systems

The asymmetry of diurnal systems (Species Factor $\Pi \gg 1$; See Eq. 10) is mathematically similar to semidiurnal systems. However, in this case, terms 6-7 in Equation 8a will modulate the diurnal asymmetry amplitude. From Equation 9, the bed stress is ebb dominant ($\tau_R < 0$) when:

$$\left(\frac{4}{7}U^2 + 2\left((1 + \varepsilon_1^2)U_1^2 + (1 + \varepsilon_2^2)U_2^2 + \frac{2}{3}u_R^2\right)\right)u_R <$$
$$-U_1^2 U_2(1 + 2\varepsilon_1\delta_3 + 2\varepsilon_1\varepsilon_2\delta_4)cos(2\phi_1 - \phi_2) \tag{13}.$$

which gives an ebb dominant threshold in terms of a "Diurnal Asymmetry Parameter" as follows:

$$\varepsilon_{R1} < -\Lambda_1 cos(2\phi_1 - \phi_2) \tag{14},$$

where $\varepsilon_{R1} = \frac{u_R}{U_1}$ is the "Residual Asymmetry Parameter" for the diurnal-dominant case,

and $\Lambda_1 = \frac{U_1 U_2(1 + 2\varepsilon_1\delta_3 + 2\varepsilon_1\varepsilon_2\delta_4)}{\left(\frac{4}{7}U^2 + 2\left((1 + \varepsilon_1^2)U_1^2 + (1 + \varepsilon_2^2)U_2^2 + \frac{2}{3}u_R^2\right)\right)}$ is the "Diurnal Asymmetry Parameter".

Equation 14 states that when ε_{R1} is less than $-\Lambda_1 cos(2\phi_1 - \phi_2)$, then the bed stress is ebb dominant, otherwise the bed stress is flood dominant (Figure 1.4b). Without residual velocity ($u_R = 0$), Equation 14 reduces to $cos(2\phi_1 - \phi_2) < 0$ (see Hoitink et al.

39

2003). In contrast to the semidiurnal asymmetry, the Diurnal Asymmetry Parameter is modulated by overtides (terms 6 and 7 in Equation 8a), the effect of which is scaled by $(2\varepsilon_1\delta_3 + 2\varepsilon_1\varepsilon_2\delta_4)$. In situations when $(2\varepsilon_1\delta_3 + 2\varepsilon_1\varepsilon_2\delta_4) \ll 1$, the influence of overtides on the diurnal asymmetry can be neglected, to first-order (see discussion below).

As for semidiurnal systems, a relatively small residual velocity can reverse the direction of flood/ebb dominance of the diurnal asymmetry. However, because astronomical tides are typically much larger than overtides, a larger residual velocity is required to reverse the direction of the diurnal asymmetry. For example, when the tidal component is flood dominant $(cos(2\phi_1 - \phi_2) = 1)$, $U_2 = U_1$, and $U_3 = U_4 = 0$, the species factor $\Pi \rightarrow \infty$ due to the lack of overtides and overtide asymmetry (see Eq. 10b). In this case, the residual bed stress is ebb dominant if $u_R < -\frac{1}{6}U_1$, according to Equation 14 (Figure 1.4b). Like the semidiurnal asymmetry, the diurnal asymmetry can be modulated by species other than U_1 and U_2, even if $\Pi \gg 1$ (i.e., even when the bed stress asymmetry is diurnally dominant). For example, if $U_4 \cong \frac{1}{3}U_2$, but $cos(2\phi_2 - \phi_4) = 0$, the bed stress would be ebb dominant approximately when $u_R < -\frac{1}{7}U_1$.

Because U_k and ϕ_k (see Equation 2) vary over the tidal month, the residual bed stress, and hence the asymmetry parameters Λ_1 and Λ_2, are also time-variable. Thus, the residual velocity thresholds defining ebb-dominant bed stress changes throughout the tidal month (see Equations 12 and 14). The velocity field illustrated in Figure 1.3b, for example, has a greater diurnal velocity during tropic tides than during equatorial tides,

which alters the magnitude of the diurnal asymmetry in bed stress (Figure 1.5a and c). At the same time, the phase difference $2\phi_1 - \phi_2$ transitions from flood dominant during periods of strong diurnal inequality ("tropic tides", t < 5 days and t > 8 days) to ebb dominant during periods with less diurnal inequality (more "equatorial tides", 5 days < t < 8 days; Figure 1.5b). As a result, the residual (and tidally-averaged) bed stress also transitions from flood to ebb dominant (Figure 1.5d). However, because the residual velocity is negative, the residual bed stress remains ebb dominant for a longer period (3 days < t < 10 days; Figure 1.5c,d) than is implied by the phase difference $2\phi_1 - \phi_2$. Because the magnitude of U_1 is greater during tropic tides, a larger residual velocity threshold is required to switch between ebb/flood dominant residual bed stress than during equatorial tides (Figure 1.5c).
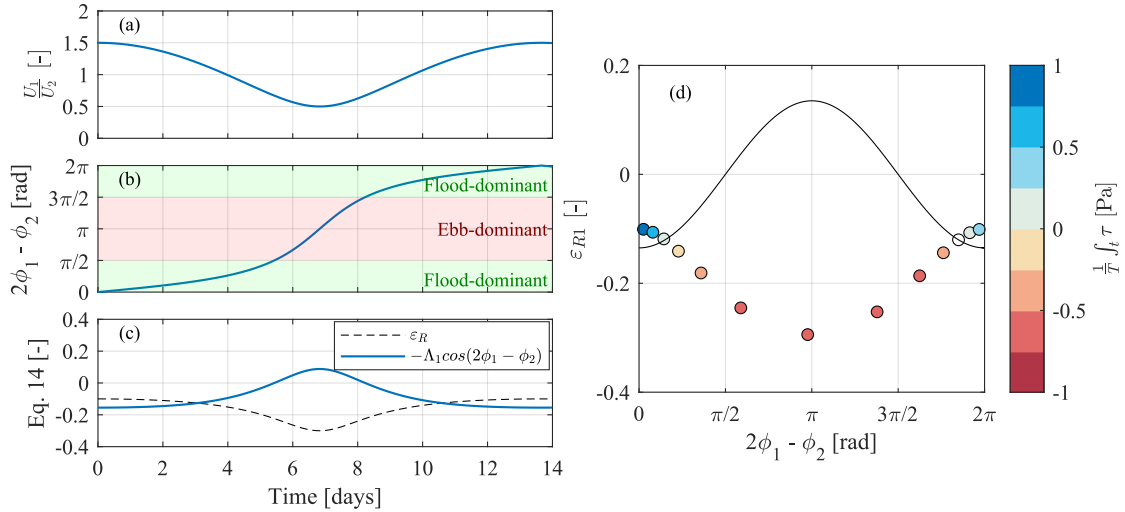
Figure 1.5. Example timeseries of $\frac{U_1}{U_2}$ (a), $2\phi_1 - \phi_2$ (b), and Equation 14 (c) for residual velocity $u_R = -0.15$ ms^{-1}, $U_{M2} = U_{K1} = 1$ ms^{-1}, $U_{O1} = 0.5$ ms^{-1}, with all constituent phases set to zero (same as Figure 1.3 b,d). The residual velocity scale ε_{R1} (colored circles) is greater/less than $-\Lambda_1 cos(2\phi_1 - \phi_2)$ (black line) during tropic/equatorial tide indicating flood/ebb-dominant residual bed stress (d).

41

In the diurnal case, it is also important to acknowledge the possible influence of terms 6 and 7 in Equation 8a on the relationship provided by Equation 14. Term 6 is the more likely of the two to be important because U_2 is likely to be enlarged by production of U_{M2} as an overtide of $U_{K1}+U_{O1}$, and because we expect $\varepsilon_1\varepsilon_2 \ll 1$. While ε_1 and ε_2 are considered to be small, overtides can still dominate the diurnal asymmetry in bed stress when $\cos(2\phi_1 - \phi_2)$ approaches zero, because the tidal asymmetry phase parameters δ_3 and δ_4 (see Equation 8) may be much larger than unity. However, the period of time when $\delta_3,\delta_4 \gg 1$ is limited to short intervals during the tidal month. For example, $\left|\frac{1}{\cos(2\phi_1-\phi_2)}\right| > 2$ occurs during the intervals when $2\phi_1 - \phi_2 = \left(\frac{\pi}{3},\frac{2\pi}{3}\right)$ and when $2\phi_1 - \phi_2 = \left(\frac{4\pi}{3},\frac{5\pi}{3}\right)$, each of which lasts about 1.5 days (see Figure 1.5b). Thus, for this example, $|\delta_3|$ and $|\delta_4|$ will be close to unity during most of the tidal month, and the values of δ_3 and δ_4 will be positive when terms 6 and 7 are in phase with term 5 and negative when they are $180°$ out of phase with term 5. These considerations allow simplification of the diurnal asymmetry parameter:

$$\Lambda_1 \cong \frac{U_1 U_2 (1\pm 2\varepsilon_1(1+\varepsilon_2))}{\left(\frac{4}{7}U^2+2\left((1+\varepsilon_1^2)U_1^2+(1+\varepsilon_2^2)U_2^2+\frac{2}{3}u_R^2\right)\right)} \tag{15},$$

where the term $2\varepsilon_1(1 + \varepsilon_2)$ is positive when terms 6 and 7 are in phase with term 5, and negative when terms 6 and 7 are $180°$ out of phase with term 5.

Equations 14 and 15 illustrate that overtides will either increase or decrease the residual velocity threshold for ebb dominant bed stress by a factor of about $2\varepsilon_1(1 + \varepsilon_2)$. For example, consider a velocity field similar to Figure 1.5, but also including $U_{MK3} = 0.2$

ms^{-1} and $U_{MO3} = 0.1 \text{ ms}^{-1}$, with $\phi_{MK3} = \phi_{MO3} = \pi$. In this case, $\varepsilon_1 = 0.2$, $\varepsilon_2 = 0$, and δ_3

is typically less than two during most of the fortnightly cycle (Figure 1.6a). Although δ_3

ranges from $-\infty$ to ∞, for a few days as term 5 transitions between flood and ebb

dominance ($4.5\text{d} < t < 6\text{d}$; and $7.5\text{d} < t < 9\text{d}$; Figures 1.6a and 1.5b), this period occurs

when both term 5 and 6 are close to zero and so the overtide asymmetry has a modest

influence on the ebb/flood dominance of the residual bed stress during these times

(Figure 1.6b). However, because terms 5 and 6 are out of phase throughout the tidal

month (Figure 1.6a,b), overtides will reduce the diurnal asymmetry in Equation 14 by a

factor of about $-2\varepsilon_1(1 + \varepsilon_2) = -0.4$, which decreases the residual velocity threshold for

ebb dominant bed stress by roughly 40% (compare Figures 1.5c and 1.6c).
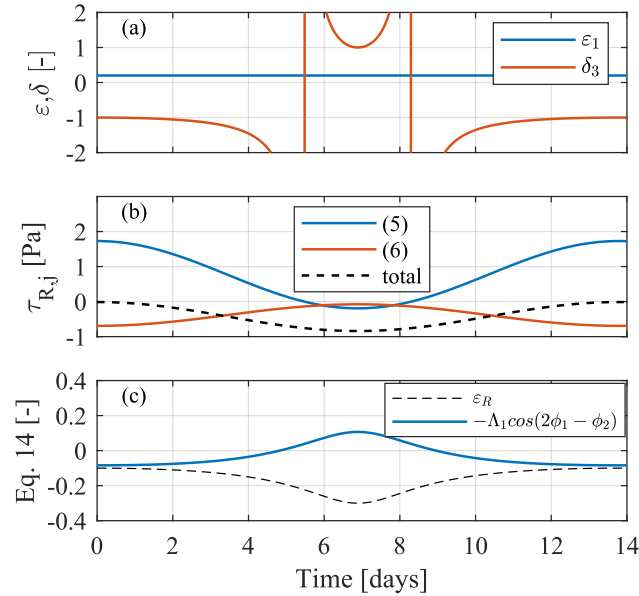
Figure 1.6. Example timeseries of ε_1 and δ_3 (a); terms 5 (blue line) and 6 (red line) of Equation 8a (dashed line) (b); and Equation 14 (c). In this figure, $u_R = -0.15 \text{ ms}^{-1}$, $U_{M2} = U_{K1} = 1 \text{ ms}^{-1}$, $U_{O1} = 0.5 \text{ ms}^{-1}$, $U_{MK3} = 0.2 \text{ ms}^{-1}$, and $U_{MO3} = 0.1 \text{ ms}^{-1}$, with $\phi_{MK3} = \phi_{MO3} = \pi$; all other constituent phases are set to zero.

43

1.4.3 Bed Stress Asymmetry in Mixed Tidal Systems

The mixed-tide case ($\Pi \cong 1$) is more difficult to describe concisely because the tidal asymmetry in Equation 8a is defined by the balance between seven terms with four tidal interaction terms. In this case, an expression similar to Equations 12 and 14 can be used to delineate flood and ebb dominance in the bed stress because they scale the magnitude of the semidiurnal and diurnal asymmetry relative to the residual velocity. Essentially, the residual velocity must be greater than the sum of the tidal asymmetry driven by the phase relationships between the diurnal, semidiurnal, terdiurnal, and quarterdiurnal waves (which may or may not be in phase). Combining Equations 12 and 14 gives the following residual velocity threshold for ebb-dominant bed stress in mixed tide systems:

$$\varepsilon_{R2} < -\Lambda_2 cos(2\phi_2 - \phi_4) - \Lambda_1 F_u cos(2\phi_1 - \phi_2) \tag{16},$$

which reduces to Equation 12 when $cos(2\phi_1 - \phi_2) \cong 0$, and to Equation 14 when $cos(2\phi_2 - \phi_4) \cong 0$. In the mixed tide case, the asymmetries reinforce each other if the cosine terms share the same sign, and an even greater negative residual velocity is required to switch from flood- to ebb-dominant residual bed stress, compared to the diurnal or semidiurnal cases. Similarly, an even greater positive residual velocity is required to switch from ebb to flood dominant. The four asymmetries in Equation 8a can also partially cancel each other when their signs differ, reducing the tidal asymmetry in bed stress and hence the residual velocity that is needed to change the sign of the residual bed stress.

Again, U_k and ϕ_k (see Equation 2) vary in time, modulating the residual bed stress (Equation 8) and the velocity threshold (right-hand side of Eq 16) over the tidal month. Moreover, the semidiurnal and diurnal asymmetries oscillate over the spring/neap (14.77d) and tropic/equatorial (13.66d) tidal cycles, respectively, which introduces semiannual (182.6d) variability into Equation 8, and hence Equation 16, for mixed-tide systems due to the harmonic convergence and divergence of the synodic and sidereal months. For example, consider the velocity field illustrated in Figure 1.5, but now including $U_{S2} = 0.5$ ms^{-1} and $U_{M4} = 0.2$ ms^{-1} (Figure 1.7a). In this case, U_2 varies over the tidal month, like U_1, but with a period of 14.77 days. After about 90 days, U_1 and U_2 are 180º out of phase (Figure 1.7b), which decreases the residual bed stress and thereby the residual velocity threshold (right-hand side of Equation 16; Figure 1.7e,f). Indeed, the residual bed stress is uniformly ebb dominant over the tidal month when U_1 and U_2 are roughly 180º of phase (60d < t < 120d), because ε_{R2} is always less than the right-hand side of Equation 16 (Figure 1.7e,f). Finally, the tidal bed stress asymmetry alternates between D$_1$-dominant and D$_2$-dominant over the tidal month (Figure 1.7d), following oscillations in $2\phi_1 - \phi_2$ (Figure 1.7c), with the largest values of Π occurring during tropic tides when U_1 and U_2 are roughly 90º out of phase (e.g., 50d < t < 70d). Of course, the residual velocity also varies seasonally in most systems, and will alter the results discussed here, in a manner that depends on the system, and varies from year to year.

45
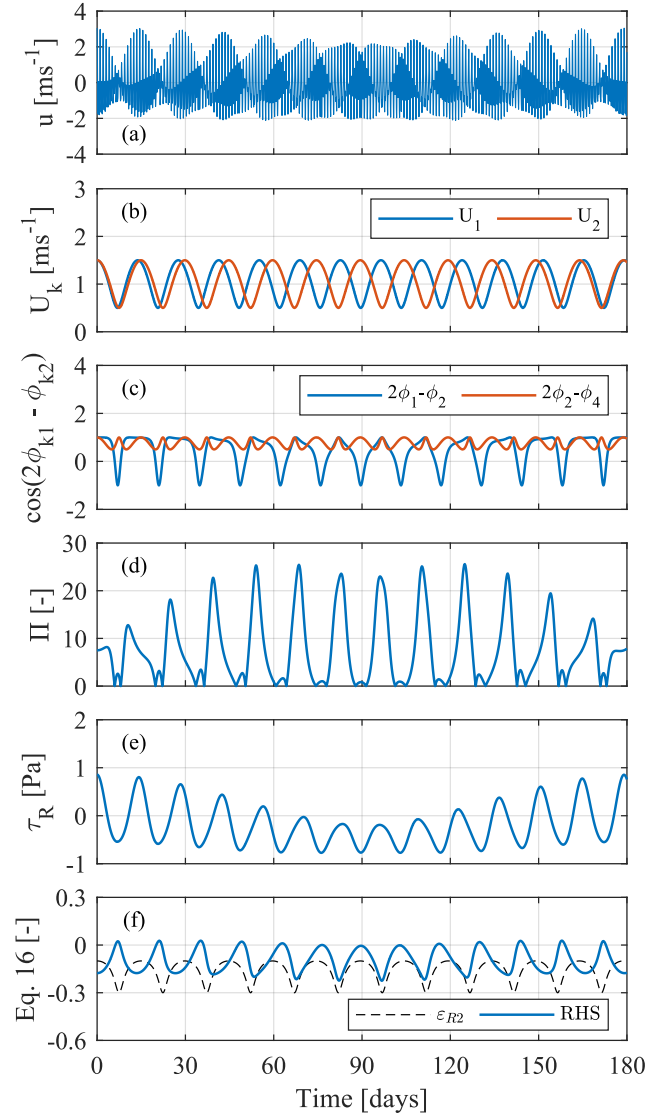
Figure 1.7. Example timeseries of u (a), U_k (b), $\cos(2\phi_{k1} - \phi_{k2})$ (c), Π (d), the residual bed stress τ_R (e) and Equation 16 (f) for residual velocity $u_R = -0.15$ ms^{-1}, $U_{M2} = U_{K1} = 1$ ms^{-1}, $U_{O1} = U_{S2} = 0.5$ ms^{-1}, and $U_{M4} = 0.2$ ms^{-1} with all constituent phases set to zero.

Another tidal interaction in mixed-tide estuaries that influences the residual bed stress and sediment transport is the diurnal inequality, which occurs when two ebb/food tides of unequal magnitude occur during the tidal day. Sediment transport in a mixed-tide estuary is greatest, and may only occur, during greater ebb/flood when the bed stress is

also greatest, particularly when the diurnal inequality is large. It can be shown that this mechanism for transport is captured by the framework described herein, because the phase relationships driving tidal bed stress asymmetry and the diurnal inequality are the same. Or more precisely, the phase relationships that create large diurnal inequalities are those that lead to large asymmetries in bed stress. For example, consider a velocity field composed of u_1 and u_2:

$$u(t) = U_1 cos(\omega_1 t - \phi_1) + U_2 cos(2\omega_1 t - \phi_2) \tag{17},$$

where the times of flood and ebb can be determined by setting $\frac{du}{dt} = 0$ and solving for t (see USCGS,1952). Assuming that U_k and ϕ_k are approximately constant over the course of the tidal day gives:

$$\frac{1}{2}\frac{U_1}{U_2} sin(\omega_1 t - \phi_1) + sin(2\omega_1 t - \phi_2) = 0 \tag{18}.$$

There are three limits to consider for Equation 18: D_1-dominant currents $\left(\frac{U_1}{U_2} \gg 2\right)$, D_2-dominant currents $\left(\frac{U_1}{U_2} \ll 2\right)$, and mixed D_1-D_2 currents $\left(\frac{U_1}{U_2} \approx 2\right)$.

For the D_1-dominant case, Equation 18 becomes $sin(\omega_1 t - \phi_2) = 0$, which implies that only one maximum and one minimum exist within the diurnal tidal period $t = [0, \frac{2\pi}{\omega_1})$. In other words, when $\frac{U_1}{U_2} \gg 2$ no diurnal inequality occurs, which requires two maxima and two minima per day, and the magnitude of the velocity during flood and ebb for D_1-dominant currents is given by:

$$u_{m,D1} = U_1 cos(m\pi) + U_2 cos(2\phi_1 - \phi_2 + 2m\pi), \qquad m = \{0, 1\} \tag{19},$$

47

where the values of m are restricted to provide flood and ebb velocities during one tidal period.

For D2-dominant currents, Equation 18 becomes $sin(2\omega_1 t - \phi_2) = 0$, and the times of flood and ebb are

$$t_{D2} = \frac{m\pi + \phi_2}{2\omega_1}, \qquad m = 0, 1, 2, ... \tag{20},$$

which, after substitution into Equation 17 gives the magnitude of the velocity during flood and ebb:

$$u_{m,D2} = U_1 cos\left(\frac{1}{2}(2\phi_1 - \phi_2 - m\pi)\right) + U_2 cos(m\pi), \qquad m = \{0, 1, 2, 3\} \tag{21}.$$

Note that the first term changes sign with the relative phase difference $2\phi_1 - \phi_2$, while the second term does not, leading to alternating addition/opposition of the two contributions.

Finally, for mixed D_1-D_2 currents, Equation 18 becomes

$$sin(\theta_2) + sin(\theta_1) = 2sin\left(\frac{\theta_2 + \theta_1}{2}\right) cos\left(\frac{\theta_2 - \theta_1}{2}\right) = 0 \tag{22},$$

where $\theta_k = \omega_k t - \phi_k$. Solving for t gives:

$$t_{D1-D2} = \frac{2m\pi + \phi_2 + \phi_1}{3\omega_1}, \qquad m = 0, 1, 2, ... \tag{23a},$$

$$t_{D1-D2} = \frac{2m\pi + \phi_2 - \phi_1}{\omega_1}, \qquad m = \frac{1}{2}, \frac{3}{2}, \frac{5}{2}, ... \tag{23b},$$

which, after substitution into Equation 18 gives:

$$u_{m,D1-D2} = U_1 \cos\left(\frac{1}{3}(2\phi_1 - \phi_2 - 2m\pi)\right)$$
$$+U_2 \cos\left(\frac{1}{3}(2\phi_1 - \phi_2 + 4m\pi)\right) \quad , \qquad m = \{0, 1, 2\} \qquad (24a).$$

$$u_{m,D1-D2} = U_1 \cos(2\phi_1 - \phi_2 - 2m\pi)$$
$$+U_2 \cos(2\phi_1 - \phi_2 - 4m\pi) \quad , \qquad m = \frac{1}{2} \qquad (24b).$$

Now the diurnal inequality can be determined from Equations 21 and 24 by taking the difference between greater flood/ebb and lesser flood/ebb velocity for corresponding values of m. For example, the diurnal inequality of flood velocity for D_2-dominant currents is given by $u_{0,D2} - u_{2,D2}$ (see Figure 1.8b):

$$2U_1 \cos\left(\frac{1}{2}(2\phi_1 - \phi_2)\right) \qquad (25a),$$

and the diurnal inequality of flood velocity for mixed D_1-D_2 currents is given by $u_{0,D1-D2} - u_{\frac{1}{2},D1-D2}$ (see Figure 1.8c):

$$U_1\left[\cos\left(\frac{1}{3}(2\phi_1 - \phi_2)\right) + \cos(2\phi_1 - \phi_2)\right]$$
$$+U_2\left[\cos\left(\frac{1}{3}(2\phi_1 - \phi_2)\right) - \cos(2\phi_1 - \phi_2)\right] \qquad (25b).$$

Equations 25a,b illustrate that the diurnal inequality of flood tides is greatest when $2\phi_1 - \phi_2 = 0$, and equals $2U_1$ for both D_2-dominant and mixed currents, and decreases to about $\sqrt{2}U_1$ when $2\phi_1 - \phi_2 = \frac{\pi}{2}$ (see Figure 1.8b,c). The diurnal inequality of flood tides is minimal when $2\phi_1 - \phi_2 = \pi$, but during this time greater ebb is larger than greater flood and the velocity field is ebb dominant—under these conditions the diurnal inequality of ebb tides is greatest and equals $2U_1$ (see Figure 1.8b,c).

49

Thus, the diurnal inequality, and more specifically the magnitude of the velocity during flood and ebb, is scaled by $cos(2\phi_1 - \phi_2)$—the same as for the diurnal bed stress asymmetry (Term 5 in Equation 8a). For example, when u_1 and u_2 are in phase ($2\phi_1 - \phi_2 \cong 0$), the flood velocity is greater than ebb velocity for D_1-dominant currents (Figure 1.8a), which creates flood dominant residual bed stress. Systems with D_2-dominant and mixed D_1-D_2 currents show a similar pattern, except that the magnitude of the velocity during the lesser flood is smaller than during either ebb (Figure 1.8b,c). However, when averaged over the tidal cycle, the velocity (and residual bed stress) remains flood dominant. As the phase difference $2\phi_1 - \phi_2$ increases, the magnitudes of the velocity during flood and ebb converge, equaling each other when $2\phi_1 - \phi_2 = \frac{\pi}{2}$ (Figure 1.8b,c), which reduces the diurnal asymmetry to zero. In the example above, the diurnal inequality of flood tides and hence flood dominance of the diurnal tidal asymmetry is greatest when spring and tropic tides coincide, because u_1 and u_2 reach their maximum values and are in phase (see Figures 1.7 and 1.8). Different phasing of the diurnal and semidiurnal waves can lead to strong flood- or ebb-dominant tidal asymmetry on these large tides. In either case, this is the type of asymmetry that we refer to as "linear", because it is created by phase differences between astronomical tidal species, not nonlinear overtides. Accordingly, it is often larger in mixed diurnal-semidiurnal systems, than nonlinear asymmetry driven by overtides.
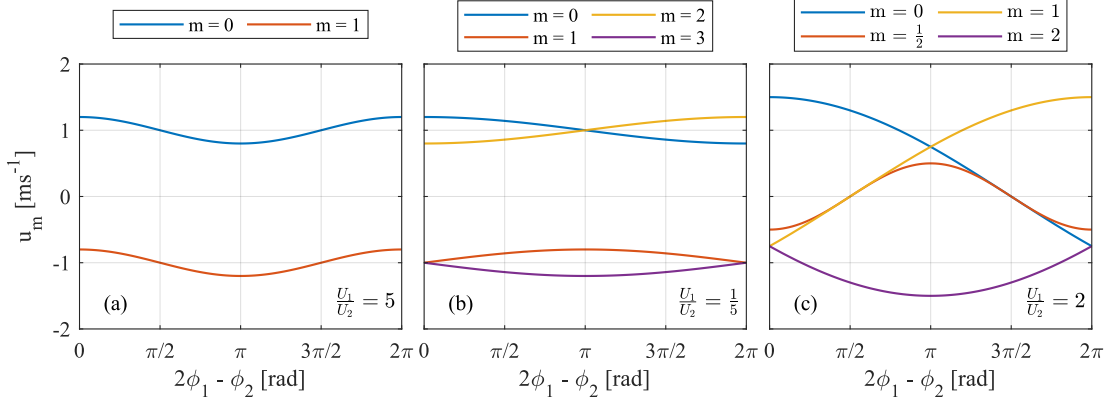
Figure 1.8. Velocity magnitude during flood and ebb for D_1-dominant system (a), D_2-dominant system (b), and mixed D_1-D_2 system (c). In this figure, $U_1 = 1$ ms^{-1} and $U_2 = 0.2$ ms^{-1} (a); $U_1 = 0.2$ ms^{-1} and $U_2 = 1$ ms^{-1} (b); and $U_1 = 1$ ms^{-1} and $U_2 = 0.5$ ms^{-1} (c).

1.5 Results and Discussion: Bed Stress Asymmetry and Sediment Transport

1.5.1 Excess Bed Stress

The asymmetry parameters Λ_1 and Λ_2 (Equations 12 and 15, respectively) are now compared to sediment transport metrics to illustrate how they can be used to characterize sediment transport patterns related to bed stress asymmetry. We assume that lag effects are relatively small, so that the suspended sediment field is closely related to instantaneous bed stress. Then the net sediment transport due to time variability of the instantaneous bed stress τ_b (Equation 1) can be evaluated by considering the tidal-cycle integral of the excess bed stress ($|\tau_b|$-τ_c), squared (see Dyer 1986):

$$\tau_E = \int_t sign\,(\tau_b)H(|\tau_b| - \tau_c)(|\tau_b| - \tau_c)^2 dt \qquad (26),$$

where the $sign(\tau_b)$ is needed to maintain direction of transport as τ_b changes sign, and $H(|\tau_b| - \tau_c)$ is the Heaviside step function that zeroes out negative values of $(|\tau_b| - \tau_c)$.

51

The τ_E metric of Equation 26 takes into consideration both transport thresholds and the non-linear nature of sediment transport. When evaluating the transport asymmetry for different particles, there are two limits to consider. The first applies to regions with a critical bed stress much smaller than the maximum bed stress over the tidal cycle ($\frac{\tau_c}{\tau_{max}} \ll$ 1), and is equivalent to evaluating the tidal cycle integral of τ_b^2. As τ_c increases, however, less of the curve is integrated over the tidal cycle (see Figure 1.2). Once τ_c is close to the maximum bed stress during the tidal cycle ($\frac{\tau_c}{\tau_{max}} \cong 1$), evaluating asymmetry reduces to evaluating the maximum bed stress (or a power of velocity) during flood vs. ebb (see also Dronkers 1986). Thus, the influence of τ_c (and indirectly, of particle size) on net transport can be evaluated using the tidal cycle integral of τ_b^2 (for easily eroded particles) and the sum of the bed stress during ebb and flood (for particles eroded only during peak current levels).

Other transport metrics that are prevalent in the literature involve long term averages of u^n, where n is some power between 2 and 7 (Dyer 1986; Dronkers 2016). For example, Hoitink et al. (2003) evaluated bed load transport induced by tidal asymmetry of M_2, K_1 and O_1 using long-term averages of u^3 and u^5. Van Maren et al. (2004) also uses u^3 as a bed load transport metric to study morphologic changes in the Red River Delta, while Guo et al. (2016) assume that the total load is proportional to u^5, following Engelund and Hansen (1967). Equations 6, 8 and 26 suggest that evaluating the residual bed stress (Equation 8) is analogous to a tidal cycle average of u^3, and evaluating the

excess bed stress squared with $\tau_c \approx 0$ is analogous to tidal cycle averages of u^6, a range

which brackets the range of exponents typically used to study sediment transport.

For the D$_2$-dominant case ($\Pi \ll 1$), the transition from flood to ebb and dominant

transport occurs when $\varepsilon_{R2} < -2\Lambda_2 cos(2\phi_2 - \phi_4)$ when $\frac{\tau_c}{\tau_{max}} \ll 1$ and when $\varepsilon_{R2} <$

$-3\Lambda_2 cos(2\phi_2 - \phi_4)$ for $\frac{\tau_c}{\tau_{max}} \cong 1$ (Figure 1.9). By inspection, these two limits can be

combined into a single functional relationship between the critical bed stress and

transport asymmetry: $\varepsilon_{R2} < -C\Lambda_2 cos(2\phi_2 - \phi_4)$, where C is between 2 and 3 for

$\frac{\tau_c}{\tau_{max}} < 1$, and zero for $\frac{\tau_c}{\tau_{max}} \geq 1$:

$$\varepsilon_{R2} < -H(|\tau_{max}| - \tau_c)(2 + \frac{\tau_c}{\tau_{max}})\Lambda_2 cos(2\phi_2 - \phi_4) \qquad (27),$$

which is similar in form to Equation 12 for bed stress asymmetry. The right-hand side of

Equation 27 increases with τ_c because a larger residual velocity is needed to shift the

ebb/flood dominance of the peaks in bed stress than is required to shift ebb/flood

dominance of the area beneath the bed stress curve (see Figure 1.2).
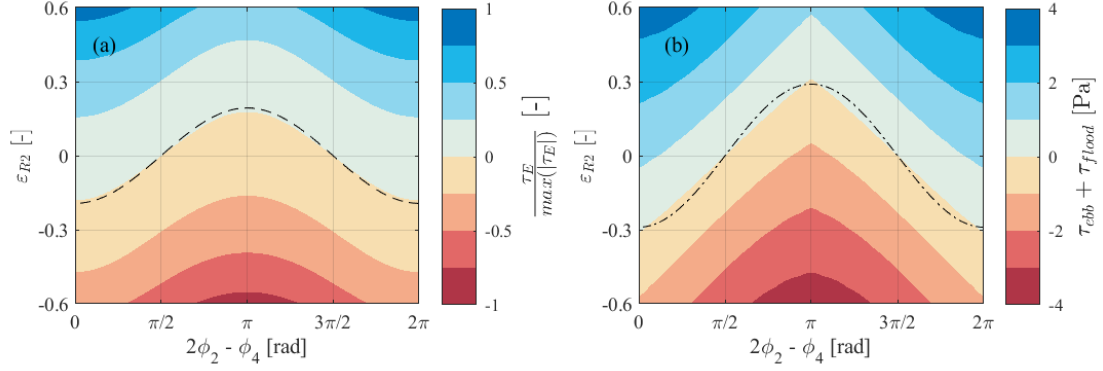
Figure 1.9. Sample colormap of τ_E (a) and $\tau_{ebb} + \tau_{flood}$ (b) as a function of $\varepsilon_{R2} = \frac{u_R}{U_2}$ and phase difference $2\phi_2 - \phi_4$. Parameter space is plotted for $\frac{\tau_c}{\tau_{max}} \ll 1$ (left) and $\frac{\tau_c}{\tau_{max}} \approx 1$ (right). Dashed line denotes $-2\Lambda_2 cos(2\phi_2 - \phi_4)$ and dash-dotted line denotes $-3\Lambda_2 cos(2\phi_2 - \phi_4)$, with both lines marking the approximate boundary between flood dominance (blue) and ebb dominance (red). τ_E is normalized to the maximum value in the parameter space. In this figure, $U_2 = 0.6$ ms^{-1}, $U_4 = 0.2$ms^{-1}, and $u_R = [-0.4, 0.4]$ ms^{-1}.

D$_1$-dominant transport behaves the same as the D$_2$ case described above:

$$\varepsilon_{R1} < -H(|\tau_{max}| - \tau_c)(2 + \frac{\tau_c}{\tau_{max}})\Lambda_1 cos(2\phi_1 - \phi_2) \tag{28},$$

which is analogous to equation 14 for bed stress asymmetry.
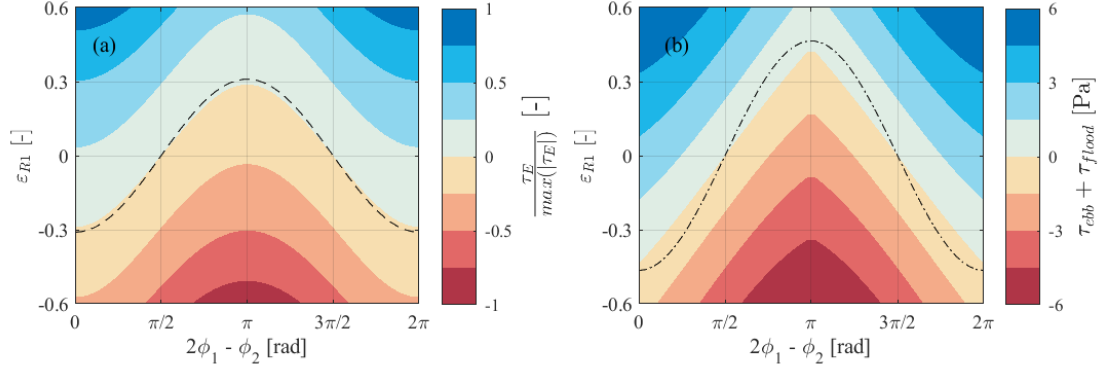
Figure 1.10. Sample colormap of τ_E (a) and $\tau_{ebb} + \tau_{flood}$ (b) as a function of $\varepsilon_{R1} = \frac{u_R}{U_1}$ and phase difference $2\phi_1 - \phi_2$. Parameter space is plotted for $\frac{\tau_c}{\tau_{max}} \ll 0$ (left) and $\frac{\tau_c}{\tau_{max}} \approx 1$ (right). Dashed line denotes $-2cos(2\phi_1 - \phi_2)$ and dash-dotted line denotes $-3cos(2\phi_1 - \phi_2)$ (right), with both lines marking the approximate boundary between flood dominance (blue) and ebb dominance (red). T$_E$ is normalized to the maximum value in the parameter space. In this figure, $U_1 = U_2 = 0.6$ ms^{-1}, and $u_R = [-0.4, 0.4]$ ms^{-1}.

Equations 27 and 28 imply that the thresholds on the residual velocity u_R that delineate between ebb and flood dominant sediment transport are greater than the thresholds for ebb/flood dominant bed stress. For example, sediment transport for the flood-dominant D$_2$ case discussed in Figure 1.4 becomes ebb dominant $u_R < -\frac{2}{9}U_2$ for $\frac{\tau_c}{\tau_{max}} \ll 1$ and when $u_R < -\frac{3}{9}U_2$ for $\frac{\tau_c}{\tau_{max}} \approx 1$, assuming $U_4 \cong \frac{1}{3}U_2$ (Figure 1.9). In other words, ebb dominance occurs when the magnitude of the downstream directed residual flow exceeds $\frac{2}{9}U_2$ and $\frac{3}{9}U_2$. The flood-dominant D$_1$ case (assuming $U_1 = U_2$) has ebb dominant sediment transport if the residual velocity is less than about $-\frac{2}{6}U_1$ or $-\frac{3}{6}U_1$ for $\frac{\tau_c}{\tau_{max}} \ll 1$ and $\frac{\tau_c}{\tau_{max}} \approx 1$, respectively (Figure 1.10). Note that different values of U_k and ϕ_k will yield different thresholds for which residual velocities switch transport direction. As with the tidal bed stress asymmetry, residual sediment transport in mixed-tide

estuaries is a function of both the semidiurnal and diurnal asymmetries, which will increase the residual velocity threshold for ebb dominant sediment transport when the two asymmetries are in phase.

Because the critical bed stress threshold for transport is influenced by particle size, and because sediment transport is determined by time integrated processes, different particles may experience different directions of transport within the same velocity field (Dronkers 1986; Postma 1961). Similarly, biotic factors which can raise or reduce erosion thresholds (see e.g., Widdows & Brinsley, 2002) can also influence transport direction, for the same forcing. Thus, the spatial distribution of bed stress asymmetry can act as a filter for sorting material within an estuary, notwithstanding hiding effects, settling lag effects, vertical variability in both residual and tidal velocities, and other confounding factors.

1.5.2 Classification of Bed Stress Asymmetry

The discussions above can be summarized using a bed stress asymmetry parameter space (Table 1.3; Figure 1.11) that organizes the dynamics of bed stress asymmetry according to three classes depending on the relative strength and direction of the near-bed residual velocity (terms 1-3 in Equation 8b), the semidiurnal- and diurnal asymmetry (terms 4 & 5 in Equation 8b), and the ebb/flood dominance of the residual bed stress, τ_R. We use bed stress asymmetry here, not the transport asymmetry of the previous sub-section, because transport asymmetry depends on τ_c, while τ_R does not. Class I, "Concordant Bed-Stress Asymmetry" occurs when ε_R, $\Lambda\cos\Delta\phi$, and τ_R all share the same

sign, where ε_R and $\Lambda\cos\Delta\phi$ are defined according to Equation 12 or Equation 14 depending on whether the bed stress asymmetry is semidiurnally- or diurnally-dominant (see also Table 1.4). Additionally, two "Mixed Bed-Stress" situations occur, when ε_R and $\Lambda\cos\Delta\phi$ are of opposite sign. Class II or "Residual-Dominant Bed-Stress Asymmetry" occurs when ε_R and τ_R share the same sign (but $\Lambda\cos\Delta\phi$ does not), and Class III or "Tide-Dominant Bed-Stress Asymmetry" is observed when $\Lambda\cos\Delta\phi$ and τ_R share the same sign (Table 1.3; Figure 1.11). For example, a location in an estuary with weak, ebb-dominant tidal asymmetry and strong, flood-dominant residual currents would produce a flood-dominant τ_R and would be classified as Class II$^+$, with the superscript representing the sign of τ_R. Further, the origin of the tidal component of the bed stress asymmetry (D_1, D_2 or mixed tidal asymmetry) is indicated with a subscript (1, 2, or M) for any of the classes, though this is most relevant for Classes I and III; e.g., Class III$_2^+$ bed- stress asymmetry would be driven by the semidiurnal tides and be flood dominant.

Table 1.3. Bed stress asymmetry classification according to the sign of ε_R, $\Lambda\cos\Delta\phi$, and τ_R.

Bed Stress Asymmetry Class	Description	ε_R	$\Lambda\cos\Delta\phi$	τ_R
I$^+$	Concordant Flood Dominance	(+)	(+)	(+)
I$^-$	Concordant Ebb Dominance	(−)	(−)	(−)
II$^+$	Residual Dominant Flood Dominance	(+)	(−)	(+)
II$^-$	Residual Dominant Ebb Dominance	(−)	(+)	(−)
III$^+$	Tide Dominant Flood Dominance	(−)	(+)	(+)
III$^-$	Tide Dominant Ebb Dominance	(+)	(−)	(−)

The bed stress asymmetry parameter space of Figure 1.11 highlights several nuances of sediment transport, discussed above. First, sediment can move in a direction opposite of the residual current, u_R (Type III asymmetry). Second, sediment that moves in a direction opposite of the residual currents or residual bed stress is more likely in estuaries with strong semidiurnal- or diurnal asymmetry because this region of the parameter space grows with $-\Lambda\cos(\Delta\phi)$. And finally, because bed stress is constant along contours parallel to $\varepsilon_R = -\Lambda\cos(\Delta\phi)$ (Figure 1.4; and Equations 12, 14 and 16), while sediment transport is constant along contours parallel to $\varepsilon_R = -H(|\tau_{max}| - \tau_c)(2 + \frac{\tau_c}{\tau_{max}})\Lambda\cos(\Delta\phi)$ (Figures 1.9 and 1.10; and Equations 27 and 28), spatial gradients in sediment transport can occur in a spatially uniform bed stress field, especially if bed texture varies.
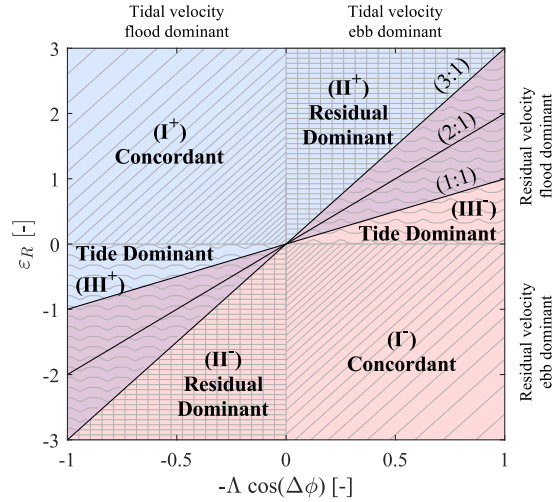
Figure 1.11. Tidal bed stress asymmetry parameter Space. Positive and negative residual bed stress is shown by blue and red shading, respectively. Transition between ebb and flood dominant bed stress is shown by 1:1 line. Transition between ebb and flood dominant sediment transport for $\frac{\tau_c}{\tau_{max}} \ll 1$ and $\frac{\tau_c}{\tau_{max}} \cong 1$ is shown by 2:1 and 3:1 line, respectively. Class II regions where the residual sediment transport opposes the residual bed stress is shown by purple shading. ε_R, Λ, and $\Delta\phi$, defined according to Equations 12 and 14, depending on whether the system is semidiurnal- or diurnal-dominant, or mixed. The bed asymmetry classifications I, II, and III are defined in Table 1.3.

1.5.3 Morphodynamic Equilibrium

The framework outlined herein also provides insight into the morphodynamic evolution of alluvial river-estuary systems. In this context, we consider a system to be in morphodynamic equilibrium when the net (tidal cycle average) sediment fluxes Q_s are spatially uniform (Dronkers 2016). If along-channel sediment fluxes are convergent ($\frac{dQ_s}{dx} < 0$), for example, then material accumulates on the bed until spatial gradients in sediment transport are eliminated (Friedrichs 1995; Lanzoni and Seminara 2002; Pittaluga et al 2015; Schuttelaars and De Swart 1997). Formally, the net sediment flux through a river section is given by the tidal cycle and cross-section average of the product

between the along-channel velocity u and the sediment concentration C: $Q_s|_x =$

$\frac{1}{T}\int_t \frac{1}{B}\int_y \frac{1}{H}\int_z u(y,z,t)\, C(y,z,t)\, dz\, dy\, dt$, where y and z represent the cross-channel

and vertical dimensions, respectively, and $B(x,t)$ and $H(x,t)$ are river width and depth.

However, assuming that sediment transport scales with one of the metrics discussed in

Section 4.1, the net sediment flux can be characterized by the residual bed stress. As

discussed above, this simplification assumes that lag effects are minimal, and that lateral

and vertical variations in uC do not materially alter Q_s (e.g., are small or uniform enough

so u^3 is representative of Q_s). This approach also neglects the influence of bedforms,

spatial variability in the critical bed stress for erosion and deposition, and sediment

specific behavior such as hiding, consolidation, flocculation, and biotic effects. Accepting

these limitations, spatial gradients in the residual bed stress (Equation 8) can provide

meaningful insights into how bed stress asymmetry can influence morphological changes,

even if the results are not wholly accurate. Using the non-dimensional numbers defined

above, the residual bed stress (Equation 8) can be expressed as follows:

$$\tau_R = \alpha_R U_2\big(\varepsilon_{R2} + \Lambda_2(1 + \Pi)cos(2\phi_2 - \phi_1)\big) \tag{29a},$$

which for D_2-dominant systems ($\Pi \ll 1$) reduces to

$$\tau_R = \alpha_R U_2\big(\varepsilon_{R2} + \Lambda_2 cos(2\phi_2 - \phi_1)\big) \tag{29b}.$$

And for D_1-dominant systems ($\Pi \gg 1$) reduces to

$$\tau_R = \alpha_R U_1\big(\varepsilon_{R1} + \Lambda_1 cos(2\phi_1 - \phi_2)\big) \tag{29c},$$

where $\alpha_R U_k = \rho C_d \frac{b}{U} \frac{3}{4} \left(\frac{4}{7} U^2 + 2 \left((1 + \varepsilon_1^2) U_1^2 + (1 + \varepsilon_2^2) U_2^2 + \frac{2}{3} u_R^2 \right) \right) U_k$ scales the

magnitude of the velocity field, and shows that when the tidal bed stress asymmetry is

constant $\left(\frac{d}{dx} \left(\varepsilon_R + \Lambda cos(2\phi_1 - \phi_2) \right) = 0 \right)$, the bed stress can become larger if the

velocity field strengthens $\left(\frac{d}{dx} \alpha_R U_k > 0 \right.$; and vice-versa). Note that $\alpha_R U_k$ is strictly

positive, and so the sign of the bed stress (ebb/flood dominance) is determined by

$\left(\varepsilon_R + \Lambda cos(2\phi_1 - \phi_2) \right)$, as discussed above. In terms of the asymmetry parameter space

shown in Figure 1.11, $\alpha_R U_k$ represents a third dimension determining the value of the bed

stress along contours parallel to $\varepsilon_R = -\Lambda cos(\Delta\phi)$.

Setting the spatial derivative of Equation 29b,c equal to zero gives the following

condition on the residual bed stress for morphodynamic equilibrium:

$$\frac{d\tau_R}{dx} = \underbrace{\left(\varepsilon_{R,k} + \Lambda_k cos\Delta\phi_k \right) \frac{d}{dx} (\alpha_R U_k)}_{(1)} + \alpha_R U_k \underbrace{\frac{d\varepsilon_{R,k}}{dx}}_{(2)} + \alpha_R U_k \underbrace{\frac{d}{dx} (\Lambda_k cos\Delta\phi_k)}_{(3)} = 0 \quad (30),$$

where $\varepsilon_{R,k}$, Λ_k, $\Delta\phi_k$, and U_k are defined according to Equations 29b and 29c, depending

on whether the system is semidiurnal- or diurnal-dominant. The mixed-tide case can also

be developed using Equation 29a, which would include an additional term representing

spatial gradients in Π. Equation 30 demonstrates that bed stress asymmetry contributes

to morphological stability in four ways: (1) spatial gradients in the velocity field scaled

by the bed stress asymmetry; (2) spatial gradients in ε_R scaled by the velocity field; and

(3) spatial gradients in tidal asymmetry $(\Lambda_k cos\Delta\phi_k)$ scaled by the velocity field.

Whenever the left-hand side of Equation 30 is negative, the bed stress is convergent,

which leads to sediment accumulation and deposition of material on the bed. Divergent bed stress gradients that contribute to sediment export and erosion develop when the right-hand side of Equation 30 is positive.

In real systems, the parameters α, ε_R, Λ, and $\Delta\phi$ vary spatially and evolve over fortnightly to semiannual timescales due to the interaction between tidal constituents. Other hydrodynamic forcing variables, like river discharge and wind, are also constantly changing, which augments temporal variability of α, ε_R, Λ, and $\Delta\phi$. Thus, the condition of $\frac{d\tau_R}{dx} = 0$ (approximate morphodynamic equilibrium) in estuaries is likely a transient, or ephemeral state, and the morphology likely oscillates between two (or more) limits as forcing variables fluctuate over time. Nevertheless, a system can be considered to be in approximate morphodynamic equilibrium, which is to say the sediment fluxes are nearly uniform and the morphology is relatively stable, when the four terms on the left-hand side of Equation 30 roughly balance one another. For example, a hyposynchronous estuary (tidal velocity amplitudes decrease upstream, $\frac{d\alpha_R U_k}{dx} < 0$) that is flood dominant near the mouth may not be in morphodynamic equilibrium because term (1) in Equation 30 is negative and terms (2-4) are all less than or equal to zero, which causes $\frac{d\tau_R}{dx} < 0$, implying a net convergence of sediment. A flood dominant, hypersynchronous estuary (tidal velocity amplitudes increase upstream, $\frac{d\alpha_R U_k}{dx} > 0$) may, on the other hand, be in equilibrium if the spatial gradients in $cos(\Delta\phi)$ balance those of $\alpha_R U_k$ (the tidal velocity amplitude increases, but asymmetry becomes less flood dominant), or if tidal amplification is balanced by u_R becoming more negative. Pittaluga et al. (2015) suggest

the possibility that a hypersynchronous estuary cannot be in equilibrium because the sediment fluxes are not spatially uniform, however, their analysis does not include overtides or the influence of tidal asymmetry on sediment transport. Assuming a tidally symmetric bed stress, Equation 30 reduces to evaluating the spatial gradients of $\frac{d}{dx}(U_k^2 + u_R^2)$ when $|u_R| \geq U_k$, or $\frac{d}{dx}(U_k u_R)$ when $|u_R| < U_k$ (see Hudson et al. 2022), which in a hypersynchronous estuary are nonzero. Thus, tidal bed stress asymmetry is likely an important mechanism controlling the morphological stability of an estuary— especially when the spatial gradients in tidal amplitude and residual velocity are not balanced.

1.6 Summary and Conclusions

In this study we outline an analytical framework to examine tidal asymmetry in bed stress to clarify how tidal properties and residual (subtidal) currents influence bed stress and therefore sediment transport in semidiurnal, diurnal, and mixed-tide estuaries. The framework is expressed using tidal species at the diurnal, semidiurnal, terdiurnal, and quarterdiurnal frequencies, which allows evaluation of nonstationary variations in asymmetry based on 10 tidal constituents and the near-bed residual velocity. The approach is easily adaptable to include more (or different) constituents, without changing the expression defining the residual bed stress, which could facilitate the study of sediment transport patterns in systems influenced by higher frequency harmonics (e.g., M_6; see Table 1.2), or by interactions between additional astronomical constituents (e.g., P1 or K2, see Song et al. 2011). Because tidal and residual dynamics are treated together,

the theory represents a generalized approach to studying asymmetry in estuaries, and reduces to frameworks previously analyzed when the residual velocity is absent, e.g., Speer and Aubrey (1985) for semidiurnal asymmetry, and Hoitink et al. (2003) for diurnal asymmetry. The framework is summarized by three non-dimensional numbers: the Species Factor Π (the ratio of diurnal to semidiurnal-induced bed stress asymmetry); the Tidal Asymmetry Parameter Λ_k, $k = 1,2$, which scales the amplitude of the diurnal (Λ_1) and semidiurnal (Λ_2) tidal asymmetry; and the Residual Asymmetry Parameter ε_R, which scales the strength of the residual velocity relative to the tidal velocity.

The Species Factor extends the Tidal Form Factor introduced by Pugh (1987) by capturing the nonlinearity of bed stress and the influence of tidal phases (see Equation 10) to classify the tidal dynamics of bed stress asymmetry as semidiurnal ($\Pi \ll 1$), diurnal ($\Pi \gg 1$), and mixed ($\Pi \cong 1$). In a semidiurnal system, tidal asymmetry is generated by nonlinear interactions between constituents or between constituents and the residual current (e.g., M_4 is produced from M_2 and river flow). Thus, tidal asymmetry typically grows upstream of the entrance as energy is transferred from astronomical tides to shallow water overtides. In diurnal and mixed-tide systems, bed stress asymmetry is driven by the phase relationships between major tidal constituents, which can engender asymmetry before the tides enter the estuary, and as a result, the asymmetry can be greatest near the entrance or remain relatively constant throughout the system (see Nidzieko 2010). Because tidal amplitudes and phases change as tides propagate into an estuary, and the amplitudes/phases of the D_1, D_2, D_3, and D_4 species may change relative to each other (see e.g., Parker 2007), bed stress asymmetry can change between diurnal,

semidiurnal, and mixed-tide dynamics through time and space. In Part II, we explore how bed stress asymmetry varies in two estuaries (the Delaware Estuary and San Francisco Bay), and illustrate that the residual bed stress dynamics can be strongly diurnal ($\Pi \gg 1$) in a system that is classified as mixed-semidiurnal (San Francisco Bay), based on the Tidal Form Factor.

The parameters Λ, ε_R, and the phase difference between tidal species $\Delta\phi$ can be used to define a tidal bed stress asymmetry parameter space, which classifies the dynamics of the residual bed stress according to the relative strength of the residual velocity and the tidal velocity asymmetry (see Figure 1.11). Class I, or Concordant Bed Stress Asymmetry, occurs when the residual velocity, tidal velocity asymmetry and the residual bed stress all act in the same direction. We show that a relatively small residual velocity ($\varepsilon_R \ll 1$) that acts in opposition to the tidal velocity asymmetry can control flood/ebb dominance of the residual bed stress (Class II, or Residual-Dominant Bed-Stress Asymmetry). However, when the magnitude of ε_R drops below $\Lambda cos\Delta\phi$, (i.e., when the magnitude of the residual currents are relatively weak) the sign of the residual bed stress is determined by the tidal velocity asymmetry (Class III or Tide-Dominant Bed-Stress Asymmetry). Thus, the residual bed stress can be ebb dominant in a flood dominant residual velocity field (or flood dominant tidal velocity field) and vice-versa. Because the residual velocity threshold that delineates between flood/ebb dominance is smaller for the residual bed stress than for sediment transport (see Section 4.1), the sediment transport can be flood/ebb dominant even while the velocity (or even residual bed stress) is ebb/flood dominant. Moreover, ebb/flood dominance of sediment transport depends on

the critical bed stress, and indirectly on particle size (see Section 4.1), so bed stress asymmetry can contribute to particle sorting in an estuary.

Because the semidiurnal asymmetry develops from overtides, which are typically smaller than astronomical constituents, the amplitude of the diurnal (or linear) asymmetry is typically stronger than that of the semidiurnal (or nonlinear) asymmetry ($\Lambda_1 > \Lambda_2$) in D_1-dominant and mixed-tide systems. Under these conditions, the diurnal asymmetry requires a larger residual velocity to change the sign of the residual bed stress (see Sections 3.1 and 3.2) and direction of sediment transport (see Section 4.1), than is the case for the semidiurnal asymmetry. In mixed-tide systems, the semidiurnal and diurnal asymmetries can also augment or diminish residual bed stress asymmetry when they act together or in opposition, respectively, further modulating thresholds on ebb/flood dominance.

Tidal monthly variations in species velocity amplitude and phase U_k and ϕ_k introduce fortnightly variability of the bed stress asymmetry. Additionally, for regions with mixed-tides, semiannual fluctuations in the bed stress asymmetry occur due to the harmonic convergence/divergence of the synodic and sidereal months. Sediment transport is greatest during (or confined to) times when the diurnal inequality is large and the bed stress during greater flood/ebb is much larger than at other times during the tidal cycle. Thus, tidal bed stress asymmetry in mixed-tide estuaries is greatest when synodic and tropic tides coincide because u_1 and u_2 are in phase and the diurnal inequality is large (linear tidal asymmetry). Although not evaluated directly herein, variations in tidal

constituents over longer periods (e.g., the 18.6-year nodal cycle) can also influence tidal bed stress asymmetry (see Part II).

Because morphological changes in an estuary are linked to spatial gradients in bed stress and sediment transport (Dronkers 2016; Friedrichs 1995; Lanzoni and Seminara 2002; Pittaluga et al 2015; Schuttelaars and De Swart 1997), the framework outlined herein can help to interpret and explain shoaling/erosion patterns in estuaries. By expressing the residual bed stress in terms of Π, Λ, and ε_R, we illustrate how sediment divergence/convergence, and hence morphological stability, is influenced by spatial gradients in tidal phase, tidal amplitude, and residual velocity. Because residual currents are spatially variable in real estuaries, tidal asymmetry is an important mechanism for establishing and maintaining morphodynamic equilibrium, and systems wherein the along channel evolution of tidal asymmetry is not balanced by the residual velocity (or vice versa) are not likely to be in morphodynamic equilibrium ($\frac{d\tau_R}{dx} \neq 0$). Furthermore, morphodynamic equilibrium may only be approximate ($\frac{d\tau_R}{dx} \cong 0$) or attained during certain time periods in real estuaries because the tidal bed stress asymmetry is always changing, due both to tidal constituent interactions and variability in river discharge and other forcing variables.

1.7   References

Branch, R. A., Horner-Devine, A. R., Chickadel, C. C., Talke, S. A., Clark, D., & Jessup, A. T. (2021). Surface turbulence reveals riverbed drag coefficient. *Geophysical Research Letters*, 48(10), e2020GL092326.

Burchard, H., & Baumert, H. (1998). The formation of estuarine turbidity maxima due to density effects in the salt wedge. A hydrodynamic process study. *Journal of Physical Oceanography*, *28*(2), 309-321.

Burchard, H., Schuttelaars, H. M., & Ralston, D. K. (2018). Sediment trapping in estuaries. *Annual review of marine science*, *10*, 371-395.

Buschman, F. A., Hoitink, A. J. F., Van Der Vegt, M., & Hoekstra, P. (2009). Subtidal water level variation controlled by river flow and tides. *Water Resources Research*, 45(10).

Chant, R. J., Fugate, D., & Garvey, E. (2011). The shaping of an estuarine superfund site: Roles of evolving dynamics and geomorphology. *Estuaries and Coasts*, *34*, 90-105.

Chernetsky, A. S., Schuttelaars, H. M., & Talke, S. A. (2010). The effect of tidal asymmetry and temporal settling lag on sediment trapping in tidal estuaries. *Ocean Dynamics*, *60*(5), 1219-1241.

Cox, J. R., Huismans, Y., Knaake, S. M., Leuven, J. R. F. W., Vellinga, N. E., van der Vegt, M., ... & Kleinhans, M. G. (2021). Anthropogenic effects on the contemporary sediment budget of the lower Rhine-Meuse Delta channel network. *Earth's Future*, *9*(7), e2020EF001869.

Deverel, S. J., Ingrum, T., Lucero, C., & Drexler, J. Z. (2014). Impounded marshes on subsided islands: simulated vertical accretion, processes, and effects, Sacramento-San Joaquin Delta, CA USA. *San Francisco Estuary and Watershed Science*, *12*(2).

Doodson, A. T. (1921). The harmonic development of the tide-generating potential. *Proceedings of the Royal Society of London. Series A, Containing Papers of a Mathematical and Physical Character*, *100*(704), 305-329.

Doodson, A. T. (1924). Perturbations of harmonic tidal constants. Proceedings of the Royal Society of London. Series A, Containing Papers of a Mathematical and Physical Character, 106(739), 513-526.

Dronkers, J. J. (1964). Tidal computations in rivers and coastal waters. North-Holland Publishing Company.

Dronkers, J. (1986). Tidal asymmetry and estuarine morphology. *Netherlands Journal of Sea Research*, *20*(2-3), 117-131.

Dronkers, J. (2016). *Dynamics of coastal systems* (Vol. 41). World Scientific.

Dyer, K. (1986). Coastal and estuarine sediment dynamics. *John Wiley and Sons, Chichester, Sussex (UK), 1986, 358.*

Engelund, F., & Hansen, E. (1967). A monograph on sediment transport in alluvial streams. *Technical University of Denmark 0stervoldgade 10, Copenhagen K.*

Familkhalili, R., Talke, S. A., & Jay, D. A. (2020). Tide-storm surge interactions in highly altered estuaries: How channel deepening increases surge vulnerability. *Journal of Geophysical Research: Oceans*, 125(4), e2019JC015286.

Fong, D. A., Monismith, S. G., Stacey, M. T., & Burau, J. R. (2009). Turbulent stresses and secondary currents in a tidal-forced channel with significant curvature and asymmetric bed forms. *Journal of Hydraulic Engineering*, *135*(3), 198-208.

Friedrichs, C. T., & Perry, J. E. (2001). Tidal salt marsh morphodynamics: a synthesis. *Journal of Coastal Research*, 7-37.

Gerkema, T., (2019). An Introduction to Tides, Cambridge University Press, 213 pp.

Geyer, W. R. (1993). The importance of suppression of turbulence by stratification on the estuarine turbidity maximum. *Estuaries*, *16*, 113-125.

Godin, G. (1972). The Analysis of Tides. University of Toronto Press, 264 pp.

Godin, G. (1985). Modification of river tides by the discharge. *Journal of waterway, port, coastal, and ocean engineering*, *111*(2), 257-274.

Godin, G. (1991). Compact approximations to the bottom friction term, for the study of tides propagating in channels. *Continental Shelf Research*, 11(7), 579-589.

Godin, G. (1999). The propagation of tides up rivers with special considerations on the upper Saint Lawrence River. *Estuarine, Coastal and Shelf Science*, 48(3), 307-324.

Guo, L., Van der Wegen, M., Roelvink, J. A., & He, Q. (2014). The role of river flow and tidal asymmetry on 1-D estuarine morphodynamics. *Journal of Geophysical Research: Earth Surface*, *119*(11), 2315-2334.

Guo, L., Brand, M., Sanders, B. F., Foufoula-Georgiou, E., & Stein, E. D. (2018). Tidal asymmetry and residual sediment transport in a short tidal basin under sea level rise. *Advances in water resources*, *121*, 1-8.

Hoitink, A. J. F., Hoekstra, P., & Van Maren, D. S. (2003). Flow asymmetry associated with astronomical tides: Implications for the residual transport of sediment. *Journal of Geophysical Research: Oceans*, 108(C10).

Hudson, A., Jay, D., & Talke, S. (2022). The Bed Stress Minimum in Tidal Rivers. *Estuaries and Coasts*, *46*(2), 336-355.

Jay, D. A. (1991). Internal asymmetry and anharmonicity in estuarine flows. *Progress in tidal hydrodynamics*, *521*, 543.

Jay, D. A., & Flinchem, E. P. (1997). Interaction of fluctuating river flow with a barotropic tide: A demonstration of wavelet tidal analysis methods. *Journal of Geophysical Research: Oceans*, *102*(C3), 5705-5720.

Jay, D. A., & Musiak, J. D. (1994). Particle trapping in estuarine turbidity maxima. *Journal of Geophysical Research*, *99*(20), 446-20.

Jay, D. A., & Musiak, J. D. (1996). Internal tidal asymmetry in channel flows: Origins and consequences. *Mixing in estuaries and coastal seas*, *50*, 211-249.

Jay, D. A., and P. Naik. (2011). Distinguishing human and climate influences on hydrological disturbance processes in the Columbia River, USA, *Hydrological Sciences Journal,* 56, 1186-1209.

Jay, D. A., P. M. Orton, T. Chisholm, D. J. Wilson, and A. M. V. Fain, (2007), Particle trapping in stratified estuaries – II Application to Observations, *Estuaries and Coasts* 30: 1106-1125.

Lanzoni, S., & Seminara, G. (2002). Long-term evolution and morphodynamic equilibrium of tidal channels. *Journal of Geophysical Research: Oceans*, *107*(C1), 1-1.

Nidzieko, N. J. (2010). Tidal asymmetry in estuaries with mixed semidiurnal/diurnal tides. *Journal of Geophysical Research: Oceans*, 115(C8).

Parker, B. B. (2007). Tidal analysis and prediction.

Pittaluga, M.B., Tambroni, N., Canestrelli, A., Slingerland, R., Lanzoni, S., & Seminara, G. (2015). Where river and tide meet: The morphodynamic equilibrium of alluvial estuaries. *Journal of Geophysical Research: Earth Surface*, *120*(1), 75-94.

Postma, H. (1961). Transport and accumulation of suspended matter in the Dutch Wadden Sea. *Netherlands Journal of Sea Research*, *1*(1-2), 148-190.

Proudman, J. (1952). *Dynamical oceanography*. Dover.

Sanford, L. P., & Maa, J. P. Y. (2001). A unified erosion formulation for fine sediments. *Marine Geology*, *179*(1-2), 9-23.

Schuttelaars, H. M., & De Swart, H. E. (1997). An idealized long-term morphodynamic model of a tidal embayment.

Song, D., Wang, X. H., Kiss, A. E., & Bao, X. (2011). The contribution to tidal asymmetry by different combinations of tidal constituents. *Journal of Geophysical Research: Oceans*, *116*(C12).

Speer, P. E., & Aubrey, D. G. (1985). A study of non-linear tidal propagation in shallow inlet/estuarine systems Part II: Theory. *Estuarine, Coastal and Shelf Science*, *21*(2), 207-224.

Stacey, M. T., Monismith, S. G., & Burau, J. R. (1999). Measurements of Reynolds stress profiles in unstratified tidal flow. *Journal of Geophysical Research: Oceans*, *104*(C5), 10933-10949.

Talke, S. A., Horner-Devine, A. R., Chickadel, C. C., & Jessup, A. T. (2013). Turbulent kinetic energy and coherent structures in a tidal river. *Journal of Geophysical Research: Oceans*, *118*(12), 6965-6981.

Talke, S. A., Kemp, A. C., & Woodruff, J. (2018). Relative sea level, tides, and extreme water levels in Boston Harbor from 1825 to 2018. *Journal of Geophysical Research: Oceans*, *123*(6), 3895-3914.

USCGS. (1952). *Manual of Harmonic Constant Reductions* (Vol. 4). US Government Printing Office.

Van de Kreeke, J., Day, C. M., & Mulder, H. P. J. (1997). Tidal variations in suspended sediment concentration in the Ems estuary: origin and resulting sediment flux. *Journal of Sea Research*, *38*(1-2), 1-16.

Van Maren, D. S., Hoekstra, P., & Hoitink, A. J. F. (2004). Tidal flow asymmetry in the diurnal regime: bed-load transport and morphologic changes around the Red River Delta. *Ocean Dynamics*, *54*, 424-434.

Vellinga, N. E., Hoitink, A. J. F., van der Vegt, M., Zhang, W., & Hoekstra, P. (2014). Human impacts on tides overwhelm the effect of sea level rise on extreme water levels in the Rhine–Meuse delta. *Coastal engineering*, *90*, 40-50.

Widdows, J., & Brinsley, M. (2002). Impact of biotic and abiotic processes on sediment dynamics and the consequences to the structure and functioning of the intertidal zone. *Journal of sea Research*, *48*(2), 143-156.

Yu, X., Zhang, W., & Hoitink, A. J. F. (2020). Impact of river discharge seasonality change on tidal duration asymmetry in the Yangtze River Estuary. *Scientific reports*, *10*(1), 6304.

1.8 Appendices

1.8.1 Appendix A: Velocity representation as diurnal, semidiurnal, terdiurnal, and quarterdiurnal waves

The general expression for combining the constituents into a single wave for species k with n important constituents is:

$$u_k = \sum_{i=1}^{n} U_i \cos(\omega_i t - \phi_i) = U_k \cos(\omega_k t - \phi_k) \qquad \text{Equation S1a,}$$

where U_i, ω_i and ϕ_i are the tidal current amplitude, angular frequency, and phase of the ith constituent. The amplitude (U_k) and phase (ϕ_k) of the combined wave are:

$$U_k^2 = \sum_{i,j} U_i U_j \cos(\theta_i - \theta_j) \qquad \text{Equation S1b,}$$

$$\tan(\phi_k) = \frac{\sum_i U_i \sin(\theta_i)}{\sum_i U_i \cos(\theta_i)} \qquad \text{Equation S1c.}$$

where $\theta_i = \omega_i t - \phi_i$, and the summation in Equation S1b occurs over constituents i and j.

Thus, substitution of u_{K1} and u_{O1} into Equation S1a gives the diurnal wave as follows:

$$u_1 = u_{K1} + u_{O1} = U_1 \cos(\omega_1 t - \phi_1) \qquad \text{Equation S2a,}$$

where U_1 and ϕ_1 are defined as follows:

$$U_1 = [U_{K1}^2 + U_{O1}^2 + 2U_{K1}U_{O1} \cos(2\omega_2 t + \phi_{O1} - \phi_{K1})]^{1/2} \qquad \text{Equation S2b,}$$

$$\phi_1 = \tan^{-1}\left(\frac{U_{K1}\sin(\phi_{K1}-\omega_2 t)+U_{O1}\sin(\phi_{O1}+\omega_2 t)}{U_{K1}\cos(\phi_{K1}-\omega_2 t)+U_{O1}\cos(\phi_{O1}+\omega_2 t)}\right) \qquad \text{Equation S2c.}$$

and ω_1, ω_2 are the first two basic angular frequencies introduced by Doodson (1921).

Likewise, substitution of u_{M2}, u_{S2} and u_{N2} into Equation S1a gives the semidiurnal wave:

$$u_2 = u_{M2} + u_{S2} + u_{N2} = U_2 \cos(2\omega_1 t - \phi_2)$$ Equation S3a,

$$
\begin{aligned}
U_2 = [&U_{M2}^2 + U_{S2}^2 + U_{N2}^2 + 2U_{M2}U_{S2}\cos(2(\omega_2 - \omega_3)t + \phi_{M2} - \phi_{S2}) \\
&+ 2U_{M2}U_{N2}\cos(\omega_2 t + \phi_{N2} - \phi_{M2}) \\
&+ 2U_{S2}U_{N2}\cos((3\omega_2 - 2\omega_3)t + \phi_{N2} - \phi_{S2})]^{1/2}
\end{aligned}
$$ Equation S3b,

$$\phi_2 = \tan^{-1}\left(\frac{U_{M2}\sin(\phi_{M2}) - U_{S2}\sin(2(\omega_2-\omega_3)t-\phi_{S2}) + U_{N2}\sin(\omega_2 t+\phi_{N2})}{U_{M2}\cos(\phi_{M2}) + U_{S2}\cos(2(\omega_2-\omega_3)t-\phi_{S2}) + U_{N2}\cos(\omega_2 t+\phi_{N2})}\right)$$ Equation S3c.

where ω_3 is the third basic angular frequency introduced by Doodson (1921).

The terdiurnal wave is represented as

$$u_{MK3} + u_{MO3} = u_3 = U_3 \cos(3\omega_1 t - \phi_3)$$ Equation S4a,

$$U_3 = [U_{MK3}^2 + U_{MO3}^2 + 2U_{MK3}U_{MO3}\cos(2\omega_2 t + \phi_{MO3} - \phi_{MK3})]^{1/2}$$ Equation S4b,

$$\phi_3 = \tan^{-1}\left(\frac{U_{MK3}\sin(\phi_{MK3}-\omega_2 t) + U_{MO3}\sin(\phi_{MO3}+\omega_2 t)}{U_{MK3}\cos(\phi_{MK3}-\omega_2 t) + U_{MO3}\cos(\phi_{MO3}+\omega_2 t)}\right)$$ Equation S4c.

Finally, the quarter diurnal wave:

$$u_{M4} + u_{MS4} + u_{MN4} = u_4 = U_4 \cos(4\omega_1 t - \phi_4)$$ Equation S5a,

$$
\begin{aligned}
U_4 = [&U_{M4}^2 + U_{MS4}^2 + U_{MN4}^2 + 2U_{M4}U_{MS4}\cos(2(\omega_2 - \omega_3)t + \phi_{M4} - \phi_{MS4}) \\
&+ 2U_{M4}U_{NN4}\cos(\omega_2 t + \phi_{MN4} - \phi_{M4}) \\
&+ 2U_{MS4}U_{MN4}\cos((3\omega_2 - 2\omega_3)t + \phi_{MN4} - \phi_{MS4})]^{1/2}
\end{aligned}
$$ Equation S5b,

$$\phi_4 = \tan^{-1}\left(\frac{U_{M4}\sin(\phi_{M4}) - U_{MS4}\sin(2(\omega_2-\omega_3)t-\phi_{MS4}) + U_{MN4}\sin(\omega_2 t+\phi_{MN4})}{U_{M4}\cos(\phi_{M4}) + U_{MS4}\cos(2(\omega_2-\omega_3)t-\phi_{MS4}) + U_{MN4}\cos(\omega_2 t+\phi_{MN4})}\right)$$ Equation S5c,

Now the velocity can be represented as a combination of diurnal, semidiurnal, terdiurnal, quarterdiurnal and residual motions:

$$u = U_1 \cos(\omega_1 t - \phi_1) + U_2 \cos(2\omega_1 t - \phi_2) \\ + U_3 \cos(3\omega_1 t - \phi_3) + U_4 \cos(4\omega_1 t - \phi_4) + u_R$$

Equation S6.

1.8.2 Appendix B: Parameters and non-dimensional numbers used in the analytical framework

Table 1.4. Parameters and non-dimensional numbers used in the analytical framework, listed in order of appearance within the main text.

Name	Symbol	Definition
Tidal Velocity Parameter	$\varepsilon_1, \varepsilon_2$	$\dfrac{U_3}{U_1}, \quad \dfrac{U_4}{U_2}$
Tidal Asymmetry Phase Parameter	δ_3, δ_4	$\dfrac{cos(\phi_1+\phi_2-\phi_3)}{cos(2\phi_1-\phi_2)}, \quad \dfrac{cos(\phi_1+\phi_3-\phi_4)}{cos(2\phi_1-\phi_2)}$
Species Factor	Π	$\left\| \dfrac{U_1^2(1+2\varepsilon_1\varepsilon_3+2\varepsilon_1\varepsilon_2\varepsilon_4)cos(2\phi_1-\phi_2)}{\varepsilon_2 U_2^2 cos(2\phi_2-\phi_4)} \right\|$
Tidal Velocity Form Factor	F_u	$\dfrac{U_1}{U_2}$
Tidal Form Factor	F	$\dfrac{\zeta_{K1}+\zeta_{O1}}{\zeta_{M2}+\zeta_{S2}}$
Residual Asymmetry Parameter	$\varepsilon_{R2}, \varepsilon_{R1}$	$\dfrac{u_R}{U_2}, \quad \dfrac{u_R}{U_1}$
Semidiurnal Asymmetry Parameter	Λ_2	$\dfrac{\varepsilon_2 U_2^2}{\left(\frac{4}{7}U^2+2\left((1+\varepsilon_1^2)U_1^2+(1+\varepsilon_2^2)U_2^2+\frac{2}{3}u_R^2\right)\right)}$
Diurnal Asymmetry Parameter	Λ_1	$\dfrac{U_1 U_2(1+2\varepsilon_1\delta_3+2\varepsilon_1\varepsilon_2\delta_4)}{\left(\frac{4}{7}U^2+2\left((1+\varepsilon_1^2)U_1^2+(1+\varepsilon_2^2)U_2^2+\frac{2}{3}u_R^2\right)\right)}$

1.8.3 Appendix C: Summary of trigonometric identities used to derive Equation 8a

Substituting Equation 5 into Equation 6 results in 40 terms corresponding to residual (subtidal) and tidal frequencies. Isolating the terms that contribute to the residual frequency bed stress (Equation 8a) leverages the following trigonometric identities:

$$cos(x)cos(y) = \frac{1}{2}[cos(x-y) + cos(x+y)]$$

Equation S7a,

$$cos(x)cos(y)cos(z) = \frac{1}{4}[cos(x-y-z) + cos(x+y-z) \\ + cos(x-y+z) + cos(x+y+z)]$$

Equation S7b.

For example, the product $u_1^2 u_2$ is given by

$$u_1^2 u_2 = U_1^2 U_2 \frac{1}{4}[cos((\omega_1 t - \phi_1) - (\omega_1 t - \phi_1) - (2\omega_1 t - \phi_2)) \\ + cos((\omega_1 t - \phi_1) + (\omega_1 t - \phi_1) - (2\omega_1 t - \phi_2)) \\ + cos((\omega_1 t - \phi_1) - (\omega_1 t - \phi_1) + (2\omega_1 t - \phi_2)) \\ + cos((\omega_1 t - \phi_1) + (\omega_1 t - \phi_1) + (2\omega_1 t - \phi_2))]$$

Equation S8a,

which can be simplified to

$$u_1^2 u_2 = U_1^2 U_2 \frac{1}{4}[cos((2\omega_1 t - \phi_2)) \\ + cos(2\phi_1 - \phi_2) \\ + cos((2\omega_1 t - \phi_2)) \\ + cos(4\omega_1 t - 2\phi_1 - \phi_2)]$$

Equation S8b.

Thus, the product $u_1^2 u_2$ produces terms at the semidiurnal frequency (first and third term on the RHS), quarterdiurnal frequency (fourth term on the RHS), and residual frequency (second term on the RHS), which represents the diurnal asymmetry term (Term 5) in Equation 8a. Similar relationships can be developed for the other products of $(u_1 + u_2 + u_3 + u_4 + u_R)^3$ using Equations S7a and S7b.

Chapter 2: Tidal Bed Stress Asymmetry and Sediment Transport in Estuaries, Part II: Application to observations and system classification

This chapter has been submitted to the Journal of Geophysical Research: Earth Surface.

See author contribution statement below.

Contributing Authors:

Austin Scott Hudson

David A. Jay

Stefan A. Talke

Author Contributions:

Austin Hudson: Conceptualization, methodology, investigation, formal analysis, writing – original draft, review and editing.

David A. Jay: Conceptualization, writing – review and editing.

Stefan A. Talke: Conceptualization, writing – review and editing.

2.1 Abstract

Residual sediment transport patterns in estuaries can be strongly influenced by tidal asymmetry in bed stress, which can occur from both linear and non-linear tidal interactions among astronomical tidal constituents. The magnitude and direction of bed stress asymmetry is controlled by the tidal velocity amplitudes and phases, and the residual velocity. Here, we apply the non-dimensional numbers (species number Π, and diurnal and semidiurnal asymmetry numbers Λ_1, and Λ_2) developed by Hudson et al. (2023; Part I) to near bed velocity measurements in two prototype estuaries (the Delaware Estuary and San Francisco Bay), to improve understanding of how bed stress and therefore sediment transport patterns respond to tidal and river forcing in these systems. While the along channel variability of residual bed stress differs between the two estuaries, both exhibited multiple regions with convergent bed stress gradients, providing conditions favorable for a net convergence of sediment. Convergence zones were found to overlap with estuary turbidity maxima and regions with relatively high shoaling rates, and may even act as filters or seasonal barriers for sediment moving through an estuary. Channel development and flow regulation can alter tidal bed stress asymmetry near convergence zones and thereby shift sediment transport thresholds, with implications for channel shoaling, sediment supply to the ETM and wetlands, and concentrations and distribution of sediment-borne contaminants. Bed stress asymmetry can be diurnal in estuaries traditionally classified as semidiurnal (and vice versa), but the parameters applied herein (Π, Λ_1, and Λ_2) can help clarify estuarine sediment transport and retention mechanisms.

2.2 Introduction

Bed stress, or the force per unit area applied by flowing water on the riverbed, is a fundamental factor governing the erosion and deposition of sediment, and helps determines the mixing and transport characteristics of both cohesive and non-cohesive sediments (REF). Within estuaries and tidal rivers, the bed stress varies spatially due to bathymetric variability and frictional processes (REF). These spatial patterns evolve over timescales ranging from hours to decades, due to variations in bathymetry, river discharge, and tides. While tidal variability is often considered to be cyclic, non-linear frictional interactions (e.g., between residual flow and major tidal constituents), and the linear superposition of tidal constituents (e.g., $K_1 + O_1 + M_2$), can result in tidally asymmetric bed stress, which is further modulated by residual circulation patterns. These interactions, combined with the observation that erosion and deposition occur over and under a critical bed-stress threshold, can induce a preferential bias in sediment transport directions. Evaluated over an estuary, spatial/temporal variations in bed stress and sediment transport can create/shift locations of deposition and erosion.

To better understand and evaluate how tidal currents interact with the residual (subtidal) velocity to influence spatial/temporal variability of bed stress asymmetry, Hudson et al. (2023) defined a framework in which to evaluate residual bed stress and sediment transport patterns in estuaries. While the framework focuses on residual bed stress patterns, rather than tidal cycle variations in bed stress, it captures the tidal interactions that produce asymmetrical tidal cycle variations (e.g., the diurnal inequality) and thereby provides insight into tidal cycle average (or integrated) sediment transport

patterns (see Hudson et al. 2023 for more details). The framework is summarized by three non-dimensional numbers Π (the Species Number), and Λ_1 and Λ_2 (the diurnal and semidiurnal Asymmetry Numbers, respectively). These numbers describe the relative strength of the diurnal and semidiurnal-induced asymmetry, and the ebb/flood dominance of the bed stress in semidiurnal, diurnal, and mixed-tide estuaries. Here, we apply the framework to two estuarine systems (Delaware Estuary, and San Francisco Bay) to illustrate the approach and highlight the differences between tidal asymmetry driven by the phase relationship between semidiurnal and quarterdiurnal species ($2\phi_2 - \phi_4$; semidiurnal, or non-linear asymmetry) and tidal asymmetry driven by the phase relationship between diurnal and semidiurnal species ($2\phi_1 - \phi_2$; diurnal, or linear asymmetry). Although tidal currents in both the Delaware Estuary and San Francisco Bay are dominated by the semidiurnal species, there are significant differences in the tidal bed stress asymmetry observed in these two systems, the causes of which are clarified through use of the non-dimensional numbers above.

A comparison of the results herein to observations of sediment transport in these two systems, as cited in the literature, suggests that tidal bed stress asymmetry may indeed play an important role in sediment transport and particle trapping (see Sections 4.1 and 4.2). Because bed stress asymmetry is a function of tidal properties, river discharge, and channel geometry, human modifications and/or climate variability can alter sediment transport and particle trapping induced by asymmetrical bed stress, with important implications for water quality, channel shoaling, and estuarine ecosystems (see Section 4). This study aims to clarify how natural and human induced variability in estuaries can

influence tidal bed stress asymmetry through application of the above non-dimensional numbers to in-situ current data from two estuaries. In particular, we will address the following research questions:

1. How does river discharge influence sediment transport and particle trapping driven by bed stress asymmetry?
2. How does bed stress asymmetry and associated sediment transport vary over monthly, annual, and decadal tidal cycles?
3. How do historical changes and along channel variations in channel geometry affect bed stress asymmetry and related residual sediment transport patterns?

This paper begins with an overview of the analytical framework (Section 2), followed by a description of how it can be applied to in situ measurements to study residual bed stress patterns (Section 3). The approach is then applied to observations in the Delaware Estuary and San Francisco Bay, and the causes and consequences of bed stress asymmetry are then interpreted in the context of the sediment transport behavior and historical changes of each system, as cited in the literature (Section 4). Finally, a summary of the results, conclusions, and potential avenues for future research is given in Section 5.

2.3   Analytical Framework

This section provides a brief overview of the analytical framework for studying tidal bed stress asymmetry. Evaluation of bed stress asymmetry is summarized for semidiurnal, diurnal, and mixed tide systems, and then interpreted in terms of simple

metrics that provide insight into sediment transport directions and magnitudes. For more details see Hudson et al. (2023).

Following standard practice, we define bed stress in terms of the near-bed fluid velocity u, fluid density ρ, and a drag coefficient representing the roughness of the bed C_d (Proudman 1952):

$$\tau_b = \rho C_d u |u| \qquad (1).$$

where the absolute value accounts for the reversal in stress direction that occurs when tidal velocities change sign. By convention, the drag coefficient C_d is typically estimated approximately 1 m from the bed, and can vary from about 0.001 to 0.015, depending on location, roughness features such as ripples and dunes, and flow direction (Sanford & Lien, 1999; Fong et al., 2009; Branch et al., 2021). Factors such as density stratification can alter near bed shear $\frac{du}{dz}$ and the Reynolds stress profile, which can vary the effective drag over the tidal cycle and produce pulses of residual circulation (e.g., Jay & Musiak, 1996; Stacey & Ralston, 2005). Here, we neglect spatial/temporal variations in the drag coefficient and focus on how changes in the tidal and residual (subtidal) velocity field influence bed stress and transport direction. The influence of tidal-fluvial interactions on bed stress and bed-stress asymmetry is approximated by expanding $u|u|$ into a number of contributing terms. While many approaches exist, we employ a two-term approximation following Doodson (1924) and Godin (1991) that simplifies the resulting algebra:

$$u'|u'| \approx a u' + b u'^3 \qquad (2),$$

where u' is the dimensionless velocity:

$$u \stackrel{\text{def}}{=} Uu' \tag{3},$$

and U is a dimensional velocity scale equal to the maximum value of the current such that $-1 \leq u' \leq 1$. The coefficients a and b are determined in a least squares sense and are set equal to 0.3 and 0.7, respectively (Godin 1991).

Following Hudson et al. (2023) the near-bed velocity is prescribed as the summation of the residual (subtidal) motion (u_R), and tidal oscillations expressed with the diurnal (u_1), semidiurnal (u_2), terdiurnal (u_3), and quarterdiurnal species (u_4):

$$\begin{aligned}
u &= u_1 + u_2 + u_3 + u_4 + u_R \\
&= U_1 \cos(\omega_1 t - \phi_1) + U_2 \cos(2\omega_1 t - \phi_2) \\
&\quad + U_3 \cos(3\omega_1 t - \phi_3) + U_4 \cos(4\omega_1 t - \phi_4) + u_R
\end{aligned} \tag{4},$$

where ω_1 is the first angular frequency (1 cy/day) introduced by Doodson (1921); and U_k and ϕ_k are the amplitude and phases of tidal species, which vary over the tidal month due to the interaction between the constituents in a given frequency band (see Appendix 2.9.1). By convention, we assume that positive velocity is directed landward (flood). The residual velocity can be either positive or negative, depending on which mechanism is dominant (e.g., gravitational circulation vs river discharge).

Substitution of Equation 4 into Equation 2, and expanding the cubic term, results in 40 terms corresponding to the residual and tidal frequencies. The dimensional residual frequency bed stress is given by:

$$\tau_R = \rho C_d \left\{ \underbrace{aUu_R}_{(1)} + \frac{b}{U}\frac{3}{4}\left[\underbrace{\frac{4}{3}u_R^3}_{(2)} + \underbrace{2(U_1^2 + U_2^2 + U_3^2 + U_4^2)u_R}_{(3)} \right. \right.$$

$$+ \underbrace{U_2^2 U_4 \cos(2\phi_2 - \phi_4)}_{(4)} + \underbrace{U_1^2 U_2 \cos(2\phi_1 - \phi_2)}_{(5)} \qquad (5a).$$

$$\left. \left. + \underbrace{2U_1 U_2 U_3 \cos(\phi_1 + \phi_2 - \phi_3)}_{(6)} + \underbrace{2U_1 U_3 U_4 \cos(\phi_1 + \phi_3 - \phi_4)}_{(7)} \right] \right\}$$

Equation 5a shows that the residual (subtidal) bed stress is driven by a linear residual velocity term (1); non-linear velocity term (2); the semidiurnal asymmetry (term 4); and diurnal asymmetries (terms 5-7). While u_2 contributes to the last three terms in Equation 5a, we label these asymmetries diurnal because they are not possible without the diurnal constituents, and because "M$_2$" in strongly diurnal systems is partially an overtide of K$_1$ and O$_1$. Equation 5a can be simplified by treating the last two terms on the right-hand side as modulations to the fifth term:

$$\tau_R = \rho C_d \left\{ \underbrace{aUu_R}_{(1)} + \frac{b}{U}\frac{3}{4}\left[\underbrace{\frac{4}{3}u_R^3}_{(2)} + \underbrace{2\big((1 + \varepsilon_1^2)U_1^2 + (1 + \varepsilon_2^2)U_2^2\big)u_R}_{(3)} \right. \right.$$

$$\left. \left. + \underbrace{\varepsilon_2 U_2^3 \cos(2\phi_2 - \phi_4)}_{(4)} + \underbrace{U_1^2 U_2(1 + 2\varepsilon_1\delta_3 + 2\varepsilon_1\varepsilon_2\delta_4)\cos(2\phi_1 - \phi_2)}_{(5)} \right] \right\} \qquad (5b),$$

where $\varepsilon_1 = \frac{U_3}{U_1}$ and $\varepsilon_2 = \frac{U_4}{U_2}$ scale the tidal velocity amplitudes of terms 6 and 7 relative to term 5. Thus, while the amplitude of term 5 is first order in Equation 5a, term 6 and 7 are $\mathcal{O}(\varepsilon)$ and $\mathcal{O}(\varepsilon^2)$, respectively. Moreover, the semidiurnal asymmetry (term 4) is $\mathcal{O}(\varepsilon)$ because U_4 is small, further emphasizing the importance of the diurnal (linear) asymmetry (term 5). The parameters $\delta_3 = \frac{\cos(\phi_1 + \phi_2 - \phi_3)}{\cos(2\phi_1 - \phi_2)}$ and $\delta_4 = \frac{\cos(\phi_1 + \phi_3 - \phi_4)}{\cos(2\phi_1 - \phi_2)}$ scale

the strength of the tidal asymmetry phase relationship (e.g., strongly flood/ebb dominant vs symmetrical), and suggests that terms 6 and 7 may become important to residual bed stress patterns during certain windows of the tidal month when $cos(2\phi_1 - \phi_2) \cong 0$, even if ε_1 and ε_2 are small (see Hudson et al. 2023, Part 1). Finally, the overtide contributions to the tidal-fluvial interaction term (term 3) are also $\mathcal{O}(\varepsilon^2)$.

Hudson et al. (2023) expressed Equation 5b in terms of three non-dimensional numbers in order to highlight the parametric relationships that govern ebb/flood dominance of the residual bed stress:

$$\tau_R = \alpha_R U_2 \big(\varepsilon_{R2} + \Lambda_2 (1 + \Pi) cos(2\phi_2 - \phi_4)\big) \qquad (5c),$$

where $\alpha_R U_2 = \rho C_d \dfrac{b}{U} \dfrac{3}{4} \left(\dfrac{4}{7} U^2 + 2 \left((1 + \varepsilon_1^2) U_1^2 + (1 + \varepsilon_2^2) U_2^2 + \dfrac{2}{3} u_R^2\right)\right) U_2$ scales the

magnitude of the velocity field; $\varepsilon_{R2} = \dfrac{u_R}{U_2}$ scales the strength of the residual velocity

relative to the semidiurnal velocity amplitude; $\Lambda_2 = \dfrac{\varepsilon_2 U_2^2}{\left(\dfrac{4}{7} U^2 + 2 \left((1 + \varepsilon_1^2) U_1^2 + (1 + \varepsilon_2^2) U_2^2 + \dfrac{2}{3} u_R^2\right)\right)}$ is the

Semidiurnal Asymmetry Number and scales the semidiurnal asymmetry amplitude relative to the magnitude of the velocity field; $cos(2\phi_2 - \phi_4)$ scales the strength of the

semidiurnal asymmetry phase relationship; and $\Pi = \dfrac{U_1^2 (1 + 2\varepsilon_1 \delta_3 + 2\varepsilon_1 \varepsilon_2 \delta_4) cos(2\phi_1 - \phi_2)}{\varepsilon_2 U_2^2 cos(2\phi_2 - \phi_4)}$ is the

Species Factor, which scales the magnitude of the diurnal and semidiurnal induced asymmetry. See Table 2.6 in Appendix 2.9.2 for a list of parameters used in the analytical framework.

Note that the Species Factor can be used to classify the tidal dynamics of bed stress asymmetry as semidiurnal or D_2-dominant ($|\Pi| \ll 1$), diurnal or D_1-dominant ($|\Pi| \gg 1$), and mixed ($|\Pi| \cong 1$). The Species Factor is closely related to the "Tidal Form Factor" ($F = \frac{\zeta_{K1} + \zeta_{O1}}{\zeta_{M2} + \zeta_{S2}}$), defined in terms of the vertical amplitudes (ζ_i) of the diurnal and semidiurnal tidal constituents, and the "Tidal Velocity Form Factor" ($F_u = \frac{U_1}{U_2}$), which employs velocity amplitudes instead of water levels. Using the Tidal Form Factor, tides may be roughly classified as follows (Pugh 1987):

$F = 0 \; to \; 0.25$ semidiurnal
$F = 0.25 \; to \; 1.50$ mixed-semidiurnal
$F = 1.50 \; to \; 3.00$ mixed-diurnal
$F > 3.00$ diurnal

In terms of the Tidal Velocity Form Factor, the Species Factor can be expressed as:

$$\Pi = \frac{F_u^2}{\varepsilon_2} \left| \frac{(1 + 2\varepsilon_1 \delta_3 + 2\varepsilon_1 \varepsilon_2 \delta_4)\cos(2\phi_1 - \phi_2)}{\cos(2\phi_2 - \phi_4)} \right| \tag{6},$$

which emphasizes the importance of tidal phases to residual bed stress and sediment transport patterns, and illustrates that tidal bed stress asymmetry can be predominantly diurnal ($\Pi \gg 1$) in estuaries that are traditionally classified as semidiurnal ($F<0.25$) if $\cos(2\phi_2 - \phi_4) \cong 0$, for example.

Because $\alpha_R U_2 > 0$, the sign of the residual bed stress (ebb/flood dominance) is determined by a balance between ε_{R2} and $\Lambda_2 (1 + \Pi)\cos(2\phi_2 - \phi_4)$. From Equation 5c, The bed stress is ebb dominant (negative) when:

$$\varepsilon_{R2} < -\Lambda_2(1+\Pi)cos(2\phi_2 - \phi_4) \tag{6a},$$

which reduces to

$$\varepsilon_{R2} < -\Lambda_2 cos(2\phi_2 - \phi_4) \tag{6b},$$

for D_2-dominant systems ($|\Pi| \ll 1$), and to

$$\varepsilon_{R1} < -\Lambda_1 cos(2\phi_1 - \phi_2) \tag{6c},$$

for D_1-dominant systems ($|\Pi| \gg 1$), where $\varepsilon_{R1} = \frac{u_R}{U_1}$ and

$$\Lambda_1 = \frac{U_1 U_2 (1 + 2\varepsilon_1 \delta_3 + 2\varepsilon_1 \varepsilon_2 \delta_4)}{\left(\frac{4}{7}U^2 + 2\left((1+\varepsilon_1^2)U_1^2 + (1+\varepsilon_2^2)U_2^2 + \frac{2}{3}u_R^2\right)\right)}$$ is the Diurnal Asymmetry Parameter.

Equations 5 and 6 highlight several key features of bed stress asymmetry. First, U_k and ϕ_k are species values that vary over the tidal month, which introduces fortnightly variability in the residual bed tress. Second, because tidal asymmetry is a function of tidal phase and amplitude, estuaries traditionally classified as semidiurnal may have residual bed stress and sediment transport patterns driven primarily by diurnal constituents (and vice versa) if $cos(2\phi_2 - \phi_4) \approx 0$, for example, as summarized by the Species Factor Π. Third, Λ_2 appears at $\mathcal{O}(\varepsilon)$, because U_4 is (usually) small compared to U_2, while Λ_1 appears to first-order, and so the diurnal (linear) asymmetry may be much stronger than the semidiurnal (non-linear) asymmetry in mixed-tide systems. And finally, the asymmetry parameters Λ_1 and Λ_2 are less than one, which suggests the residual bed stress switches sign (ebb/flood dominance) for values of $|u_R| < U_k$.

Hudson et al. (2023) also evaluated Equations 6b-c in terms of different sediment transport metrics and show that conditions preferential for ebb dominant sediment transport occur when:

$$\varepsilon_R < -H(|\tau_{max}| - \tau_c)(2 + \frac{\tau_c}{\tau_{max}})\Lambda cos(\Delta\phi) \tag{7},$$

where ε_R, Λ, and $\Delta\phi$, are defined according to Equations 6b and 6c, depending on whether the system is semidiurnal- or diurnal-dominant; τ_c is the critical bed stress threshold that must be exceeded before particles begin to move; τ_{max} is the maximum bed stress during the tidal cycle; and $H(|\tau_{max}| - \tau_c)$ is the Heaviside step function that zeroes out negative values of $(|\tau_{max}| - \tau_c)$. The right-hand side of Equation 7 increases with τ_c because a larger residual velocity is needed to shift the ebb/flood dominance of the peaks in bed stress than is required to shift ebb/flood dominance of the area beneath the bed stress curve. When $\tau_c > \tau_{max}$, no sediment transport occurs.

In addition to highlighting the factors that control flood/ebb dominance of the residual bed stress, the framework above can also provide insight into the factors driving morphological changes in an estuary. Because sediment transport is scaled by the bed stress, setting the spatial derivative of Equation 5c equal to zero defines a necessary (though not sufficient) condition that produces spatially uniform sediment fluxes, which many studies have interpreted as producing relatively stable morphology, or morphodynamic equilibrium (e.g., Friedrichs 1995; Lanzoni and Seminara 2002; Pittaluga et al 2015; Schuttelaars and De Swart 1997). Many factors might modify equilibrium and produce erosion or deposition even if $\frac{d\tau_R}{dx} = 0$, including a spatially

90

variable critical bed stress for erosion and deposition, and in-water column processes such settling lag, flocculation, time varying stratification, gravitational circulation, turbulent coherent structures, and other processes that can influence mixing, residual circulation, and sediment distribution in the water column (see, e.g., Jay and Musiak (1994); Chernetsky et al. (2010); Talke et al. (2009); Winterwerp (2002); and Winterwerp (2011) for more information on these processes). Nonetheless, setting $\frac{d\tau_R}{dx} = 0$ provides insights into how bed stress asymmetry influences morphodynamic equilibrium:

$$\frac{d\tau_R}{dx} = \underbrace{(\varepsilon_{R,k} + \Lambda_k cos\Delta\phi_k)\frac{d}{dx}(\alpha_R U_k)}_{(1)} + \alpha_R U_k \underbrace{\frac{d\varepsilon_{R,k}}{dx}}_{(2)} + \alpha_R U_k \underbrace{\frac{d}{dx}(\Lambda_k cos\Delta\phi_k)}_{(3)} = 0 \qquad (8),$$

where: $\alpha_R = \rho C_d \frac{b}{U} \frac{3}{4}\left(\frac{4}{7}U^2 + 2\left((1 + \varepsilon_1^2)U_1^2 + (1 + \varepsilon_2^2)U_2^2 + \frac{2}{3}u_R^2\right)\right)$, and the subscript k equals 1 in diurnal-dominant systems and 2 in semidiurnal-dominant systems. In mixed systems, a factor of $(1 + \Pi)$ is included in term 3 (see Equation 5c). Whenever the left-hand side of Equation 8 is negative (positive), the bed stress is convergent (divergent), which leads to sediment accumulation (export) and deposition (erosion) of material on the bed. Thus, the morphology of an estuary can be considered relatively stable when spatial gradients in the velocity field, residual currents, and tidal asymmetry are roughly balanced ($\frac{d\tau_R}{dx} = 0$).

Part I also defines a bed-stress asymmetry parameter space. Class I (Concordant Bed-Stress Asymmetry) occurs when ε_R, $\Lambda cos\Delta\phi$, and τ_R are all of the same sign. Residual-Dominant Bed-Stress Asymmetry (Class II) occurs when ε_R and τ_R have the same sign, whereas Class III (Tidal-Dominant Bed-Stress Asymmetry) occurs when

$\Lambda\cos\Delta\phi$ and τ_R are of the same sign, as summarized in Table 2.1, repeated from Part I. Any of the three classes may have either landward ("+" superscript) or seaward-oriented ("-" superscript) bed stress, and a subscript ("1", "2" or "M") can be used for Classes I and III to indicate whether the source of the tidal asymmetry is diurnal, semidiurnal, or mixed, respectively.

Table 2.1. Bed stress asymmetry classification according to the sign of ε_R, $\Lambda\cos\Delta\phi$, and τ_R.

Bed Stress Asymmetry Class	Description	ε_R	$\Lambda\cos\Delta\phi$	τ_R
I^+	Concordant Flood Dominance	(+)	(+)	(+)
I^-	Concordant Ebb Dominance	(−)	(−)	(−)
II^+	Residual Dominant Flood Dominance	(+)	(−)	(+)
II^-	Residual Dominant Ebb Dominance	(−)	(+)	(−)
III^+	Tide Dominant Flood Dominance	(−)	(+)	(+)
III^-	Tide Dominant Ebb Dominance	(+)	(−)	(−)

Finally, the equations above can be expressed in terms of river discharge Q_R or water level ζ (if u_R and/or U_k are strongly correlated with Q_R or ζ_k, where ζ_k is the tidal amplitude for species k; see Section 3), which allows evaluation of bed stress asymmetry over longer time periods than are generally available with velocity measurements. This is important because observations of near-bed velocity in the prototypes explored below are typically several months in duration, while river discharge and water level records span several decades. Thus, the framework described above can also be used to study seasonal, and interannual variations in bed stress asymmetry due to variations in hydrology and long period tidal cycles, as will be illustrated below.

2.4   Methods

The framework reviewed above was applied to in-situ current observations from two estuaries with very different physical and sedimentary characteristics to illustrate the concepts and implications for bed stress asymmetry. This section provides a physical description of each system, followed by a description of data sources and data processing that were used to estimate the residual bed stress (Equation 5) and bed stress gradients (Equation 8), and sediment transport asymmetry (Equation 7).

2.4.1   Site Description

2.4.1.1   Delaware Estuary

The Delaware Estuary is a 220km long estuary on the east coast of the United States (Figure 2.1a). After initially widening from an entrance width of about 18 km, the estuary is approximately funnel shaped upstream of Rkm 20. The width is 45 km near Rkm 20 and decreases exponentially upstream of that point, dropping to 10 km near Rkm 60, 2 km near Rkm 120, and 0.3 km near Rkm 220 (Figure 2.1; Pareja-Roman et al. 2020). The mean depth of the estuary is 8m, but mean channel depths exceed 10m at the entrance, near Rkm 120, and around Rkm 150 (Pareja-Roman et al. 2020).
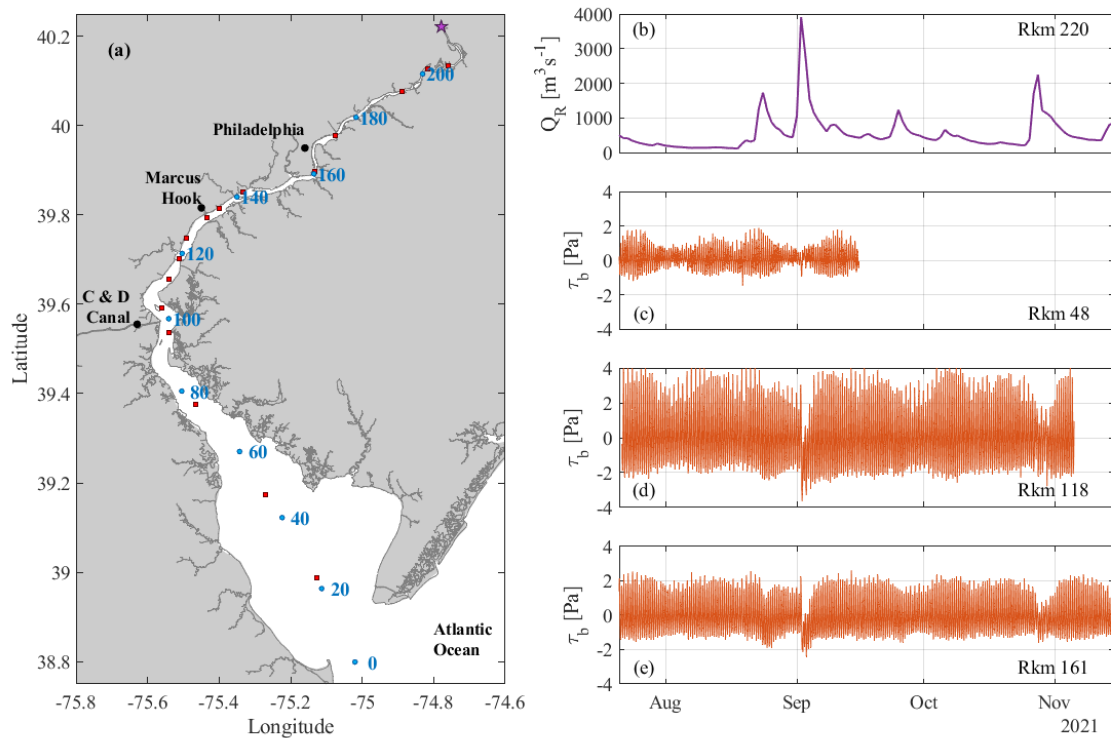
Figure 2.1. (a) Overview map of the Delaware Estuary. Numbers indicate approximate river kilometers, referenced to the entrance. Red squares indicate locations of NOAA near bed current measurements; the purple star indicates location of river discharge estimates. Timeseries of river discharge (b), and bed stress estimated at Rkm 48 (c), Rkm 118 (d), and Rkm 161 ©. Bed stress is estimated by substituting near-bed velocity measurements collected by NOAA into Equation 1.

The mainstem Delaware River, the Schuylkill River, and the Brandywine-Christina River supply roughly 80% of the total freshwater inflow (with mean annual discharges of 330, 77, and 19 m3/s, respectively) and contribute over 80% of the total annual suspended sediment load delivered to the estuary (Sommerfield and Wong 2011). Salinity intrusion into the estuary increases during times of low river discharge and typically ranges from Rkm 80 to Rkm 120 (Aristizábal and Chant 2013), which roughly coincides with the estuary turbidity maximum (ETM) zone that moves between about Rkm 90 and 105, during high and low river discharge conditions, respectively (Sommerfield and

95

Wong 2011). Tidal oscillations in water level are predominately semidiurnal. The tidal

form factor F is 0.23 near the entrance and decreases to 0.17 near Rkm 200 (Table 2.2;

$F = 0$ to 0.25 is classified as semidiurnal).

Table 2.2. Vertical tidal amplitudes of dominant diurnal and semidiurnal constituents, and tidal form factor F, as a function of Rkm in the Delaware Estuary. Values are estimated using harmonic constituent amplitudes reported by NOAA.

NOAA Station	River Kilometer	K_1 [m]	O_1 [m]	M_2 [m]	S_2 [m]	F [-]
8555889	24	0.11	0.08	0.70	0.12	0.23
8537121	65	0.11	0.08	0.81	0.12	0.20
8551762	104	0.10	0.08	0.77	0.10	0.21
8545240	165	0.11	0.08	0.83	0.09	0.21
8548989	207	0.11	0.08	1.08	0.12	0.16

Observations of near bed velocity in the Delaware Estuary were evaluated

between July and November 2021 (See Section 3.2). During this time period, the mean

inflow was 550 m^3s^{-1} but ranged between 115 m^3s^{-1} during low flow periods and 4,400

m^3s^{-1} during a high flow event in early September (Figure 2.1b). Such large variability

facilitates analysis of how river discharge influences tidal asymmetry. As river discharge

increases, tidal current amplitudes decrease, but the effect of discharge on the velocity

field decreases closer to the entrance of the estuary, where the cross-sectional area greatly

increases (Figure 2.1b-e).

2.4.1.2   San Francisco Bay

San Francisco Bay is the largest estuary on the west coast of the United States south of the Salish Sea/Puget Sound region. Upstream of the entrance, the estuary opens up into the Central Bay, which connects to South Bay and San Pablo Bay to the north (Figure 2.6a). This study focuses on the northern part of San Francisco Bay, which extends roughly 90 km from the entrance and consists of a series of embayments connected by narrow straights (Figure 2.6a). Water depths in San Pablo and Suisun Bays are typically less than 5 m (Barnard et al. 2013), but the thalweg through North San Francisco Bay is about 9 to 11 m deep (Schoellhamer 2000), and reaches about 20 m near Point San Pablo (~Rkm 20) and Carquinez Straight (~Rkm 45).
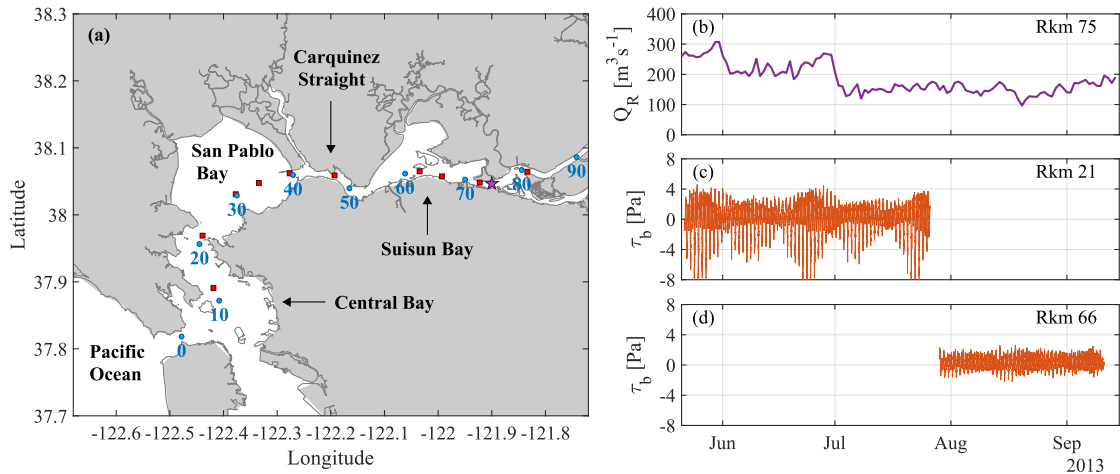
Figure 2.2. (a) Overview map of San Francisco Bay. Numbers indicate approximate river kilometers, referenced to the Golden Gate Bridge. Red squares indicate locations of NOAA near bed current measurements. Purple star indicates location of river discharge estimates. Timeseries of river discharge (b), and bed stress estimated at Rkm 21 (c) and Rkm 66 (d). Bed stress is estimated by substituting near-bed velocity measurements collected by NOAA into Equation 1.

River discharge through northern San Francisco Bay is supplied by the Sacramento–San Joaquin Delta and is estimated near Rkm 75 using the Net Delta Outflow Index (NDOI), which averaged 580 m^3s^{-1} between 2000 and 2020, but reached a maximum of 10,600 m^3s^{-1} during February of 2017 (https://data.ca.gov/dataset/dayflow). Salinity intrusion into the estuary increases during times of low river discharge; the 2 psu near-bed isohaline ranged from about Rkm 40 to Rkm 90 between 2000 and 2020 (https://data.ca.gov/dataset/dayflow). Tidal oscillations in water level are mixed-semidiurnal. The tidal form factor F is 0.83 near the entrance and decreases to 0.75 near Rkm 100 (Table 2.3; $F = 0.25$ to 1.5 is classified as mixed-semidiurnal; see also discussion in Parker, 2007).

Table 2.3. Vertical tidal amplitudes of dominant diurnal and semidiurnal constituents, and tidal form factor F, as a function of Rkm in the San Francisco Bay. Values are estimated using harmonic constituent amplitudes reported by NOAA.

NOAA Station	River Kilometer	K_1 [m]	O_1 [m]	M_2 [m]	S_2 [m]	F [-]
9414290	0	0.37	0.23	0.58	0.14	0.83
9415056	30	0.37	0.22	0.64	0.15	0.75
9415144	62	0.28	0.16	0.47	0.10	0.77
9415316	98	0.22	0.11	0.37	0.07	0.75

The ETM zone in northern San Francisco Bay ranges from about Rkm 40 to Rkm 80, depending on longitudinal and vertical salinity gradients and tidal amplitudes/phases (Schoellhamer 2000). A near-bed ETM is often found in Carquinez Straight (~Rkm 50) due to increased channel depths that enhance stratification and gravitational circulation (Schoellhamer 2000). During spring tides, vertical mixing increases, which increases suspended sediment concentrations and decreases stratification in Carquinez Straight,

leading to a surface ETM (Schoellhamer 2000). During neap tides, vertical mixing is reduced, thereby enhancing stratification and gravitational circulation in Carquinez Straight, which shifts the surface ETM further upstream into Suisun Bay (Schoellhamer 2000). Another ETM zone can also form along northern San Pablo Bay due to sediment input from the Petaluma River and Sonoma Creek, where the concentration and spatial extent of suspended sediment greatly increase during spring tides (Schoellhamer et al. 2007; Ruhl et al. 2010).

Observations of near bed velocity in San Francisco Bay were evaluated from measurements collected between May and September 2013 (see Section 3.2). During this time period, the system was in a prolonged drought; river discharge averaged 180 m^3s^{-1}, but ranged from about 100 to 300 m^3s^{-1} (Figure 2.6b). Therefore, this dataset allows analysis of bed stress asymmetry only during low river discharge periods. According to the formula of Monismith et al (2002), the salinity intrusion X_2 (location where bottom salinity = 2 psu) ranged between Rkm 75 to 85 during the study period, so the values observed in summer 2013 are close to the maximum intrusion that is expected to occur with present system management. Results are shown during two different time periods because data downstream of Rkm 40 were collected between May and July of 2013, while those upstream of Rkm 40 were collected between July and Sep of 2013 (see Table 2.8 and Figure 2.6).

2.4.2 Data Sources and Data Processing

2.4.2.1 Using Velocity Measurements to Study Bed Stress Dynamics

Velocity measurements used in this study were collected by the National Oceanic and Atmospheric Administration (NOAA; https://tidesandcurrents.noaa.gov/) and timeseries are about three months in duration (see Table 2.7 and Table 2.8 in Appendix). Observations were made with Acoustic Doppler Current Profilers (ADCPs) located on the bed within the main channel, and are provided at 6-min intervals within roughly 1-meter bins throughout the water column. For the purposes of this study, the bin closest to the bed was used to define the near-bed velocity. Due to the physical height of the bottom-mounted instrument and blanking distance for ADCPs, measurements in the lowest bin were typically 2-3 meters off the bed, which is greater than the conventional height of estimating bed stress (about 1 meter off the bed), and may overestimate the bed stress if vertical velocity shear $\left(\frac{du}{dz}\right)$ near the bed is large. In all cases, observations were made within the bottom 25% of the water column (see Table 2.7 and Table 2.8). As point measurements, these data are not necessarily representative of the width average conditions. However, they have the advantage of being actual measurements, rather than model projections or theoretical estimates. River discharge into the Delaware Estuary was taken from the United States Geological Survey (USGS) Station 01463500 near Rkm 200. And the Net Delta Outflow Index (NDOI; https://data.ca.gov/dataset/dayflow) near Rkm 75 was used to quantify river discharge into San Francisco Bay.

For each system, the residual (subtidal, or tidally filtered) velocity and tidal current amplitudes and phases are estimated from point measurements of near bed

velocity timeseries using CWT_Multi (Lobo et al. 2023), a program that implements

continuous wavelet transforms to estimate amplitudes and phases of tidal species and/or

constituents from timeseries data. Wavelets are useful for this study despite their limited

frequency resolution because they are able to resolve tidal properties on weekly or daily

timescales (Jay & Flinchem, 1995, 1997; Flinchem & Jay, 2000). Resolution on such

short time scales is important in estuaries because tides are non-stationary, varying on

daily to monthly timescales with river discharge and spring-neap cycles (Flinchem and

Jay, 1997; Kukulka and Jay, 2003). Moreover, CWT_Multi directly estimates the tidal

species properties that appear in Equations 5-8, so that species properties do not need to

be estimated as a sum of constituents, though such a procedure would also be valid.

Asymmetry in bed stress and sediment transport is then analyzed by substituting

the estimated amplitudes and phases of the tidal species into the equations outlined in

Section 2. For example, the residual bed stress can be estimated from CWT_Multi output

by substitution of the residual velocity u_R, and the tidal species velocity amplitudes and

phases (U_k and ϕ_k) into Equation 5. At all stations, the water density ρ was assumed to

be 1,000 kg m^{-3} (because salinity/density measurements were not available at all

locations) and the drag coefficient C_d was assumed to be 0.003, following prior studies in

tidal rivers (Giese and Jay 1989; Friedrichs and Aubrey 1994; Ralston et al. 2019).

Because the water density and drag coefficient vary spatially in estuaries, which influence

the bed stress (see Equation 1), the results herein are most indicative of residual bed

stress and sediment transport direction (which is determined by $u|u|$) rather than

magnitude.

Finally, along channel gradients of bed stress between two observation points were estimated by using the slope $\left(\frac{y_2-y_1}{x_2-x_1}\right)$ of the terms in Equation 8 to define spatial derivatives. Along channel gradients are then shown at the midpoint between the two observations points. While other finite difference schemes can provide more accurate estimates of spatial derivatives (e.g., central difference or leapfrog), they utilize data farther afield from where the derivative is being evaluated (Strikwerda 2004) and so are more suitable for densely sampled data. The observation points evaluated herein were about 5-10 km apart (sometimes farther), and often separated by topographic features with similar (or smaller) length scales. We believe these topographic features significantly influence bed stress asymmetry, as will be discussed below, so we opted against a multistep scheme that would smooth out local variability. Again, we iterate that the difference between two successive point measurements can be influenced by many factors beyond along-channel variability (e.g., sensor placement) and so the trends presented herein are intended to provide a general indication of spatial gradients (i.e., convergent vs divergent) rather than exact values.

2.4.2.2 Analysis of longer-term dynamics

The above analyses for Delaware and San Francisco Bays provide snapshots of the sediment transport dynamics of the systems, based on relatively short ADCP data sets. How can we achieve a longer-term perspective? We argue that the dynamical framework of Section 2 can be used to provide a longer-term perspective using water level time series at a station where velocity data are available, if several conditions are met:

- The tidal velocities for each tidal species are well correlated with the corresponding tidal heights for the same species at a station.

- The residual flow at the station can be similarly related to the river discharge.

- Bathymetric change is not so large as to render irrelevant the velocity-height and velocity-discharge correlations based on a limited-duration velocity record.

Several caveats apply. The first is the same as with velocity data— point measurements of water level and discharge do not fully characterize the dynamics of the cross-sections where they are located, even if these are relatively narrow. Second, there should be sufficient dynamic range in river flow and tidal range to provide strong relationships between the current and height parameters.

In the Delaware Estuary, bed stress dynamics near Rkm 118 and Rkm 132 were evaluated between 2002 and 2022 using water level measurements collected by NOAA near Rkm 104 (NOAA Station 8551762) and Rkm 165 (NOAA Station 8545240) to define U_k and ϕ_k (see Figure 2.3), and river discharge measured near Rkm 200 (USGS Station 01463500) to define u_R (see Figure 2.4). While water level measurements are available closer Rkm 132, the station at Rkm 165 provided the longest, continuous record to evaluate long-term patterns of bed stress. At each location, the amplitude and phase of tidal species were estimated using CWT_Multi, and then water level species were mapped to near bed velocity amplitude and phase using Ordinary Least Squares Regression in MATLAB (see Figure 2.3). Phases estimated by CWT_Multi were shifted by increments of 2π as needed to keep ϕ_k within the interval $[0,2\pi]$, which improved the regression parameter estimates while maintaining the mathematical representation of the

physics (because $cos(\phi) = cos(\phi \pm 2\pi)$). Note that the relationship between the quarterdiurnal velocity phase ϕ_4 and water level phase $\phi_{\zeta 4}$ at Rkm 118 changed during high river discharge (possibly due to downstream translation of the salinity field) and so a robust fitting option was used in MATLAB for these two variables, which improved parameter estimates of the regression, but also limits the results to conditions when Q_R is less than about 1,000 ms^{-3} (see Figure 2.3f). Finally, correlations between the terdiurnal velocity and water level amplitude and phase were weak, so this species was not included in analysis of long-term dynamics.
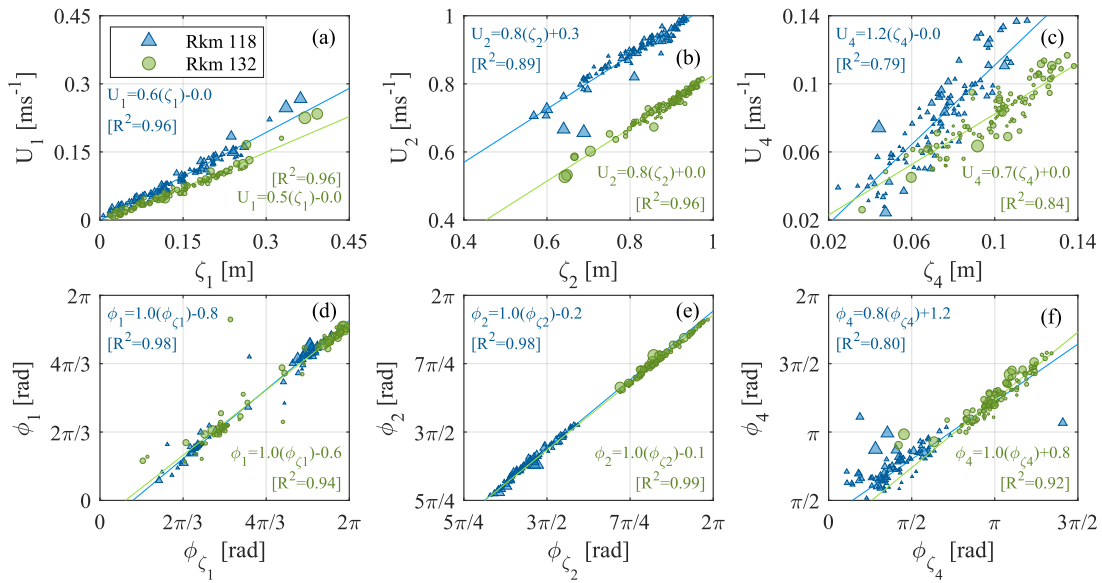
Figure 2.3. Tidal velocity amplitude vs tidal water level amplitude (a-c) and tidal velocity phase vs tidal water level phase (d-f) near Rkm 118 (blue triangles) and Rkm 132 (green circles) in the Delaware Estuary. Marker size increases with the relative magnitude of river discharge. Tidal amplitude and phase are derived using CWT_Multi with near-bed velocity measurements collected by NOAA near Rkms 118 and 132, and water level measurements collected by NOAA near Rkms 104 and 165. Data represent conditions between 21-July-2021 and 15-Nov-2021.
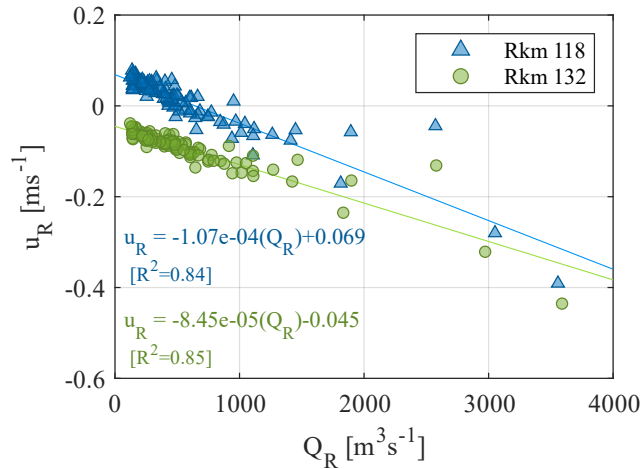
Figure 2.4. Residual velocity estimated at Rkm 118 (blue triangles) and Rkm 132 (green circles) vs river discharge in the Delaware Estuary. Data represent conditions between 21-July-2021 and 15-Nov-2021.

Data in San Francisco Bay were processed in a similar manner. In this case, water level measurements collected at Port Chicago (~Rkm 62; NOAA Station 9415144) were used as a proxy for near bed velocity measurements near Rkm 62. The dynamic range of river discharge during NOAA ADCP deployment was quite small, however, which precluded meaningful estimates of the residual velocity. Moreover, the overtide (D_3 and D_4) velocity amplitude and/or phase were not well correlated with water level amplitude and phase during the study period. We focus, therefore, on decadal scale variability of the diurnal asymmetry (Term 5 in Equation 5a) between 1980 and 2020, as an illustration of the possibilities for future analysis with a wider-ranging velocity dataset. The relevant correlations are provided in Figure 2.5 for Rkm 62.
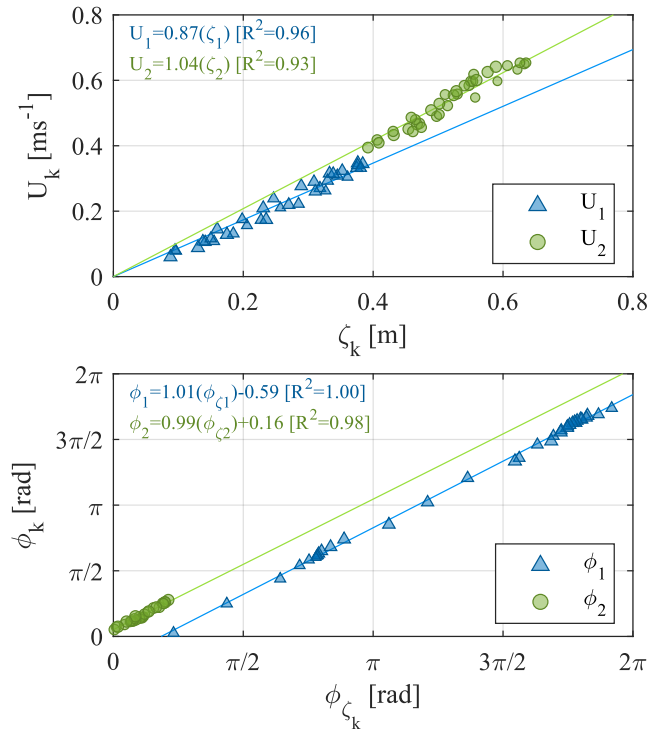
Figure 2.5. Tidal velocity amplitude vs tidal water level amplitude (a) and tidal velocity phase vs tidal water level phase (b) near Rkm 62 in San Francisco Bay. Tidal amplitude and phase are derived using CWT_Multi with near-bed velocity measurements collected by NOAA at station SFB1323, and water level measurements collected by NOAA at Port Chicago (station 9415144). Data represent conditions between 01-Aug-2013 and 05-Sep-2013.

2.4.3   Application to Other Systems

Finally, the analyses described above are also applied to five other estuaries wherein NOAA near-bed velocity measurements are available (Table 2.4). In these systems, measurements are analyzed at one or two locations to provide a rough classification of the bed stress dynamics and cursory overview of bed stress gradients near known convergence zones. Systems with only one location analyzed did not have observations conducive for estimating bed stress gradients, either because proximate

measurements were not collected during the same time period (Humbolt Bay) or were

simply not available (Mobile Bay).

Table 2.4. Location and observation period of the seven estuaries wherein bed stress asymmetry is classified and bed stress gradients are examined (see Section 5.3).

System	Latitude	Longitude	Observation Period
Hudson River	40.77	-74.00	12-Aug-19 to 20-Oct-19
Delaware Estuary	39.70	-75.51	23-Jul-21 to 05-Nov-21
Cape Fear Estuary	33.98	-77.95	19-Mar-16 to 14-Apr-16
Saint James River	30.40	-81.39	16-Apr-98 to 04-Jun-98
Mobile Bay	30.23	-88.03	14-Nov-10 to 06-Feb-11
Humbolt Bay	40.79	-124.2	12-Dec-02 to 02-Jan-03
San Francisco Bay	38.06	-122.0	28-Jul-13 to 10-Sep-13

2.5 Results

2.5.1 Delaware Estuary

Tidal currents in the Delaware Estuary were D_2-dominant during the study period, with U_2 comprising roughly 80% of the tidal current amplitude during low river discharge and 55% during a high river discharge event in early September 2021 (Figures 2.6a-b). Upstream of the entrance, U_2 increased (likely due to channel convergence) to a local maximum near Rkm 118, and thence decreased further upstream (Figure 2.6a-b). Quarterdiurnal (D_4) current amplitudes were about 10% of U_2, on average, and the phase relationship $2\phi_2 - \phi_4$ was ebb dominant near the mouth, weakly ebb dominant between about Rkm 50 and Rkm 80 (depending on river discharge), and flood dominant further

107

upstream (Figure 2.6c-d and 10). Spring-neap variability in $2\phi_2 - \phi_4$ was prominent near the mouth, but diminished upstream of Rkm 100 (Figure 2.7).
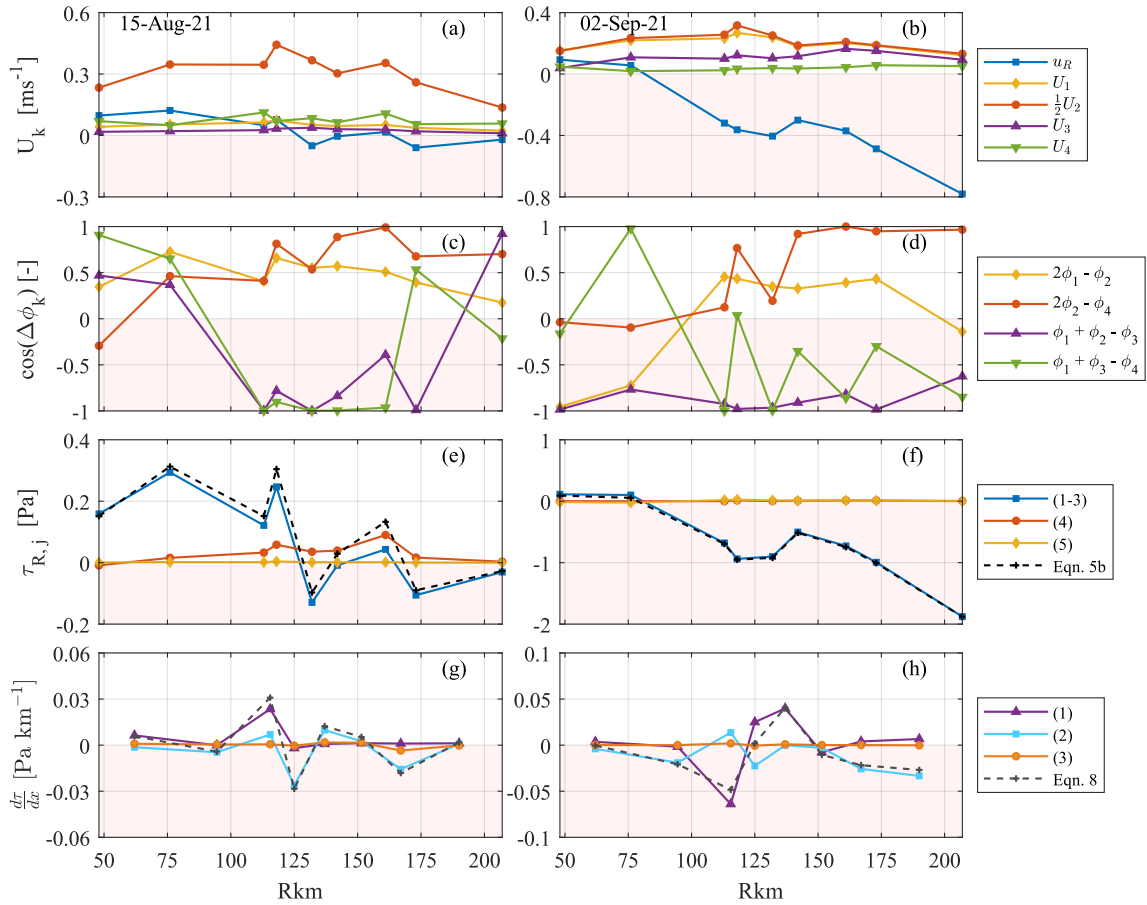
Figure 2.6. Currents amplitudes (a,b); cosine of phase differences for tidal asymmetries in Equation 5a (c,d); residual bed stress components (e,f); and residual bed stress gradients (g,h) as function of river kilometer in the Delaware Estuary during low river discharge (left) and during high river discharge (right). (1-3) represents the sum of the first three terms in Equation 5b, (4) is the fourth term in Equation 5b and (5) is the fifth term. Values are estimated using CWT_Multi with near-bed velocity measurements collected by NOAA and the equations outlined in Section 2. Note the changing scale on y-axis. Pink shading denotes negative values in plot.

During low river discharge, $U_1 \ll U_2$, and U_3 was smaller yet (Figure 2.6a-b), which limited the influence of the diurnal asymmetry on the residual bed stress (term 5 in

Figure 2.6e-f). During the high river discharge event in early September, however, $U_1 \cong \frac{1}{2}U_2$ and U_3 was larger than U_4 (Figure 2.6b). This event occurred during a tropical spring tide (see Figure 2.8b), and so $U_1 \cong \frac{1}{2}U_2$ partly because K_1 and O_1 were in phase, and partly because river discharge damped U_2 more than U_1 (preferential damping of M_2 by river discharge is also observed in mixed systems; see e.g., Moftakhari et al., 2013 or Talke et al., 2020). During this time, the tidal bed stress asymmetry was actually driven by a balance between the diurnal asymmetries and u_R ($\Pi \gg 1$; see Figure 2.8d). However, the residual velocity was sufficiently large to control ebb/flood dominance of the bed stress (Figure 2.6f), which were both ebb dominant in the upstream reaches of the estuary and switched to flood dominant downstream of Rkm 76 (Figure 2.6b), possibly due to stratification of the salinity field. During low river discharge, u_R was positive near the entrance, and negative upstream of Rkm 118; but near Rkm 161, u_R became positive during low river discharge (Figure 2.6a). Coupled with low residual velocities (Figure 2.6a), the local peak in flood dominant semidiurnal asymmetry (Figure 2.6e) lead to flood dominant bed stress between Rkm 142 and Rkm 161 (Figure 2.6e).

Bed stress asymmetry in the Delaware Estuary was typically Class I or Class II (residual bed stress and residual velocity oriented in the same direction). However, both ε_R and $-\Lambda cos\Delta\phi$ became more negative near Rkm 140, establishing a region with Class III$^+$ asymmetry during low river discharge (Figure 2.7). Under these conditions, particles with larger critical thresholds for transport ($\frac{\tau_c}{\tau_{max}} \approx 1$) may be flood-dominant ($\varepsilon_R > -3\Lambda cos\Delta\phi$), while those with smaller critical thresholds for transport ($\frac{\tau_c}{\tau_{max}} \ll 1$) may be

ebb-dominant ($\varepsilon_R < -2\Lambda cos\Delta\phi$). This region coincides within a distinct down-estuary

gradient in bed composition, and separates the dominantly sand and gravel bedded tidal

river from the dominantly mud bedded estuary (Sommerfield and Madsen 2003). Thus,

the tidal asymmetry in bed stress combined with critical stress thresholds appears to be an

important mechanism for sorting particles in the Delaware Estuary.
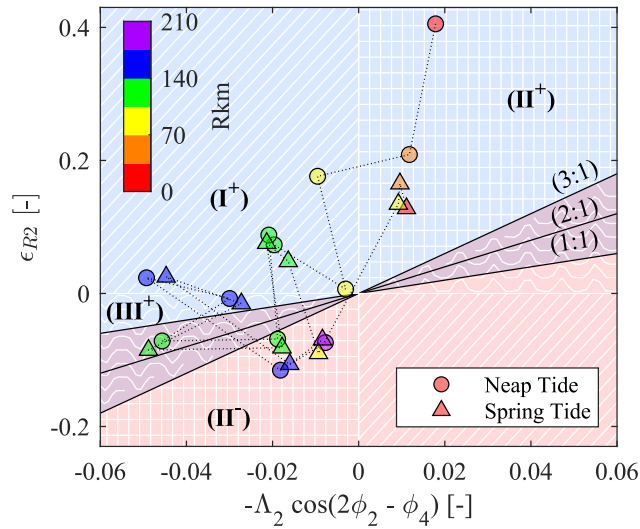
Figure 2.7. Tidal asymmetry parameter space for the Delaware Estuary. Values are estimated using CWT_Multi with near-bed velocity measurements collected by NOAA and the equations outlined in Section 2. Results are shown for spring tide (triangles; 09-Aug-21) and neap tide (circles; 15-Aug-21) conditions during low river discharge ($Q_R \cong 150m^3s^{-1}$).

Spatial gradients in the residual bed stress were typically greatest between about

Rkm 100 and Rkm 140 (Figure 2.6e-h), suggesting that the morphology within this

region is more dynamic than elsewhere in the system. Indeed, about 80% of all material

dredged from the Philadelphia-Sea Shipping Channel is derived from the 30 km reach

between the Chesapeake & Delaware Canal and Marcus Hook (~Rkm 100 to 130;

USACE 2013). Moreover, geophysical surveys of Sommerfield and Madsen (2003)

reveal that fine-grained sediment accumulation within the channel between Rkm 100 and

Rkm 160 occurs as discrete depocenters within the Marcus Hook−New Castle reach

(~Rkm 115 to Rkm 130). Analysis of radioisotopes suggests that deposition at these

depocenters occurs rapidly (up to centimeters per month) on a seasonal basis

(Sommerfield and Madsen 2003). Temporal variability of $\frac{d\tau_R}{dx}$ between about Rkm 110

and Rkm 140 agrees with the observed seasonality of deposition. During low river

discharge, the bed stress was divergent ($\frac{d\tau_R}{dx} > 0$) near Rkm 120 and convergent ($\frac{d\tau_R}{dx} < 0$)

near Rkm 125 (Figure 2.6g). During high river discharge, on the other hand, the bed

stress appeared to be convergent near Rkm 120, and divergent near Rkm 140 (Figure

2.6h). Thus, material passing through this zone that is deposited on the bed during high

flow flows is likely cycled further upstream as river discharge decreases. Similarly,

material that deposits on the bed during low flows may be cycled and redeposited

downstream as river discharge increases. Though water column mixing should also be

considered, the greatest potential for particle trapping in the estuary appears to occur

during low flows near Rkm 120, because the bed stress and $\frac{d\tau_R}{dx}$ are both positive

downstream of this point and both negative further upstream (Figure 2.6e,g). Bed stress

gradients were typically weakest downstream of Rkm 100 (Figure 2.6g,h), suggesting

that particle trapping in this region of the estuary is driven by other mechanisms.

Bed stress gradients appear to be dominated by spatial variability in the residual

flow (term 2 in Equation 8), and by spatial gradients in the velocity field scaled by the

tidal asymmetry (term 1 in Equation 8). Thus, bed stress asymmetry likely plays a

significant role in establishing convergence/divergence of residual bed stress patterns. For example, if the bed stress was tidally symmetric near Rkm 120 ($\varepsilon_R + \Lambda cos\Delta\phi = 0$), then bed stress gradients in this region would have been divergent during high flows (when $\tau_R < 0$), suggesting a net export of sediment downstream. Because bed stress gradients downstream of Rkm 110 were controlled primarily by spatial variability in ε_R (Figure 2.6g & 2h), bed stress asymmetry apparently does not contribute to particle trapping within the ETM (located near Rkm 100), aside from storing and supplying material from further upstream.
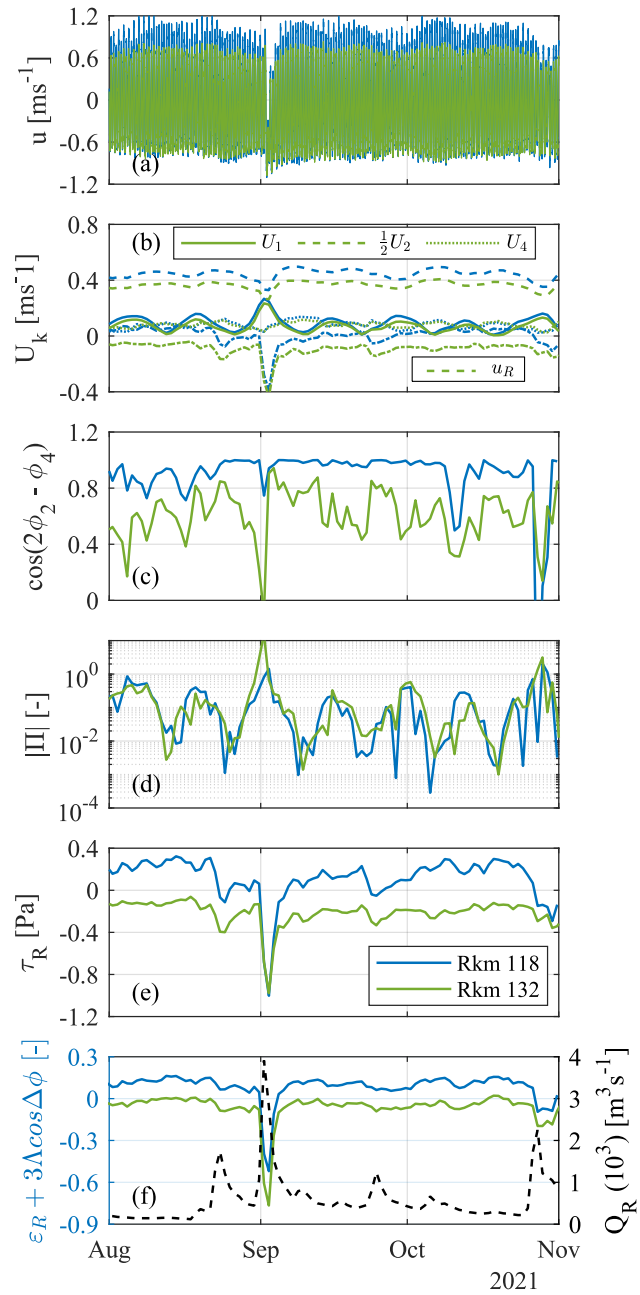
Figure 2.8. Timeseries of near-bed velocity u (a); U_k (b); $cos(2\phi_2 - \phi_4)$ (c); Π (d); τ_R (e); Equation 7 and Q_R (f) in the Delaware Estuary. Values are estimated using CWT_Multi with near-bed velocity measurements collected by NOAA and the equations outlined in Section 2. Results are shown for Rkm 118 (blue), Rkm 132 (green).

Channel topography of the Delaware Estuary likely exerts a strong influence on the bed stress patterns discussed above. For example, near Rkm 118, there is a channel constriction and local maximum in mean channel depth (Pareja-Roman et al. 2020), which enhances density driven residual currents (Figure 2.6a) that remained positive whenever the river discharge was less than about 500 m^3s^{-1} (Figure 2.4). According to Equation 6, the residual bed stress near Rkm 118 remained flood dominant ($\varepsilon_R + 3\Lambda cos\Delta\phi > 0$) so long as Q_R was less than about 600 to 1,000 m^3s^{-1} (see Figure 2.8e,f). And according to Equation 7, the residual sediment transport near Rkm 118 remained flood dominant while Q_R was less than about 1,000 to 1,400 m^3s^{-1} (Figure 2.8f). Above this threshold, bed stress asymmetry is conducive for sediment to move from the tidal river downstream to the estuary. Indeed, analysis of sediment fluxes by Sommerfield and Wong (2011) suggest that the tidal freshwater reach seasonally stores sediments from tributaries on the bed, which are later dispersed downstream and supplied to the ETM during higher river discharge ($Q_R > \sim1,000$ m^3s^{-1}). Upstream of salinity intrusion, there is local minimum in mean channel depth of about 5 m near Rkm 130 (Pareja-Roman et al. 2020), which leads to strong residual currents that were ebb dominant during all river discharge conditions observed during the study period (Figure 2.4). Bed stress gradients between Rkm 120 and 130 appear to increase as river discharge decreases (Figure 2.8e). And according to Equation 7, the sediment transport can actually become flood dominant ($\varepsilon_R + 3\Lambda cos\Delta\phi > 0$) near Rkm 132 during certain tidal conditions when Q_R drops below about 180 m^3s^{-1} (Figure 2.8f), providing a threshold for low-flow shoaling events in this region.

2.5.2   San Francisco Bay

Tidal currents in San Francisco Bay were D_2-dominant during the study period, with U_2 comprising roughly 80% of the tidal current amplitude during tropical neap tides and 60% during tropical spring tides (Figure 2.9a-d). Despite large semidiurnal amplitudes, U_4 was relatively small in the seaward 90 kms of the system (Figure 2.9a-d), and contributed little to the residual bed stress (Figure 2.9i-l). The terdiurnal (D_3) current amplitudes were also relatively small, but grew in strength upstream of Rkm 60 during tropic tides (Figure 2.9a-d). However, the magnitude of the D_3 asymmetry (term 6) remained smaller than the first four terms in Equation 5a, partly because U_3 was small, but also because $\cos(\phi_1 + \phi_2 - \phi_3) \cong 0$ in Suisun Bay (Rkm 62 to Rkm 73) during tropic tides (Figure 2.9h). Diurnal (D_1) current amplitudes dampened slightly in the upstream direction and were about twice as large during tropic tides (when $U_1 \cong \frac{1}{2}U_2$) than during equatorial tides (Figure 2.9-d). Values of Π were typically much greater than unity (D_1 dominant), except for a few days during the tidal month when the diurnal asymmetry switched from ebb to flood dominant (see Figure 2.11). Thus, the residual bed stress was driven primarily by a balance between the residual velocity (terms 1 to 3 in Equation 5a) and the D_1 tidal asymmetry (term 5 in Equation 5a; Figure 2.9i-l).
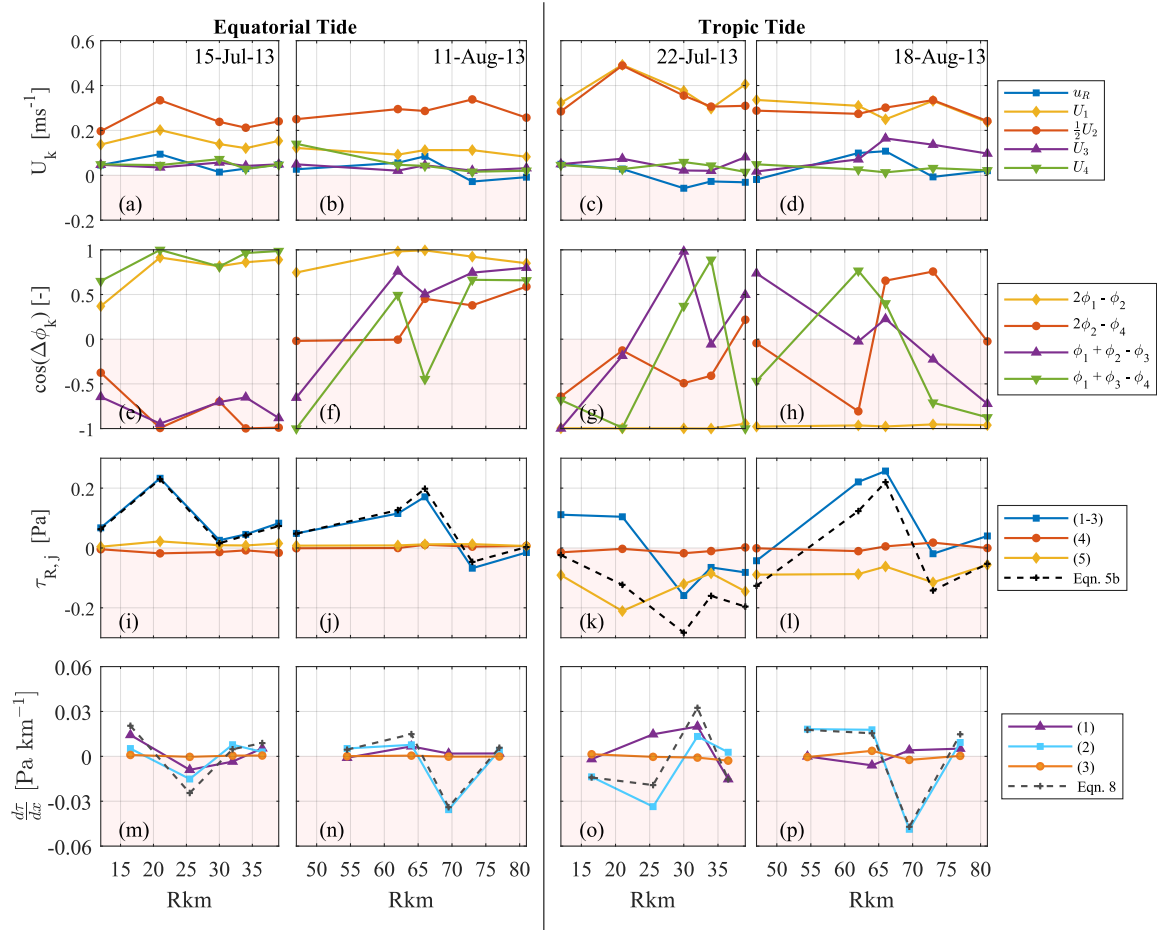
Figure 2.9. Currents amplitudes (a-d); cosine of phase differences for tidal asymmetries in Equation 5a (e-h); residual bed stress components (i-l); and residual bed stress gradients (m-p) as function of river kilometer in San Francisco Bay during equatorial tides (left) and tropic tides (right). (1-3) represents the sum of the first three terms in Equation 5b, (4) is the fourth term in Equation 5b and (4) is the fourth term. Values are estimated using CWT_Multi with near-bed velocity measurements collected by NOAA and the equations outlined in Section 2. Pink shading denotes negative values in plot.

The diurnal asymmetry was stronger during ebb-dominant tropic tides than during flood-dominant equatorial tides (Figure 2.9i-l) because the ebb-tide diurnal inequality was greater than the flood-tide diurnal inequality (Figure 2.11g,h). During equatorial tides, the bed stress asymmetry was typically Class I$^+$ (uniformly flood dominant), because K_1 and O_1 are out of phase (decreasing U_l), and so the residual bed stress is

driven primarily by the residual velocity (Figures 2.9i-j and 2.10). As U_I became larger

during tropic tides the bed stress asymmetry transitioned to Class I⁻ (Concordant, ebb

dominant Asymmetry), between about Rkm 30 and 47, and Class III⁻ (Tide-Dominant,

ebb dominant Asymmetry) elsewhere (Rkm 12 to 21 and Rkm 62 to 81). Thus, ebb

dominant asymmetry must be overcome by a positive residual velocity in order for the

residual bed stress to become flood dominant (Figures 2.9k-l and 2.10). Indeed, the only

location with flood-dominant residual bed stress during tropic tides is between Rkm 60

and 66 (Figure 2.9) where the residual currents are roughly one third of U_1 (Figure 2.9d).

This agrees with Equation 6, the residual bed stress becomes flood dominant near Rkm

60 and 66 about when $u_R > \frac{1}{8} U_1$. While the residual velocity is positive downstream of

Rkm 21 during tropic tides, the residual bed stress remains ebb dominant because the ebb

dominant diurnal asymmetry is greater than the first three terms in Equation 5a (Figure

2.9k). Upstream of Rkm 81, the residual velocity likely becomes increasingly important

(because tides dampen as they propagate upstream), leading to Class I ebb dominance in

the Sacramento River; however, further research is needed to examine patterns in the

Sacramento-San Joaquin Delta because the near bed velocities needed to apply our theory

upstream of Rkm 81were unavailable.
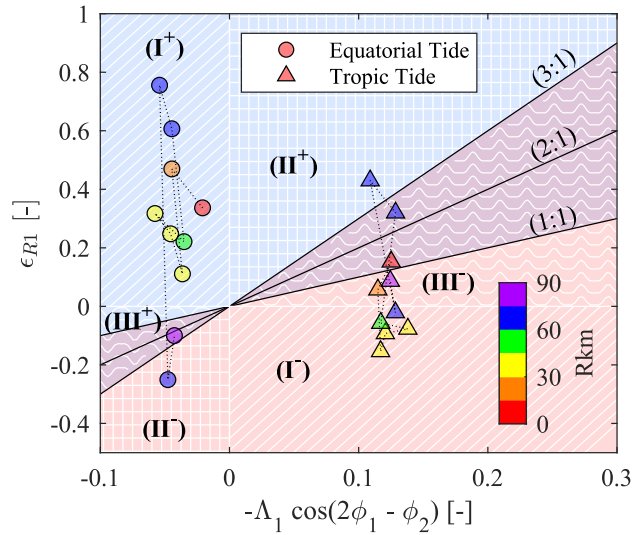
Figure 2.10. Tidal asymmetry parameter space for San Francisco Bay. Values are estimated using CWT_Multi with near-bed velocity measurements collected by NOAA and the equations outlined in Section 2. Results are shown for spring tide (triangles; 22-July-13 downstream of Rkm 40 and 18-Aug-13 upstream of Rkm 40) and neap tide (circles; 15-July-13 downstream of Rkm 40 and 11-Aug-13 upstream of Rkm 40) conditions during low river discharge ($Q_R \cong 150 \text{m}^3\text{s}^{-1}$).

During the study period, spatial gradients in the residual bed stress were persistently convergent in two locations, potentially contributing to particle trapping. The first convergence zone occurred in San Pablo Bay between Rkm 20 and Rkm 30 (Figure 2.9) and collocates with a reach of the federal navigation channel that requires frequent dredging to maintain navigable depths (https://www.dmmosfbay.org/). The second convergence zone occurred in Suisun Bay between Rkm 66 and Rkm 73, which overlaps with the along channel distribution of the ETM zone in North San Francisco Bay (Schoellhamer 2000). Both convergence zones were driven primarily by spatial gradients in ε_R (term 2 in Equation 8), while bed stress asymmetry coupled with along channel variability in the velocity field (term 1 in Equation 8) typically acted to reduce

118

convergence (Figure 2.9m-p). Qualitatively, both these regions are marked by large intertidal regions and wetlands, consistent with being a deposition zone.

Near the downstream end of San Pablo Bay (Rkm 21), the residual velocity was flood dominant throughout the study period, increasing slightly during equatorial/neap tides (Figure 2.11c), possibly because vertical mixing was smaller, thereby enhancing stratification and gravitational circulation (Monismith et al. 1996; Stacey et al. 2001). Ebb dominant diurnal asymmetry during spring tides causes the residual bed stress near Rkm 21 to become negative for a few days during the tidal month (Figure 2.11k). The direction of sediment transport, as represented by Equation 7, on the other hand, appears to be ebb dominant most of the tidal month near Rkm 21, becoming flood dominant for a few days during equatorial tides, according to Equation 7 (Figure 2.11m). Near Rkm 30, u_R and $\cos(\Delta\phi)$ were positive during equatorial tides and negative during tropic tides (Figure 2.11c,e), leading to ebb dominant residual bed stress and sediment transport (according to Equation 7) during most of the tidal month (Figure 2.11k,m). Thus, sediment potentially moves downstream through San Pablo Bay during tropic tides, despite flood-oriented residual velocities, and upstream during equatorial tides, which is consistent with observed spatial patterns of surface turbidity in San Pablo Bay, which show higher turbidity levels that extend further seaward during spring tide than during neap tide (Ruhl et al. 2001).
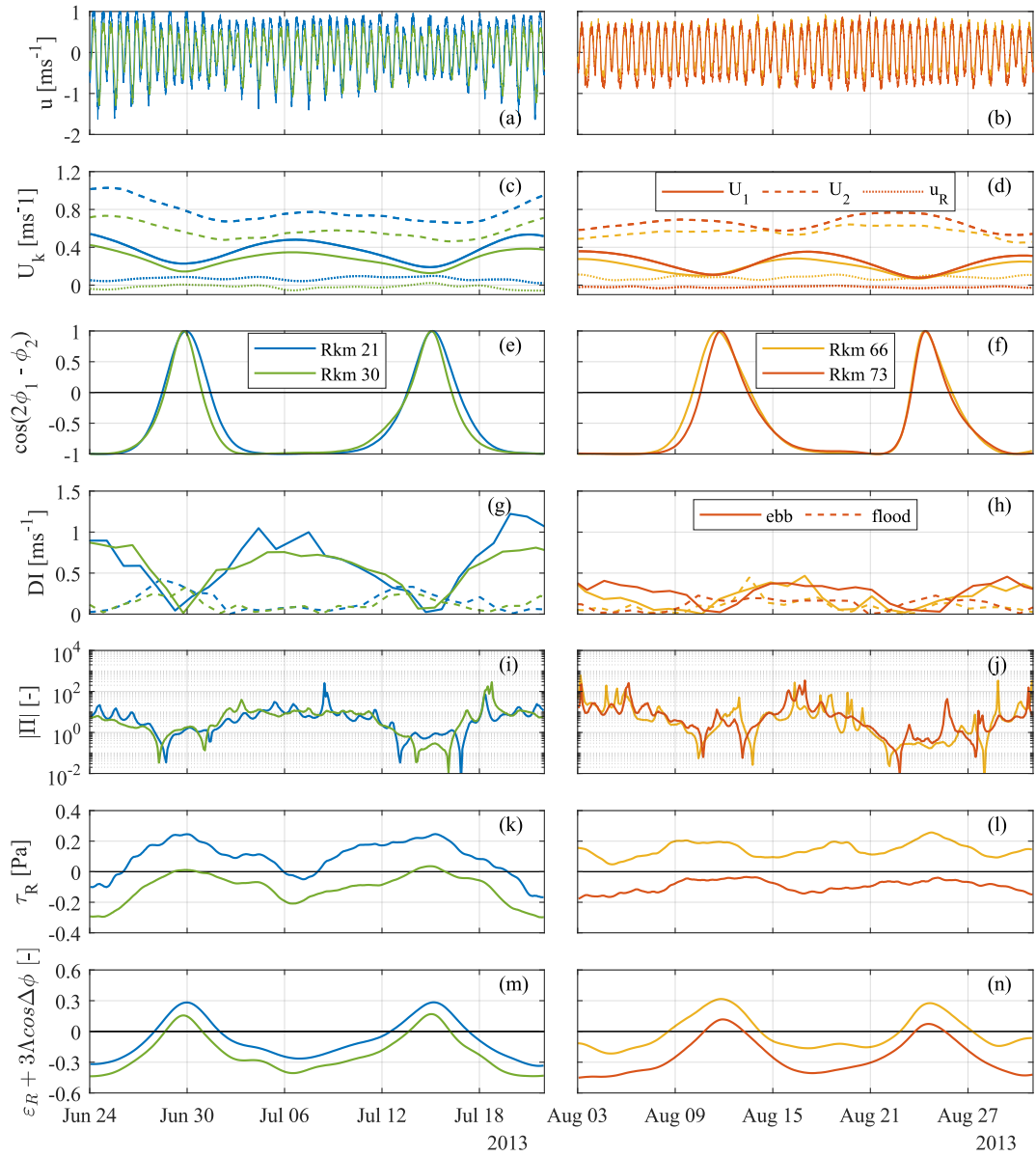
Figure 2.11. Timeseries of near-bed velocity u (a,b); U_k (c,d); $cos(2\phi_1 - \phi_2)$ (e,f); diurnal inequality during flood (dashed line) and ebb (solid line) (g,h); Π (i,j); τ_R (k,l); and components of Equation 7 (m,n) in San Francisco Bay. Values are estimated using CWT_Multi with near-bed velocity measurements collected by NOAA and the equations outlined in Section 2. Results are shown for Rkm 21 (blue), Rkm 39 (green), Rkm 66 (yellow), and Rkm 73 (red).

120

At the upstream convergence zone (Rkm 66 to Rkm 73), the tropic and synodic tidal cycles were nearly 180º out of phase (Figure 2.11d), which along with smaller U_1 magnitudes, damped tidal-monthly variability of the residual bed stress, as compared to further downstream (Figure 2.11l). The residual velocity was uniformly flood dominant near Rkm 66 and ebb dominant near Rkm 73 during the study period (Figure 2.11d). Because ebb-dominant tropic tides near Rkm 66, and flood-dominant equatorial tides near Rkm 73, were not strong enough to counteract the residual velocity, the residual bed stress followed the residual velocity (Class II asymmetry). Similar to the downstream convergence zone, sediment transport in Suisun Bay appears to move upstream during equatorial tides and downstream during tropic tides, according to Equation 7 (Figure 2.11n). Divergent bed stress gradients between Rkm 30 and 66 coupled with flood dominant transport (Figure 2.9i-p) suggests that material in San Pablo Bay and Carquinez Straight is cycled upstream to Suisun Bay during low discharge conditions and trapped near the upstream limits of salinity intrusion (see Schoellhamer 2000), at least based on these limited time series.

Equation 8 suggests that bed stress convergence in Suisun Bay likely decreases with river discharge, as the salinity field is shifted further downstream, because $\frac{d\varepsilon_R}{dx}$ would decrease. However, there may be an intermediate river discharge that compresses and stratifies the salinity field without fully expelling it from Suisun Bay, which would enhance $\frac{d\varepsilon_R}{dx}$ and bed stress convergence. Because San Pablo Bay is always downstream of X_2 (Monismith et al. 2002), convergence between Rkm 20 and 30 likely grows monotonically with increasing river discharge, as the density field becomes more

stratified and laterally compressed. However, during the study period, X_2 varied only

between about Rkm 75 and Rkm 85 (https://data.ca.gov/dataset/dayflow), and a longer

timeseries would be needed to explore how the results above are influenced by a larger

dynamic range of river discharge. Note that subtidal sediment dynamics in San Francisco

Bay are also driven by seasonal fluctuations in wind direction and magnitude

(Schoellhamer 2002), which may influence the patterns of bed stress asymmetry

discussion above and warrants further investigation with a longer dataset.

2.5.3   Low Frequency Variations of Bed Stress Asymmetry

The results above are now discussed in terms of low frequency tidal cycle

variations using the relationships between tidal velocity and water level, and residual

velocity and river discharge developed in Section 3.2.2. By "low frequency" variations,

we mean oscillations with frequencies less than 1 cy/day that are created by the

interaction between tidal constituents, and in particular we focus on fortnightly,

semiannual, and 18.6-yr nodal cycle variations in tidal amplitude/phase. Because bed

stress scales nonlinearly with velocity (Equation 2), low frequency oscillations in tidal

properties are amplified in the residual bed stress and bed stress asymmetry, as will be

shown below. In the Delaware Estuary, bed stress dynamics are examined near the

convergent zone observed between Rkm 118 and Rkm 132 (see Figure 2.2). In San

Francisco Bay, we focus on the diurnal asymmetry (term 5 in Equation 5a) because

reliable estimates of residual velocity could not be generated, due to the small dynamic

range of river discharge during NOAA ADCP deployment, which precludes estimates of

the first three terms defining the residual bed stress in Equation 5a.

2.5.3.1 Delaware Estuary

In the Delaware Estuary, U_1, U_2, and U_4 varied by about $\pm14\%$, $\pm1\%$, and $\pm3\%$ over the nodal cycle (Figure 2.12b). The nodal cycle maximum of U_2, and U_4 occurred in 2014, while U_1 peaked in 2006 (at both Rkm 118 and 132). The residual velocity also exhibited decadal variability ($\pm7\%$), becoming more negative near the nodal cycle minimum of U_2, and U_4 (because larger river discharge events were more frequent between 2004 and 2012, and less frequent between 2014 and 2020), likely augmenting nodal cycle variability of the bed stress. The residual bed stress appeared to oscillate with the nodal cycle near Rkm 118, but the hydrological cycle near Rkm 132, possibly due to local topography, varying by about $\pm26\%$ and $\pm7\%$, and peaking near 2015 and 2006, respectively. As a result, bed stress gradients between Rkm 118 and 132 varied by about $\pm5\%$ and were more convergent near the nodal cycle maximum of U_2, and U_4.

Semiannual variability of U_1 was about $\pm15\%$, while U_2, and U_4 varied by about $\pm1\%$, all peaking near the summer and winter solstices (Figure 2.12b). The residual velocity near Rkm 118 varied by about $\pm21\%$ and was greatest (most positive) near the summer/winter solstice, while near Rkm 132 u_R varied by about $\pm6\%$, and was greatest (most) negative during spring and fall. Semiannual variability of the residual bed stress was about $\pm11\%$ near Rkm 118, peaking near the solstices, and about $\pm7\%$ near Rkm 132, peaking (becoming most negative) near the equinoxes (or rather, during high discharge events). As a result, bed stress gradients between Rkm 118 and Rkm 132 varied by about $\pm3\%$ over the year (not accounting for seasonal fluctuations in river discharge).

The discussion above focuses on temporal variability due to tidal constituent interactions. River discharge will modulate these results, especially during years with high river discharge. For example, the residual velocity near Rkm 132 varies by an order of magnitude within the dynamic range of river discharge, increasing from about -0.04 to -0.4 ms^{-1} when Q_R increases from 100 to about 3,500 m^{3}s^{-1} (see Figure 2.4). Nevertheless, bed stress gradients between Rkm 118 and Rkm 132 were persistently convergent (see Figure 2.12c) and $\frac{d\tau_R}{dx}$ only became positive (divergent) when River discharge exceeded about 2,000 m^{3}s^{-1} (or about the 99th percentile of river discharge between 2000 and 2022; Figure 2.12a).
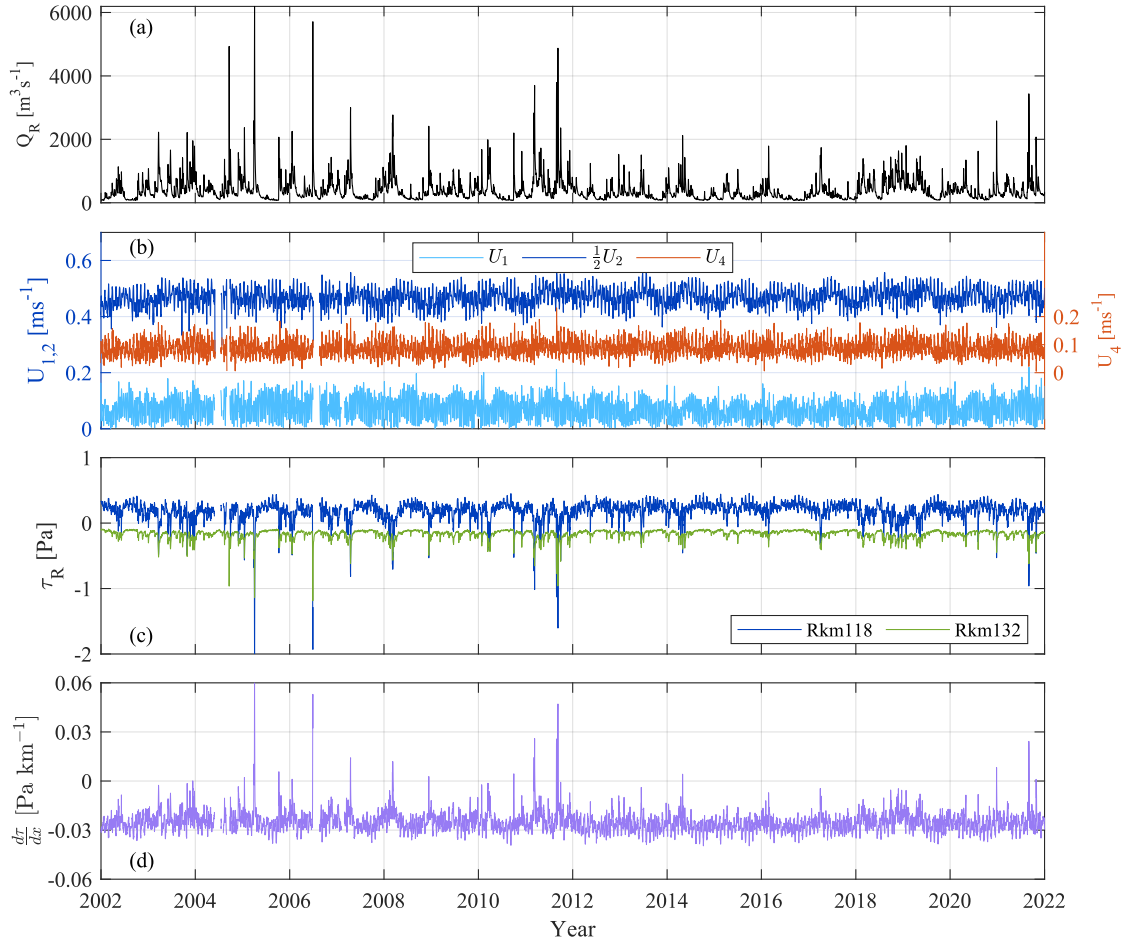
Figure 2.12. Time series of river discharge (a), U_1, U_2, and U_4 (b), residual bed stress (c), and bed stress gradients between Rkm 118 and Rkm 132 (d) in the Delaware Estuary. Velocity amplitude and phase are inferred from water level measurements as summarized in Section 3.2.2.

Fortnightly variations of tidal velocity amplitude were greater than semiannual and nodal cycle variability, with U_1, U_2, and U_4 varying by about $\pm 45\%$, $\pm 5\%$, and $\pm 20\%$, respectively. Over the spring neap cycle, the residual velocity varied by about $\pm 6\%$ near Rkm 118 and $\pm 2\%$ near Rkm 132; and the residual bed stress varied by about $\pm 20\%$ near Rkm 118 but only by about $\pm 1\%$ near Rkm 132, further emphasizing the

125

dominance of river discharge near Rkm 132. As a result, fortnightly variations in bed stress gradients between Rkm 118 and Rkm 132 were roughly $\pm 10\%$.

2.5.3.2 San Francisco Bay

In San Francisco Bay, nodal cycle variations were greater than in the Delaware Estuary because bed stress asymmetry is driven by the diurnal species, which are more variable than semidiurnal species. Nodal cycle variations in U_1 and U_2 are roughly $\pm 12\%$ and $\pm 4\%$, respectively, with U_1 peaking in 1987 and 2006 and U_2 peaking in 1997 and 2015 (about 180° out of phase), which leads to roughly a $\pm 20\%$ variation in the tropic tide diurnal asymmetry (term 5) that peaks during the nodal cycle maximum of U_1 (Figure 2.13b,c). Semiannual fluctuations are about $\pm 20\%$ for U_1, and $\pm 3\%$ for U_2, leading to about $\pm 30\%$ oscillations in the tropic tide diurnal asymmetry over the year (with all three peaking near the winter/summer solstices). Like the Delaware Estuary, fortnightly variations in San Francsico Bay are greater than lower frequency components, with U_1 and U_2, varying by about $\pm 45\%$ and $\pm 15\%$, respectively, and the diurnal asymmetry varying by about $\pm 100\%$ between tropic and equatorial tides and by about $\pm 50\%$ over the spring-neap cycle (Figure 2.13).
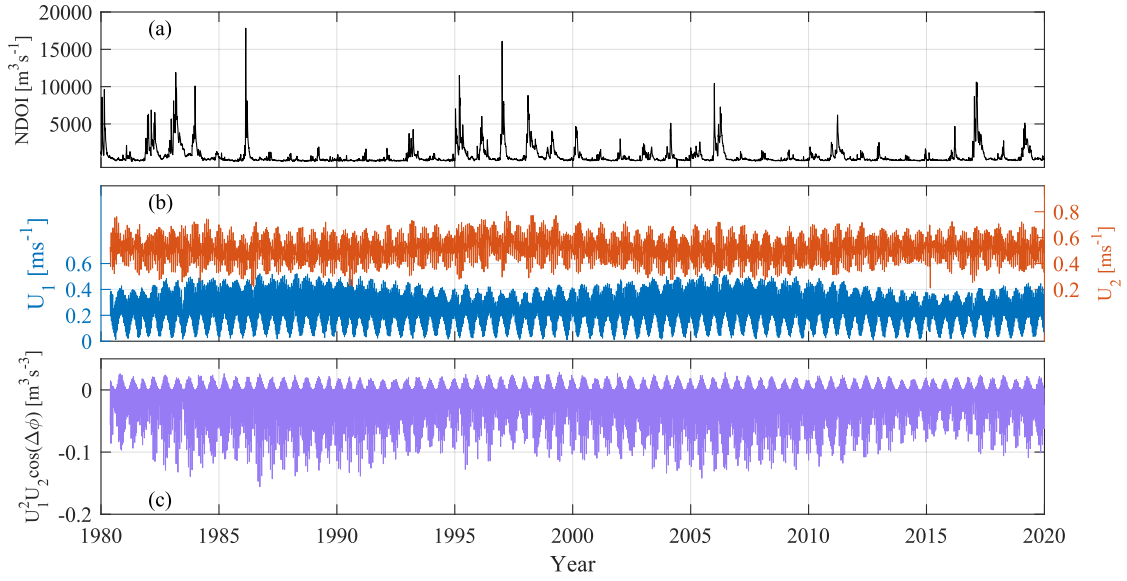
Figure 2.13. Time series of river discharge (a), U_1 and U_2 (b), and diurnal bed stress asymmetry—term 5 in Equation 5a (c) near Rkm 62 in San Francisco Bay. Velocity amplitude and phase are inferred from water level measurements as summarized in Section 3.2.2.

The dataset examined herein occurred near the nodal cycle minimum of the diurnal asymmetry, and so the residual bed stress may tend towards Class III asymmetry and be more ebb dominant during times that are closer to the nodal cycle maximum (2005 or 1987, for example). Seasonal fluctuations in river discharge, which are not considered in Figure 2.13b-c, may further increase temporal variability of the diurnal asymmetry (term 5) because tidal amplitudes are damped during periods of high river discharge (Moftakhari et al. 2013). Note that the nodal cycle maximum of the diurnal asymmetry during the late 1980s overlapped with a period of relatively low river discharge (Figure 2.13a,c), which may have decreased particle trapping and contributed to the loss of bed sediment volume observed during that time (see Schoellhamer 2011). However, further analysis is needed to investigate long term patterns of the bed stress

asymmetry in San Francisco Bay because the residual bed stress is set by u_R, in addition to U_k.

2.6   Discussion

2.6.1   Implications for Sediment Management

The patterns described above suggest that sedimentation patterns in the Delaware Estuary and San Francisco Bay have contrasting responses to changes in river discharge, which has important implications for management practices and ecological functioning. For example, a critical location for shoaling within the Federal Navigation Channel in the Delaware Estuary, occurs between Rkm 100 and 130. Within this reach, the bed stress is consistently convergent and the sediment transport near a local minimum in mean channel depth near Rkm 130 may become flood-dominant when river discharge is less than about 180 m^3s^{-1}. Thus, shoaling in this region likely increases during years with a greater frequency of low flow days. Indeed, annual dredging volumes in the main channel below Philadelphia are highly correlated with the frequency of low flow days defined as $Q_R < 180$ m^3s^{-1} ($R^2 = 0.88$; Figure 2.14).

128
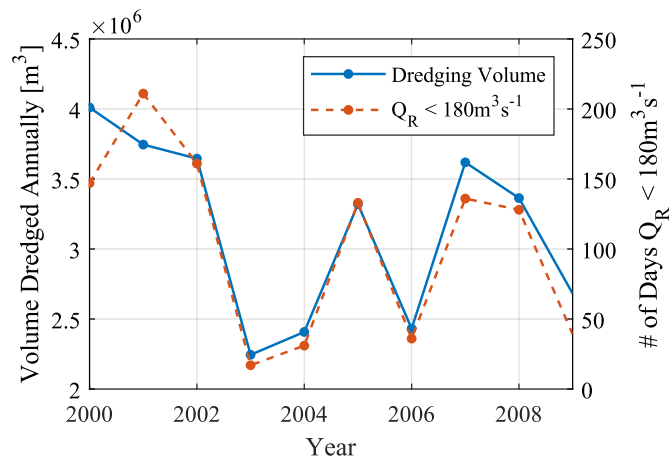
Figure 2.14. Annual dredging volumes in the Delaware navigation channel and # of low flow days ($Q_R < 180$ m^{3}s^{-1}) between 2000 and 2009. Dredging volumes represent quantities from the navigation channel downstream of Philadelphia (USACE 2013).

In contrast, dredging records in San Pablo Bay suggest that shoaling increases with river discharge. Between 2005 and 2020, roughly 3.4 million cubic meters of material was removed from the federal navigation channel in San Pablo Bay (USACE 2011; USACE 2023). During this time, baseline dredging volumes were about 175,000 m^3 annually, but increased about 3- to 4-fold in 2006 and 2017 during high flow years (Figure 2.15). Large dredging volumes during high flow years likely reflect an increase in sediment supply to San Francisco Bay, which greatly increases during years with high annual runoff (Mckee et al. 2013), but also suggest increased particle trapping (otherwise sediment supplied to the estuary would be exported further downstream). For example, while annual dredging volumes in San Pablo Bay appeared to be well correlated with annual cumulative river discharge $\sum Q_R$ ($R^2 = 0.74$), those in Suisun Bay did not ($R^2 = 0.09$). As discussed above, particle trapping in San Pablo Bay likely increases monotonically with river discharge because this reach of the estuary is consistently downstream of X_2, and larger river discharge increases spatial gradients in the density field thereby enhancing flood-dominant near-bed residual currents. Particle trapping in Suisun Bay, on the other hand, may decrease during high flows when the salinity field is translated further downstream. Note that the relationship between annual dredging volumes and annual cumulative river discharge is nonlinear, and dredging volumes do not increase above baseline levels until river discharge exceeds certain thresholds, which likely reflects both sediment transport processes and the logistics/funding for dredging.

129
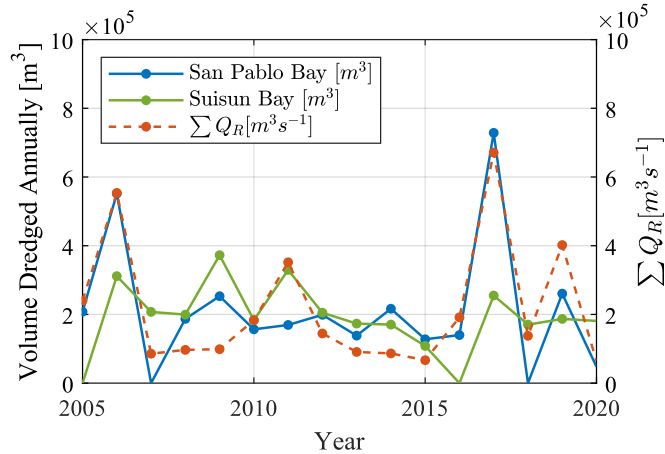
Figure 2.15. Annual dredging volumes in San Pablo and Suisun Bays, and annual cumulative river discharge $\sum Q_R$ between 2005 and 2020. Dredging volumes were accessed from the Dredged Material Management Office of San Francisco Bay (https://www.dmmosfbay.org/).

The systems discussed here are typical of the many estuaries in the world that have been heavily modified by anthropogenic activities, with profound impacts on the residual sediment transport patterns discussed above. For example, dredging in the Delaware Estuary has increased mean water depths from about 5 m in the 1800s to about 8 m today, which has reduced the effective drag and amplified tidal current amplitudes upstream of Rkm 20 (Dilorenzo et al. 1993; Pareja-Roman et al. 2020). At the same time, the shoreline of the Delaware Estuary has become increasingly hardened over the past century—over 75% of the shoreline upstream of Rkm 120 is bulkheaded (Sommerfield and Madsen 2003). While the influence of shoreline hardening on tidal velocity phases has not been directly evaluated in the Delaware Estuary (but see Lee et al. 2017), a reduction in tidal flat area, or a more channelized river, has been associated with more flood dominant M_2-M_4 phase relationships (Speer and Aubrey 1985). Indeed, numerical modeling of Pareja-Roman et al. 2020 indicates that channel deepening has slightly

130

increased the flood dominant phase relationship between M_2 and M_4 upstream of about

Rkm 100. Thus, it is plausible that channel modifications can alter bed stress asymmetry

(e.g., through increases in U_2 or shifts to $\Delta\phi_2$) and thereby shift thresholds for sediment

transport. In the Delaware Estuary, for example, larger tidal amplitudes and stronger

flood dominant phase relationships may increase river discharge thresholds for sediment

transport from the tidal freshwater reach downstream to the lower estuary.

Traditionally channel shoaling has been addressed by dredging, or by increasing

velocity (changing ε_R) to promote scour, e.g., by narrowing the thalweg through

installation of pile dikes or weirs, and/or by changing channel geometry. In regions where

bed stress gradients are influenced by tidally asymmetric velocities, however, changes in

ε_R alone can nudge the morphology out of equilibrium, according to Equation 8. In fact,

changes in ε_R and $\Lambda cos\,(\Delta\phi)$ that move locations within an estuary perpendicular to the

contours in the asymmetry parameter space are most likely to affect morphological

equilibrium. For example, diking and filling in an estuary that decreases the tidal flat area

may increase ε_R and $\Lambda cos\,(\Delta\phi)$, which would tend towards flood dominant asymmetry

and particle trapping. On the other hand, permeable pile dikes or lower elevation dikes

that flood under high flow conditions may increase tidal flat area and enhance ebb

dominant asymmetry. Thus, managing and maintaining tidal flat area may be a technique

that could be used to manage shoaling in an estuary.

San Francisco Bay has also been drastically impacted by humans in terms of

sediment supply, intertidal habitat area, contaminant concentrations, and hydrology

(Barnard et al. 2013). For example, Moftakhari et al. (2013, 2015) suggest that annual

flow to San Francisco Bay has reduced by about 25-35% since the 19th century, which along with decreased sediment supply has resulted in a ~50% reduction in annual sediment delivery to San Francisco Bay. Because lower river discharge leads to a decrease in gravitational circulation and an increase in tidal amplitudes, flow regulation may also reduce particle trapping near and downstream of X_2 (through reductions in u_R) and increase sediment export (through increases in U_1 and U_2). Because historical land use practices have introduced a reservoir of contaminants in the sediments of the estuary, which can out-weigh contemporary loading from the watershed, reduced particle trapping coupled with increased sediment export may expose and erode historical deposits, which could increase contaminant concentrations in the water column and spread contaminated sediments to new locations (Davis et al. 2007; Schoellhamer 2007).

Particle trapping and sediment transport process are strongly linked to the ecological functioning of estuarine habitats. The very existence of certain in-water habitats relies on the sedimentary processes that sustain their morphology. Wetland conditions, for example, represent a relatively short-term balance between changes in mean sea level, sediment supply, and the frequency/duration of inundation (Friedrichs and Perry 2001). Sediment accumulation and accretion rates of estuarine marshes in the lower Delaware Estuary appear to be linked more strongly to sediment availability, rather than flooding frequency/duration (Boyd et al. 2016). Thus, increased river discharge thresholds over the past century for supplying sediment to the lower estuary from the tidal freshwater reach may limit the ability of wetlands to adapt to sea leave rise as compared to the pre-deepened system. Accretion rates of wetlands in San Francisco Bay

are also tied to sediment availability (Callaway 2012; Deverel et al. 2014), and reduced

sediment supply in San Francisco Bay over the past century and into the future may

reduce the resilience of wetlands and inter-tidal habitats to sea level rise (Ganju and

Schoellhamer 2010; Morris et al. 2022). Reduced river discharge due to flow

management or climate change that decreases particle trapping could further compound

the limited sediment supply available to wetlands. Despite these constraints related to

sediment supply, accretion rates in wetlands in both the Delaware Estuary and San

Francisco Bay appear to be keeping pace with contemporary rates of relative sea level

rise (Boyd et al. 2016; Callaway 2012). Nevertheless, sediment transport processes are

extremely non-linear and typically activate only when forcing variables exceed certain

thresholds, after which they can intensify by orders of magnitude as forcing variables

increase in amplitude or frequency (e.g., shoaling volumes in the navigation channels).

2.6.2   Estuarine Classification

Estuarine tidal amplitudes and phases vary greatly; thus, there is a broad spectrum of

tidal bed stress asymmetry, regionally and globally. One approach for classifying tidal

dynamics is by using the tidal form factor F given by Pugh (1987), defined as the ratio of

the vertical amplitudes (ζ_i) of the diurnal and semidiurnal tidal constituents (see Section

2). However, because tidal asymmetry is a function of velocity amplitudes AND phases,

classifications of tidal dynamics may be misrepresented by the tidal form factor (see

Song et al. 2011). For example, near bed velocity measurements collected by NOAA in seven estuaries around the United States (see Table 2.4) indicate that while the tidal dynamics are predominately semidiurnal along the Atlantic, bed stress asymmetry in estuaries of the Gulf of Mexico and along the Pacific are driven by the diurnal (linear) asymmetry ($\Pi \gg 1$). Even in estuaries that are considered to be mixed-semidiurnal, based on the Tidal Velocity Form Factor, the residual bed stress can be heavily influenced by the amplitude and phase of the diurnal species (e.g., San Francisco Bay and Humbolt Bay; see Table 2.5 and Figure 2.16). In the Delaware Estuary, where the Tidal Velocity Form Factor typically ranges from 0 to 0.25, the diurnal asymmetry even became larger than the semidiurnal asymmetry during a high river discharge event, though the residual velocities were sufficiently large to control ebb-flood dominance of the bed stress. Nevertheless, study of other estuaries may reveal additional examples where the residual bed stress is controlled by diurnal asymmetries, even though tidal oscillations in water level and velocity are governed by semidiurnal species, and vice versa. In any case, the results herein suggest that a different non-dimensional number (similar to Π) should be used to classify tidal dynamics of bed stress asymmetry and sediment transport (see also Nidzieko 2010 and Song et al. 2011). Note that $\Pi = \frac{F_u^2}{\varepsilon_2} \frac{cos(2\phi_1 - \phi_2)}{cos(2\phi_2 - \phi_4)}$, which captures the non-linearity of bed stress, in addition to the influence of tidal phase on sediment transport.
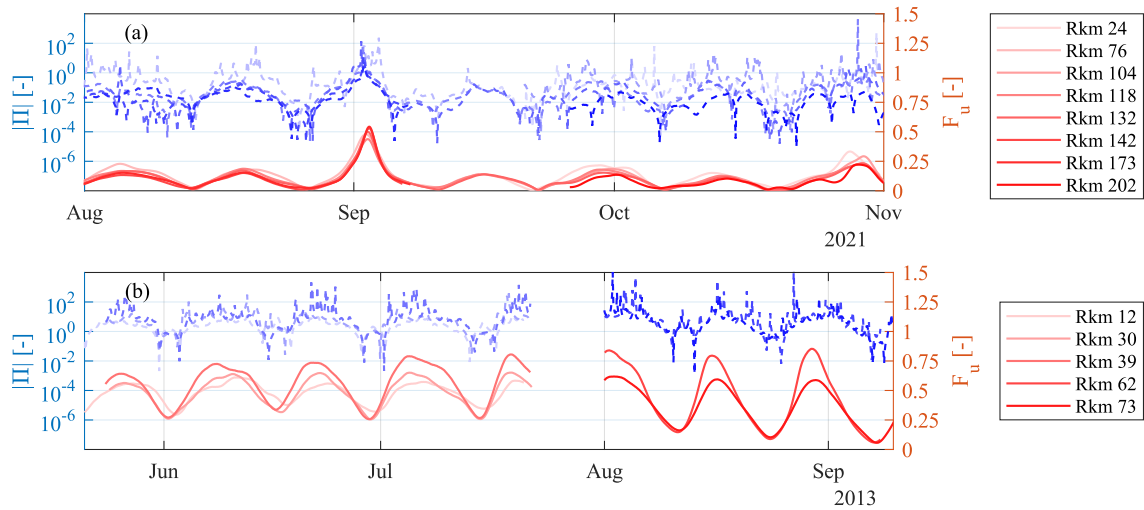
Figure 2.16. Time series of Π and F_u in the Delaware Estuary (a) and San Francisco Bay (b). Values are estimated using CWT_Multi with near-bed velocity measurements collected by NOAA.

Tidal bed stress asymmetry is clearly an important mechanism influencing residual sediment transport and particle trapping in many systems. Even if the tidal asymmetry is relatively weak, spatial gradients in bed stress can be dominated by bed stress asymmetry if the velocity field is strong (term 1 in Equation 8). The non-dimensional numbers defined herein can be used to classify the bed stress asymmetry to help clarify the mechanisms contributing to particle trapping. Classification of the bed stress asymmetry is summarized with the asymmetry parameter space (see Figure 2.17), which is partitioned into six regions (see Table 2.1) according to the relative strength and sign of the residual velocity (represented by ε_R; y-axis) and tidal velocity asymmetry (represented by $\Lambda cos\Delta\phi$; x-axis). Because the velocity amplitude and phase of tidal species vary over the tidal month, the asymmetry classification alternates between Concordant (Class I), Residual Dominant (Class II), and Tide Dominant (Class III), and

135

also between positive (flood dominant) and negative (ebb dominant) classes (i.e., Class I⁻). Temporal variability in the residual velocity cause similar shifts. For example, observations in the seven estuaries listed in Table 2.5 were made near or downstream of salinity intrusion, so oscillations in U_k lead to a positive shift in ε_R during neap/equatorial tides relative to spring/tropic tides (Figure 2.17), particularly in D_1 dominant systems (because U_1 was more variable than U_2), establishing a tendency towards Class I+/II+ asymmetry (i.e., flood dominant residual velocity and bed stress). The D_1 dominant estuaries analyzed also alternated between ebb and flood dominant tidal velocity asymmetry (represented by $\Lambda cos\Delta\phi$) over the tidal month, which, in combination with fortnightly oscillations in ε_R, created a slight tendency towards Class III asymmetry (i.e., flood dominant tidal velocity and bed stress) during tropic tides. Several systems plotted between lines representing flood dominant bed stress ($\varepsilon_R > -\Lambda cos\Delta\phi$) but ebb dominant sediment transport ($\varepsilon_R < -3\Lambda cos\Delta\phi$), and vice-versa, suggesting that bed stress asymmetry coupled with particle-dependent transport thresholds could contribute to particle sorting in these estuaries. (see Equation 7 and Figure 2.17).

Residual bed stress gradients at these locations were typically greater during spring/tropic than neap/equatorial tides (Figure 2.18). In the Hudson River and Saint James River, $\frac{d\tau_R}{dx}$ increased due to elevated residual velocity gradients (term 2 in Equation 8). But in the Cape Fear Estuary, fortnightly variations in the tidal velocity asymmetry (Term 3 in Equation 8) seemed also important to scaling bed stress gradients.

Table 2.5. Classification of the seven estuaries included in the asymmetry parameter space shown in Figure 2.17. Non-dimensional numbers are reported as median values during the observation period.

136

System	F_u	Π
Hudson River (HR)	0.14	0.17
Delaware Estuary (DE)	0.09	0.07
Cape Fear Estuary (CFR)	0.07	0.06
Saint James River (SJR)	0.13	0.12
Mobile Bay (MB)	5.9	100
Humbolt Bay (HB)	0.41	3.4
San Francisco Bay (SFB)	0.34	4.4
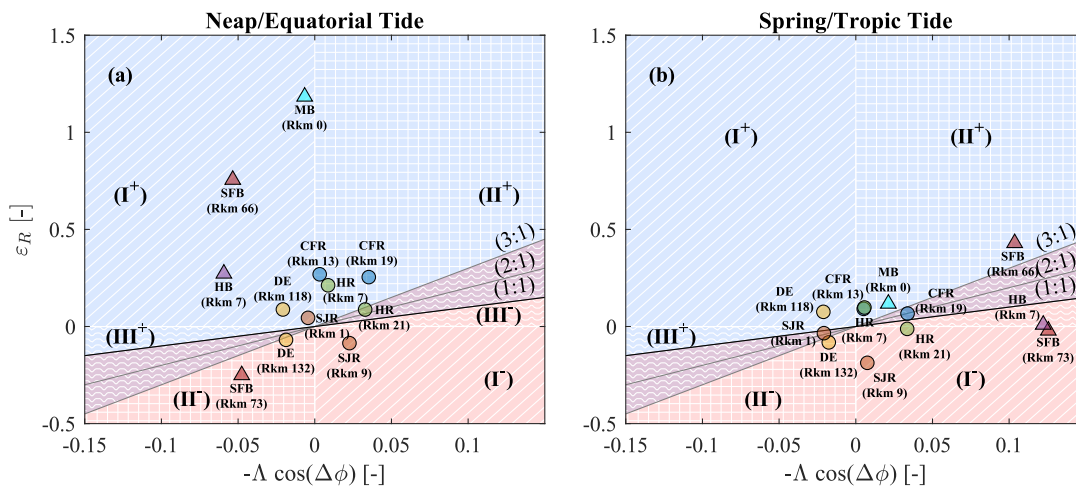
Figure 2.17. Tidal asymmetry parameter space for example estuaries during neap/equatorial tides (a) and tropic spring/tropic tides (b) for D_2 (circles) D_1 (triangles) dominant systems. Each system is indicated by a different color.
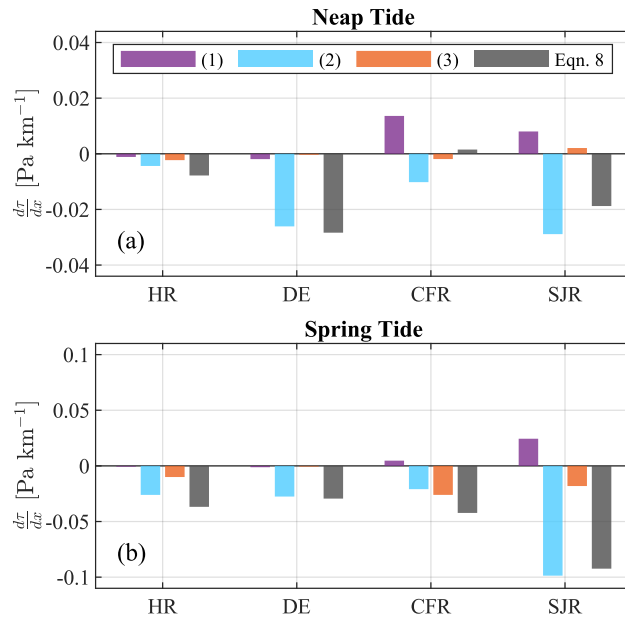
Figure 2.18. Components of $\frac{d\tau_R}{dx}$ (Equation 8) near convergence zones in example estuaries, as cited in the literature, during neap (a) and spring (b) tides. (1) represents the first term in Equation 8, (2) is the second term in Equation 8, etc. Bed stress gradients determined from substituting NOAA observations of near bed velocity into Equation 1 are shown by blue bars.

2.7   Summary and Conclusions

Residual sediment transport patterns in estuaries can be strongly influenced by tidal asymmetry in bed stress, which can be driven by both non-linear tidal interactions and by linear interactions among astronomical tidal constitutes. In this study we apply the framework developed by Hudson et al. (2023) to near bed velocity measurements in two estuaries (the Delaware Estuary and San Francisco Bay) to gain further insight into how river discharge, channel geometry, and long-period tidal cycles influence tidal asymmetry and resulting sediment transport patterns. While tidal currents were semidiurnal dominant in both systems, bed stress asymmetry in San Francisco Bay was found to be strongly influenced by the amplitude and phase of the diurnal species, due to fortnightly variations in the diurnal inequality (linear or diurnal asymmetry). Thus, investigations of similar systems that ignore diurnal oscillations in velocity may misinterpret the dynamics of sediment transport, which could limit the practical applicability of the results. Because Π, Λ_1, and Λ_2 include amplitude and phase information of the diurnal, semidiurnal, terdiurnal, and quarter diurnal species, these non-dimensional numbers are more appropriate for classifying the dynamics of tidal asymmetry. While other classifications for tidal asymmetry have been proposed, these non-dimensional numbers directly scale the influence of the various terms that comprise the residual bed stress and lead to tidal bed stress asymmetry, and so are natural parameters to consider when studying sediment transport.

While most studies on asymmetric sediment transport have focused on semidiurnal systems (or semidiurnal asymmetry), this study highlights a different class of

139

estuaries on the Gulf of Mexico and the West Coast that are driven by diurnal asymmetry (D_1 dominant). In contrast to semidiurnal systems, D_1 dominant estuaries can alternate between ebb and flood dominant bed stress throughout the tidal month due to fortnightly variations in the diurnal inequality. Moreover, because annual and 18.6-year nodal cycle variations in the diurnal species are typically greater than semidiurnal species, D_1 dominant estuaries can exhibit greater temporal variations in bed stress asymmetry. Because the bed stress scales non-linearly with velocity, monthly, semiannual, and nodal cycle (18.6-year) variations in the residual bed stress are typically greater than variations in tidal velocity amplitudes.

Bed stress asymmetry can be classified according to the dominant mechanism controlling residual bed stress patterns (e.g., Residual Dominant vs Tide Dominant), but the class of asymmetry varies over low frequency tidal cycles (e.g., spring/neap and 18.6-yr nodal cycle) because tides in estuaries are non-stationary, in addition to temporal variations in meteorology. Thus, the dominant mechanism controlling bed stress and sediment transport may not be equal during spring and neap tides, or during high and low river discharge, for example. The dynamics of bed stress asymmetry also varies spatially, due to channel geometry and friction, which can establish convergent bed stress gradients favorable for particle trapping. Local variations in topography strongly influence the residual bed stress and can shift the asymmetry classification over relatively small spatial scales, which can enhance bed stress gradients and cause adjacent locations within a river to have different have different mechanisms controlling asymmetry and associated sediment transport (e.g., Rkm 118 and Rkm 132 in the Delaware Estuary). River

140

discharge and channel geometry control bed stress asymmetry by amplification/damping of tidal and residual velocity magnitudes and by shifting the relative phase between tidal species. Thus, channel modifications and changes in river discharge can potentially alter bed stress asymmetry and associated particle trapping/sorting, which could impact morphodynamic equilibrium and/or the sediment supply to downstream reaches of an estuary.

This study analyzes sediment transport behavior in estuaries using an analytical representation of tidal bed stress asymmetry and limited data. While qualitative agreement exists between the results here and the sediment transport characteristics cited in the literature, further investigation is needed to solidify the conclusions herein. CWT_Multi proved to be an indispensable tool for applying the analytical framework to observations because estuarine tidal dynamics are non-stationary. Together with the analytical framework, wavelet analysis of velocity data in other estuaries would add further insight into the causes and consequences of bed stress asymmetry. And wavelet analysis of suspended sediment concentrations or sediment fluxes could help validate or disprove the connection between bed stress asymmetry and sediment transport.

2.8   References

Aristizábal, M., & Chant, R. (2013). A numerical study of salt fluxes in Delaware Bay estuary. *Journal of Physical Oceanography*, *43*(8), 1572-1588.

Barnard, P. L., Schoellhamer, D. H., Jaffe, B. E., & McKee, L. J. (2013). Sediment transport in the San Francisco Bay coastal system: an overview. *Marine Geology*, *345*, 3-17.

Branch, R. A., Horner-Devine, A. R., Chickadel, C. C., Talke, S. A., Clark, D., & Jessup, A. T. (2021). Surface turbulence reveals riverbed drag coefficient. *Geophysical Research Letters*, 48(10), e2020GL092326.

Chant, R. J., Fugate, D., & Garvey, E. (2011). The shaping of an estuarine superfund site: Roles of evolving dynamics and geomorphology. *Estuaries and Coasts*, *34*, 90-105.

Chernetsky, A. S., Schuttelaars, H. M., & Talke, S. A. (2010). The effect of tidal asymmetry and temporal settling lag on sediment trapping in tidal estuaries. *Ocean Dynamics*, *60*(5), 1219-1241.

Cloern, J. E., Knowles, N., Brown, L. R., Cayan, D., Dettinger, M. D., Morgan, T. L., ... & Jassby, A. D. (2011). Projected evolution of California's San Francisco Bay-Delta-River system in a century of climate change. *PloS one*, *6*(9), e24465.

Davis, J. A., Hetzel, F., Oram, J. J., & McKee, L. J. (2007). Polychlorinated biphenyls (PCBs) in San Francisco Bay. *Environmental Research*, *105*(1), 67-86.

Dettinger, M. D., Anderson, J., Anderson, M. L., Brown, L. R., Cayan, D. R., & Maurer, E. P. (2016). Climate change and the Delta, San Francisco Estuary and Watershed Science.

DiLorenzo, J. L., Huang, P., Thatcher, M. L., & Najarian, T. O. (1993). Dredging impacts on Delaware Estuary tides. In *Estuarine and Coastal Modeling* (pp. 86-104). ASCE.

Deverel, S. J., Ingrum, T., Lucero, C., & Drexler, J. Z. (2014). Impounded marshes on subsided islands: simulated vertical accretion, processes, and effects, Sacramento-San Joaquin Delta, CA USA. *San Francisco Estuary and Watershed Science*, *12*(2).

Doodson, A. T. (1921). The harmonic development of the tide-generating potential. *Proceedings of the Royal Society of London. Series A, Containing Papers of a Mathematical and Physical Character*, *100*(704), 305-329.

Doodson, A. T. (1924). Perturbations of harmonic tidal constants. Proceedings of the Royal Society of London. Series A, Containing Papers of a Mathematical and Physical Character, 106(739), 513-526.

Flinchem, E. P., & Jay, D. A. (2000). An introduction to wavelet transform tidal analysis methods. *Estuarine, Coastal and Shelf Science*, *51*(2), 177-200.

Fong, D. A., Monismith, S. G., Stacey, M. T., & Burau, J. R. (2009). Turbulent stresses and secondary currents in a tidal-forced channel with significant curvature and asymmetric bed forms. *Journal of Hydraulic Engineering*, *135*(3), 198-208.

Friedrichs, C. T., & Aubrey, D. G. (1994). Tidal propagation in strongly convergent channels. *Journal of Geophysical Research: Oceans*, *99*(C2), 3321-3336.

Friedrichs, C. T. (1995). Stability shear stress and equilibrium cross-sectional geometry of sheltered tidal channels. *Journal of Coastal Research*, 1062-1074.

Friedrichs, C. T., & Perry, J. E. (2001). Tidal salt marsh morphodynamics: a synthesis. *Journal of Coastal Research*, 7-37.

Ganju, N. K., & Schoellhamer, D. H. (2010). Decadal-timescale estuarine geomorphic change under future scenarios of climate and sediment supply. *Estuaries and Coasts*, *33*, 15-29.

Giese, B. S., & Jay, D. A. (1989). Modelling tidal energetics of the Columbia River estuary. *Estuarine, Coastal and Shelf Science*, *29*(6), 549-571.

Jay, D. A., & Musiak, J. D. (1994). Particle trapping in estuarine tidal flows. *Journal of Geophysical Research: Oceans*, *99*(C10), 20445-20461.

Kukulka, T., & Jay, D. A. (2003). Impacts of Columbia River discharge on salmonid habitat: 1. A nonstationary fluvial tide model. *Journal of Geophysical Research: Oceans*, *108*(C9).

Lanzoni, S., & Seminara, G. (2002). Long-term evolution and morphodynamic equilibrium of tidal channels. *Journal of Geophysical Research: Oceans*, *107*(C1), 1-1.

Lee, S. B., Li, M., & Zhang, F. (2017). Impact of sea level rise on tidal range in Chesapeake and Delaware Bays. *Journal of Geophysical Research: Oceans*, *122*(5), 3917-3938.

Lobo, M, Jay, D. A., Innocenti, S.,Talke, S. A., Dykstra, S. & Matte, P. (2023). Implementing Super-Resolution of Non-Stationary Tides with Wavelets: An Introduction to CWT_Multi, submitted to *Journal of Atmospheric and Oceanic Technology*.

McKee, L. J., Lewicki, M., Schoellhamer, D. H., & Ganju, N. K. (2013). Comparison of sediment supply to San Francisco Bay from watersheds draining the Bay Area and the Central Valley of California. *Marine Geology*, *345*, 47-62.

Moftakhari, H. R., Jay, D. A., Talke, S. A., Kukulka, T., & Bromirski, P. D. (2013). A novel approach to flow estimation in tidal rivers. *Water Resources Research*, *49*(8), 4817-4832.

Moftakhari, H. R., Jay, D. A., Talke, S. A., & Schoellhamer, D. H. (2015). Estimation of historic flows and sediment loads to San Francisco Bay, 1849–2011. *Journal of hydrology*, *529*, 1247-1261.

Monismith, S. G., Burau, J. R., & Stacey, M. (1996). Stratification dynamics and gravitational circulation in northern San Francisco Bay. *San Francisco Bay: The Ecosystem*, *123*, 153.

Monismith, S. G., Kimmerer, W., Burau, J. R., & Stacey, M. T. (2002). Structure and flow-induced variability of the subtidal salinity field in northern San Francisco Bay. *Journal of physical Oceanography*, *32*(11), 3003-3019.

Morris, J. T., Drexler, J. Z., Vaughn, L. J., & Robinson, A. H. (2022). An assessment of future tidal marsh resilience in the San Francisco Estuary through modeling and quantifiable metrics of sustainability. *Frontiers in Environmental Science*, *10*, 1039143.

Nidzieko, N. J. (2010). Tidal asymmetry in estuaries with mixed semidiurnal/diurnal tides. *Journal of Geophysical Research: Oceans*, 115(C8).

Parker, B. B. (2007). Tidal analysis and prediction.

Pittaluga, M.B., Tambroni, N., Canestrelli, A., Slingerland, R., Lanzoni, S., & Seminara, G. (2015). Where river and tide meet: The morphodynamic equilibrium of alluvial estuaries. *Journal of Geophysical Research: Earth Surface*, *120*(1), 75-94.

Proudman, J. (1952). Dynamical oceanography. *Dover.*

Pugh, D. T. (1987). Tides, surges and mean sea level. *John Wiley & Sons*.

Ralston, D. K., Talke, S., Geyer, W. R., Al-Zubaidi, H. A., & Sommerfield, C. K. (2019). Bigger tides, less flooding: Effects of dredging on barotropic dynamics in a highly modified estuary. *Journal of Geophysical Research: Oceans*, *124*(1), 196-211.

Ruhl, C. A., Schoellhamer, D. H., Stumpf, R. P., & Lindsay, C. L. (2001). Combined use of remote sensing and continuous monitoring to analyze the variability of suspended-sediment concentrations in San Francisco Bay, California. *Estuarine, Coastal and Shelf Science*, *53*(6), 801-812.

Sanford, T. B., & Lien, R. C. (1999). Turbulent properties in a homogeneous tidal bottom boundary layer. *Journal of Geophysical Research: Oceans*, *104*(C1), 1245-1257.

Schoellhamer, D. H. (2000). Influence of salinity, bottom topography, and tides on locations of estuarine turbidity maxima in northern San Francisco Bay. In *Proceedings in marine science* (Vol. 3, pp. 343-357). Elsevier.

Schoellhamer, D. H. (2002). Variability of suspended-sediment concentration at tidal to annual time scales in San Francisco Bay, USA. *Continental Shelf Research*, *22*(11-13), 1857-1866.

Schoellhamer, D. H., Mumley, T. E., & Leatherbarrow, J. E. (2007). Suspended sediment and sediment-associated contaminants in San Francisco Bay. Environmental Research, 105(1), 119-131.

Schoellhamer, D. H. (2011). Sudden clearing of estuarine waters upon crossing the threshold from transport to supply regulation of sediment transport as an erodible sediment pool is depleted: San Francisco Bay, 1999. *Estuaries and Coasts*, *34*(5), 885-899.

Schuttelaars, H. M., & De Swart, H. E. (1997). An idealized long-term morphodynamic model of a tidal embayment.

Sommerfield, C. K., Madsen, J. A., & Hall, P. (2003). Sedimentological and geophysical survey of the upper Delaware estuary. *Final Report to the Delaware River Basin Commission, West Trenton, New Jersey*.

Sommerfield, C. K., & Wong, K. C. (2011). Mechanisms of sediment flux and turbidity maintenance in the Delaware Estuary. *Journal of Geophysical Research: Oceans*, *116*(C1).

Song, D., Wang, X. H., Kiss, A. E., & Bao, X. (2011). The contribution to tidal asymmetry by different combinations of tidal constituents. *Journal of Geophysical Research: Oceans*, *116*(C12).

Speer, P. E., & Aubrey, D. G. (1985). A study of non-linear tidal propagation in shallow inlet/estuarine systems Part II: Theory. *Estuarine, Coastal and Shelf Science*, *21*(2), 207-224.

Stacey, M. T., Burau, J. R., & Monismith, S. G. (2001). Creation of residual flows in a partially stratified estuary. *Journal of Geophysical Research: Oceans*, *106*(C8), 17013-17037.

Strikwerda, J. C. (2004). *Finite difference schemes and partial differential equations*. Society for Industrial and Applied Mathematics.

Talke, S. A., de Swart, H. E., & Schuttelaars, H. M. (2009). Feedback between residual circulations and sediment distribution in highly turbid estuaries: an analytical model. *Continental Shelf Research*, *29*(1), 119-135.

USACE (2011). Pinole Shoal Channel FY 2011 Maintenance Dredging Tier I Evaluation.

USACE (2013). Delaware Estuary Regional Sediment Management Plan.

USACE (2023). Pinole Shoal Channel 2023 Tier I Evaluation O&M Dredging.

Winterwerp, J. C. (2002). On the flocculation and settling velocity of estuarine mud. *Continental shelf research*, *22*(9), 1339-1360.

Winterwerp, J. C. (2011). Fine sediment transport by tidal asymmetry in the high-concentrated Ems River: indications for a regime shift in response to channel deepening. *Ocean Dynamics*, *61*(2-3), 203-215.

2.9 Appendices

2.9.1 Appendix A: Velocity representation as diurnal, semidiurnal, terdiurnal, and quarterdiurnal waves.

The general expression for combining the constituents into a single wave is given as follows:

$$\sum_i u_i = \sum_i U_i \cos(\omega_i t - \phi_i) = U\cos(\omega t - \phi) \qquad \text{Equation S1a,}$$

where U_i, ω_i and ϕ_i are the tidal current amplitude, angular frequency, and phase of the ith constituent. The amplitude (U) and phase (ϕ) of the combined wave are:

$$U^2 = \sum_{i,j} U_i U_j \cos(\phi_i - \phi_j) \qquad \text{Equation S1b,}$$

$$\tan(\phi) = \frac{\sum_i U_i \sin(\phi_i)}{\sum_i U_i \cos(\phi_i)} \qquad \text{Equation S1c.}$$

Thus, substitution of u_{K1} and u_{O1} into Equation S1a gives the diurnal wave as follows:

$$u_1 = u_{K1} + u_{O1} = U_1 \cos(\omega_1 t - \phi_1) \qquad \text{Equation S2a,}$$

where U_1 and ϕ_1 are defined as follows:

$$U_1 = [U_{K1}^2 + U_{O1}^2 + 2U_{K1}U_{O1}\cos(2\omega_2 t + \phi_{O1} - \phi_{K1})]^{1/2} \qquad \text{Equation S2b,}$$

$$\phi_1 = \tan^{-1}\left(\frac{U_{K1}\sin(\phi_{K1}-\omega_2 t)+U_{O1}\sin(\phi_{O1}+\omega_2 t)}{U_{K1}\cos(\phi_{K1}-\omega_2 t)+U_{O1}\cos(\phi_{O1}+\omega_2 t)}\right) \qquad \text{Equation S2c.}$$

and ω_1, ω_2 are the first two basic angular frequencies introduced by Doodson (1921).

Likewise, substitution of u_{M2}, u_{S2} and u_{N2} into Equation S1a gives the semidiurnal wave:

$$u_2 = u_{M2} + u_{S2} + u_{N2} = U_2\cos(2\omega_1 t - \phi_2)$$ Equation S3a,

$$\begin{aligned}U_2 = [&U_{M2}^2 + U_{S2}^2 + U_{N2}^2 + 2U_{M2}U_{S2}\cos(2(\omega_2 - \omega_3)t + \phi_{M2} - \phi_{S2}) \\ &+ 2U_{M2}U_{N2}\cos(\omega_2 t + \phi_{N2} - \phi_{M2}) \\ &+ 2U_{S2}U_{N2}\cos((3\omega_2 - 2\omega_3)t + \phi_{N2} - \phi_{S2})]^{1/2}\end{aligned}$$ Equation S3b,

$$\phi_2 = tan^{-1}\left(\frac{U_{M2}\sin(\phi_{M2}) - U_{S2}\sin(2(\omega_2-\omega_3)t-\phi_{S2}) + U_{N2}\sin(\omega_2 t+\phi_{N2})}{U_{M2}\cos(\phi_{M2}) + U_{S2}\cos(2(\omega_2-\omega_3)t-\phi_{S2}) + U_{N2}\cos(\omega_2 t+\phi_{N2})}\right)$$ Equation S3c.

where ω_3 is the third basic angular frequency introduced by Doodson (1921).

The terdiurnal wave is represented as

$$u_{MK3} + u_{MO3} = u_3 = U_3\cos(3\omega_1 t - \phi_3)$$ Equation S4a,

$$U_3 = [U_{MK3}^2 + U_{MO3}^2 + 2U_{MK3}U_{MO3}\cos(2\omega_2 t + \phi_{MO3} - \phi_{MK3})]^{1/2}$$ Equation S4b,

$$\phi_3 = tan^{-1}\left(\frac{U_{MK3}\sin(\phi_{MK3}-\omega_2 t) + U_{MO3}\sin(\phi_{MO3}+\omega_2 t)}{U_{MK3}\cos(\phi_{MK3}-\omega_2 t) + U_{MO3}\cos(\phi_{MO3}+\omega_2 t)}\right)$$ Equation S4c.

Finally, the quarter diurnal wave:

$$u_{M4} + u_{MS4} + u_{MN4} = u_4 = U_4\cos(4\omega_1 t - \phi_4)$$ Equation S5a,

$$\begin{aligned}U_4 = [&U_{M4}^2 + U_{MS4}^2 + U_{MN4}^2 + 2U_{M4}U_{MS4}\cos(2(\omega_2 - \omega_3)t + \phi_{M4} - \phi_{MS4}) \\ &+ 2U_{M4}U_{NN4}\cos(\omega_2 t + \phi_{MN4} - \phi_{M4}) \\ &+ 2U_{MS4}U_{MN4}\cos((3\omega_2 - 2\omega_3)t + \phi_{MN4} - \phi_{MS4})]^{1/2}\end{aligned}$$ Equation S5b,

$$\phi_4 = tan^{-1}\left(\frac{U_{M4}\sin(\phi_{M4}) - U_{MS4}\sin(2(\omega_2-\omega_3)t-\phi_{MS4}) + U_{MN4}\sin(\omega_2 t+\phi_{MN4})}{U_{M4}\cos(\phi_{M4}) + U_{MS4}\cos(2(\omega_2-\omega_3)t-\phi_{MS4}) + U_{MN4}\cos(\omega_2 t+\phi_{MN4})}\right)$$ Equation S5c,

149

Now the velocity can be represented as a combination of diurnal, semidiurnal, terdiurnal, quarterdiurnal and residual motions:

$$u = U_1 \cos(\omega_1 t - \phi_1) + U_2 \cos(2\omega_1 t - \phi_2)$$
$$+ U_3 \cos(3\omega_1 t - \phi_3) + U_4 \cos(4\omega_1 t - \phi_4) + u_R$$

Equation S6.

2.9.2 Appendix B: Parameters and non-dimensional numbers used in the analytical framework

Table 2.6. Parameters and non-dimensional numbers used in the analytical framework, listed in order of appearance within the main text.

Name	Symbol	Definition
Tidal Velocity Parameter	$\varepsilon_1, \varepsilon_2$	$\dfrac{U_3}{U_1}, \dfrac{U_4}{U_2}$
Tidal Asymmetry Phase Parameter	δ_3, δ_4	$\dfrac{cos(\phi_1+\phi_2-\phi_3)}{cos(2\phi_1-\phi_2)}, \dfrac{cos(\phi_1+\phi_3-\phi_4)}{cos(2\phi_1-\phi_2)}$
Species Factor	Π	$\left\| \dfrac{U_1^2(1+2\varepsilon_1\varepsilon_3+2\varepsilon_1\varepsilon_2\varepsilon_4)cos(2\phi_1-\phi_2)}{\varepsilon_2 U_2^2 cos(2\phi_2-\phi_4)} \right\|$
Tidal Velocity Form Factor	F_u	$\dfrac{U_1}{U_2}$
Tidal Form Factor	F	$\dfrac{\zeta_{K1}+\zeta_{O1}}{\zeta_{M2}+\zeta_{S2}}$
Residual Asymmetry Parameter	$\varepsilon_{R2}, \varepsilon_{R1}$	$\dfrac{u_R}{U_2}, \dfrac{u_R}{U_1}$
Semidiurnal Asymmetry Parameter	Λ_2	$\dfrac{\varepsilon_2 U_2^2}{\left(\frac{4}{7}U^2+2\left((1+\varepsilon_1^2)U_1^2+(1+\varepsilon_2^2)U_2^2+\frac{2}{3}u_R^2\right)\right)}$
Diurnal Asymmetry Parameter	Λ_1	$\dfrac{U_1 U_2(1+2\varepsilon_1\delta_3+2\varepsilon_1\varepsilon_2\delta_4)}{\left(\frac{4}{7}U^2+2\left((1+\varepsilon_1^2)U_1^2+(1+\varepsilon_2^2)U_2^2+\frac{2}{3}u_R^2\right)\right)}$

2.9.3 Appendix C: List of NOAA stations used to define near bed velocity

Table 2.7. NOAA stations used to define near-bed velocity in the Delaware Estuary.

Station ID	Rkm	Deployment Period	Approximate Station Depth [m]	Approximate Bin Depth [m]
DEB2105	24	14-Sep-21 to 03-Nov-21	14.5	12.5
DEB2108	48	16-Jul-21 to 15-Sep-21	14.0	12.0
DEB2110	76	17-Jul-21 to 18-Sep-21	13.5	10.7
DEB2112	96	17-Sep-21 to 09-Nov-21	15.4	13.3
DEB2115	104	17-Sep-21 to 04-Nov-21	13.3	11.2
DEB2116*	113	23-Jul-21 to 17-Sep-21	15.8	12.6
DEB2117	118	21-Jul-21 to 05-Nov-21	16.9	14.3
DEB2118*	123	21-Sep-21 to 04-Nov-21	15.1	12.4
DEB2119	132	23-Jul-21 to 09-Nov-21	8.8	6.9
DEB2120	136	21-Sep-21 to 10-Nov-21	9.4	7.8
DEB2121	142	20-Jul-21 to 09-Sep-21	11.9	10.4
DEB2128	161	20-Jul-21 to 16-Nov-21	15.5	13.5
DEB2130*	173	23-Jul-21 to 10-Sep-21	13.7	12.6
DEB2132	193	22-Sep-21 to 15-Nov-21	12.5	9.8
DEB2134*	207	23-Jul-21 to 10-Sep-21	12.1	10.5

Instruments at these stations were mounted at or near the surface, looking down.

Table 2.8. NOAA stations used to define near-bed velocity in San Francisco Bay.

Station ID	Rkm	Deployment Period	Approximate Station Depth [m]	Approximate Bin Depth [m]
SFB1309	12	17-May-13 to 23-Jul-13	14.8	12.2
SFB1312	21	21-May-13 to 26-Jul-13	24.0	18.2
SFB1314	30	21-May-13 to 24-Jul-13	12.2	9.6
SFB1315	34	17-May-13 to 25-Jul-13	8.9	6.9
SFB1316	39	20-May-13 to 24-Jul-13	13.1	10.1
SFB1320	47	30-Jul-13 to 12-Sep-13	37.8	29.6
SFB1323	62	29-Jul-13 to 11-Sep-13	11.4	8.8
SFB1324	66	28-Jul-13 to 10-Sep-13	12.2	9.2
SFB1325	73	28-Jul-13 to 13-Sep-13	12.9	9.9
SFB1331	81	30-Jul-13 to 14-Sep-13	11.2	9.7

Instruments at these stations were mounted at or near the surface, looking down.

Chapter 3: The Bed Stress Minimum in Tidal Rivers

This chapter has been published in Estuaries and Coasts. See author contribution

statement below.

<u>Citation:</u>

Hudson, A., Jay, D., & Talke, S. (2023). The Bed Stress Minimum in Tidal

Rivers. *Estuaries and Coasts*, *46*(2), 336-355.

<u>Contributing Authors:</u>

Austin Scott Hudson

David A. Jay

Stefan A. Talke

<u>Author Contributions:</u>

Austin Hudson: Conceptualization, methodology, investigation, formal analysis, writing

– original draft, review and editing.

David A. Jay: Conceptualization, writing – review and editing.

Stefan A. Talke: Conceptualization, writing – review and editing.

3.1 Abstract

Bed stress patterns control erosion and deposition in tidal rivers and thereby govern changes in geomorphology. Management of river discharge and shipping channel geometry perturbs rivers from their natural state, leading to hotspots of sand deposition and erosion. Here, we investigate the along-channel variability in bed stress for a tidal river of constant depth with semidiurnal tides and convergent geometry using a Fourier decomposition of the quadratic bed stress and analytical approximations of tidal and river velocity. Under some river discharge and tidal conditions, bed stress profiles exhibit a local bed stress minimum, x_{min}, within a region marked by strong gradients in cross-sectionally averaged velocity. These gradients can lead to convergent sediment fluxes and shoaling near x_{min}. Factors decreasing river velocity (flow management, channel deepening, and weak channel convergence) move x_{min} and depositional areas upstream. Analytical estimates of x_{min} were validated using fifty-two two-dimensional Adaptive Hydraulics (AdH) numerical model simulations, and agree well with the sediment transport behavior of three prototype systems (Columbia River, Hudson River, and Delaware Estuary). Climate changes in seasonal flow cycles and mean river discharge, and the reservoir management response to these changes, may significantly alter the dynamics of x_{min}, affecting ecosystem dynamics and the stability of wetlands and coastal beaches as sea level rises. The analytical formulation of x_{min} developed herein will make it easier to understand how climate and human induced changes to a river can impact long-term erosion/accretion patterns, and can help guide future investments for managing sediment.

155

3.2   Introduction

This study analyzes along-channel variations in bed stress in tidal rivers to better understand what factors control system-scale shoaling and erosion patterns. Bed stress defines the amount of force per unit area imparted by the water on the riverbed, and is an important consideration for informed sediment management practices because of its strong influence on the fate and transport of sediment (Dyer 1986). The cost of managing sediment highlights the need to better understand the processes controlling deposition in the tidal-fluvial environment. For example, every year the United States Army Corps of Engineers dredges roughly 200 million cubic yards of sediment, at a cost which has exceeded $1 billion annually since 2008 (USACE 2020). Much of this dredging is in estuaries and tidal rivers. Depositional regions can also contain elevated concentrations of legacy or emerging contaminants, which pose a risk to environmental and human health and could cost hundreds of millions of dollars to remediate (EPA 2014, 2016, 2017). Changes in tides, channel geometry, and river discharge can influence the magnitude and location of shoaling (Meade 1969; de Jonge et al. 2014; Pittaluga et al. 2015). Thus, improving practical knowledge of how the bed stress responds to adjustments in river discharge, tides, and channel geometry is critical for informed management of fluvial resources, especially for transient systems adapting to climate change or human development.

The link between spatial gradients in bed stress (or velocity) and morphological changes in tidal rivers and estuaries is well established. For example, during the development of the Federal Navigation Channel (FNC) in the Columbia River, local

expansions in river width were acknowledged to decrease water velocity (and bed stress) and create shoaling hot spots that were then managed by artificially constricting river width with pile dikes and man-made islands (Hickson 1930, 1961). Likewise, Friedrichs (1995) examined 26 systems and established that the cross sectional area of a tidal channel increases or decreases to minimize along-channel gradients in bed stress. In theory, bed aggradation will occur in the lower reaches of convergent tidal rivers until an equilibrium depth profile is achieved that eliminates spatial gradients in sediment transport (Guo et al. 2014; Pittaluga et al. 2015). But bed aggradation can also lead to more cataclysmic morphological changes in rivers by producing zones that have an increased likelihood of channel avulsions during flood events (Nittrouer et al. 2012, Chatanantavet et al. 2012). Adjustment of some reaches may be limited by hard-rock features such that they remain out of equilibrium.

Morphological changes are influenced by the interaction of fluvial, tidal and baroclinic transport processes, which can trap sediment in many ways. Density driven estuarine circulation can create an estuary turbidity maximum (ETM) near the upstream limit of salinity intrusion, which results from convergent near-bed transport of fine sediments (Festa & Hansen 1978; Talke et al. 2009), and cause local peaks in channel shoaling (Meade 1968). Landward sediment transport and particle trapping is also generated by settling and scour lag (Chernetsky et al. 2010; Friedrichs et al. 1998; Postma 1961), tidal asymmetry in current magnitudes and durations (Allen et al. 1980; Hoitink et al. 2003; Speer and Aubrey 1985), spatial gradients in vertical mixing due to salinity stratification (Geyer 1993), and correlations of velocity shear and vertical mixing (Jay

157

and Musiak 1994; Jay et al., 2007a; 2015; Burchard et al. 1998, 2018). Collectively, exchange flows that are influenced by variations in eddy viscosity are now termed Eddy-Viscosity Shear Covariance (ESCO; Dijkstra et al., 2017), and are known to influence sediment trapping (Jay and Musiak, 1994; Burchard et al. 2018). Changes to estuarine circulation and tidal asymmetries induced by channel modification may increase sedimentation in estuaries (Chant et al. 2011; Sherwood et al. 1990), and even lead to hyperturbid and/or hypoxic conditions (Chernetsky et al. 2010; Talke et al. 2009).

Analytical models of tidal sediment trapping and ETM formation usually focus on fine suspended sediments and assume morphodynamic equilibrium, i.e., that erosion equals deposition (Friedrichs et al., 1998, Huijts et al., 2006, Talke et al. 2009b, Dijkstra et al. 2019), so that the models are valid only for small departures from equilibrium. In addition, bed stress, which is typically proportional to a power of the velocity, is often linearized to be proportional to the near bed velocity (e.g., Chernetsky et al., 2010). Thus, the nonlinear interactions between river flow and tidal forcing, and their influence on bed stress (see e.g., Godin et al., 1991), are typically not considered in analytical morphodynamic models. Indeed, analytical representations of bed stress variability due to river/tide interaction are rarely attempted (but see Buschmann et al., 2009 and Familkhalili et al., 2022); rather, the integrated response of coupled sediment/tidal behavior, which includes sediment settling lag effects, is evaluated (e.g., Chernetsky et al., 2010). In this contribution, we develop an analytical expression for the along-channel variability in bed stress, which explicitly details the nonlinear interactions between river

flow and tidal forcing, to better understand how frictional nonlinearities influence sediment trapping.

Frictional river/tide interactions can influence the spatial variability in bed stress and produce local minima in bed stress, which are thought to be hotspots of sediment trapping, particularly of the coarser fraction of sand, which is less influenced by water-column settling lag effects (Jay et al. 1990). Transport of sand, whether as bed load or suspended load, is a primary mode of sediment transport in energetic, sand bedded river estuaries (see Templeton and Jay 2012), and is directly related to velocity and bed stress through the Shields parameter (Dyer 1995). However, since most studies of sediment transport in estuaries focus on fine sands, cohesive sediments, and the formation of ETMs from suspended sediment, the possibility that bed stress minima might influence deposition of the coarser sand fraction is much less studied (but see Dalrymple et al. 1992).

3.3   Background

Following standard practice, we define bed stress τ_b in terms of the near-bed fluid velocity u_b, fluid density ρ, and a drag coefficient representing the roughness of the bed C_d (Proudman 1952):

$$\tau_b \equiv \rho C_d u_b |u_b| \tag{1},$$

where the absolute value accounts for the reversal in stress direction that occurs when tidal velocities change sign. If τ_b exceeds a critical threshold, τ_c , sediment is considered to mobilize off the bed. Sediment transport then scales non-linearly with τ_b (Dyer 1986).

Because both the fluid velocity and bed roughness vary in space and time (Branch et al. 2021), gradients in bed stress develop that influence erosion and deposition patterns.

In a tidal river, the cross-sectionally averaged bottom velocity u_b is driven by the hydraulic gradients set up by precipitation/watershed runoff and ocean tides, which are referenced herein as the riverine (residual) velocity (U_R) and tidal velocity (U_T). In a 1-D framework (cross-sectionally averaged), assuming a single tidal constituent with no reflected wave, the near bed velocity at a given location x can be described as follows

$$u_b = U_T cos \left(\frac{2\pi t}{T} - \phi\right) + U_R \hspace{4cm} (2),$$

where $U_T(x)$ is tidal velocity amplitude, T is the tidal period, $\varphi(x)$ is tidal phase, $U_R(x) \equiv Q_R/hb$ is the residual (non-tidal) velocity, $h(x)$ is the tidally averaged river depth, $b(x)$ is river width, and $Q_R < 0$ is river discharge. $x = 0$ at the ocean and $x = L$ at the head of tides where $U_T \sim 0$. In the absence of tributary input, Q_R is constant in space. Therefore, convergent channels in which the cross-sectional area decreases monotonically in the upstream direction exhibit river velocities that increase in the upstream direction (Figure 3.1). Tidal velocity, by contrast, is forced at the ocean boundary and typically decreases in the upstream direction due to frictional damping. Strong cross-sectional convergence can locally amplify tidal velocity as the wave propagates upstream, but the general trend is for $U_T(x)$ to decrease in the upstream direction in systems with strong river discharge. The result of these two opposing gradients is a local minimum in u_b, and more importantly in τ_b, that leads to convergent sediment fluxes and that may control the morphological character of an alluvial system (Dalrymple et al. 1992).
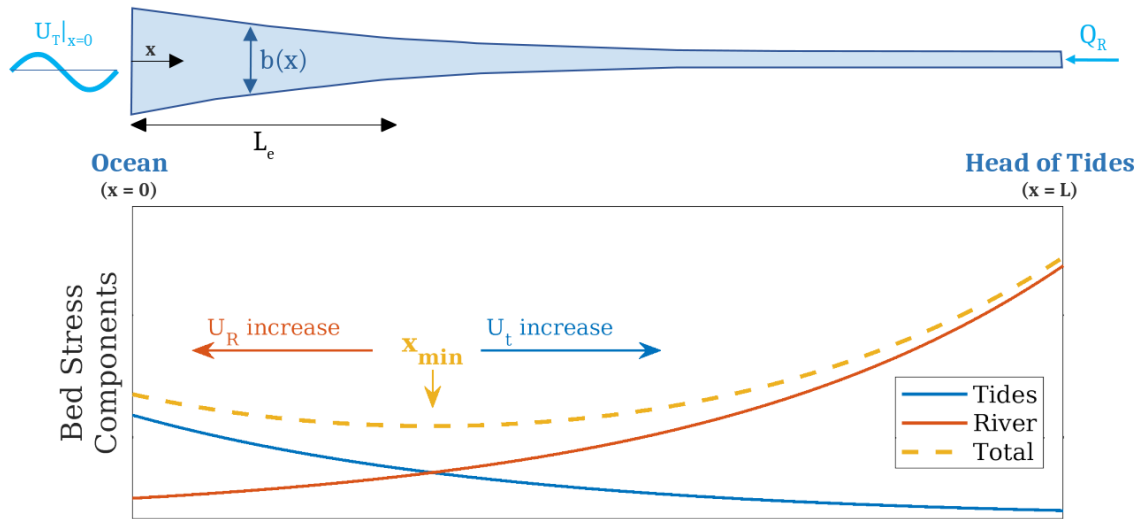
Figure 3.1. Plan view of idealized convergent river (top) and resulting along-channel profile of bed stress (bottom)

While a bed stress minimum (and preferential deposition zone) is believed to be common in tidal rivers, the literature is limited on analytical characterizations of its location. Nittrouer et al. (2012) showed that the cross-sectional area of the Mississippi River increases in the downstream direction during low/moderate river discharge, which causes a local minimum in velocity (or bed stress) near the mouth of the river with sediment deposition occurring upstream thereof. Their analysis, however, neglects the influence of tidal velocity on the bed stress and is thus restricted to systems with minimal tidal input, as is appropriate for the micro-tidal environment of the Mississippi. Evaluation of meso and macro-tidal systems requires consideration of the coupled interaction between the tidal and fluvial velocity fields (Hoitink and Jay, 2016).

Giese et al. (1989), Jay et al. (1990) and Jay et al. (2016) evaluated the energy balance in the Lower Columbia River Estuary (LCRE) demonstrating that, because of tidal damping and channel geometry, tidal/fluvial dissipation are monotonically decreasing/increasing functions from the mouth of the river. As a result, the total dissipation, or bed stress, reaches a minimum at some location upstream of the mouth, x_{min} (Figure 3.1). In the LCRE this local minimum occurs within a locus of sand deposition that extends from roughly river kilometer (*Rkm*) 30 to 56 and that requires anomalously high dredging quantities to maintain authorized depths in the FNC. The estuary turbidity maximum is also often found in the downstream end of this reach. The evaluation of Giese et al. (1989) implies that an increase in fluvial dissipation during high river discharge events would shift x_{min} seaward, but a detailed evaluation of the bed stress minimum location was beyond the scope of their analysis.

The ability to evaluate the factors that influence x_{min} is particularly important in the LCRE because, like other systems, the river has been extensively modified since the 19th century. The authorized depth of the Lower Columbia River FNC has more than doubled from 6 to 13 m over the twentieth century (Helaire et al. 2019). At the same time flow regulation has reduced peak flows, and the mean river discharge during the spring freshet (May-July) has decreased from 13,610 m^3 s^{-1} before 1900 to 7,060 m^3 s^{-1} between 1970 and 2004 (Naik and Jay 2011). Both channel deepening and flow regulation decrease fluvial dissipation in the system; however, the influence of these activities on x_{min}, and the locus of sand deposition, remains unclear.

162

To test the hypothesis of Giese et al. (1989) and Jay et al. (2016), we explore the sensitivity of x_{min} to channel geometry and river discharge by adapting the bed stress linearization introduced by Proudman (1952), and later extended by Dronkers (1964). The approach includes spatial variability induced by tidal damping and channel convergence to obtain analytical estimates of x_{min}. Estimates of x_{min} were validated using the 2-D Adaptive Hydraulics (AdH) numerical model using nine convergent channel geometries and six river discharges, a total of 54 simulations. In testing the parameter space, we found that x_{min} is topographically constrained by channel convergence, but indeed exhibits variability induced by channel geometry and river discharge as hypothesized above. The theoretical considerations developed herein were applied to three prototype estuaries and show good agreement with their sediment transport characteristics, as described in the literature.

3.4 Methods

This section introduces an analytical framework for estimating the location of the bed stress minimum as a function of channel geometry, river discharge, and tidal amplitude. The framework employs a Fourier series decomposition of the non-linear bed stress and the theory of tidal propagation to establish an along-channel profile of the bed stress magnitude $\tau(x)$. This evaluation provides a relatively straightforward approach to examine the spatial distribution of bed stress without the need to solve the equations of motion. The location of the minimum bed stress within the domain, x_{min}, is found using the along-channel derivative of $\tau(x)$, and validated using AdH numerical model simulations.

163

3.4.1 Fourier Decomposition

Assuming bed velocity is driven by a single tidal constituent and river discharge, the bed stress produces a signal at the fundamental, overtide, and residual frequencies. Following Proudman (1952), the bed stress (Equation 1) can be decomposed into contributing frequencies using a Fourier Cosine Series of velocity u_b (Equation 2):

$$u_b|u_b| \approx \sum_{n=0}^{\infty} a_n \cos\left(\frac{n\pi t}{T}\right) \tag{3},$$

where n represents the individual elements of the series. Because we are interested only in the amplitude of $\tau(x)$, its along-channel phase variability can be neglected. Thus, we use a symmetric cosine series, assuming that phase $\varphi = 0,\ \pi,\ 2\pi,\ ...$ in Equation 2 for all x.

The Fourier coefficients a_n are determined by using the orthogonality of the cosine function (Haberman 2004):

$$a_n = \frac{2}{T} \int_0^T u_b\,|u_b|\cos\left(\frac{n\pi t}{T}\right) dt \tag{4},$$

and the absolute value is addressed by substituting $u_b{}^2$ into the integrand above and recognizing the change in sign induced over the interval [0, T]

$$a_n = \frac{2}{T}\left[2\int_0^{t_1} u_b^2 \cos\left(\frac{n\pi t}{T}\right) dt - \int_{t_1}^{t_2} u_b^2 \cos\left(\frac{n\pi t}{T}\right) dt\right] \tag{5},$$

where:

$$t_1 = \frac{T}{2\pi}\cos^{-1}\left(\frac{-U_R}{U_T}\right) t_2 = T - t_1 \tag{6}.$$

Substitution of Equation 2 into Equation 5 and evaluating for different values of n gives the magnitude of the bed stress at various frequencies. For a dominantly semidiurnal system, the diurnal tide can be neglected, and the fundamental frequency is given by $n = 2$:

$$a_2 = U_T^2 \left[\frac{3}{\pi} sin \left(cos^{-1} \left(\frac{-U_R}{U_T} \right) \right) + \frac{1}{3\pi} sin \left(3cos^{-1} \left(\frac{-U_R}{U_T} \right) \right) \right]$$
$$+ U_R U_T \left[\frac{2}{\pi} sin \left(2cos^{-1} \left(\frac{-U_R}{U_T} \right) \right) + \frac{4}{\pi} cos^{-1} \left(\frac{-U_R}{U_T} \right) - 2 \right] \qquad (7).$$
$$+ U_R^2 \left[\frac{4}{\pi} sin \left(cos^{-1} \left(\frac{-U_R}{U_T} \right) \right) \right]$$

Evaluating Equation 5 for $n = 0$ gives the bed stress magnitude at residual frequency:

$$a_0 = U_T^2 \left[\frac{1}{2\pi} sin \left(2cos^{-1} \left(\frac{-U_R}{U_T} \right) \right) + \frac{1}{\pi} cos^{-1} \left(\frac{-U_R}{U_T} \right) - \frac{1}{2} \right]$$
$$+ U_R U_T \left[\frac{4}{\pi} sin \left(cos^{-1} \left(\frac{-U_R}{U_T} \right) \right) \right] \qquad (8).$$
$$+ U_R^2 \left[\frac{2}{\pi} cos^{-1} \left(\frac{-U_R}{U_T} \right) - 1 \right]$$

We note that both the tidally varying and the residual terms are functions of the tidal velocity squared U_T^2, the product $U_R U_T$, and the river velocity squared U_R^2 (cf. Buschman et al., 2009). The remaining Fourier coefficients describe the distribution of the bed stress signal across frequency space, which may manifest at frequencies of other tidal constituents and/or shallow water overtides. When the velocity is composed of a single tidal constituent and river discharge (Equation 2), no energy is transferred to odd elements of the series (i.e., $an = 0$ for $n = 1, 3, 5, ...$). The non-zero coefficients in

Equation 3 will decrease in magnitude as n increases, and only the first three elements are considered here, i.e., $n = 0, 2, 4$. The first overtide is given by $n = 4$:

$$a_4 = U_T^2 \left[\frac{1}{\pi} \sin\left(2\cos^{-1}\left(\frac{-U_R}{U_T}\right)\right) + \frac{1}{\pi}\cos^{-1}\left(\frac{-U_R}{U_T}\right) + \frac{1}{4\pi}\sin\left(4\cos^{-1}\left(\frac{-U_R}{U_T}\right)\right) - \frac{1}{2}\right]$$
$$+ U_R U_T \left[\frac{4}{\pi}\sin\left(\cos^{-1}\left(\frac{-U_R}{U_T}\right)\right) + \frac{4}{3\pi}\sin\left(3\cos^{-1}\left(\frac{-U_R}{U_T}\right)\right)\right] \qquad (9).$$
$$+ U_R^2 \left[\frac{2}{\pi}\sin\left(2\cos^{-1}\left(\frac{-U_R}{U_T}\right)\right)\right]$$

While the overtide M_6 ($n=6$) is important in systems with small mean flows, its importance relative to M_4 ($n=4$) recedes quickly as river flow increases in amplitude from zero. Thus, the M6 term can be safely ignored in the systems considered here.

Equations 7 thru 9 are challenging to interpret but can be simplified by noting that when $U_R/U_T = 0$ and 1, respectively, $\cos^{-1}(U_R/U_T) = \pi/2$ and 0, which allows Equation 7 to be approximated as follows:

$$a_2 \approx \frac{8}{3\pi}U_T^2 + \frac{4}{\pi}U_R^2 \qquad\qquad 0 \leqslant |U_R| < |U_T| \qquad\qquad (10)$$

$$a_2 \approx -2U_R U_T \qquad\qquad |U_R| \geqslant |U_T| \qquad\qquad (11).$$

Equations 10 and 11 state that when there is no river discharge, the bed stress magnitude at the fundamental frequency is equal to $8/3\pi(U_T)^2$, which is the classical value cited in the literature (Dronkers 1964; Proudman 1952). The bed stress increases quadratically with U_R for $|U_R| < |U_T|$, and approximately linearly with $|U_R|$ when $|U_R| \geq |U_T|$ (Figure 3.2). Note that the error in each approximation grows as U_R/U_T deviates from their respective intervals (Figure 3.2).

The coefficient a_0 can be simplified to:

$$a_0 \approx \frac{4U_R U_T}{\pi} \qquad\qquad 0 \leq |U_R| < |U_T| \qquad\qquad (12)$$

$$a_0 \approx -\left(\frac{U_T^2}{2} + U_R^2\right) \qquad\qquad |U_R| \geq |U_T| \qquad\qquad (13).$$

In contrast to the tidal frequency bed stress, Equations 12 and 13 indicate that a_0 is linear in U_R at low river velocities and quadratic at higher velocities (Figure 3.2). When tides are absent, the zero-frequency bed stress is simply the square of the river velocity (but opposite in sign).
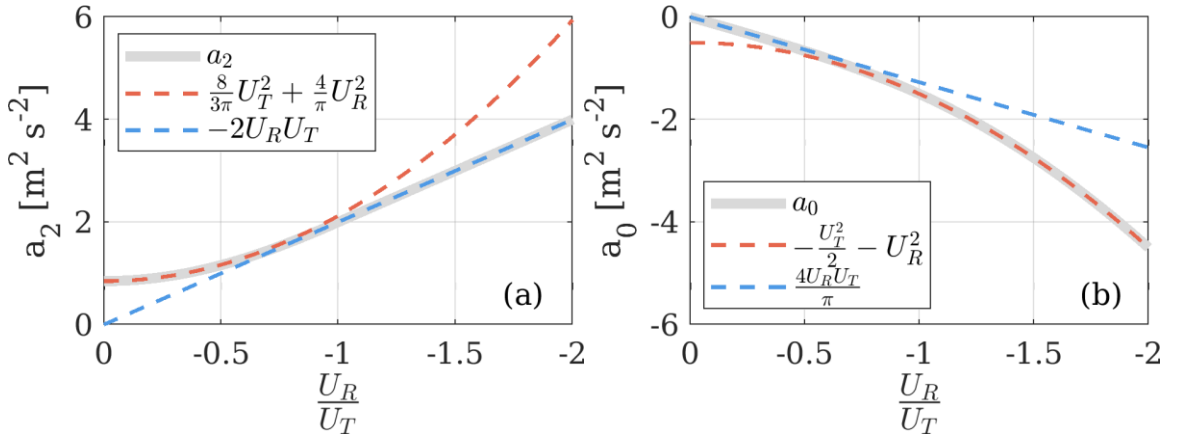
Figure 3.2. Tidal frequency bed stress a_2 (a) and zero frequency bed stress a_0 (b) as a function of U_R/U_T. Equations 7 and 8 shown by gray solid line, approximations are shown in dashed lines.Equation 9 can be approximated as:

$$a_4 \approx \frac{2.4 U_R U_T}{\pi} \qquad\qquad 0 \leq |U_R| < |U_T| \qquad\qquad (14)$$

$$a_4 \approx \frac{-U_T^2}{2} \qquad\qquad |U_R| \geq |U_T| \qquad\qquad (15).$$

Thus, a_4 is approximately proportional to the tidal amplitude U_T and increases approximately linearly with U_R at low river discharge. However, once the river velocity exceeds the tidal velocity a_4 is no longer a function of U_R (Figure 3.3). Because a_4 approaches a constant value while a_2 continues to grow as river velocity increases, there

167

is a U_R/U_T value for which a_4/a_2 is maximum. Plotting equations 7 and 9 reveals this ratio

is maximum when $U_R/U_T \approx -0.6$ (Figure 3.3b). Note that a_4 is negative because it

represents the transfer of energy to the first overtide from the interaction between the

fundamental frequency and river discharge.
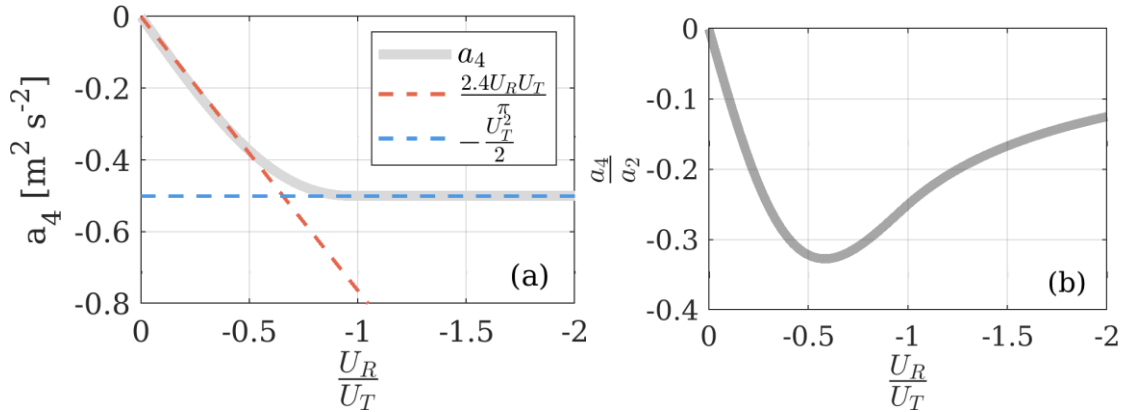
Figure 3.3. First overtide frequency bed stress a_4 as a function of U_R/U_T (a) with Equation 9 shown by gray solid line and approximations shown in dashed lines. Ratio of a_4/a_2 as a function of U_R/U_T using Equations 7 and 9 (b).Equation 14 highlights the requirement for

a nonzero river flow (or other tidally averaged flow) for a frictional overtide to be

produced, which is not true for all overtide modes (i.e., when $U_R = 0$, $a_4 = 0$ but $a_6 \neq 0$).

Also, a_4 is limited by the tidal velocity scale U_T because it is bound from above by U_T^2,

such that a_4 is always less than a_2, reaching up to about one third of the fundamental

frequency (Figure 3.3b). Because a_4 is generally much smaller than a_2, the overtide mode

is not included in subsequent development of the bed stress minimum location. However,

overtides are developed in the numerical model discussed below, and the consequences

of neglecting a_4 are explored by comparing analytical and numerical model results.

The approximations defined in Equations 10-15 can also be derived using

Chebyshev polynomials (see Chapter 8, Section 8 in Dronkers 1964), but the cosine

series has simpler basis functions, which improves the clarity of exposition. Approximating the bed stress with Chebyshev polynomials is especially useful when deriving analytical solutions to the shallow water equations, because the bed stress can be accurately represented by two or three terms (Godin 1991). A Fourier cosine series, on the other hand, explicitly renders the amplitude of the bed stress at each frequency, which facilitates interpretation of how the bed stress responds to changes in channel geometry and boundary conditions. The Chebyshev polynomials require an extra step using trigonometric identities to decompose the nonlinear terms into the tide/overtide modes (Godin 1991). Because we are interested in studying the spectral signature of the bed stress throughout the domain, not solving the equations of motion, a Fourier cosine series is used herein. Fourier's theorem guarantees convergence of the cosine series (Haberman 2004), and the cosine series also avoids the need to change variables associated in defining the Chebyshev polynomials. Finally, in situ observations and numerical modeling of tides are conventionally analyzed using harmonic functions, and so the elements of a Fourier cosine series are more readily compared to results from these other tools.

3.4.2 Bed Stress Minimum Location

The bed stress varies in time due to seasonal fluctuations in river discharge, and because U_T and U_R are opposed during flood but in the same direction on ebb. Tidal velocities also vary on daily, monthly, and annual time scales. For our analysis, we focus on spatial variations in peak ebb bed stress magnitude because in a system with substantial river flow such as the Columbia River, the largest stress—and therefore sediment transport—typically occurs during ebb, at least in the parts of the system without salinity intrusion. The interaction of semidiurnal and diurnal tides, which also creates an ebb asymmetry in tidal currents on the US West Coast (see Nidzieko 2010), will be considered in a future analysis. Below, we investigate the conditions required for this assumption to be valid. Subtracting Equation 10 from 13 gives

$$|\tau_{ebb}| = a_0 - a_2 \approx \frac{-4}{\pi} U_T^2 - \frac{7}{\pi} U_R^2 \tag{16}.$$

Equation 16 captures the magnitude of bed stress during peak ebb, which occurs at different times along the ocean-river continuum. This approach allows evaluation of neap-spring and seasonal variations in bed stress. In rivers wherein the largest bed stress occurs during flood, the bed stress minimum location may be examined using along-channel profiles of peak flood bed stress by adding Equations 10 and 13 (rather than subtracting).

Using Equations 10 and 13 limits the applicability of Equation 16 to regions where $U_R/U_T < 1$. Outside of this range, the tidal frequency bed stress is overestimated by Equation 10 (Figure 3.2). Note, however, that along-channel profiles of bed stress

estimated using ($-4/\pi\ U_T{}^2 - 7/\pi\ U_R{}^2$) and ($a_0 - a_2$) were found to be consistent in the vicinity

of the bed stress minimum, and so this limitation does not practically constrain the utility

of using the simpler approximation when deriving an expression for x_{min}.

The along-channel variability of $|\tau_{ebb}|$ is evaluated by developing functional forms

for U_T and U_R. The domain of interest extends from the ocean (x=0) to the head of tides

(x=L) , where U_T(L) = 0 (Figure 3.1). Following Jay (1991), U_T is defined using the

shallow water equation by assuming a spatially constant tidally averaged river depth $h(x)$

= H and convergent width, $b(x) = e^{\gamma x}$. While real systems have local variations in

depth and width, this simple representation approximates the geometry of many coastal

plain estuaries, allows an analytical solution of the tidal velocity throughout the domain,

and is a common approach used in the literature when studying tidal propagation in

estuaries (Ianniello 1979; Lanzoni and Seminara 2002; Savenije 2005; Talke & Jay,

2020). This approach assumes that the tidal amplitude is small relative to H, the flow is

unstratified (though non-zero salinity and a weak mean salinity gradient may be present

in the domain), and the spatial acceleration term is negligible. In an estuary with

moderate topography and no reflected wave, the tidal amplitude takes the form of an

exponential function (Jay 1991):

$$U_T \approx U_{T0}e^{\left(p-\frac{\gamma}{2}\right)x} \tag{17},$$

where U_{T0} is the tidal amplitude at the mouth, $p < 0$ is the damping modulus, and γ scales

the width convergence ($b(x) = e^{\gamma x}$) and is defined using an e-folding length scale Le ($\gamma = $

$-1/Le < 0$). When friction is stronger than topographic funneling ($|p| > |\gamma/2|$), the tidal

velocity decays exponentially from the mouth. The use of an approximate tidal velocity (Equation 17) to estimate the location of the bed stress minimum is validated through comparison with AdH Model results (see next section).

The river velocity U_R is defined by the river discharge divided by the channel cross section. Assuming an exponentially convergent width ($b(x) = B_0\,e^{\gamma x} + B_1$) gives

$$U_R = \frac{Q_R}{(B_0 e^{\gamma x} + B_1)H} \tag{18},$$

where B_0 is river width at the mouth and B_1 is river width as $x \to \infty$.

Substituting Equations 17 and 18 into Equation 16, and evaluating when the x-derivative equals zero, provides an implicit solution for x_{min}:

$$\frac{x_{min}}{L_e} = -\ln\left[\left(\frac{7}{4}\left(\frac{Q_R}{HB_0 U_{T0}}\right)^2 \left(\frac{p}{\gamma} - \frac{1}{2}\right)^{-1} e^{(2\gamma - 2p)x_{min}}\right)^{1/3} - \frac{B_1}{B_0}\right] \tag{19}.$$

Finally, developing an explicit equation facilitates interpretation of the sensitivity of x_{min}. Assuming a range of typical values for p [$-5(10^{-5})$, $-1(10^{-6})$ m^{-1}], γ [$-5(10^{-5})$, $-1(10^{-5})$ m^{-1}] and x [0, 100 km], the average of $e^{(2\gamma - 2p)x/3}$ equals one and the standard deviation is 0.26 (see Figure 3.14 in Appendix). And so x_{min} can be approximated by assuming $e^{(2\gamma - 2p)x/3}$ is equal to one:

$$\frac{x_{min}}{L_e} = -\ln\left[\left(\frac{7}{4}\left(\frac{Q_R}{HB_0 U_{T0}}\right)^2 \left(\frac{p}{\gamma} - \frac{1}{2}\right)^{-1}\right)^{1/3} - \frac{B_1}{B_0}\right] \tag{20}.$$

Note that $e^{(2\gamma - 2p)x/3}$ equals one when $p = \gamma$. When $p/\gamma < 1$, Equation 20 underestimates Equation 19, while weaker convergence relative to damping $p/\gamma > 1$ leads to over-estimates by Equation 20 (see Figure 3.15 in Appendix).

172

3.4.3 AdH Model

Equation 20 was validated using the 2-Dimensional, vertically integrated module of the AdH numerical model (Savant et al. (2011); see also https://hdl.handle.net/ 11681/39080). The domain, which extended 200 km landward from the ocean boundary, was defined as an exponentially convergent channel that relaxes to a constant width far upstream: ($b = 4,000e^{\gamma x} + 800\ m$) (see Figure 3.1). Bed elevation was constant throughout the domain, and the grid contained anywhere between 1,500 and 3,000 elements, depending on γ. The channel geometry was chosen to produce a large range in x_{min} values when using the inputs from Table 3.1 in Equation 20. The model was forced by the M_2 tide at the mouth with an amplitude of 0.8m, and constant river discharge at the upstream boundary. Simulations were run for two weeks using a maximum time step of 300 s. Trials were carried out under three different convergence length scales, three river depths, and six river discharges, yielding 54 individual runs (Table 3.1).

Table 3.1 River discharge, depth, and convergence length scenarios used in AdH runs.

River Discharge, Q_R [m^3s^{-1}]	-{2000, 4000, 6000, 10000, 14000, 18000}
River Depth, H [m]	{6, 9, 12}
E-folding Length, L_e [km]	{40, 80, 120}

In order to define the bed stress minimum location for each trial (x_{adh}), time series of velocity at each node were extracted from the AdH model output to define the bed stress throughout the domain as $\tau = \rho\, Cd\, U\, |U|$, where ρ is water density, C_d is a drag coefficient, and U is the cross-sectionally averaged along-channel velocity (ebb velocity negative). The drag coefficient within a real system can vary between roughly 0.001 and 0.01 (Branch et al. 2021) and was assumed to equal 0.0026, following prior studies in tidal rivers (Giese and Jay 1989; Friedrichs and Aubrey 1994; Ralston et al. 2019). Along-channel profiles of the bed stress were then plotted at each time step to define an envelope of bed stress along the river that illustrate the maximum, minimum, and range of bed stress at each location during the tidal cycle (see, for example, the gray shading in Figure 3.4). For each trial the location of the x_{adh} was defined as the location where the bed stress envelope shows a local minimum during ebb (red squares in Figure 3.4). Of the 54 simulations, 30 exhibited a bed stress minimum within the domain. For these trials, x_{min} was defined by substituting the boundary conditions and geometry of the AdH model into Equation 20. The damping modulus p and U_{T0} were estimated by harmonic analysis of the AdH-derived velocity field.

174

This study focuses on spatial patterns of bed stress, the location of the bed stress minimum in particular, to infer general trends in sediment transport. Other measures that are traditionally considered for evaluating long term erosion and deposition patterns are flow predominance and net sediment transport. These two criteria were assessed using AdH model simulations to highlight the influence of the bed stress minimum on sediment transport. Flow predominance was defined using tidally-averaged bed stress profiles and AdH derived bed stress envelopes (as defined below). Excess bed stress ($|\tau_b|$-τ_c) is commonly used to estimate sediment transport (see Dyer 1995) and the sum of this value squared during the AdH model simulation τ_E was used as a proxy for net sediment transport:

$$\tau_E = \int_t sign\,(\tau_b)(|\tau_b| - \tau_c)^2 \tag{21},$$

where the *sign()* is needed to maintain direction of transport as τ_b changes sign, and only τ_b values greater than τ_c are included in the integration. Unless otherwise noted, τ_c is assumed to be 0.2 N m^{-2}. This uses Shields criterion (Dyer 1995): $\tau_c = 0.05(\rho_s$-$\rho)gD_{50}$, where $\rho_s = 2650$ kg m^{-3} is the particle density, $D_{50} = 0.2\ mm$ is particle diameter, g is the acceleration of gravity.

3.5   Results

This section outlines comparisons between analytical estimates of the bed stress minimum location (Equation 20) and AdH model simulations. The sensitivity of x_{min} to channel geometry, tidal amplitude, and river discharge is then explored by studying the properties of Equation 20.

175

3.5.1   AdH Model and Validation

AdH-derived bed stress envelopes highlight the connection between the bed stress minimum location and the transition from tidally to fluvially dominated dynamics in the river. As tidal velocities decrease in the upstream direction due to friction, the range of bed stress over a tidal cycle is also smaller (Figure 3.4). The proportion of time during the tidal cycle when the bed stress is greater than zero (flood tide) also becomes smaller, tending towards zero somewhere near the bed stress minimum. Because river velocity is largest in the narrow, upstream part of the model domain, the most negative, tidally averaged bed stress typically occurs at the upstream boundary (solid gray line in Figure 3.4). Moving downstream, increases in channel width decrease the river velocity and the fluvial contribution to the bed stress (Figures 3.5 and 3.6). A local minimum in modeled bed stress, x_{adh}, manifests where the tidal contribution begins to balance the downstream decrease in U_R. While x_{adh} sometimes occurred in the region where $\frac{1}{3} < |\,UR/UT\,| < 14$, over half of the trials exhibited bed stress minima within the tidal-fluvial transition wherein $1 < |\,UR/UT\,| < 3$. As width convergence and discharge increased, the tidal-fluvial transition and x_{adh} were found to move downstream.
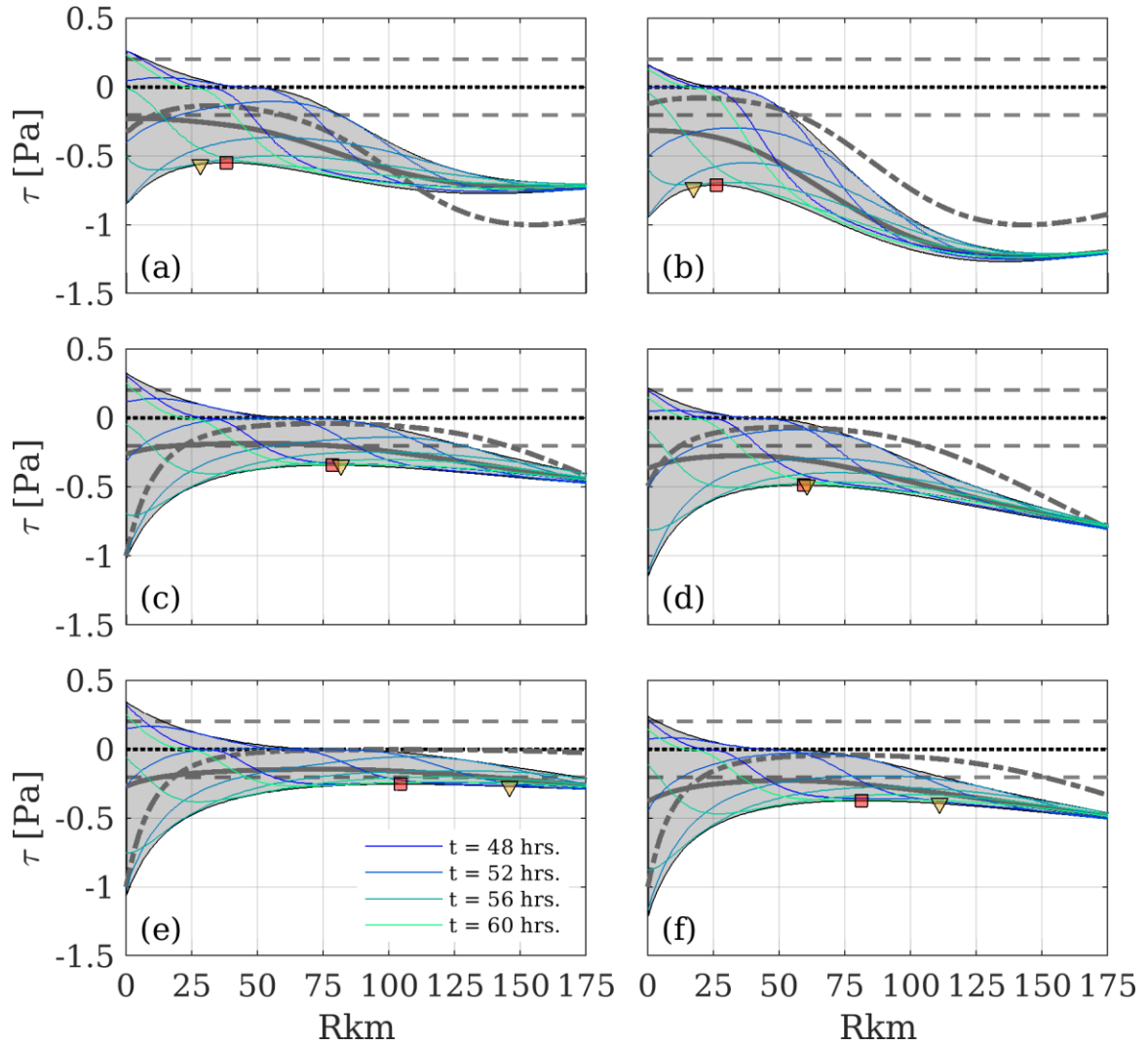
Figure 3.4. Along-channel profile of bed stress computed in AdH models when river discharge equals 4,000 m^{3}s^{-1} (left) and 6,000 m^{3}s^{-1} (right), and e-folding length scale equals 40 Rkm (top), 80 Rkm (middle) and 120 Rkm (bottom). Tidally-averaged bed stress shown by solid line. Excess bed stress τ_E, normalized by its maximum value in the domain, is shown by dash-dotted lines. Dashed lines represent critical shear stress for fine sand $D_{50} = 0.25$mm, defined using Shields Diagram. Dotted line shows zero bed stress. Red square marks x_{adh}. Yellow triangle marks x_{min}.

Although the velocity acts primarily at residual and tidal frequencies, the overtide

mode also contributes to U in the AdH simulations (solid lines in Figure 3.5). The

overtide contribution reaches a maximum between the mouth and x_{adh}, reaching about

15% of the total velocity. While the relative phase difference between U2 and U4 ($2\varphi_2 - \varphi_4$) indicates that the tidal velocity is slightly flood dominant throughout the domain ($0 < 2\varphi_2 - \varphi_4 < \pi/2$), the total velocity is ebb dominant because U_R is greater than U_4.
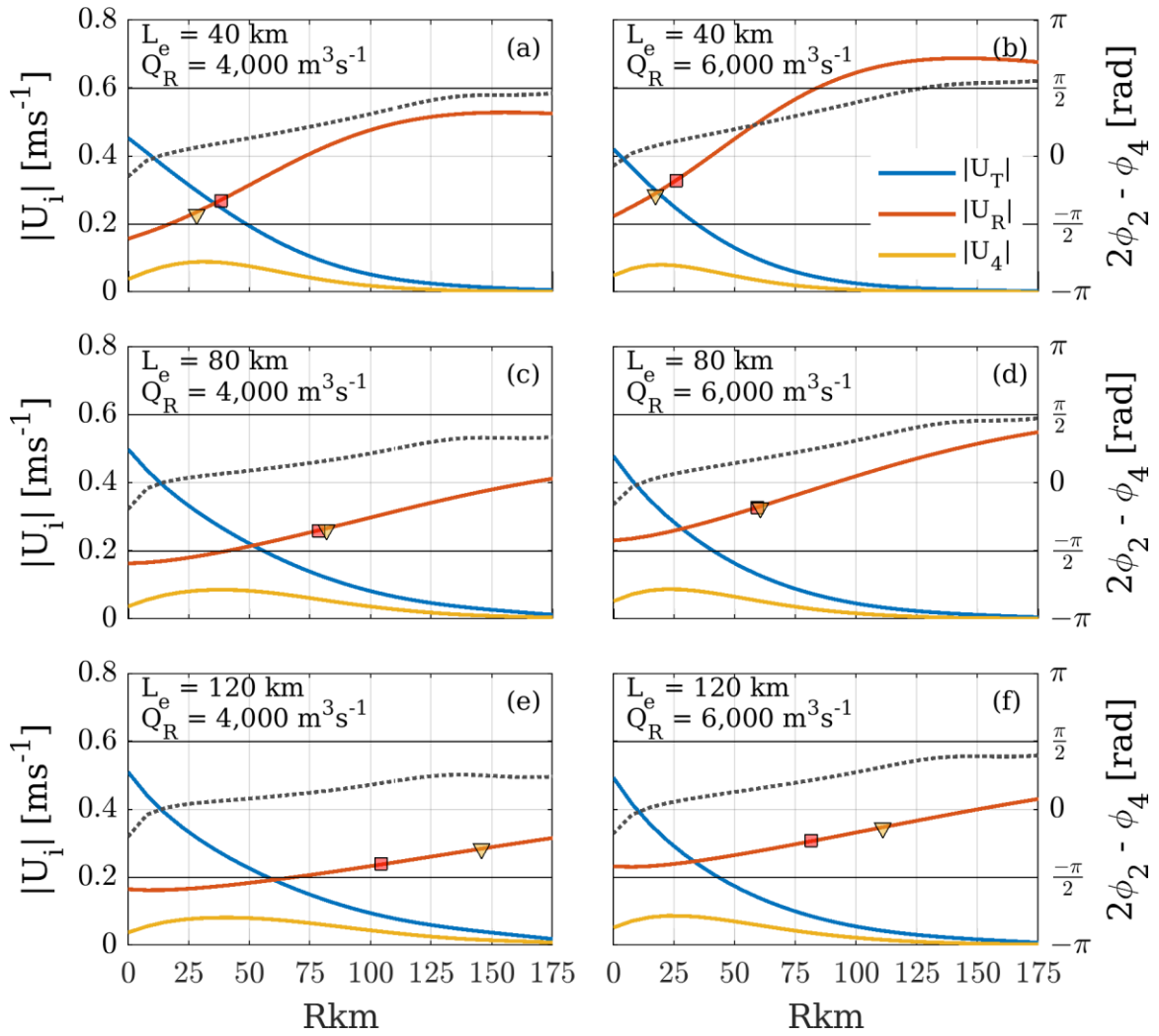
Figure 3.5. Along-channel profile of velocity at residual (solid red lines), tidal (solid blue lines), and overtide (solid yellow lines) frequency computed using harmonic analysis of AdH modeled velocity. Results are shown for river discharge of 4,000 m³s⁻¹ (left) and 6,000 m³s⁻¹ (right), and e-folding length scales of 40 Rkm (top), 80 Rkm (middle) and 120 Rkm (bottom). Phase difference between U_T and U_4 ($2\varphi_2 - \varphi_4$) is shown by a gray dotted line and indicates that the tidal velocity is flood dominant. Red squares denote x_{adh}, and yellow triangles x_{min}.

179

The overtide mode also contributes to AdH-derived bed stress, but in this case the relative phase difference between a_2 and a_4 ($2\theta_2 - \theta_4$) transitions from ebb dominant near the mouth ($2\theta_2 - \theta_4 \approx \pi$) to slightly flood dominant near and upstream of x_{adh} (Figure 3.6). Again, a_0 is greater than a_4 and so the total bed stress is ebb dominant. Because Equation 16 does not include a_4, analytical estimates of τ_{ebb} will overestimate AdH ebb tide bed stress in regions where the bed stress is flood dominant, and underestimate AdH in ebb dominant regions (see dashed vs solid lines in Figure 3.6). The difference between τ_{ebb} and AdH ebb tide bed stress was typically small and did not exceed 0.05 m^2s^{-2} at any given location.
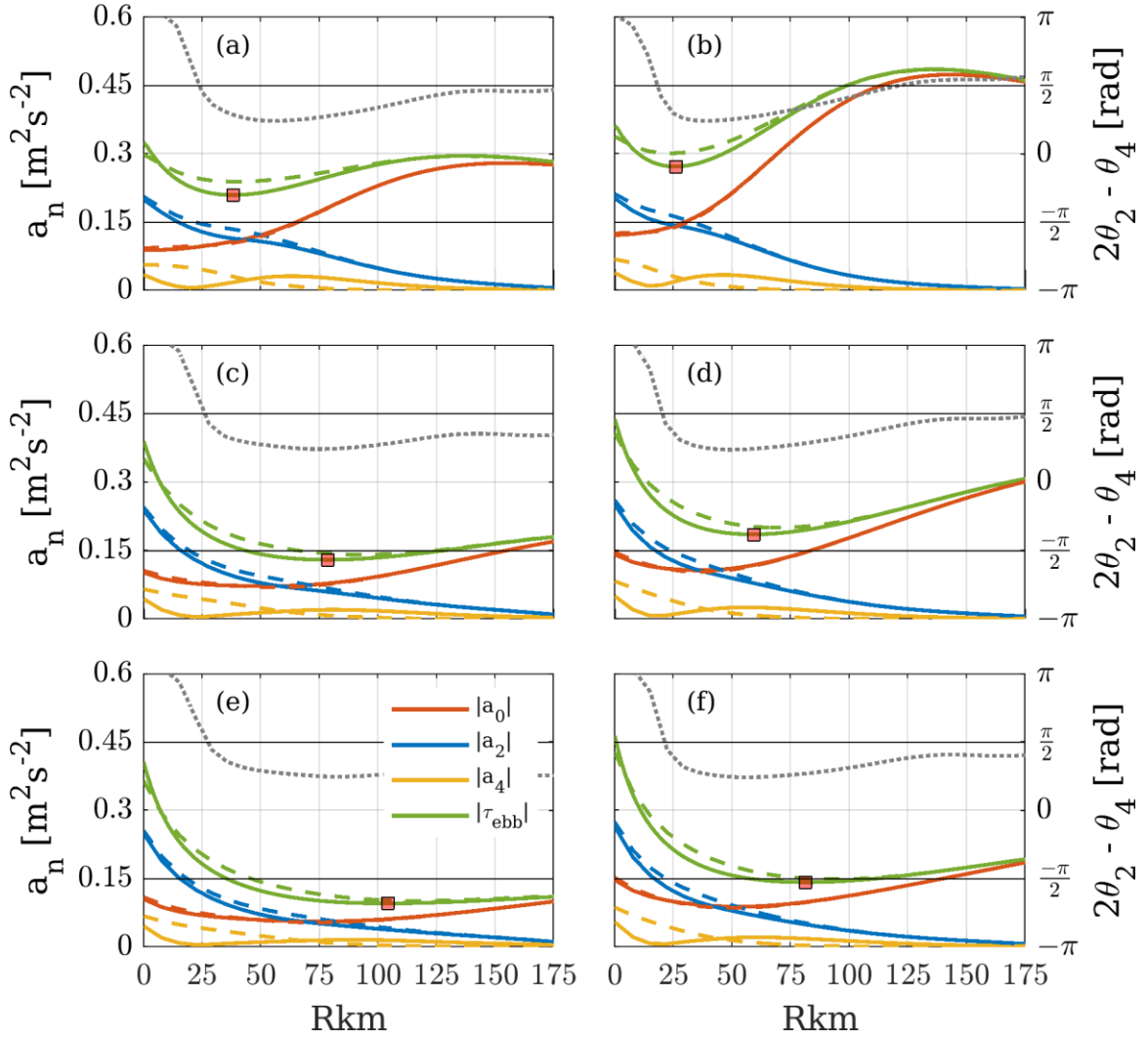
Figure 3.6. Along-channel profiles of Fourier coefficients (a proxy for bed stress) for river discharge of 4,000 m³s⁻¹ (left) and 6,000 m³s⁻¹ (right), and e-folding length scales of 40 Rkm (top), 80 Rkm (middle) and 120 Rkm (bottom). Coefficients are shown at residual (red lines), tidal (blue lines), and overtide (yellow lines) frequency. Analytical estimates (Equations 7-9) are shown by dashed lines. Harmonic analysis of AdH modeled bed stress ($U/|U|$) is sown by solid lines. Total bed stress during ebb in AdH simulation (solid) and Equation 16 (dashed) are shown by green lines. The relative phase difference between a_2 and a_4 are shown as dotted lines. Red squares denote x_{adh}.

Analytical estimates of the residual and tidal bed stress components (Equations 7-8) agree well with harmonic analysis of AdH bed stress (within 0.02 m²s⁻²; Figure 3.6) .

Small discrepancies are evident near where along-channel profiles of |U4| reach a

maximum (see Figures 3.5 & 3.6), likely because U4 is not included in Equation 2.

Analytical estimates of the overtide frequency bed stress (Equation 9) generally do not

agree with AdH estimates because Equation 9 represents the bed stress produced by the

interaction of UR and UT alone, whereas AdH also includes the contribution of U4.

Errors between Equation 9 and AdH reach about 0.05 m^2s^{-2}, but the greatest difference

between the two approaches is that Equation 9 does not produce the shift from ebb to

flood dominance that is evident in the AdH model. Further study of the overtide

frequency bed stress must, therefore, include the U4 contribution to the velocity field

when calculating the Fourier coefficients for U|U|.

Despite the discrepancies noted above, comparisons between x_{adh} and x_{min}

(Equation 20) show that, even when omitting the first overtide in Equation 2, the

analytical results are qualitatively consistent with numerical results. Estimates of x_{adh} and

x_{min} were found to be well correlated ($R^2 = 0.8$, and p-value ≈ 0) and to share a linear

relationship that follows a 1:1 slope (see Figure 3.7). Equation 20 is biased above x_{adh}

during low flows when $Le = 120$ km (Figure 3.4), however, which can be attributed to the

lack of an overtide mode in the analytical formulation. These trials also had p/γ ratios

close to three, which can lead to over-estimates of the bed stress minimum location using

Equation 20 (see Figure 3.15 in Appendix). The ~70 *km* discrepancies observed in these

trials correspond to a bed stress envelope with small along-channel gradients in the upper

reaches of the river where the bed stress minimum was located (e.g., Figure 3.4f). Under

such conditions the bed stress minimum is better described as a ~50 *km* region rather

than a discrete location of reduced bed stress, in which case the discrepancies in Figure 3.7 are less significant. Also, x_{min} shows greatest sensitivity to small changes in boundary conditions and geometry when the bed stress minimum is upstream of Le (see Figure 3.8), which may also contribute to the bias observed for these trials.
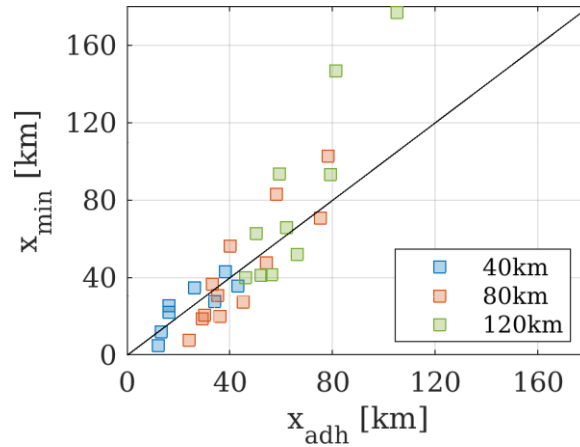
Figure 3.7. Location of bed stress minimum in Equation 20 vs x_{adh}. Solid line depicts a 1:1 slope.

Excess bed stress (Equation 21) is largest at the upstream boundary for strongly convergent geometries and at the river mouth for weakly convergent geometries (dash-dotted lines in Figure 3.4). In both cases the along-channel profile of τ_E shows a local minimum somewhere near x_{adh}. Excess bed stress τ_E was found to be negative (ebb-dominant) throughout the model domain, so the gradients in τ_E imply sediment accumulation upstream of x_{adh} (at any given control volume, more sediment enters at the upstream boundary than leaves through the downstream boundary) and sediment loss downstream of x_{adh}. Substituting different values of D_{50} into Equation 21 changed the magnitude of τ_E throughout the domain, but not the qualitative aspects of its along-channel distribution. τ_E exhibited a local minimum near x_{adh} for both finer and coarser

183

grain sizes. Larger particles resulted in a region of limited particle mobility wherein $\tau_E = 0$, which was centered on x_{adh}.

3.5.2 Sensitivity Study

The non-dimensional location of the bed stress minimum x_{min}/L_e is a function of three non-dimensional variables: the ratio of river velocity to tidal velocity at the mouth $Q_R/(HB_0U_{T0})$, the ratio of tidal damping to convergence p/γ, and the ratio of the river widths at the upstream and seaward boundaries B_1/B_0 (Equation 20). The sensitivity of x_{min} to these parameters is discussed below. Throughout this section, all parameters in Equation 20 are assumed to be equal to the values outlined in Table 3.2 unless otherwise noted.

Table 3.2. Assumed values for variables used in sensitivity studies, which are representative of the Lower Columbia River Estuary.

River Discharge, Q_R [m^3s^{-1}]	-6,000
River Depth, H [m]	10
River Width at Ocean Boundary, B_0 [m]	4,000
River Width at Upstream Boundary. B_1 [m]	800
E-folding Length, L_e [km]	40
Tidal Amplitude at Ocean Boundary, U_{T0} [ms^{-1}]	1.0
Damping Modulus, p [m^{-1}]	$-2e^{-5}$

Because the location of the bed stress minimum is defined through the natural

logarithm, x_{min} is most sensitive to changes in boundary conditions and/or geometry when

the argument of the natural log function is close to zero, or when:

$$\left(\frac{7}{4}\left(\frac{Q_R}{HB_0U_{T0}}\right)^2\left(\frac{p}{\gamma}-\frac{1}{2}\right)^{-1}\right)^{1/3} \approx \frac{B_1}{B_0} \tag{22}.$$

With the parameters used here, this threshold occurs when $|Q_R/(HB_0U_{T0})| = 0.04$, which

represents the furthest upstream limit of the applicability of the equations. Values smaller

than this yield a complex number from the log function. Values just larger than 0.04

produce the maximum sensitivity of x_{min} to external forcing (Figure 3.8a). In other words,

the spatial variability of the bed stress minimum is greatest when x_{min} is near the upstream

reaches of the domain (e.g., when river discharge is small) and decreases as x_{min}

approaches the mouth. A greater sensitivity of x_{min} in the narrowest part of the river is

reasonable because small changes in discharge or geometry have greater effect on the

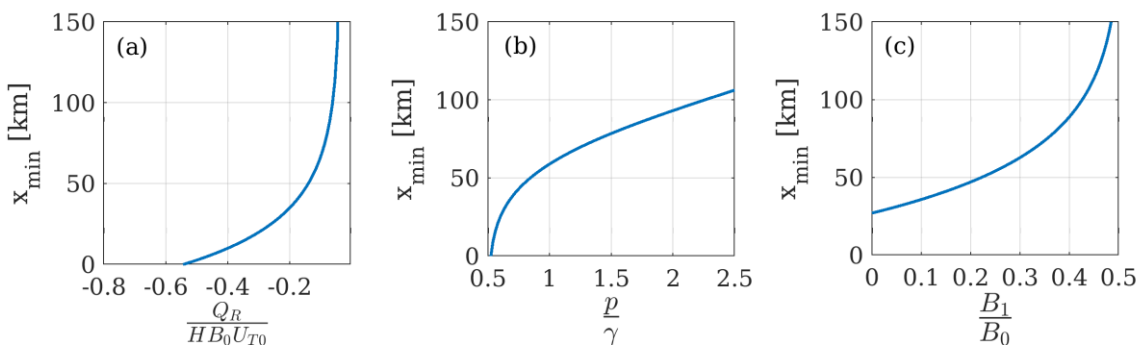river velocity (and hence bed stress) in that location than in wider reaches of the river.

Figure 3.8. x_{min} as a function of Q_R/HB_0U_{T0} (left), p/γ (center), and B_1/B_0 (right)

The condition for which x_{min} is exported to the ocean in the analytical model occurs when the argument of the logarithm (see Equation 20) is less than or equal to unity:

$$\left(\frac{7}{4}\left(\frac{Q_R}{HB_0U_{T0}}\right)^2 \left(\frac{p}{\gamma}-\frac{1}{2}\right)^{-1}\right)^{1/3} - \frac{B_1}{B_0} \leq 1 \tag{23}.$$

Under these conditions $x_{min} \leq 0$, which is outside the validity of the model, and the minimum stress within the domain occurs at $x = 0$. Recall that the analytical model assumes a single layer (barotropic) flow, and so the bed stress minimum may reside further upstream or require greater river discharge for export when baroclinic circulation dominates velocities near the bed. Solving for Q_R in Equation 23 provides the river discharge at which the bed stress minimum is exported:

$$Q_{R0} \geq -HB_0U_{T0}\left(\frac{4}{7}\left(\frac{p}{\gamma}-\frac{1}{2}\right)\left(1+\frac{B_1}{B_0}\right)^3\right)^{1/2} \tag{24}.$$

In fact, the river discharge required for the bed stress minimum to reside at any location x within the domain is given by:

$$Q_{Rx} = -HB_0U_{T0}\left(\frac{4}{7}\left(\frac{p}{\gamma}-\frac{1}{2}\right)\left(e^{\gamma x}+\frac{B_1}{B_0}\right)^3\right)^{1/2} \tag{25}.$$

For parameter values which resemble the Columbia River (Table 3.2), Equation 24 and 25 indicate that the discharge needs to reach about 7,000 m^3s^{-1} or 22,000 m^3s^{-1} for the bed stress minimum to be located at the e-folding length scale or be exported to the ocean, respectively. The former value is slightly less than the modern average flow

and about 90% of the historic mean flow (Naik and Jay, 2011). The latter value is about

equal to the two-year return flow before 1900; i.e., before system alteration (Jay and

Naik, 2011). In other words, x_{min} equals about 40km on average in the LCRE, and the bed

stress minimum is exported only during extreme events (see Figure 3.11b). Note that for

QR = 22,000 m^3 s^{-1}, the LCRE is mostly freshwater and so the assumption of depth-

integrated conditions is justified (Al-bahadily 2020). A minimum bed stress occurs within

the domain when the ratio of river transport to tidal discharge $|Q_R/(HB_0U_{T0})|$ is < 0.54.

Thus, x_{min} is exported when Q_R is more than about half of the tidal discharge. Less

convergent systems require a greater Q_R/Q_T ratio to export the bed stress minimum,

because x_{min} is typically located further upstream in such systems (Equation 24; Figure

3.8b).

Equation 20 suggests that increasing river velocity, whether by changing river

discharge or by decreasing cross-sectional area, tends to move x_{min} downstream. Thus,

stronger convergence relative to tidal damping reduces x_{min} (Figure 3.8b). Likewise,

decreasing B_1 relative to B_0 (narrower upstream cross-sections), reduces x_{min} (Figure

3.8c). Physically this represents the relative increase in the fluvial contribution to the bed

stress in the upriver reaches when convergence increases, thus translating x_{min} seaward to

a location where U_R decreases enough to produce a local minimum. Similarly, shallower

systems exhibit bed stress minima that are further seaward relative to deeper systems

(Figure 3.8a).

The functional form of Equation 20 highlights that x_{min} is defined as the product between the e-folding length scale and some function of the river geometry and boundary conditions:

$$x_{min} = L_e * f(Q_R, U_{T0}, p, \gamma, B_0, B_1, H) \tag{26}.$$

Therefore, x_{min} is closely related to L_e, and will move downstream and exhibit less sensitivity to changing boundary conditions as convergence increases (Figure 3.9). Experimentation with different geometries and boundary conditions reveals that the bed stress minimum in large rivers like the LCRE has the greatest likelihood of occurring at or just upstream of the e-folding length scale. For example, when Le equals 60 km and all other variables in Equation 20 are uniformly sampled across the sets defined in Table 3.3, x_{min} equals 69 km on average with a standard deviation of 80km. When Le equals 120 km, x_{min} equals 180 km on average with a standard deviation of 160km (Figure 3.10). Qualitatively, larger variations of x_{min} in less convergent channels result from a smaller along-channel gradient in river velocity (Figure 3.5), wherein changes to boundary conditions cause relatively larger translations in x_{min}. Bed stress minima situated further upstream are also associated with smaller along-channel gradients in tidal velocity, which supplements larger translations in x_{min}. Finally, because the range of x_{min} values moves downstream as L_e decreases, stronger convergence means the bed stress minimum is exported to the ocean ($x_{min} < 0$) over a greater range of the parameter space (Figure 3.10).

Table 3.3. Variable sets sampled for producing x_{min} probability distributions in Figure 3.10.

River Discharge, Q_R [$m^3 s^{-1}$]	[-20000, -1000]
River Depth, H [m]	[5, 40]
River Width at Ocean Boundary, B_0 [m]	[1000, 6000]
River Width at Upstream Boundary. B_1 [m]	[400, 1000]
Tidal Amplitude at Ocean Boundary, U_{T0} [ms^{-1}]	[0.2, 2]
Damping Modulus, p [m^{-1}]	[$-5e^{-5}$, $-1.5e^{-5}$]
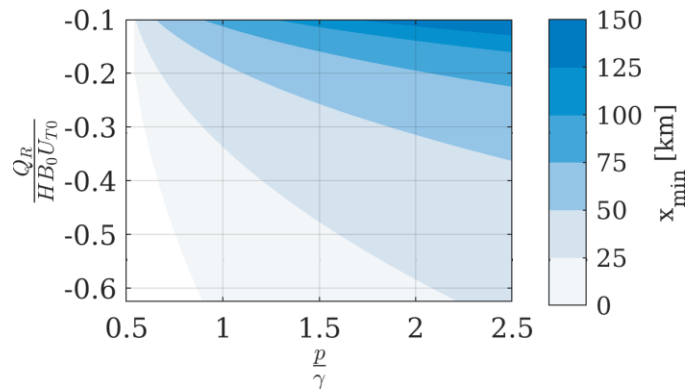
Figure 3.9. x_{min} parameter space as function of velocity scale (y-axis) and friction scale (x-axis). Values are produced using variables from Table 3.2 in Equation 20.

Hypersynchronous estuaries lead to a complex number in Equation 20 because $(p/\gamma - \frac{1}{2})$ is negative. In such systems, the spatial gradients in the tidal and river velocities are not conducive for the formation of a bed stress minimum because both increase in the upstream direction. Some estuaries are hypersynchronous near the mouth, but at some point further upstream the changes in width become inconsequential, and

tidal velocity decreases. Presumably, this puts the bed stress minimum farther upstream. Weakly convergent channels host bed stress minima near the upstream boundary because the river velocity is relatively constant along the channel. When tidal damping is minimal *(p/γ ~ ½)* the bed stress minimum is located near the mouth because the tidal velocity is relatively constant (Figure 3.9).
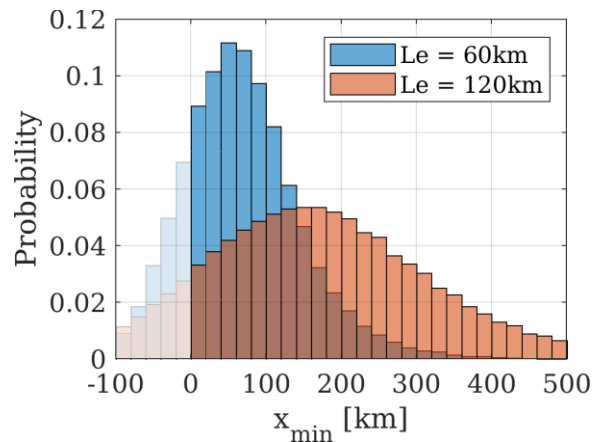
Figure 3.10. Probability distribution of xmin as estimated by Equation 20 using variable sets listed in Table 3.3. x_{min} less than zero indicates the bed stress minimum has been exported to the ocean, but holds no other physical meaning.

3.6   Discussion

The dependence of x_{min} on depth and river discharge suggests that any shifts to system morphology and boundary conditions, whether caused naturally or by system management, can result in large shifts in the bed stress minimum and therefore the locations of sediment deposition. Rivers all over the world are being deepened to facilitate passage for ever larger vessels (Talke and Jay 2020), which suggests that the bed stress minimum has migrated upstream in many rivers. In this section, historical changes in bed stress profiles and bed stress minimum locations are explored in three

190

prototype systems (Lower Columbia River Estuary or LCRE, Delaware Estuary, and

Hudson River) to illustrate how management over the last century may have influenced

sediment transport and deposition near x_{min}. For each system, daily averaged river

discharge observations between 2000 and 2020 and idealized geometry (Table 3.4) are

substituted into Equation 20 to develop probability distributions of x_{min} for modern and

historical channel depths. Bed stress profiles are generated using $|\tau_{ebb}| = a_0 - a_2$ (see

Section 2).

Table 3.4. Idealized representation of example estuaries.

Variable	Delaware Estuary[a]	Hudson River Estuary[b,c]
B_0 [m]	45,000	1,900
B_1 [m]	300	200
L_e [km]	35	60
U_{T0} [ms^{-1}]	0.8	0.7
p [m^{-1}]	-2e^{-5}	-1.5e^{-5}

[a]pareja-Roman et al. (2020), [b]Ralston and Geyer (2017), [c]NOAA tide and current
predictions.

3.6.1 Lower Columbia River Estuary

Before channel improvements beginning in the late 1870s, controlling depths in

the LCRE were about 6-8m (Hickson 1961; Helaire et al. 2019). While in-water

placement of dredged material has maintained shallower depths outside the FNC, the

increase in ship-draft over the last 150yr has driven depth increases all along the river.

Historical cross sections before channel improvement show many reaches with an average depth of 7 m or less (Hickson 1961). In contrast, recent bathymetry surveys indicate the average depth of the LCRE is on the order of 10 m upstream of the estuary (Rkm 50), consistent with the idea that dredging has exceeded sand supply for most years since 1905 (Templeton and Jay 2012). As has happened in other systems where hydropower regulation of flow has reduced flows, sediment supply has decreased (Jay and Simenstad, 1996; Naik and Jay, 2010, 2011). Agricultural diversion, flood control, reservoir trapping of sediment, and decreased flows due to climate change since the late 1800s have all contributed to decreased sediment input at the same time that dredging has removed large amounts of sand (Naik and Jay, 2011).

Substitution of values representative of the LCRE (Table 3.2) into Equation 20 along with daily average river discharge measured at Rkm 87 from 2000 to 2020 suggests how the probability distribution of x_{min} may have shifted due to channel deepening. Assuming an average river depth of 7 m before 1900, the average value of x_{min} is 33 km and seasonal variability in river discharge shifts x_{min} by 75 km (Figure 3.11b). During low flow, late summer months, x_{min} is near Rkm 75, while it is within a few kilometers of the mouth during flood events. With a deeper river ($H = 10$ m), the average location for the bed stress minimum shifts upstream by 15 km to Rkm 48, and seasonal patterns in the hydrograph shifts x_{min} by roughly 100 km, from Rkm 5 to Rkm 115. Because the parameterization of tidal amplitude does not include the damping effects of river discharge (U_{T0} and p are constant in Table 3.2), seasonal fluctuations in x_{min} are potentially greater in the LCRE than Equation 20 suggests.
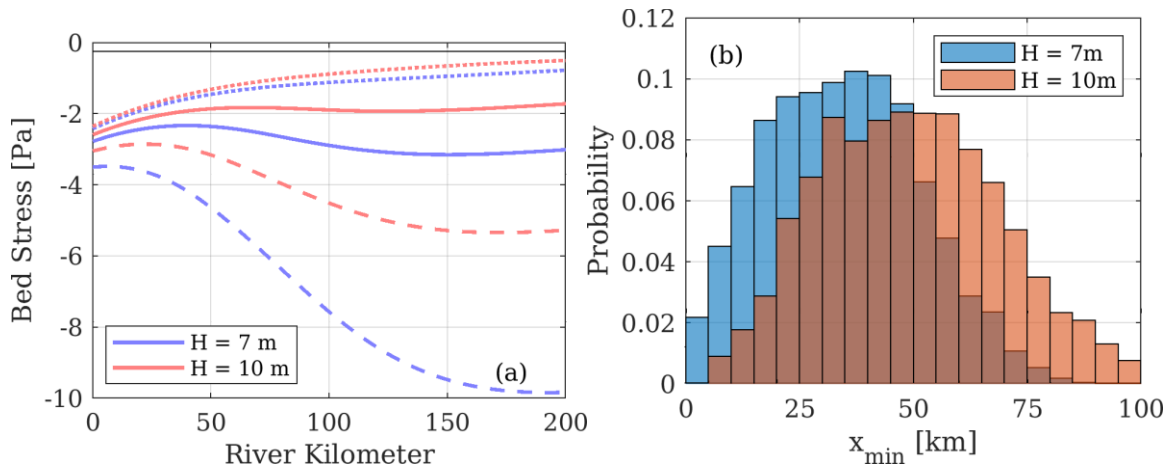
Figure 3.11. Left: Bed stress profiles (Equation 16) in idealized Columbia River for river discharge of 2,000 (dotted lines), 5,000 (solid lines), and 10,000 (dashed lines) m^3s^{-1} assuming historical (blue lines) and contemporary channel depths (red lines). Solid black line denotes critical bed stress for movement of medium sand (D_{50} = 0.25 mm). Right: Columbia River x_{min} as calculated using Equation 20 using river discharge measurements > 2,000 m^3s^{-1} collected between 2000 and 2020 at USGS Station 14246900 (~Rkm 86).

Channel deepening can influence shoaling volumes upstream of x_{min} through modifications to the along-channel profile of bed stress. For example, a deeper channel exhibits smaller bed stress magnitudes and reduced bed stress gradients upstream of x_{min} than a shallower channel (Figure 3.11a). Because the bed stress is uniformly greater than the critical value for particle movement, as defined using Shields Diagram with a mean particle diameter $D50$ = 0.25 mm, sand deposition is controlled by spatial gradients in transport, which suggests that deepening could reduce shoaling upstream of x_{min} even though the bed stress decreases.

Flow regulation on the LCRE has influenced the bed stress minimum through a reduction in peak seasonal flows. For example, the mean river discharge during the spring freshet (May-July) decreased from 13,610 m^3 s^{-1} before 1900 to 7,060 m^3 s^{-1}

193

between 1970 and 2004 (Naik and Jay 2010). According to Equation 20, this decrease in river discharge results in an upstream shift in x_{min} of 25 km during the freshet (from Rkm 15 to Rkm 40). In fact, the bed stress minimum does not occur in the estuary under pre-regulation peak freshet flows (~22,000m^3 s^{-1}), whereas $x_{min} \approx 30$ km during present day peak freshet flows (~9,000m^3 s^{-1}). While salinity intrusion limits sand export, salinity was essentially expelled from the Columbia River estuary on greater ebbs during pre-1900 high flows (Sherwood et al. 1990, Al-bahadily 2020). Together with the changes in river depth, flow regulation has created a system that is likely no longer capable of exporting the bed stress minimum (except under very large flood events), which suggests less material is being supplied to the Columbia River plume and the Washington coast now than was a century ago. Indeed, shoreline erosion near the mouth of the Columbia River since the 1950's has been attributed to insufficient sediment supply from the estuary (Kaminsky et al. 2010; Elias et al. 2012). According to Equation 24, river discharge needs to reach about 22,000 m^3 s^{-1} under present day river depths and 15,000 m^3 s^{-1} when H = 7 m before the bed stress minimum is expelled. Daily averaged discharge at Rkm 87 exceeded Q_{R0} on only three days between 1970 and 2020, whereas Q_{R0} was exceeded on 455 days between 1880 and 1930 (Jay and Naik 2011).

Baroclinic effects somewhat limit the validity of this analysis in the Columbia within about 5-15 km of the mouth, because the estuary is highly stratified within this reach during periods of large river discharge when x_{min} is shifted this far downstream (Jay and Smith 1990). Moreover, river discharge through the estuary is split between the north and south channel downstream of Rkm 40, with the portion of flow through the

194

south channel decreasing as river discharge increases (Al-bahadily 2020), which may also modulate the relationship between x_{min} and Q_R. The theory still provides additional insight on the factors controlling deposition in an estuary, however. While the traditional perspective has been that the ETM of the LCRE forms by gravitational circulation (Gelfenbaum 1983) and tidal asymmetry (Jay and Musiak 1996; Jay et al. 2007b), the bed stress minimum caused by the interplay of tidal and river currents may also be important. Indeed, sand accumulation in the estuary occurs most rapidly near the upstream end of the energy flux divergence minimum (~Rkm 50), upstream of all salinity intrusion (Jay et al. 1990), and near the average location for the bed stress minimum (Figure 3.11). Because the material trapped by the bed stress minimum travels as bed load, rather than the suspended load that makes the ETM, a wider gradation of material can also become deposited. That is, when river discharge is large enough, and x_{min} is shifted downstream near the salt wedge, greater volumes and gradations of material can become trapped in the ETM than would otherwise occur without a local minimum in bed stress. Indeed, the ETM of the LCRE is sand-bedded with long-term trapping of fines occurring in peripheral areas, on neaps, and during the low-flow season (Jay et al. 2007b).

Creating and maintaining deeper water in the LCRE navigation channel has been achieved in large part through the construction of pile dikes and artificial islands throughout the river, and so the river has become narrower in many places as well as deeper. For example, pile dikes at Henrici Bar (~Rkm 145) decreased the river width from about 1,400 m in 1909 to 870 m in 1959 (Hickson 1961). Reduction of river widths near the upstream boundary of a tidal river (B1) may counteract upstream migration of

195

x_{min} due to channel deepening and flow reduction (see Figure 3.8c), and may also enhance deposition upstream of x_{min} due to stronger spatial gradients in bed stress. Changes in river width are less studied than changes in depth, but have been shown to contribute to changes in tides and river flow velocities (e.g., Talke et al., 2021). The theory presented here suggests width alterations could play an important role in the sediment transport patterns controlled by the bed stress minimum for systems like the LCRE. Further exploration of the influence of river width is beyond the scope of this study, but could provide additional insights to how channel improvement structures and land reclamation has altered sand deposition in the LCRE.

3.6.2   Delaware Estuary

Like the Columbia River, the Delaware Estuary contains a region with anomalously high shoaling rates. Roughly 60% of all material dredged from the Philadelphia-Sea shipping channel is derived from the Marcus Hook–New Castle reach around Rkm 105 to 130 (Sommerfield et al. 2003). This region also coincides with a distinct down-estuary transition in bed composition from coarse to fine grain material that occurs between Rkm 120 to 140 (Sommerfield et al. 2003). Together, these depositional patterns imply that the system energy decreases as one moves downstream through this reach. Indeed, x_{min} occurs near Rkm 120 on average (Figure 3.12b), and near Rkm 95 during peak spring discharge (QR = 2, 500 m^3 s^{-1}), which is also near where the tidally averaged bottom current is zero (Sommerfield and Wong 2011).

Channel development up to Rkm 200 has increased mean water depths in the Delaware Estuary from about 5 m in 1848 to 8 m in 2014 (DiLorenzo et al. 1993; Pareja-Roman et al. 2020). As a result, the calculated bed stress minimum location has moved upstream 10 km on average (Figure 3.12b), and 15 km during peak spring discharge. Increased water depths have also decreased bed stress magnitudes and relaxed spatial gradients in bed stress upstream of x_{min} (Figure 3.12a). Along-channel bed stress profiles even drop below the critical value of τ_c for medium-coarse sand mobility (D50 = 0.5 mm) during average spring season discharge ($Q_R \leq 600$ m3 s−1), hinting at a zone of limited mobility and temporary storage of medium sands. Indeed, most of the sediment delivered to the estuary turbidity maximum (ETM) likely originates from bed storage within the tidal freshwater river reach that extends from roughly Rkm 150 to 200 (Sommerfield and Wong 2011). Material likely accumulates upstream of x_{min} during low flows until river discharge increases enough to generate bed stresses greater than τc through the bed stress minimum. According to Equation 16, this threshold occurs when $Q_R \geq 600$ m^3 s^{-1} for $H = 8$ m, but when $Q_R \geq 375$ m^3 s^{-1} under historical channel depths. The deposition zone also spans a longer stretch of the river presently than was the case in the 19th century. During low river discharge ($Q_R = 330$ m^3 s^{-1}), τ_{ebb} is less than τ_c between Rkm 118 and 206 when $H = 8$ m, but between Rkm 127 and 163 when $H = 5$ m (Figure 3.12a). In other words, the Delaware Estuary now likely stores a larger volume of sediment over a greater area that requires higher river discharge to disperse than was the case before the channel was deepened.
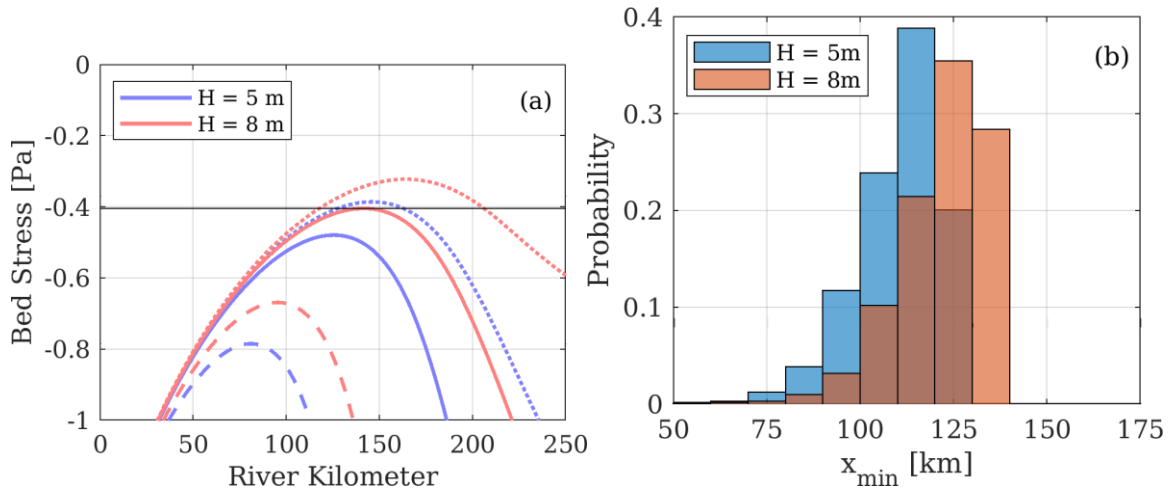
Figure 3.12. Left: Bed stress profiles (Equation 16) in idealized Delaware Estuary for river discharge of 330 (dotted lines), 600 (solid lines), and 2,500 (dashed lines) m^3s^{-1} assuming historical (blue lines) and contemporary channel depths (red lines). Solid black line denotes critical bed stress for movement of medium-coarse sand ($D_{50} = 0.5$ mm). Right: Delaware Estuary x_{min} as calculated using Equation 20 using river discharge measurements > 330 m^3s^{-1} collected between 2000 and 2020 at USGS Station 01463500 (~Rkm 200).

3.6.3 Hudson River

The Hudson River also features seasonal storage of sediment in the tidal-freshwater reach and downriver fining of bed composition. Ralston and Geyer (2017) note that the tidal freshwater reach of the river (upstream of Poughkeepsie, ~Rkm 120) traps about 40% of the sediment input from the watershed. Measurements by Nitsche et al. (2007) highlight a downstream fining of grain size from fluvially sourced sand/gravel to mud between roughly Rkm 200 and Rkm 100. Indeed, x_{min} is close to Rkm 150 during spring freshet conditions ($Q_R = 2,000$ m3 s−1) (Figure 3.13a), and over the past 20 years, the minimum value for xmin is estimated at about 110 km on 29th of August 2011. Furthermore, bed stress profiles in the Hudson River imply convergent sediment fluxes

198

upstream of x_{min} during higher river discharge ($Q_R > 1,000\text{m}^3\ \text{s}^{-1}$), and little to no

transport of medium sand ($D_{50} = 0.3$ mm) upstream of Rkm 200 during lower river

discharge ($Q_R \approx 100\ \text{m}^3\ \text{s}^{-1}$). Thus, sediments are likely trapped upstream of x_{min} due to

convergent sediment fluxes during high discharge, with the coarser fraction ($D_{50} \geq 0.3$

mm) also experiencing limited transport during low discharge where τ_{ebb} drops below τ_c.
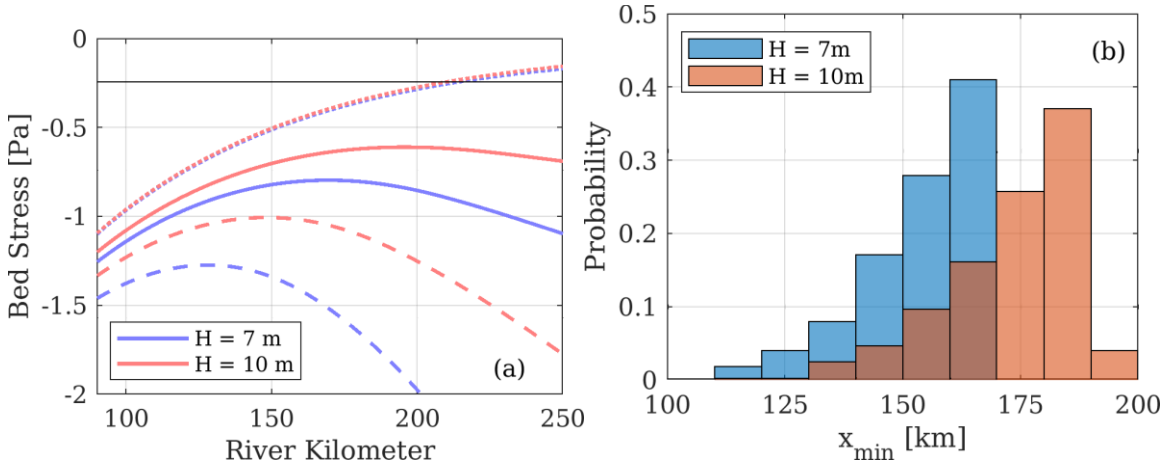
Figure 3.13. Left: Bed stress profiles (Equation 16) in idealized Hudson River Estuary for river discharge of 100 (dotted lines), 1,000 (solid lines), and 2,000 (dashed lines) m^3s^{-1} assuming historical (blue lines) and contemporary channel depths (red lines). Solid black line denotes critical bed stress for movement of medium sand ($D_{50} = 0.3$ mm). Right: Hudson River Estuary x_{min} as calculated using Equation 20 using river discharge measurements $> 1,000\ \text{m}^3\text{s}^{-1}$ collected between 2000 and 2020 at USGS Station 01358000 (~Rkm 240). In this figure, the river is evaluated upstream of Newburgh (~ Rkm 90) in order to honor the assumption of a convergent channel in the derivation of Equation 20.

Up to Rkm 240, the Hudson River has been deepened from about 7 m to 10 m

between 1860 and 2015 (Ralston et al. 2019), which has moved the bed stress minimum

calculated by Equation 20 upstream about 20 km. For example, the average value for x_{min}

has increased from 150 to 170 km (Figure 3.13b). Increased water depths have also

reduced bed stress magnitudes upstream of the bed stress minimum in the Hudson River,

which may have reduced the trapping efficiency upstream of x_{min} during higher river discharge.

Due to climate change, water withdrawal, and flow regulation, river discharge in the Hudson River during the spring freshet has decreased by about 17% (Ralston et al. 2019). Assuming a spring freshet discharge of 2,400 m^3 s^{-1} puts the bed stress minimum close to Rkm 120 under historical channel depths (Equation 20). When Q_R equals 2,000 m^3 s^{-1} and H equals 7 m, the x_{min} estimate resides near Rkm 130 (Figure 3.13a). Thus, the bed stress minimum location during the freshet has likely moved upstream by about 20 km due to channel deepening and another 10 km due to changes in river discharge. Especially with the Hudson, natural variations in depth are substantial and the river can be much deeper than the average (Nitsche 2007); hence, localized, geometrically fixed hotspots of deposition may occur. Therefore, the upstream x_{min} shift suggested by theory should be interpreted as a general tendency, rather than an absolute.

3.6.4   Further Considerations

The above examples may underestimate historical shifts in x_{min}, because the tidal amplification observed in many deepened estuaries and flow regulated rivers (Chernetsky et al. 2010; Winterwerp et al. 2013; Al-bahadily 2020; Talke and Jay 2020; Pareja-Roman et al. 2020) is not considered. As hypothesized in the Introduction, an increase in tidal velocity U_{T0} (or decrease in tidal damping p) will increase x_{min} (Figure 3.8a), which could lead to greater discrepancies between historical and modern x_{min} positions. Likewise, increased tidal velocities during spring tides will shift x_{min} further upstream than during neap tides, but the neap/spring shift will attenuate under larger river

discharges. Further insight into the effects of tidal interactions on x_{min} is limited using the theory developed herein because only one tidal constituent is considered. The introduction of additional constituents at the ocean boundary will alter the functional form of the Fourier coefficients (Equations 7 and 8) so a new relationship between x_{min} and forcing variables must be developed. Such an endeavor is beyond the scope of this paper, but would provide a worthwhile complement to the results described above–especially for mixed-semidiurnal systems like the LCRE, which can produce tidal asymmetries through the interaction between semidiurnal and diurnal constituents (Hoitink et al. 2003; Nidzieko 2010).

The evaluation in this paper focuses on the bed stress during ebb because it is assumed that this is the most energetic time period with the strongest likelihood of significant transport (Equation 16). However, Aubrey and Speer (1985) demonstrate that certain U_T and U_4 phase differences produce flood dominant currents, which can control the direction of transport and fate of sediments in an estuary. There are two river discharge thresholds to consider in this regard:

1. Moderate/strong river discharge ($U_R > U_4$) wherein the velocity is ebb dominant regardless of the phase difference between U_T and U_4. In fact, phase relations which produce flood dominant tidal velocity ($U_T + U_4$) will, under these circumstances, produce ebb dominant total velocity ($U_T + U_4 + U_R$) in both magnitude and duration.

2. Low river discharge ($U_R < U_4$) wherein ebb-flood dominance depends on phase difference between U_T and U_4.

Thus, the assumption that the maximum bed stress occurs during ebb, regardless of U_T and U_4 phase difference, requires that $U_R > U_4$. This condition is satisfied in the Columbia River for $Q_R > 2,000$ m^3 s^{-1} , and in the Hudson River for $Q_R > 1,000$ m^3 s^{-1} . Coincidentally these two discharge thresholds are the same for the development of a bed stress minimum. In other words, if $Q_R < 2,000$ m^3 s^{-1} in the LCRE, then no bed stress minimum occurs. Thus, the ebb dominant assumption fails only when there is no bed stress minimum to examine.

The Delaware River is different from the other two examples because its cross section is much larger, and $U_R < U_4$ near and downstream of x_{min} for all discharge conditions. In addition, U_T and U_4 are roughly in phase upstream of Rkm 40 (Pareja-Roman et al. 2020). Therefore, below x_{min} the maximum velocity occurs on flood tide not ebb. Upstream of x_{min}, however, $U_R > U_4$ and the total velocity is ebb dominant. Thus, x_{min} occurs near the transition between ebb dominant currents upstream and flood dominant currents downstream. The convergence in the velocity field set up by tidal asymmetry traps sediment and is augmented by the bed stress minimum.

The motivation for this study stemmed from observations of high volumes of sediment deposition in the Lower Columbia River FNC within the energy dissipation (bed stress) minimum reach. The analytical development provides insight into how the bed stress minimum migrates according to river discharge and channel geometry, yet

further study of how this relationship manifests in the sediment transport patterns is warranted. While AdH simulations and bed stress profiles (Equation 16) suggest sediment accumulation near x_{min} due to convergent sediment fluxes, the magnitude of deposition cannot be specified based solely on the considerations discussed in this paper. Guo et al. (2014) employed a 1-D hydrodynamic model to examine the equilibrium bed elevation in the Yangtze estuary and found the upper reaches of the river to favor aggradation during high river discharge, resulting in shoaling on the order of 2-3 meters over the course of several hundred years between approximately Rkm 200 and 550. Using the parameters outlined in their study, Equations 21 and 16 estimate a bed stress minimum at Rkm 150, with convergent sediment fluxes extending 300 km upstream of that point, which suggests a link between the bed stress minimum and long-term deposition patterns. Bed stress profiles imply that more material becomes trapped near the bed stress minimum as x_{min} decreases, but further research is needed in order to better understand the depositional consequences for changes in x_{min}.

Bed stress profiles in systems with strong topography exhibited a bed stress maximum upstream of x_{min} (Figure 3.4b). Together, the location and magnitude of the bed stress minimum and maximum scale the sediment flux convergence upstream of x_{min}, and so further study of the bed stress maximum could help clarify how changes in channel depth and river discharge influence sediment deposition in tidal rivers. The bed stress maximum was observed in areas where U_R dominated currents near the bed (Figure 3.5b), and apparently resulted from opposing gradients in river width and river depth. While Equation 16 leads to an implicit formula for x_{min}, $4/\pi\ U_T^2 - 7/\pi\ U_R^2$, it is not capable of

producing a bed stress maximum because the tidal frequency bed stress is overestimated as U_R/U_T grows larger (Figure 3.2). Investigation of the bed stress maximum could be carried out using different approximations to a_2 and a_0, or perhaps a numerical approach defining x_{min}.

Observations by Friedrichs (1995) in 26 tidal systems imply that the bed stress in an alluvial system will uniformly tend towards a single value, the stability shear stress τ_s that maintains a zero gradient in the net along-channel sediment transport. What does this mean for the theory evaluated herein, where the existence of a bed stress minimum and maximum requires along-channel variation in bed stress? It means that a constant depth, width-convergent tidal river is out of equilibrium with regards to the spatial distribution of bed stress, and will continually accrete material near the bed stress minimum in order to establish spatially uniform sediment transport (cf. Pittaluga et al. 2015). This result has profound implications for managing dredged material in alluvial tidal rivers, which have been progressively modified to emulate a constant depth channel to accommodate large container vessels. Moreover, there are also many systems that are not alluvial, where hard-rock topography and/or manmade structures limit the ability of the system to adjust toward a stable profile; some reaches of the LCRE are in this category. Such systems are also likely to need continual dredging.

3.7   Summary and Conclusions

Long-term trends in sediment transport have substantial implications for managing ecosystems and infrastructural investments in rivers. The spatial distribution of bed stress in tidal rivers that controls sand transport exhibits system scale patterns that manifest through non-linear interactions between tides and river discharge. The non-linear interactions between tidal forcing and river flow can lead to a bed stress minimum, which has previously been identified as a contributing factor to persistent, anomalous sand accumulation in the lower reaches of the Columbia River (Jay et al. 1990). Together with local topographic controls on bed stress (not discussed here), the variations in tidal forcing and river flow produced conditions for deposition of sand throughout the estuary/tidal river domain, sometimes far upstream of salinity intrusion and the traditional estuary turbidity maximum.

In this study, a Fourier series decomposition of the bed stress was used to develop an expression for how changes to river discharge and channel geometry influence the location of the bed stress minimum (x_{min}) . While x_{min} was found to be topographically fixed by the channel convergence length scale, factors increasing river velocity shift x_{min} downstream, and those increasing tidal velocity shift x_{min} upstream. We note that flow regulation and channel deepening work together to move x_{min} upstream, suggesting the locus of sand deposition has migrated as rivers have been progressively modified.

The theory developed herein was applied to idealized geometries approximating the Lower Columbia River, the Delaware River, and the Hudson River. Because of differences in channel geometry and river discharge, these systems display a wide range

of sediment transport behavior associated with the bed stress minimum. In particular, they differ in the importance of river flow. In rivers with higher river velocity (like the LCRE), $|\tau_{ebb}|$ is everywhere greater than τ_c, while in lower velocity rivers like the Delaware River, $|\tau_{ebb}(x)| \sim \tau_c$. The Hudson is intermediate between the other two systems. Analytical representations of bed stress profiles and x_{min} in these systems suggest:

- The locus of deposition is determined primarily by spatial gradients in bed stress in alluvial systems with higher river velocity, and by transport thresholds in lower velocity rivers. In the former, deposition peaks during high river discharge when gradients in bed stress are greatest, and in the latter deposition can increase during lower river discharge when τ_{ebb} drops below τ_c.

- In high river velocity systems like the Columbia a river discharge threshold Q_{R0} exists, above which x_{min} can be exported to the ocean, feeding sediment to the littoral system. Flow regulation can decrease the frequency of such events.

- Transport thresholds in lower velocity rivers likely manifest as seasonal storage of sediments in the upper river that disperse when river discharge is large enough. Channel deepening has apparently increased the frequency and spatial extent of storage in the tidal-freshwater reach of the Delaware Estuary.

- Channel deepening leads to decreased bed stress magnitudes and bed stress gradients, which may decrease shoaling upstream of x_{min} in high velocity rivers, yet increase shoaling in low velocity rivers.

- Down-river fining of bed material features prominently in low-velocity rivers because $|\tau_{ebb}(x)| \cong \tau_c$. This can be particularly important in governing the substrate

206

composition of in-water habitats, and should be considered when evaluating the influence of climate change and anthropogenic activities on habitat quality.

3.8   References

Al-bahadily, Aqeel. (2020). Long Term Changes to the Lower Columbia River Estuary (LCRE) Hydrodynamics and Salinity Patterns. PhD thesis. Portland State University.

Allen, G. P., Salomon, J. C., Bassoullet, P., Du Penhoat, Y., & De Grandpre, C. (1980). Effects of tides on mixing and suspended sediment transport in macrotidal estuaries. *Sedimentary Geology*, *26*(1-3), 69-90.

Aubrey, D. G., & Speer, P. E. (1985). A study of non-linear tidal propagation in shallow inlet/estuarine systems Part I: Observations. *Estuarine, coastal and shelf science*, *21*(2), 185-205.

Branch, R. A., Horner-Devine, A. R., Chickadel, C. C., Talke, S. A., Clark, D., & Jessup, A. T. (2021). Surface turbulence reveals riverbed drag coefficient. *Geophysical Research Letters*, *48*(10), e2020GL092326.

Burchard, H., & Baumert, H. (1998). The formation of estuarine turbidity maxima due to density effects in the salt wedge. A hydrodynamic process study. *Journal of Physical Oceanography*, *28*(2), 309-321.

Burchard, H., Schuttelaars, H. M., & Ralston, D. K. (2018). Sediment trapping in estuaries. *Annual review of marine science*, *10*, 371-395.

Buschman, F. A., Hoitink, A. J. F., Van Der Vegt, M., & Hoekstra, P. (2009). Subtidal water level variation controlled by river flow and tides. *Water Resources Research*, *45*(10).

Chant, R. J., Fugate, D., & Garvey, E. (2011). The shaping of an estuarine superfund site: Roles of evolving dynamics and geomorphology. *Estuaries and Coasts*, *34*, 90-105.

Chatanantavet, P., Lamb, M. P., & Nittrouer, J. A. (2012). Backwater controls of avulsion location on deltas. *Geophysical Research Letters*, *39*(1).

Chernetsky, A. S., Schuttelaars, H. M., & Talke, S. A. (2010). The effect of tidal asymmetry and temporal settling lag on sediment trapping in tidal estuaries. *Ocean Dynamics*, *60*(5), 1219-1241.

Dalrymple, R. W., Zaitlin, B. A., & Boyd, R. (1992). Estuarine facies models; conceptual basis and stratigraphic implications. *Journal of Sedimentary Research*, *62*(6), 1130-1146.

de Jonge, V. N., Schuttelaars, H. M., van Beusekom, J. E., Talke, S. A., & de Swart, H. E. (2014). The influence of channel deepening on estuarine turbidity levels and dynamics, as exemplified by the Ems estuary. *Estuarine, Coastal and Shelf Science*, *139*, 46-59.

Dijkstra, Y. M., Schuttelaars, H. M., & Burchard, H. (2017). Generation of exchange flows in estuaries by tidal and gravitational eddy viscosity-shear covariance (ESCO). *Journal of Geophysical Research: Oceans*, *122*(5), 4217-4237.

Dijkstra, Y. M., Schuttelaars, H. M., Schramkowski, G. P., & Brouwer, R. L. (2019). Modeling the transition to high sediment concentrations as a response to channel

deepening in the Ems River Estuary. *Journal of Geophysical Research: Oceans*, *124*(3), 1578-1594.

DiLorenzo, J. L., Huang, P., Thatcher, M. L., & Najarian, T. O. (1993, September). Dredging impacts on Delaware Estuary tides. In *Estuarine and Coastal Modeling* (pp. 86-104). ASCE.

Dronkers, J. J. (1964). Tidal computations in rivers and coastal waters. North-Holland Publishing Company.

Dyer, K. (1986). Coastal and estuarine sediment dynamics. John Wiley and Sons.

Dyer, K. R. (1995). Sediment transport processes in estuaries. In *Developments in Sedimentology* (Vol. 53, pp. 423-449). Elsevier.

Elias, E. P., Gelfenbaum, G., & Van der Westhuysen, A. J. (2012). Validation of a coupled wave-flow model in a high-energy setting: The mouth of the Columbia River. *Journal of Geophysical Research: Oceans*, *117*(C9).

EPA. (2014). "RECORD OF DECISION, Lower Duwamish Waterway Superfund Site".

EPA. (2016). "RECORD OF DECISION, Lower 8.3 Miles of the Lower Passaic River Part of the Diamond Alkali Superfund Site Essex and Hudson Counties, New Jersey".

EPA. (2017). "RECORD OF DECISION, Portland Harbor Superfund Site Portland, Oregon".

Familkhalili, R., & Talke, S. A. (2016). The effect of channel deepening on tides and storm surge: A case study of Wilmington, NC. *Geophysical research letters*, *43*(17), 9138-9147.

Familkhalili, R., Talke, S. A., & Jay, D. A. (2022). Compound flooding in convergent estuaries: insights from an analytical model. *Ocean Science*, *18*(4), 1203-1220.

Festa, J. F., & Hansen, D. V. (1978). Turbidity maxima in partially mixed estuaries: A two-dimensional numerical model. *Estuarine and Coastal Marine Science*, *7*(4), 347-359.

Friedrichs, C. T. (1995). Stability shear stress and equilibrium cross-sectional geometry of sheltered tidal channels. *Journal of Coastal Research*, 1062-1074.

Friedrichs, C. T., & Aubrey, D. G. (1994). Tidal propagation in strongly convergent channels. *Journal of Geophysical Research: Oceans*, *99*(C2), 3321-3336.

Friedrichs, C. T., Armbrust, B. A., & deSwart, H. E. (1998). Hydrodynamics and equilibrium sediment dynamics of shallow, funnel-shaped tidal estuaries.

Giese, B. S., & Jay, D. A. (1989). Modelling tidal energetics of the Columbia River estuary. *Estuarine, Coastal and Shelf Science*, *29*(6), 549-571.

Guo, L., Van der Wegen, M., Roelvink, J. A., & He, Q. (2014). The role of river flow and tidal asymmetry on 1-D estuarine morphodynamics. *Journal of Geophysical Research: Earth Surface*, *119*(11), 2315-2334.

Haberman, R. (2004). Applied Partial Differential Equations with Fourier Series and Boundary Value Problems. Pearson Prentice Hall.

Helaire, L. T., Talke, S. A., Jay, D. A., & Mahedy, D. (2019). Historical changes in Lower Columbia River and estuary floods: A numerical study. *Journal of Geophysical Research: Oceans*, *124*(11), 7926-7946.

Hickson, R. E. (1930). Shoaling on the lower Columbia River. *The Military Engineer*, *22*(123), 217-219.

Hickson, R. E. (1961). Columbia River ship channel improvement and maintenance. *Journal of the Waterways and Harbors Division*, *87*(3), 71-94.

Hoitink, A. J. F., Hoekstra, P., & Van Maren, D. S. (2003). Flow asymmetry associated with astronomical tides: Implications for the residual transport of sediment. *Journal of Geophysical Research: Oceans*, *108*(C10).

Hoitink, A. J. F., & Jay, D. A. (2016). Tidal river dynamics: Implications for deltas. *Reviews of Geophysics*, *54*(1), 240-272.

Huijts, K. M. H., Schuttelaars, H. M., De Swart, H. E., & Friedrichs, C. T. (2009). Analytical study of the transverse distribution of along-channel and transverse residual flows in tidal estuaries. *Continental Shelf Research*, *29*(1), 89-100.

Ianniello, J. P. (1979). Tidally induced residual currents in estuaries of variable breadth and depth. *Journal of Physical Oceanography*, *9*(5), 962-974.

Jay, D. A. (1991). Green's law revisited: Tidal long-wave propagation in channels with strong topography. *Journal of Geophysical Research: Oceans*, *96*(C11), 20585-20598.

Jay, D. A., Giese, B. S., & Sherwood, C. R. (1990). Energetics and sedimentary processes in the Columbia River Estuary. *Progress in oceanography*, *25*(1-4), 157-174.

Jay, D. A., Leffler, K., & Degens, S. (2011). Long-term evolution of Columbia River tides. *Journal of waterway, port, coastal, and ocean engineering*, *137*(4), 182-191.

Jay, D. A., Borde, A. B., & Diefenderfer, H. L. (2016). Tidal-fluvial and estuarine processes in the Lower Columbia River: II. Water level models, floodplain wetland inundation, and system zones. *Estuaries and Coasts*, *39*, 1299-1324.

Jay, D. A., & Musiak, J. D. (1994). Particle trapping in estuarine tidal flows. *Journal of Geophysical Research: Oceans*, *99*(C10), 20445-20461.

Jay, D. A., & Naik, P. K. (2011). Distinguishing human and climate influences on hydrological disturbance processes in the Columbia River, USA. *Hydrological Sciences Journal*, *56*(7), 1186-1209.

Jay, D. A., & Simenstad, C. A. (1996). Downstream effects of water withdrawal in a small, high-gradient basin: erosion and deposition on the Skokomish River delta. *Estuaries*, *19*, 501-517.

Jay, D. A., & Smith, J. D. (1990). Circulation, density distribution and neap-spring
transitions in the Columbia River Estuary. *Progress in Oceanography*, *25*(1-4),
81-112.

Jay, D. A., Orton, P. M., Chisholm, T., Wilson, D. J., & Fain, A. M. (2007). Particle
trapping in stratified estuaries: Consequences of mass conservation. *Estuaries and
Coasts*, *30*, 1095-1105.

Jay, D. A., Talke, S. A., Hudson, A., & Twardowski, M. (2015). Estuarine turbidity
maxima revisited: Instrumental approaches, remote sensing, modeling studies,
and new directions. *Developments in sedimentology*, *68*, 49-109.

de Jonge, V. N., Schuttelaars, H. M., van Beusekom, J. E., Talke, S. A., & de Swart, H. E.
(2014). The influence of channel deepening on estuarine turbidity levels and
dynamics, as exemplified by the Ems estuary. *Estuarine, Coastal and Shelf
Science*, *139*, 46-59.

Kaminsky, G. M., Ruggiero, P., Buijsman, M. C., McCandless, D., & Gelfenbaum, G.
(2010). Historical evolution of the Columbia River littoral cell. *Marine
Geology*, *273*(1-4), 96-126.

Lanzoni, S., & Seminara, G. (2002). Long-term evolution and morphodynamic
equilibrium of tidal channels. *Journal of Geophysical Research:
Oceans*, *107*(C1), 1-1.

Meade, R. H. (1969). Landward transport of bottom sediments in estuaries of the Atlantic
coastal plain. *Journal of Sedimentary Research*, *39*(1), 222-234.

Naik, P. K., & Jay, D. A. (2011). Human and climate impacts on Columbia River hydrology and salmonids. *River Research and Applications*, *27*(10), 1270-1276.

Naik, P. K., & Jay, D. A. (2011). Distinguishing human and climate influences on the Columbia River: Changes in mean flow and sediment transport. *Journal of hydrology*, *404*(3-4), 259-277.

Nidzieko, N. J. (2010). Tidal asymmetry in estuaries with mixed semidiurnal/diurnal tides. *Journal of Geophysical Research: Oceans*, *115*(C8).

Nitsche, F. O., Ryan, W. B. F., Carbotte, S. M., Bell, R. E., Slagle, A., Bertinado, C., ... & McHugh, C. (2007). Regional patterns and local variations of sediment distribution in the Hudson River Estuary. *Estuarine, Coastal and Shelf Science*, *71*(1-2), 259-277.

Nittrouer, J. A., Shaw, J., Lamb, M. P., & Mohrig, D. (2012). Spatial and temporal trends for water-flow velocity and bed-material sediment transport in the lower Mississippi River. *Bulletin*, *124*(3-4), 400-414.

NOAA tide and current predictions. https://tidesandcurrents.noaa.gov/map/index.html. *Accessed: 01 September 2021.*

Pareja-Roman, L. F., Chant, R. J., & Sommerfield, C. K. (2020). Impact of historical channel deepening on tidal hydraulics in the Delaware Estuary. *Journal of Geophysical Research: Oceans*, *125*(12), e2020JC016256.

Pittaluga, B.M., Tambroni, N., Canestrelli, A., Slingerland, R., Lanzoni, S., & Seminara, G. (2015). Where river and tide meet: The morphodynamic equilibrium of alluvial estuaries. *Journal of Geophysical Research: Earth Surface*, *120*(1), 75-94.

Postma, H. (1961). Transport and accumulation of suspended matter in the Dutch Wadden Sea. *Netherlands Journal of Sea Research*, *1*(1-2), 148-190.

Proudman, J. (1952). Dynamical oceanography. Dover.

Ralston, D. K., & Geyer, W. R. (2017). Sediment transport time scales and trapping efficiency in a tidal river. *Journal of Geophysical Research: Earth Surface*, *122*(11), 2042-2063.

Ralston, D. K., Talke, S., Geyer, W. R., Al-Zubaidi, H. A., & Sommerfield, C. K. (2019). Bigger tides, less flooding: Effects of dredging on barotropic dynamics in a highly modified estuary. *Journal of Geophysical Research: Oceans*, *124*(1), 196-211.

Savant, G., Berger, C., McAlpin, T. O., & Tate, J. N. (2011). Efficient implicit finite-element hydrodynamic model for dam and levee breach. *Journal of Hydraulic Engineering*, *137*(9), 1005-1018.

Savenije, H. H. (2005). *Salinity and tides in alluvial estuaries*. Gulf Professional Publishing.

Sherwood, C. R., Jay, D. A., Harvey, R. B., Hamilton, P., & Simenstad, C. A. (1990). Historical changes in the Columbia River estuary. *Progress in Oceanography*, *25*(1-4), 299-352.

Sommerfield, C. K., Madsen, J. A., & Hall, P. (2003). Sedimentological and geophysical survey of the upper Delaware estuary. *Final Report to the Delaware River Basin Commission, West Trenton, New Jersey*.

Sommerfield, C. K., & Wong, K. C. (2011). Mechanisms of sediment flux and turbidity maintenance in the Delaware Estuary. *Journal of Geophysical Research: Oceans*, *116*(C1).

Speer, P. E., & Aubrey, D. G. (1985). A study of non-linear tidal propagation in shallow inlet/estuarine systems Part II: Theory. *Estuarine, Coastal and Shelf Science*, *21*(2), 207-224.

Talke, S. A., Mahedy, A., Jay, D. A., Lau, P., Hilley, C., & Hudson, A. (2020). Sea level, tidal, and river flow trends in the lower Columbia River Estuary, 1853–present. *Journal of Geophysical Research: Oceans*, *125*(3), e2019JC015656.

Talke, S. A., de Swart, H. E., & Schuttelaars, H. M. (2009). Feedback between residual circulations and sediment distribution in highly turbid estuaries: an analytical model. *Continental Shelf Research*, *29*(1), 119-135.

Talke, S. A., de Swart, H. E., & De Jonge, V. N. (2009). An idealized model and systematic process study of oxygen depletion in highly turbid estuaries. *Estuaries and coasts*, *32*, 602-620.

Talke, S. A., Familkhalili, R., & Jay, D. A. (2021). The influence of channel deepening on tides, river discharge effects, and storm surge. *Journal of Geophysical Research: Oceans*, *126*(5), e2020JC016328.

217

Talke, S. A., & Jay, D. A. (2020). Changing tides: The role of natural and anthropogenic factors. *Annual review of marine science*, *12*, 121-151.

Templeton, W. J., & Jay, D. A. (2013). Lower Columbia River sand supply and removal: estimates of two sand budget components. *Journal of waterway, port, coastal, and ocean engineering*, *139*(5), 383-392.

USACE. 2020. USACE RSM Program Update. https://rsm.usace.army.mil/techtransfer/FY20/RSM-IPR-Aug2020/briefs/1_01_2020_RSM_ERDC_ProgramUpdate.pdf. *Accessed 04 August 2021*.

Winterwerp, J. C., Wang, Z. B., Van Braeckel, A., Van Holland, G., & Kösters, F. (2013). Man-induced regime shifts in small estuaries—II: a comparison of rivers. *Ocean Dynamics*, *63*, 1293-1306.

3.9 Appendices

3.9.1 Appendix A: Simplification for Equation 20

The location of the bed stress minimum is given by an implicit formula (Equation 19), which makes it challenging to interpret the sensitivity of x_{min} to the relevant parameters. An explicit approximation is obtained by assuming $e^{(2\gamma-2p)x/3}$ is approximately one for the typical ranges of p, γ, and x (Equation 20). While the average value of $e^{(2\gamma-2p)x/3}$ is equal to one, the probability distribution of this function spans from approximately zero to five when using the parameter ranges noted in Section 1 (Figure 3.14). In order for $e^{(2\gamma-2p)x/3}$ to equal one, the exponent must equal zero, which occurs when the damping modulus equals the convergence length scale ($p=\gamma$). Assuming a convergent channel ($\gamma <$ 0), values of $e^{(2\gamma-2p)x/3}$ are greater than one when $p/\gamma > 1$ and less than one when $p/\gamma < 1$.

When $p/\gamma < 1$, Equation 20 tends to underestimate the analytical bed stress minimum location. For example, when using values from Table 3.2, p/γ equals 0.8 and x_{min} is estimated to be 62 and 47 km when using Equations 19 and 20, respectively (Figure 3.15). However, both equations are based on an approximation to the bed stress profile during ebb ($-4/\pi\ U_T^2 - 7/\pi\ U_R^2$) that exhibits a bed stress minimum that is further downstream than the analytical value (a_0-a_2; see Figure 3.14). For this reason, Equation 20 underestimates, while Equation 19 overestimates the analytical bed stress minimum location, which is close to 52 km (Figure 3.15).

Weaker convergence relative to damping, $p/\gamma > 1$, causes Equation 20 to overestimate the analytical bed stress minimum location. When using the values in Table 3.2, but with $L_e = 70$ km, p/γ equals 1.4 and x_{min} is estimated to be 87 and 132 km when

using Equations 19 and 20, respectively (Figure 3.15). The analytical value (a_0-a_2) is close to 104 km.

When river discharge decreases, the discrepancies between the analytical bed stress minimum location and Equation 20 grow because x increases, driving $e^{(2\gamma-2p)x/3}$ further from unity. Weaker convergence accentuates the discrepancies because spatial gradients in bed stress are less than in more convergent channels. Estimates provided by Equation 20 are thus least accurate in weakly convergent rivers during low river discharge (see Figures 3.4 and 3.6).
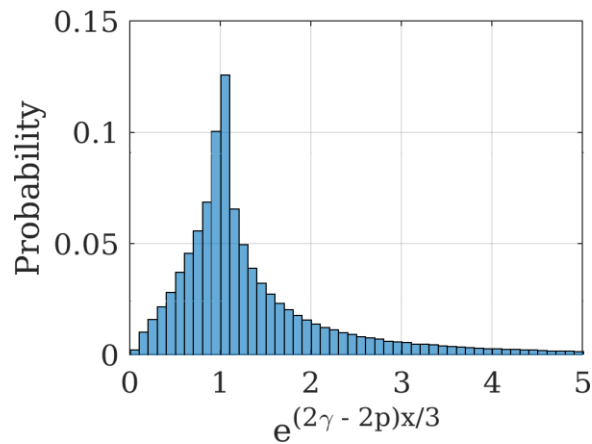

Figure 3.14. Probability distribution of $e^{(2\gamma-2p)x/3}$ in Equation 19. Ranges for each variable are as follows: $p = [-5(10-5), -1(10-6)]$ m^{-1}, $\gamma = [-5(10-5), -1(10-5)]$ m^{-1} and $x = [0, 100]$ km.
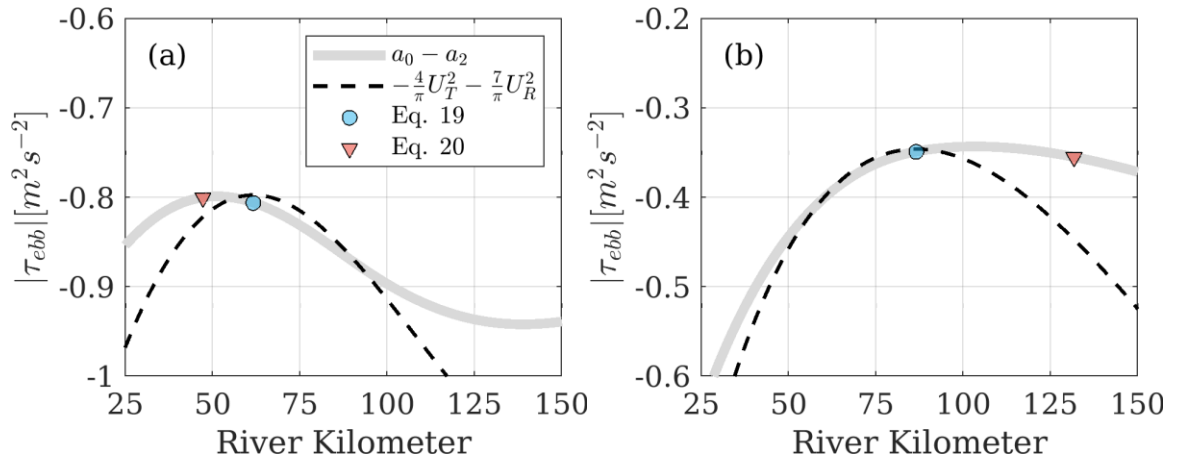
Figure 3.15. Left: Bed stress profile using Equation 16 and values listed in Table 3.2, and bed stress minimum location calculated using Equation 19 (blue circle) and Equation 20 (red triangle). Right: Bed stress profiles and minima using the values listed in Table 3.2, except $L_e = 70$km.

Summary and Conclusion

4.1   A Tool for Studying Bed Stress and Sediment Transport in Estuaries.

Sediment transport processes influence virtually every aspect of riverine and estuarine environments. Human activities and climate variability can fundamentally change sediment transport patterns, which can impact the ecological, economic, and cultural resources that rivers and estuaries provide and support. As human populations rise, our dependence and impact on rivers and estuaries increases in magnitude and scope. And so, understanding the mechanisms driving sediment transport in rivers and estuaries is crucial for ensuring the long-term viability of the benefits that these ecosystems provide.

One aspect of sediment transport that is poorly understood in rivers and estuaries—particularly in mixed tide systems—is tidal asymmetry. As discussed in the literature, tidal velocity asymmetry in estuaries can greatly influence sediment transport patterns in estuaries. However, sediment transport is fundamentally a function of bed stress, not velocity, and so our understanding of tidal asymmetry driven sediment transport is incomplete. This study is the first of its kind to directly evaluate spatial and temporal variability of bed stress asymmetry in rivers and estuaries. The evaluation is summarized by an analytical framework that helps improve understanding of sediment transport mechanisms, particle trapping/sorting, and changes in channel morphology. The framework can help project managers, scientists and engineers design and maintain waterborne transportation systems, develop restoration and mitigation activities, and

222

regulate water quality in rivers and estuaries. The prominent features of this framework are as follows; it:

- Classifies bed stress dynamics for semidiurnal, diurnal, and mixed-tide estuaries.
- Identifies the tidal species and constituents that are most influential to residual sediment transport patterns.
- Provides limits for ebb-dominant or flood-dominant bed stress and sediment transport.
- Distinguishes transport behavior based on particle size/transport thresholds.
- Directly relates changes in forcing variables (e.g., river discharge) and morphology (e.g., channel deepening) to sediment transport processes.
- Clarifies the sediment transport mechanisms governing morphological change and stability.
- Can be calibrated to water level and river discharge measurements to evaluate bed stress variation over seasonal and interannual timescales.
- Is applicable to non-stationary tides and extreme events.

While this framework was designed for evaluating bed stress patterns in rivers and estuaries, it is subject to the following limitations; it:

- Focuses on fluvial and tidal mechanisms and does not consider sediment transport by other processes (e.g., wind or waves).
- Does not consider settling or resuspension lags, which are known to influence transport of fine sediments, especially in low energy environments.
- Does not consider circulation processes arising from vertical stratification of the salinity field, which limits application to coarser sediment and bed load transport when vertical shear of salinity or velocity is strong.
- The framework is 1-Dimensional and most suitable for (predominately) uniaxial currents.

4.2   Insights Furnished by the Tidal Asymmetry Framework

In this study, theoretical exploration of the analytical framework (Chapter 1) and its application to observations in real estuaries (Chapter 2) clarified the following concepts:

- Sediment transport can be controlled by diurnal tidal constituents in estuaries traditionally classified as semidiurnal, and vice versa, which can confound efforts to understand and describe sediment transport patterns.
- Sediment can move in a direction opposite to the residual velocity, the tidal velocity asymmetry, or even the residual bed stress.
- Different sediment classes can move in different directions within the same velocity field due to disparities in their critical bed stress.
- Linear tidal asymmetry driven by phase relationships between astronomical tidal constituents can be much stronger than nonlinear asymmetry driven by shallow water overtides.
- The tidal dynamics of residual bed stress patterns are not determined solely by ratios, or the relative strength, of tidal constituent velocity amplitudes, but also the relative velocity phasing between tidal constituents.
- Spatial gradients in the residual bed stress, and by extension changes in morphology, are controlled by a balance between along channel variations in the residual flow and tidal velocity amplitudes and phases.
- Particle trapping can greatly increase, or only occur, when residual currents exceed or drop below certain thresholds (defined by the non-dimensional numbers), which can influence sediment supply and channel shoaling.
- Residual bed stress and sediment transport vary over fortnightly, semiannual, annual, and longer cycles, due to the interaction between tidal constituents.
- Morphodynamic equilibrium may only be approximate or attained during certain time periods in real estuaries because the tidal bed stress asymmetry is always

224

changing, due both to tidal constituent interactions and variability in river discharge and other forcing variables.

A particular case of bed stress asymmetry (Case I; Concordant, or Strong Asymmetry) was also explored for ebb-dominant bed stress and residual currents in a convergent estuary with strong river discharge (Chapter 3). The results therein highlight the following:

- Opposing along channel gradients in tidal and residual velocity lead to a bed stress minimum near the convergence length scale of the estuary.
- Upstream of the bed stress minimum, convergent bed stress gradients develop, which can contribute to particle trapping, deposition, and/or temporary storage of sediments on the bed.
- High river discharge and strong channel convergence increase bed stress convergence, while increases in mean channel depth and channel width reduce bed stress convergence.

4.3   Next Steps and Future Research

Although this study helps clarify sediment transport patterns in estuaries, it represents the first step in systematically evaluating tidal bed stress asymmetry and further research is needed to better understand the causes and consequences of bed stress asymmetry. In particular, the results herein motivate the following analyses:

- <u>Application of the framework to observations in other estuaries.</u> The near bed velocity measurements collected by NOAA were instrumental to exploring along-channel variability of bed stress asymmetry in the Delaware Estuary and San Francisco Bay. Observations are/will become available in many other systems (e.g., Savannah Harbor in 2023, Charleston Harbor in 2024, and the Columbia

River in 2023), and analysis thereof would help clarify and extend the results obtained herein.

- Evaluation of bed stress asymmetry in side-channels, lateral bays, and tidal flats. The analysis herein utilizes observations within the main channel of the Delaware Estuary and San Francisco Bay. However, further insight into the fate and transport of sediment could be attained by extending the analysis to peripheral regions, the physical dynamics of which are typically less studied than mainstem locations.

- Extension of bed stress asymmetry analysis in San Francisco Bay to include interannual variability in residual velocity. While water level measurements were able to elucidate long term variability in the diurnal asymmetry, long term variability in bed stress asymmetry and sediment transport cannot be evaluated without parameterization of the residual currents.

- Application of CWT_Multi to measurements of suspended sediment concentrations or sediment fluxes. This study infers sediment transport behavior using analytical representations of bed stress and observations of near bed velocity. And analysis of tidal variability in sediment fluxes could help validate and expand the conclusions herein.

- Direct assessment (modeling or observations) of sediment deposition upstream of the bed stress minimum in tidal rivers with strong river discharge.

In the context of understanding and managing estuarine ecosystems, the analyses listed above could help address/support the following research questions and practical applications:

- How do vertical and cross-channel gradients of velocity or sediment concentration influence asymmetry-driven sediment transport? How do lag effects and sediment specific behavior such as flocculation or consolidation alter the bed stress asymmetry parameter space?

- How do sediment transport patterns in estuaries vary over the 18.6-year nodal cycle? Does nodal cycle variation in bed stress asymmetry influence wetland accretion or channel shoaling? And similarly for the 4.4 and 8.8-year cycles.

- How do interannual tidal cycles influence morphodynamic equilibrium? Is estuarine morphology more dynamic during certain phases of the 18.6-year nodal cycle?

- How does tidal bed stress asymmetry influence contaminant distribution and accumulation in estuaries?

- How do system scale alterations to channel width and convergence influence erosion and deposition patterns?

- Often human alterations to rivers and estuaries are unevenly distributed (e.g., jetties built at the mouth). How does change in channel geometry and bed stress asymmetry at one location influence sediment transport and sediment supply at other locations?

- How does land reclamation and diking influence bed stress asymmetry and particle trapping? Can tidal flats be restored or constructed to intentionally shift tidal velocity phases and alter particle trapping?

- Can restoration sites or harbors be designed to passively accumulate (or export) sediment by accounting for the parameters that control tidal asymmetry in bed stress?

- Can river discharge be managed to control tidal bed stress asymmetry and mitigate channel shoaling in rivers and estuaries?